Tidal energy device hydrodynamics in non-uniform transient flows.

Chapman, John Christopher

Prifysgol Abertawe
Swansea University

Tidal Energy Device Hydrodynamics in Non-Uniform Transient Flows

John Christopher Chapman

Submitted to Swansea University in fulfilment of the requirements for the Degree of Doctor of Philosophy

Swansea University

2008

Summary

Tidal energy devices convert the flow of water induced by the tidal cycle into useful energy. Presently the most common type of tidal energy device is a horizontal axis zero head turbine. Conceptually the form of these devices is similar to modern wind turbine systems. This thesis presents the development of a flexible code that models the hydrodynamic behaviour of a tidal stream turbine rotor and its supporting structure in a non-uniform, time varying flow. Blade Element Momentum Theory (BEMT) is reviewed and its implementation is discussed. Corrections to the theory are reviewed in the context of operation in an ocean environment. The completed model operates in a three-dimensional representation of the ocean and includes the calculation of supporting structure loads using Morison's equation. The flow regime either includes boundary layer effects and a calculated wave climate or can be taken from data measured with an ADCP. Specific model features are introduced that allow realistic appraisal of the system's performance and load regime as well as specific situations such as braking of the rotor. The capability of the code is then demonstrated using a non-uniform, time varying flow and the importance of this in the design of turbine systems is discussed. The novel features introduced in this thesis are; the inclusion of non rotor-normal inflow in the BEMT equations, a new, robust approach to solving the BEMT equations and a novel blade-off modelling approach. A calibrated marine tower shadow model, a novel procedure for comparing the performance of alternative device concepts and a method to input ADCP data directly to the model system were also novel steps introduced in the thesis.

DECLARATION

This work has not previously been accepted in substance for any degree and is not being concurrentlv submitted in candidature for any degree.

Signed..... (Candidate)

Date.....14/04/09.....

STATEMENT 1

This thesis is the result of my own investigations, except where otherwise stated. Where correction services have been used, the extent and nature of the correction is clearly marked in a footnote.

Other sources are acknowledged by footnotes giving explicit references. A bibliography is appended.

Signed..... ..... (Candidate)

Date.....14/04/09.....

STATEMENT 2

I hereby give consent for my thesis, if accepted, to be available for photocopying and for inter-library loans after expiry of a bar on access approved by Swansea University.

Signed..... (Candidate)

Date.....14/04/09.....

Table of Contents

Acknowledgements

The author would like to acknowledge the financial support of the European Social fund administered by the Welsh European Funding Office and Swanturbines Ltd.

Thanks are also given to Dr. Ian Masters and Dr. James Orme for their advice, encouragement and guidance throughout the project.

Swanturbines Ltd. and its employees are also thanked for their individual collaborations throughout this period.

The author also thanks Dr. Carswell for his collaboration in the tower shadow investigation presented in this thesis.

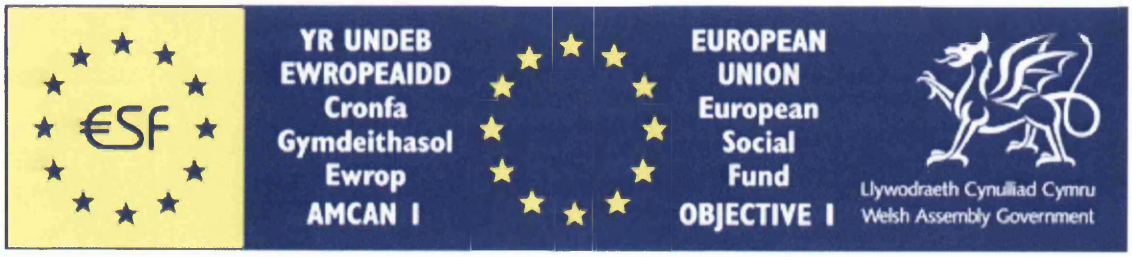

List of Figures

List of Tables

Nomenclature

Latin alphabet

A	Cross sectional stream-tube area. Distance between hub and yaw centres. Projected area of submerged member
A_0	Stream-tube area far upstream of rotor
A_1	Stream-tube area far downstream of rotor
A_s	Maximum tower wake deficit
A_{disc}	Swept area of actuator disc
a	Axial induction factor. Radius of tower in shadow calculations
a_c	Critical induction factor
$B(\psi)$	Tower shadow blockage factor
BEMT	Blade Element Momentum Theory
b	Tangential induction factor
C	Wave speed
C_a	Added mass coefficient
C_D	Drag coefficient
$C_{D'}$	Pseudo drag coefficient for tower shadow model
C_{FA}	Axial thrust coefficient
CFD	Computational Fluid Dynamics
C_L	Lift coefficient
C_{L2-D}	2D lift coefficient
C_{L3-D}	3D lift coefficient
C_m	Inertia coefficient
C_P	Power coefficient
$C_{P\text{target}}$	Target power coefficient
c	Blade chord length
c_1, c_2	Coefficients for loss factor eqn. (4.8)

D	Drag force. Wake depth. Effective Diameter
d	Normal distance between vortex sheets
d_w	Water depth
dD	Elemental drag force
dF_A	Elemental axial thrust
dF_{A1}	Momentum theory elemental axial thrust
dF_{A2}	Blade element theory elemental axial thrust
dL	Elemental lift force
dr	Element radial length
dT	Elemental torque value
dT_1	Elemental torque from momentum theory
dT_2	Elemental torque from blade element theory
F	Combined loss factor or general loss factor.
F_A	Axial force
F_I	Inertia force per unit length from Morison's equation
F_{Mor}	Hydrodynamic force per unit length in Morison's equation
F_{Rot_side}	Rotor sway force
F_D	Drag force per unit length in Morison's equation
F_{Hub}	Hub loss factor
F_{Prandtl}	Loss factor proposed by Prandtl
F_{Tip}	Tip loss factor
F_{Xu}	Loss factor proposed by Xu
f	Loss factor exponent
g	Objective function. Gravitational constant
H	Hub height from seabed. Wave height
I_{Yaw}	Yaw moment of inertia
i	Time step. Vector
j	Vector
k	Vector
L	Lift force. Wavelength

L_{Grid}	Grid length
M_{Nac}	Moment around yaw centre from nacelle
M_{Nose}	Moment around yaw centre from nose cone
$M_{Bearing}$	Resistive torque from bearing friction
M_{Rot_Yaw}	Rotor yawing moment
M_{ZN}	General yawing moment
$\dot{M}$	Mean flow rate of ADCP data
$\dot{m}$	Mass flow rate
N	Number of rotor blades
n	Power law exponent
nb	Number of blades in blade off model
P	Power
p_{amb} , p_0	Ambient pressure
p_{ud}	Pressure upstream of actuator disc
p_{dd}	Pressure downstream of actuator disc
Q	Total head of wave
R	Radius of blade tip. Rotation matrix. Boundary layer thickness
R_{hub}	Radius of blade root
R_w	Radius of wake edge from hub centre
r	Local radial distance from hub centre
$r_{yaw\ elem}$	Radial position of nacelle/ nose cone element from yaw centre
S	Translation matrix. Powles' wake model
T_c	Combined rotation and translation matrix.
T_{Gen}	Generator torque
T_{ADCP}	Required time length of ADCP data
T_{Model}	Desired modelling period
T_s	Tower shadow coefficient
TSR	Tip speed Ratio

TSR_{target}	Target *TSR*
TST	Tidal Stream Turbine
TWh/yr	Terra Watt hours per year (unit of annual energy)
U or U_{∞}	Free stream horizontal flow speed
U_1	Flow speed well downstream of rotor
U_{fs}	Free stream flow velocity
U_{local}	Local free stream flow speed (in-stream tower shadow)
U_1	Downstream flow speed
u	Local horizontal flow. Dimensionless in stream flow (tower shadow)
u_{disc}	Horizontal flow speed at actuator disc
V	Resultant inflow velocity. Volume per unit length
V_{local}	Local cross-stream flow velocity (tower shadow)
v	Dimensionless cross-stream flow (tower shadow). Flow vector in global co-ordinates.
v'	Flow vector in blade relative co-ordinates $[v_1' \; v_2' \; v_3']^T$
v_1'	Blade local flow normal to rotor plane
v_2'	Blade local flow tangential to rotor plane
v_3'	Radial blade local flow
W_s	Resultant wake velocity
W	Wake width
$X_{Hub\_to\_yaw}$	Distance between hub and yaw centres
x_p	Fractional distance along blade
x_{rotor}	Horizontal position of rotor in stream-tube
x	Dimensionless stream-wise position (tower shadow). Local axis direction
y	Dimensionless cross-stream position (tower shadow). Local axis direction

Greek alphabet

α	Angle of attack
β	Cone angle
γ	Rotor yaw angle
ΔC_L	Difference between linear extension of 2D lift curve post stall and the given lift value.
ς	Yaw angle
η	Free surface stream function
θ	Combined pitch and twist of blade. Angular position of blade from tower (shadow calculations)
Λ	Tip speed Ratio
λ	Local speed ratio
ρ	Fluid density
σ	Local blade solidity. Tilt angle
ϕ_s	Resultant outflow angle
ϕ	Resultant inflow angle
ψ	Azimuth angle or yaw error
$\psi_{spacing}$	Azimuth angle between blades
ψ_0	Half wake shadow angular section
ψ_{0nb}	Undisturbed azimuth position of blade n
Ω	Rotational speed of rotor.
Ω_{yaw}	Angular velocity of nacelle/ nose cone
$\dot{\Omega}_{yaw}$	Angular acceleration of nacelle/ nose cone
ω	Induced rotational velocity Extrapolation factor

Chapter 1: Introduction

Tidal current devices, also known as tidal stream turbines are systems that convert the energy in flowing water into kinetic energy in the device itself. In most designs, this is in the form of rotating hydrofoil blades, which are used to power an electrical generator. As the name suggests, the water flow is primarily from the tide but the technology may also capture energy from river flows and ocean currents. The type of device considered in this thesis is a horizontal axis Tidal Stream Turbine (TST). The 'horizontal axis' refers to the axis of rotation of the turbine blades and conceptually this type of turbine is much like the most common design of wind turbine. The tidal resource is significant, particularly around the UK and estimates of the available power are given in several papers reviewed in Chapter 2. This makes development of TSTs a viable commercial concern.

There are several key differences between TSTs and wind turbines, primarily due to the different fluid involved. Seawater is of the order of one thousand times denser than air and so the density of energy in a tidal flow is greater than that of wind. The rotor of a TST will therefore have a smaller diameter than that of a wind turbine of comparable power. This increased fluid density will also mean an increase in load concentration. The characteristics of the flow also differ. Base tidal flows are highly predictable but are altered by turbulence, including wave effects. Comparatively, wind is less predictable and suffers from significant variations in flow due to turbulence and gusts. The marine environment leads to sealing, biofouling and accelerated corrosion issues. Much of the early development of wind turbine systems was aided by the ability to erect small-scale turbines to test. Deployment of a tidal turbine system is far more costly and the majority of design and development must be conducted on land before a prototype is installed in the marine environment.

The aim of this body of work is to develop a model to predict both the performance and loadings on a *TST* rotor and its supporting structure. It is

intended that this would then be used in the design process to characterise the performance and loading requirements of a system as well as testing specific features and control systems. To achieve this, non-uniformities of the flow must be captured and realistic responses by the turbine system must be approximated. A low computational demand is necessary if this is to be of use in a commercial design environment and an appropriate solution is presented for the work discussed here. The following chapter provides a review of the present state of the *TST* market before reviewing relevant literature on *TST*s and from analogous fields of research. Chapter 3 provides background information on the basic theory of the modelling system and introduces a method to model flows tangential to the rotor blade. Chapter 4 discusses correction factors to the base theory and demonstrates the implementation of these corrections. Chapter 5 then demonstrates developments in the modelling system, which provides realistic modelling capabilities of specific design features and specific scenarios. Chapter 6 demonstrates scenarios where the code may be used to aid the engineering design process, particularly in the area of fatigue analysis and the application of a computer model to measured flow data. Finally, chapter 7 provides a discussion on the work presented in the thesis.

Chapter 2: A review of the use of blade element theory for modelling tidal stream turbine performance

This chapter gives a review of the literature relevant to the modelling and performance estimation of the rotor of a tidal current turbine. A brief introduction to tidal stream turbines is first provided with an insight into the present state of the industry. Existing research directly related to tidal stream turbines is covered as well as a review of relevant research from other fields. The applicability, validity and shortcomings of blade element theory are reviewed and discussed. It is seen that despite a lack of accuracy under certain conditions, the low computational demand has lead to a wide acceptance of blade element theory for modelling of turbine rotors. A number of methods to improve the approach's accuracy are also seen in the literature.

2.1 Introduction

2.1.1 The potential of tidal stream power

Marine energy is a large and, at present, largely untapped source of non-polluting renewable energy [1]. One component of this, tidal stream energy, has a large supply potential, particularly around the UK. It has been estimated that the size of the tidal stream resource around the UK is between 18 and 128 TWh/yr [2-5] the large variation in these values is due to the approaches taken in making the estimates. The economically extractable portion of this power is estimated to be between 10 and 22 TWh/yr [4-6]. Findings from the Marine Energy Challenge [2] suggest that combined wave and tidal stream energy could provide 20% of Britain's energy demand.

Because of this promising potential, interest in tidal stream energy capture is growing. In the UK, the Carbon Trust, set up by the UK government, has commissioned the Marine Energy Challenge to support research into the field

of marine energy production systems [4-9]. The Environment Agency [10] and Scottish Heritage [11] state that Britain is well placed to utilise its resource but emphasise that care must be taken to avoid any detrimental effects on the environment. The Welsh assembly [12] and the Scottish Executive [13] have recognised the potential for tidal stream turbines to provide both power and a growth industry to the UK but again accept that there are many considerations to be taken into account when developing this technology.

Bedard *et al.* [14] give an overview of North America's tidal potential. A supply of 140TWh/yr is suggested which is approximately 3.5% of the USA's electricity demand. It is stated that sites in Canada could provide another 370TWh/yr from 190 tidal sites. A study is presented in the report for seven possible sites around the US. Predicted energy costs for these sites vary between 4.6 and 10.8 American cents per kWh.

Lewis *et al.* [15] provide an overview of Ireland's offshore energy position, it is clear that wave energy is envisaged as being a far greater resource for Ireland than tidal energy. Tidal energy is indeed almost included as an aside in these proceedings. A potential of 1-2 TWh/yr is quoted for tidal technology however and there appears to be support for Irish based company Open Hydro with some funding for the test device coming from Sustainable Energy Ireland.

J Westwood [16] emphasises the significance that rising fossil fuel costs have as an incentive to develop renewable energy systems and recognises the potential for growth in the offshore energy industry. Winskel [17] states a general increase in both interest and investment in the UK renewable energies market in recent years but highlights that many barriers to development also exist. These are mainly economic or political boundaries. One such obstacle is the perception of the high risk of a marine energy venture. Detailed and diligent work at the research and design stages is therefore vital to lessen the likelihood of future failures.

2.1.2 Present state of the tidal stream industry

As previously stated [16], the tidal stream industry is currently in its infancy but signs point to a potential for large and rapid growth in the forthcoming years. Mueller *et al.* [18] state that the UK has a high capability for tidal stream device development, testing, installation, manufacturing and grid connection. They also note that nine tidal turbine companies had been identified as having obtained governmental grants (as of 2007). The growth of the tidal turbine industry has been marked even in the period of research for this thesis. A summary of progress is given in this section.

Marine Current Turbines' [MCT] Seaflow project [19, 20] installed a 0.3MW rated prototype device off the north Devon coast for testing purposes. Results from this were promising and MCT have proceeded to build and install a 1MW device (SeaGen) in Strangford Narrows in Northern Ireland. The system is grid connected but at present is not operating at full power after a control system fault led to damage of the blades on one of the twin rotors. Details of this can be seen in MCT's press release [21]. MCT claim that this fault will not interfere with their plans to install a farm of several turbines off the coast of North Wales and other sites in the future.

Hammerfest Strom [22] have also installed a prototype device and are currently testing it in Kvalsundet, Norway, details of the performance of the system do not appear to be available at present. The company is now in collaboration with Scottish Power and plans to produce a 1MW device in 2009 [23].

Verdant Power [24], a North American company, has installed a small-scale farm in New York's East river. The company have experienced several setbacks with failures of rotor blades and "pivoting machinery" [25]. Verdant Power is however continuing with development and Verdant Power state [24] that they have obtained funding to conduct a similar project in Ontario.

Another tidal turbine company, Clean Current [26] has successfully installed a scale test device, which has been used to generate power for a small isolated island at Race Rocks, the company has suffered problems with their bearing system but plan to install a 17m diameter device in the Bay of Fundy in 2008.

The Irish company, Open Hydro, as Clean Current, have a ducted tidal turbine design. Information on their progress is provided on their website in the form of a press release [27]. A test device was installed in EMEC in 2006 and in 2008, the company connected to the grid and installed a fully submerged system with no protrusion above the water surface. The company has tenders to install devices or farms in Nova Scotia, Canada and Alderney. Open Hydro has so far attracted €50M of investment and are currently manufacturing a 1MW device.

Another ducted turbine company, Lunar Energy [28], have a £500M contract with Korea to install a 300MW farm by 2015. Fabrication and installation of the devices will be carried out by Hyundai Samho Heavy Industries. This story is reported by Clover [29]. It is not clear whether any test devices have been deployed at present.

Swanturbines [30] have tested a small-scale river device and are planning to install a marine prototype for validation of their design in the near future. One device, which departs from the horizontal axis turbine system is Stingray [31], this device employs an oscillating hydrofoil to produce power.

Jo [32] summarises a variety of tidal stream projects in South Korea, their combined planned output is 575MW and a total budget is quoted as $1556M US, project dates are set between the time of writing and 2015. Initial tests have been carried out with small-scale devices and success has been mixed, one major problem that was highlighted was that systems were becoming jammed with rubbish in the tidal flow.

It can be seen that most devices still need to be proven and that there is plenty of room for design and development at this early stage of the industry. Performance prediction will not only aid development of tidal stream systems but can be used to give predictions of the power produced and loadings suffered by a system throughout its lifetime, which can give vital information to investors. As can be seen by the mechanical failures suffered by several companies, the marine environment is harsh on machinery and detailed modelling is vital before systems are installed in the ocean environment to minimise the risk of costly device failure.

2.2 Available Marine turbine research

Due to the relatively recent interest in horizontal axis tidal stream energy, published research in the field is limited but increasing. Swansea University have published papers studying the effects of bio fouling [33], a study on a small-scale river tested device [34] and a comparison of supporting structure designs [35]. Although all papers are useful to the tidal turbine industry, only the small-scale device testing paper bears much relevance to the present area of turbine performance modelling research. The results found in the paper [34] give an indication of what results should be produced by a turbine performance prediction code for a similar design of turbine. More recently, several conference papers have been produced [36-40] that are all related to the work undertaken by the author with the aid of colleagues during the course of research for this thesis.

A large proportion of research papers have been produced by a group of researchers involved in the Sustainable Energy Research group's marine energy project [41] in Southampton University. Some of the papers produced by this group will now be discussed:

Bahaj and Myers [42] discuss the fundamental topics that must be considered when employing tidal stream turbines for energy production. They highlight that tidal energy is a predictable and relatively dense source of

renewable energy that, with multiple farms, has the potential to contribute to base load. It is noted that little research exists specific to marine turbines but that much can be learnt from wind turbines and marine propellers. The basic system design of wind turbines can be drawn upon but the operating fluid and environments differs significantly. Marine propellers share a similar operating environment to tidal systems but the function differs significantly. The paper emphasises that tidal stream devices offer some unique challenges that require specific research. These challenges come about due to operation in the harsh marine environment, leading to considerations at the design stage such as corrosion resistance, efficiency loss due to bio fouling and maintenance issues. As the fluid is of a far higher density than air, a tidal stream turbine can be much smaller than the equivalent power wind turbine. The cost of this energy concentration is relatively high loadings from the flowing water and the risk of cavitation, which is not an issue for wind turbines. A list of desirable areas of research is drawn up, these include development of analytical models for turbine performance and systems to aid rotor design, development and validation as well as a means of predicting the loads on a system.

Another topic suggested for investigation was cavitation. In Molland, Bahaj, Chaplin and Batten [43], the pressure distribution over a 2D aerofoil section was predicted using the 2D aerofoil panel method code XFoil [44]. This was used to estimate cavitation inception. These predictions were compared with flow tank tests and a good agreement was found between tests and prediction. Bahaj *et al.* [45] and Batten *et al.* [46-48] also discuss cavitation effects. Cavitation inception measurements and models are presented and it is suggested that if cavitation consideration is included at the design stage, this should not be a problem for full-scale turbine systems. These papers also present an in-depth validation of BEMT using tank testing. The results are seen to agree reasonably well. The tidal turbine specific considerations of cavitation and free surface effects are reproduced in small-scale tests. Warnings are made about the lack of inclusion of these effects in BEMT. It is also stated however that these effects can both be mitigated by suitable design and placement considerations. Further research on free surface

effects are presented by Myers [49]. Tank testing and numerical models are shown which incorporate the free surface. This research deepens the understanding of the free surface effects, primarily on the wake of the turbine rotor. The tests seem so far to be on primarily uniform flows and the free surfaces are not disturbed by wave effects. The free surface interaction in a non-uniform flow incorporating wave effects is likely to cause the turbine to behave significantly differently from these tests and further research would be of great interest in this field. The impact of these non-uniformities of flow is discussed by Bahaj *et al.* [50].

Bahaj [51] gives an overview of the current state of research on cavitation, resource modelling and turbine performance modelling. In the paper, it is stated that blade element momentum theory (BEMT, discussed in depth in Chapter 3) can be implemented from wind turbine power prediction systems with some relevant alterations. The paper suggests that BEMT and cavitation analysis can be used in combination to assess the performance of turbine blade designs. Bahaj states that these theories will provide a good basis for turbine performance prediction but further development to include aspects such as turbulence is needed. This paper notes that other research groups to that in Southampton have conducted research into the field. These groups include the EPSRC's SuperGen consortium [52] that encompasses research at Edinburgh, Strathclyde and Robert Gordon universities.

Wang, Atlar and Sampson [53] have conducted a similar cavitation study to that described in the papers above. Cavitation is clearly seen at the tip even at design operation. In off-design conditions and low immersion, a far greater degree of cavitation exists. The paper points out that as well as the mechanical implications on wear that cavitation has, the resulting acoustic noise may have environmental implications. The wake deficit behind the model turbine in the test tank was also measured in the paper and the impact on scour and deposition of sediment was discussed.

Myers and Bahaj produced several papers on tests carried out in a flow tank on 1/30th scale models of Marine Current Turbine's system, some of which

are mentioned above. Two further papers are now discussed, [54] is concerned with the wake effects of the device and discusses the surface elevation of water at different points relative to the turbine. It is interesting to note that there is a significant rise in free surface level just ahead of the rotor. Myers and Bahaj stipulate that this effect could lead to a reduction in the required depth above the rotor tip of a system, enabling larger rotors to be used to achieve higher powers. The wake study was carried out to help further the understanding of wake effects to aid the design of turbine arrays.

The second scale turbine test paper [55] is an investigation into the power output of a turbine at different yaw angles and different fluid speeds. The performance was predicted using BLADED [56] with 2-D foil data from Visualfoil [57]. BLADED is a code initially developed for wind turbine performance prediction, it is discussed later in this chapter and in chapter 4. Visualfoil was used to predict hydrofoil lift and drag data, the code employed different methods for pre and post stall data. Pre stall data was predicted using a panel method boundary layer analysis. Post stall modelling employed three different approaches; general flat plate theory, Viterna-Corrigan post stall equations and Tangler equations [these approaches are explained in the paper]. In the tank tests, it was found that experimental results agreed well with flat plate and panel method predicted outputs in largely un-stalled conditions. When turbine rotational speed was dropped, higher angles of attack were experienced by the turbine blade. Under these conditions, it was found that all prediction approaches underestimated the output of the turbine. Actual turbine output was found to be up to 140% of that predicted. The paper also investigated the effects of yaw on the system, results from this showed a varying effect on power output for differing yaw angles that was not predicted by the codes. It was suggested in the paper that the over-power produced compared to theoretical predictions was due to three-dimensional effects such as centrifugal forces creating a span-wise (along the blade length) flow. This would tend to maintain an attached flow for longer than on a two dimensional foil flow. The paper recommends that more research into the phenomenon of stall delay is desirable.

In Batten *et al.* [48], an overview of design considerations for the hydrodynamic performance of a marine turbine is considered. The paper includes information on turbine performance prediction, cavitation prediction and structural considerations for blade profiles. The paper contains little that has not been previously discussed but it does provide a useful overview of these topics.

As previously mentioned, research has been carried out related to tidal stream turbines at Robert Gordon University. Much of this has been conducted by I. Bryden in collaboration with colleagues at his university, I.T. Power (Prof. P. Fraenkel, now with Marine Current Turbines [58]) and Heriot-Watt University. Three papers; Bryden *et al.* [59], Couch and Bryden [60] and Bryden and Couch [61] were briefly examined. The research carried out for these papers is mostly concerned with the modelling of the flow in a tidal stream turbine farm or resource assessment and either assumes simple power extraction characteristics or assumes that this data is known a priori.

Physical testing of full-scale devices is difficult for several reasons. The inflow of the sea is invariably non-uniform both spatially and temporally, this leads to difficulty in flow condition characterisation. There are a limited number of turbines deployed and companies are often reluctant to share any information that is gathered due to the competitive value this information may hold. Recently, BERR [62] published guidelines for testing large-scale devices that seek to prescribe a standardised method of testing and presentation of results, which will aid future measurement and presentation of performance data. Test results of varying scale devices are available however, the work of Bahaj *et al.* has already been discussed briefly and some further test-based papers will now be covered. Clarke *et al.* [63] present initial results from tests on a contra-rotating turbine system. The measurement equipment placed on the rotor system allowed for axial and rotational loadings to be measured. More in depth studies of the system's performance are planned for the future. Germain *et al.* [64] give a summary of the use of the IFREMER free surface hydrodynamic water tunnel, the tank is 4m wide and 2m deep, allowing for blockage effects means that the test

scale of devices is reasonably small. The modelling of these small-scale tidal devices is presented, it is shown that these small-scale tests are of use for verifying theoretical predictions. The measuring equipment in this tank facility allows for accurate measurement of the flow field in the proximity of the turbine model. Accurate scale modelling such as this requires tight tolerances on the test models.

It has been seen in the papers covered that accurate modelling of the performance of a rotor blade system is considered an important area of tidal stream turbine research. This modelling is needed for prediction of the produced power and loadings on the blade, rotor system, generator assembly and supporting structure. The effect on the flow also has significance for developments of turbine farms and prediction of the impact on the environment.

2.3 Applicability of Blade element theory to turbine rotor modelling

As noted previously, several papers (e.g. [51]) suggest that much can be learnt from the wind turbine industry when predicting the performance of tidal stream turbines. One popular approach to prediction of wind turbine performance appears to be BEMT. This approach will now be discussed.

2.3.1 Basic Blade element theory

BEMT has been a widely accepted method for a long time. Initially its application was marine and aviation propellers [65] but was later applied to wind turbines and the approach is described in a number of wind turbine textbooks [66-69]. Griffiths [70] presented a clear approach to designing an optimally shaped wind turbine using BEMT. Both energy and momentum approaches were applied to derive equations for axial and torque forces at discrete blade elements. These were combined to produce a system to

optimise these values by varying the chord and angle of twist of a turbine of given foil section. The paper begins by describing simple actuator disc theory that models the turbine rotor as a disc that extracts energy from a fluid stream. This approach assumes that the fluid is inviscid, incompressible and has no rotation of flow downstream of the disc. The fluid slows down due to kinetic energy given to the actuator disc resulting in expansion of the stream tube. This approach gives an exact solution with relatively simple equations but the assumptions made compromise the accuracy of this approach. Griffiths develops the system in steps, first by employing a real windmill in a perfect fluid. At this stage, it is assumed that the flow acquires a rotation about the turbine axis in the opposite direction to turbine rotation and that the rotational speed of the fluid passing through the rotor is half that of the value well downstream. Two interference factors for axial and rotational flow are introduced which vary along the blade length and so must be calculated for a number of discrete blade elements. The final stage of complexity presented in this paper is the modelling of real fluids with a real turbine rotor. At this stage, the inviscid flow assumption is rejected. The momentum approach derivations for axial force and torque remain unchanged but the energy derivation equations now include a loss due to a viscous drag force experienced by the turbine rotor. From the equations derived at this step, rearrangements are made that give conditions for the axial and rotational interference factors that will give an optimal turbine design for given conditions.

In another text, Griffiths and Woolard [71] present an iterative system using the energy and torque equations of the previous paper that is capable of modelling the performance of a turbine system of given geometry for a given uniform upstream flow. As the flow is assumed to be incompressible yet viscosity is taken into account in these equations, altering the density of the fluid would allow this approach to be applied to tidal stream turbines.

Badreddine, Ali and David [72] report on a project to optimise the performance of a horizontal axis wind turbine. In the paper, they mention some shortcomings of BEMT. It is stated that BEMT is imprecise as it is not

able to accurately estimate wake effects or complex three-dimensional flows. In its standard form, BEMT does not take into account secondary effects from three-dimensional flows such as tip vortices and radial flow components induced by angular acceleration from the rotation of the blade system. In this paper, the vortex wake is modelled using lifting line theory. This is said to model the flow downstream of the turbine more realistically than BEMT although the model is limited to small angles of attack. The paper accepts that Navier-Stokes based methods give very good results as they are able to capture viscous and compressible flow effects but the high computational demand of such an approach limits its application. The paper presents the lifting line theory as superior to BEMT although a comparison of the theory with a corrected Blade element theory would be a useful addition to the text. This highlights the need for further development of BEMT to improve accuracy. Attempts to achieve this are discussed in the following section.

2.3.2 BEMT corrections

Kishinami *et al.* [73] conducted a comparison of a small-scale wind turbine test with a modelling approach similar to Griffith's approach. One significant difference was that rotor blade tip losses were taken into account. This was done by significantly reducing the lift coefficient of the aerofoil section from the standard empirical data for radius values larger than 97% of the total blade radius. For these points, the effective radius was taken to be the overall radius of the blade tip. The basis of deciding the reduction of the lift coefficients is not outlined but is possibly due to empirical data or prior knowledge. The experimental and theoretical results appear to follow similar trends but the values of the two results show significant disagreement. It is estimated in the paper that the error of the experimental results is approximately 18% so this contributes to the disagreement to some extent.

Robinson *et al.* [74] conducted an investigation into three-dimensional, unsteady and separated flow influences on a horizontal axis wind turbine. The paper states that wind turbine aerodynamic loads exhibit spatial and

temporal complexities, which are caused by the influences of three dimensionality, unsteadiness and dynamic separation. The paper explains that dynamic stall was deemed inconsequential for power output prediction as it tended to occur over small timescales compared to a revolution of the turbine rotor. It is reasoned though that accurate modelling of this is vital for understanding the loads on the turbine blades and supporting structure. The paper claims that the majority of wind turbine structural design codes, using BEMT, are unable to capture the full three-dimensional effects of the flow, even using empirically derived dynamic stall models. The paper, as previous papers, emphasises that BEMT is a useful tool for design comparison and analysis due to its low computational demand and good accuracy in the un-stalled flow region. A lack of detailed understanding of the true behaviour of the flow is noted, this is due to the difficulty of making accurate, localised measurements of the flow and rotor properties of a physical system. The paper concentrates on existing flow data in the stalled flow region and makes observations on the flow of a horizontal axis wind turbine. The most interesting characteristic discussed in this paper for marine turbines is that of stall delay. This is when the forces produced by the system are far higher than those predicted from 2-D theory at what should be stalled angles of attack. The paper suggests that this is due to the rotation of the blade system creating a radial flow along the blade surfaces. Visualisation using fine thread tufts showed that as separation of flow initiates, it propagates forward from the trailing edge with increasing angles of incidence. As this happens, flow in the separated region is seen to become immediately three dimensional and fluid travels from the centre of the rotor towards the blade tip. Once established, this flow was apparently highly stable. Another phenomenon studied was the effect of yawed inflows. This was seen to have highly dynamic effects, again giving far higher force outputs than predicted by stalled two-dimensional predictions. Although applied to wind turbine studies, the behaviour noted in this paper is likely to have the same characteristics for tidal turbines.

Danmei Hu *et al.* [75] conducted a study into the phenomenon of stall delay for horizontal axis wind turbines. The popularity of BEMT for predicting the

performance of wind turbines was noted and the good agreement with field measurements for attached flow conditions mentioned. The shortcoming of BEMT is again noted as its inability to accurately predict rotor power at what would be stalled conditions for two-dimensional foil theory. Over-production of power at these angles of incidence is referred to as stall delay in the paper and has been witnessed on wind turbines, propellers and helicopter rotors. The paper notes that an attempt to take into account stall delay was made by Viterna and Corrigan [76] by making a basic correction to the equation based on the blade aspect ratio. Other studies reported in the paper found that local solidity was a predominant factor in stall delay characteristics and that effective lift coefficients near the hub were higher than predicted due to a delay in stall. This paper used a full Navier Stokes equation solver 'Fluent' with 3D incompressible, steady, viscous flow equations in polar coordinates to solve the flow field for a horizontal axis wind turbine. In the 3D analysis, the Reynolds Averaged Navier-Stokes equations were used. Predictions of separation were made for 2D and 3D cases, the 3D case showed delayed separation due to rotation of the blade system. It was found that Coriolis and centrifugal forces near the root of the blade are strong during rotation, further from the hub it was seen that Reynolds number had a larger effect on separation so at these points 2D and 3D theories agree more closely. To support the findings, a test was carried out in a wind tunnel with a scale wind turbine. The downstream wind velocities were measured. The results of this were found to agree closely with the calculated 3D predictions but the 2D predictions were found to under estimate the result. This paper highlights the difficulty that blade element theory has with predicting power production at stalled angles of attack but suggests corrections that can be made to alleviate this problem. The investigation using Navier-Stokes equations are useful for research but the computational demand and time needed to develop each model render it an unsuitable approach for frequent use at the design and development stage of a tidal current turbine system at present.

Du and Selig [77] again state that BEMT is incapable of predicting post-stall conditions accurately and agrees with [75] that this is most likely due to rotational effects of the turbine. Once again, a Navier Stokes approach was

used to model the system. Steady incompressible flow was assumed and a cylindrical coordinate system implemented. The boundary layer flow over the blades was assumed to be laminar at the leading edge of the blade, becoming turbulent before the trailing edge. The position of transition was estimated using the laminar instability criterion as described in the paper. A linear adverse velocity gradient was imposed on the system to approximate the real operating condition of stall delay due to rotation. It was found that at low rotational speeds, a smaller linear adverse velocity gradient was needed to produce separation than at higher rotational speeds. It was again found that due to a reduction in Coriolis force at higher blade radii, separation was delayed by a far smaller amount than at points close to the hub. Reynolds number had a far larger effect on separation at these outer points. The paper states that the effect of the Coriolis force is greater than the effect of the centrifugal force but recommends further research into this area for better understanding of the physics of 3D stall delay.

In Mikkelsen's thesis [78], a study of the development of basic actuator disc theory into a lifting line technique was carried out. This theory and a Navier-Stokes approach were used to model the behaviour of a wind turbine system and investigate some of the assumptions made in BEMT. In the thesis, the derivations of actuator disc and blade element theory equations are shown. It is explained that there are some basic assumptions used in blade element theory that are not verified. These are that the flow can be divided into annular stream tubes, that the pressure in the wake far downstream is equal to the upstream pressure and that the induced velocity in the rotor plane is half that of the induced velocity in the far wake. It is also assumed that axial momentum theory can be applied in the differential form neglecting the resulting axial force of pressure acting on lateral boundaries of the stream tube and that conservation of circulation may be ignored. The effect of these assumptions was investigated and it was found that the maximum resulting error is 3% so despite the inherent inaccuracy of Blade element theory, the error is found to be negligible for most operating conditions. Tip correction factors are described for real rotors. An approach developed by Prandtl (see [79] for example) for tip correction using a factor 'F' was described that

corrects the aerodynamic force components. It is shown that this correction can be employed in the axial angular momentum equations of BEMT (implemented by Glauert [80]) to give updated axial and tangential flow interference factors. It is stated that this approach is well accepted but does have some inherent inconsistencies. One such inconsistent characteristic is that as the radius of the blade element tends to the overall blade radius, the axial interference factor tends to unity, meaning that axial velocity becomes zero. This is inconsistent because the applied force at the tip is zero. Refinements were made by Wilson and Lissaman [81] and De Vries [82] but these are said to lack rigorous consistency near the tip. A mathematically consistent system was introduced by Shen, Mikkelsen, Sørensen and Bak [83]. This approach overcomes the near tip inconsistency by considering a balance of momentum for a real rotor with a finite number of blades with real aerodynamic forces and ensures that the forces at the tip of the blade are zero. It is argued in the thesis that although this approach is an improvement, it still does not completely model the real situation at the tip and includes a factor that must be calibrated using model testing.

Maalawi and Badawi [84] show an approach implementing Prandtl's tip loss factor in combination with a version of the blade element theory equations to predict the performance of a turbine system. The paper aims to solve this equation system directly and hence lower the computational demand compared to iterative techniques.

Another operating condition that must deal with stalled angles of attack but can be quite different to stall delay is the start-up of wind turbines. Ebert and Wood [85] and Wright and Wood [86] are two papers produced by the University of Newcastle, Australia concentrating on the start up behaviour of small horizontal axis wind turbines. These small wind turbines rely on the wind for start up rather than using the generator as a motor to aid starting as many large wind turbines do. Because of this, understanding the start up behaviour due to the incoming flow is vital to the start up performance of the system. In both papers, start up is defined as the period from the blades being stationary to the point at which significant power is being produced.

Wright and Wood [86] outline three major challenges to the modelling of the start up behaviour of small wind turbines, these are high angles of attack, low Reynolds numbers and flow unsteadiness. The first two of these problems are equally applicable to marine turbine systems although the incoming flow for a marine turbine may be steadier than that for a wind turbine. Cyclical variations in flow velocity may be present due to wave effects and 'noise' will be present due to turbulence. Both papers predict the start-up performance in a similar way, using an adapted blade element theory approach. In this approach, it is assumed that when the rotor system is stationary, the flow of the fluid is not decelerated as it passes through the rotor system. The net torque produced on the rotor system is then equated to the product of the system's rotational moment of inertia and its angular acceleration. In both systems modelled, no load is placed on the generator until the desired cut in speed of the rotor system is approached giving a low resistive torque before this point. It was noted from field tests that the start up time was highly dependent on wind speed and at low wind speeds, the rotor would tend to idle without producing power until a gust was received to increase the rotational speed of the turbine. The low Reynolds number mentioned previously causes a problem for prediction of the lift and drag coefficients of the blade profile. Low Reynolds no. performance information is not available at high angle of attacks for many profiles and so testing or prediction of the lift and drag coefficients is needed.

Madsen *et al.* [87] analyse the performance of BEMT in comparison to a full Navier-Stokes based CFD solution. Shortcomings in accuracy are shown to be limited to the blade root and blade tip. Correction approaches are presented which are said to greatly improve the accuracy of BEMT and it is shown that, with correction procedures implemented, BEMT may be used as an accurate performance prediction approach.

2.3.3 Application of marine inflows

Barltrop *et al.* [88] have validated a BEMT based model incorporating linear wave theory against model tests. A reasonable agreement is shown between model and test results. It was concluded in the paper that waves had a significant effect on the performance of tidal turbines. A discussion on the applicability of different wave theories is given in chapter 6 of this thesis. A linear wave theory may be sufficient for many waves experienced but is probably not a sufficient model for steep waves, particularly relevant in extreme wave modelling.

Recently McCann [89] has demonstrated the operation of a BEMT based code in a flow with both irregular waves and turbulence. The waves are modelled as irregular waves and turbulence was created using a Von Karman spectral density model [90], which is a model previously employed for wind turbulence in the wind version of BLADED [56]. The inclusion of turbulence here is used to demonstrate its effect on the fatigue loading of a system but it would appear that these turbulence values have been selected arbitrarily. If this is the case, it is debateable whether inclusion of turbulence would lead to an increased modelling accuracy. The paper clearly demonstrates the capabilities and advantages of using such a model in the load characterisation process.

2.3.4 Discussion

It has been seen in this section that blade element theory can experience certain challenges in accurately predicting rotor performance. The main causes of these problems would appear to be the lack of proper modelling of three dimensional effects such as stall delay and the dependence on 2D foil data for lift and drag coefficients. There are a number of approaches to compensate for or avoid these problems however and the relatively low computational demand of the BEMT approach makes it desirable to use for a turbine rotor modelling system, which may be used as a design and development aid.

2.4 Alternative approaches for predicting turbine rotor performance

It can be seen from the previous section that Blade element theory has gained popularity as an efficient turbine blade performance prediction approach but there are certain conditions under which its accuracy requires improvement. The following papers highlight some of these conditions and show alternative approaches that may be taken to predict rotor performance.

Ahmed and Archer [91] conducted a study into the behaviour of a highly loaded wind turbine. It was found under the conditions of high loading, traditional approaches such as BEMT were not capable of accurately modelling the behaviour of the system. The reason for this was identified to be the assumption that the change in the cross sectional area of the stream tube was negligible. Due to retardation of the flow through the rotor blades, this is not the case for highly loaded turbines. An approach developed by Sanderson and Archer [92] was implemented to aid in the design process of a rotor system for highly loaded conditions and was seen to give promising results on a test system.

Sharpe [93] presents a lifting line theory with a prescribed wake. The theory is applied in order to create a wind turbine blade design code. The approach includes radial flow circulation and captures tip and hub loss effects. A slight increase in computational demand is the penalty of this approach compared to BEMT.

Baltazar [94] presents a tidal turbine computational model based on the boundary element method also known as the panel method. Baltazar states that the advantage of this theory over BEMT and lifting line theory is that it is fully three-dimensional, this allows prediction of the pressure variation around the blades which may be used for cavitation prediction but, as with basic BEMT and lifting line theory, this model struggles when the flow is outside of design conditions. At present, the model requires a wake to be prescribed, implying, as with BEMT, that the system is in a steady state flow. It would

appear that although this model gives useful information on the pressure around the blades, there is little additional benefit of employing this model for developers when considering the increased computational demand such an approach requires.

McCombes [95] presents a Navier-Stokes based turbine model that is currently under development. The approach shows great potential for capturing the wake behaviour of an unsteady flow. It would appear that this approach requires considerably more computational time than the far simpler BEMT, lending the code more to analysis of particular complicated flow situations rather than rapid generation of load estimates for system modelling.

Cardiff University [96, 97] have been developing a CFD model for tidal turbine modelling and have incorporated both a power law flow and turbulence. The model appears to function well, giving predictions of both rotor performance and wake characteristics. It would appear that the meshing and parameterisation of a three-dimensional Reynolds Averaged Navier-Stokes model such as this is far from trivial. This demand for experienced operator resources coupled with increased computational demand means that the approach does not lend itself to a flexible model for development and analysis of a variety of flow conditions.

Fabrice *et al.* [98] use a vortex-panel method to model a tidal turbine but their primary concern is the study of the wake, at present the research is at an early stage and uniform flows are being employed. It is not clear in the paper whether load results on the rotor system are obtained using this method.

One shortcoming of BEMT can be its reliance on existing foil lift and drag data. Traditionally this is found from 2D experiments. Kamoun, Afungchui and Chauvin [99] report on a system developed to predict the lift and drag performance of a two-dimensional aerofoil using a lower order code based on the singularities or panel method. The singularities method is a general method to solve Laplace's incompressible inviscid flow equation. In this

approach, an aerofoil section is approximated as a finite number of flat panels. Although results from this approach are successful at low angles of attack, the assumption of inviscid flow leads to errors at higher angles of attack. The approach could, however be useful for predicting lift and drag coefficients of an unknown hydrofoil or aerofoil section and the paper lists several existing codes that can be used to do this.

Alternative performance prediction approaches have been seen in the previous and current sections. Navier-Stokes approaches for solving the three dimensional flow are seen to be more accurate than blade element theory but the computational demand of such an approach makes it undesirable for comparisons of different systems during the design and development procedure. Alternative approaches can be used under conditions that present problems for BEMT, or adaptations to BEMT can be used to improve its performance in these ranges.

2.5 Existing turbine codes

As the wind turbine industry is at a far more mature state than the marine turbine industry, it is unsurprising that there are commercial and academic performance prediction codes available to model the performance of wind turbines. Many of these codes implement blade element theory and use tip loss correction factors along with other corrections to improve the accuracy of the system. As has already been seen, much of wind turbine theory may be relatively simply adapted to apply to marine turbines.

Buhl, Wright and Tangler [100] compare the performance of three wind turbine performance codes; BLADED [56], WT_Perf [101] and YawDyn [102]. The codes include tower loadings and dynamics but in the study, these are set as rigid to enable comparison of the flow performance. Initially, a simplified wind turbine is used to compare the basic performance prediction systems of the three codes, all of which employ blade element theory. All three codes contain means of accounting for tip-loss and all use the same

algorithm. BLADED however applies this algorithm differently to the other two codes. It uses the linearised correction model method rather than the Wilson and Lissaman method employed in the other two codes [103]. Accurate modelling of the tip loss is said to be highly dependent on a sufficient density of discrete elements near the tip of the blade. The number of solution points at the tip is a trade-off between accuracy of results and computational demand. The calculation of the aerodynamic force differs slightly between BLADED and the other two codes. The paper states that BLADED calculates the aerodynamic force per unit length at each discrete element point then assumes a linear variation between each point and integrates along the blade to obtain a solution. The other two codes take the aerodynamic force for each discrete element and apply this value at the centre of the element. The alternative approaches mean that, if an insufficient number of elements are used, BLADED will tend to under-predict the power output whereas the other codes will tend to over predict them. After this basic study, the paper goes on to compare additional features of the codes. All three codes have similar systems for modelling wind shear (variation of wind speed with respect to position). Marine turbines have a different incoming velocity distribution to wind turbines so creation of an alternative system may be more effective than modification of existing wind codes. The paper also compares tower shadow modelling, all codes include a system to model the effect that the tower has on the flow and hence performance of the turbine system. It is stated that for accurate definition of the tower shadow, a large number of time steps is needed per revolution of the turbine, this leads to a heightened computational demand. Another feature that may be adapted to marine turbines but that is only briefly mentioned in the paper is hub loss modelling, further investigation of this is desirable. Results from all codes are seen to agree reasonably well. Unfortunately, the codes are not compared to any field or scale test measurement as the models created differ to any true wind turbine. It is therefore not possible to ascertain the codes' accuracy in relation to true turbine performance.

Since the commencement of the research presented in this thesis, Garrad Hassan have released a tidal specific version of their software [104]. It is effectively the same system as their traditional wind turbine software but has added features specific to tidal devices incorporated such as wave and tide modelling.

Orme developed a tidal turbine model using a series of Excel spreadsheets during study for his PhD thesis [105]. In this, he added inertial loads from wave motion to the loads from BEMT as well as adding the capability of the model to incorporate non-uniform tidal flows and non-linear, regular waves in a time dependent model.

In this section, it has been seen that a variety of codes exist from the wind turbine industry and more recently for tidal turbines. The systems discussed all take similar basic approaches to modelling turbine performance. BEMT is used but correction factors for tip loss, tower shadow, hub loss and stall delay are implemented to improve the accuracy of the systems. This approach offers a sound platform for development of a flexible modelling system.

2.6 Conclusions

It has been seen in this paper that tidal stream turbines have a great potential for capturing a natural, renewable energy source and providing a growth industry. Much of the success of this relatively new type of renewable energy depends on accurate modelling of the rotor system's performance and expected loads. Existing research directly related to the field has been found to be limited due to the fairly recent interest in these types of system but it has been seen that much can be learnt from the relatively mature wind turbine industry. The use of BEMT has been discussed and compared to approaches such as Navier Stokes flow solutions and lifting line theory. It has been found that the accuracy of BEMT is not as high as that of appropriately constructed Navier Stokes approaches but its far lower

computational demand has lead to its development, using correction systems to improve its performance. Corrections that take into account tip losses, hub losses, three dimensional stall delay and interaction of the supporting structure have been seen that make allowances for the approach's inaccuracies under certain operating conditions. Existing turbine codes have been briefly covered and it appears that a similar approach may be taken to solving marine turbine modelling problems with alteration of conditions such as the fluid density and the incoming flow regime. It is clear that if BEMT is to be used, corrections must be made to the model. The addition of accelerative loadings presented by Orme would appear to be prudent and a system that incorporated these aspects with a flexible, three-dimensional solver including modelling of supporting structure loads is desirable.

The overall impression of the papers reviewed in this report appears to be that Navier Stokes approaches are useful for examination of flow behaviour and accurate modelling but the computational demand of such approaches renders them unsuitable as an aid in the design and development process where many blade designs may need comparison. It is in this application that BEMT excels, its reduced accuracy compared to a Navier Stokes approach is offset by its far lower computational demand. BEMT therefore appears to be a good approach to implement in a tidal stream turbine performance modelling code but calibration and validation with alternative approaches such as Navier Stokes simulations, scale testing and prior data is needed to give a good confidence of the code's predictions.

2.7 References

[1] Bahaj AS, "Editorial", Renewable energy, 2005.

[2] Callaghan J, "Future Marine Energy", Carbon Trust, UK, Jan 2006.

[3] Bryden IG, "Tidal Current Power", Next Steps for Wave & Tidal Power in Scotland (26/11/2003).

[4] Binnie Black & Veatch, "The Commercial Prospects of Tidal Stream Power", DTI UK, 2001.

[5] Black & Veatch Ltd., "UK, Europe and Global Tidal Stream Energy Resource Assessment", Carbon Trust, UK, 2004.

[6] Black & Veatch Ltd., "Tidal Stream Energy Resource and Technology Summary Report", Carbon Trust UK, 2005.

[7] Carbon Trust, "Guide to Marine Energy".

[8] Carbon Trust, "Low Carbon Technology Assessment 2002", Carbon Trust UK, 2002.

[9] Entec, "Marine Energy Challenge, Marine Energy Glossary", Carbon Trust UK, 2005.

[10] Environment Agency, "Position Statement, Generating Electricity from Tidal Power", 2004.

[11] Scottish Natural Heritage, "Marine Renewable Energy and the Natural Heritage: An Overview and Policy Statement".

[12] "Route Map to a Clean, Low Carbon and More Competitive Energy Future for Wales", Welsh Assembly Government Consultation Document.

[13] Future Energy Solutions, "Opportunities for Marine Energy in Scotland", Scottish Executive UK, 2002.

[14] Bedard, R., *et al.*, "North American Ocean energy Status", 2007.

[15] Lewis, T., E. Sweeney, and G. Brennan. "The Ocean Energy Development Strategy for Ireland" in 7th European Wave and Tidal Energy Conference. 2007, Porto.

[16] Westwood, J., "Offshore Renewable Energy", Douglas Westwood, 2005.

[17] Winkskel, M. "Marine Energy Innovation Systems: International evidence and the UK context" in World renewable energy congress. 2005: Elsevier.

[18] Mueller, M., H. Jeffrey, and A. Wallace. "The UKERC Marine Renewable Energy Technology Roadmap" in 7th European Wave and Tidal Energy Conference. 2007. Porto.

[19] Fraenkel P, "THE "SEAFLOW" PROJECT: PIONEERING THE DEVELOPMENT OF TIDAL STREAM TURBINES," SUT-ICE, 2003. London.

[20] Thake, J., "Development, Installation and Testing of a Large Scale Tidal Current Turbine", DTI, 2005.

[21] Marine Current Turbines (2008) "Delay in commissioning one of SeaGen's rotors", Online: http://www.marineturbines.com/3/news/article/11/delay_in_commissioning_one_of_seagen_s_rotors/, Accessed: 11/08/08.

[22] Diavision "Hammerfest Strom homepage", Online: www.e-tidevannsenergi.com/index.htm, Accessed: 04/05/2006.

[23] Hammerfest Strøm AS (2007) "Norwegian technology for tidal energy to be further developed in Great Britain", Online: www.hammerfeststrom.com/content/view/49/82/lang,en/, Accessed: 21/05/2007.
[24] Verdant Power (2008) "Verdant Power Helps Build Sustainable Communities Around the World", Online: http://www.verdantpower.com/, Accessed: 11/08/08.
[25] Aston, A., "Why New York City's third try with tidal power is good news for the U.S." in Business Week. 2008.
[26] Inc., C.C.P.S. (2008) "Clean Current- Renewable Energy from the Tides", Online: www.cleancurrent.com, Accessed: 11/08/08.
[27] OpenHydro Press Release (2008) "OpenHydro successfully installs subsea tidal turbine", Online: www.openhydro.com/news/OpenHydroPR-100908.pdf, Accessed: 10/09/08.
[28] Lunar Energy Ltd, "Harnessing tidal power", [online 2006 www.lunarenergy.co.uk] (accessed 12/07/06).
[29] Clover, C., "British company to build world's largest tidal power scheme", in The Daily Telegraph. 2008: London.
[30] Swanturbines Ltd. "Power from flowing water" 2006 [cited 12/11/06]; Available from: www.swanturbines.co.uk.
[31] Trapp, T. "Stingray Tidal Stream Generator", Online: www.engb.com/services07a.html, Accessed: 04/05/2006.
[32] Jo, P.C.H. "Recent Development of Ocean Energy in Korea" in World Renewable Energy Congress. 2008. Glasgow.
[33] Orme JAC, "Investigation of the effect of biofouling on the efficiency of marine current turbines", Proceedings of the 1st International Conference on Marine Renewable Energy, 2002.
[34] Orme, J.A.C. and I. Masters, "Design and Testing of a Direct Drive Tidal Stream Generator", Proceedings of the Institute of Marine Engineering Science and Technology Part B: Journal of Marine Design and Operations, 2005/6. 9: p. 31-36.
[35] Orme JAC, "Analysis and comparison of support structure concepts for TSTs", Proceedings of the 4th International Conference on Marine Renewable Energy, 2006.
[36] Masters, I., J. Orme, and J. Chapman. "Towards realistic marine flow conditions for tidal stream turbines" in 7th European Wave and Tidal Energy Conference. 2007. Porto, Portugal.
[37] Chapman, J., I. Masters, and J. Orme, "Rotor Performance Prediction for Tidal Current Turbines", in A Joint Conference of The Association for Computational Mechanics in Engineering (UK) and The Irish Society for Scientific and Engineering Computation, C.G. Armstrong, Editor. 2006, Queen's University, Belfast: Queen's University, Belfast. p. 103-106.
[38] Chapman, J., J. Orme, and I. Masters. "Velocity Mapping Procedures for Tidal Stream Turbines in an Arbitrary Flow Field and the Implications on Performance Due to Non-Uniform Flow" in Fifteenth UK Conference of the Association of Computational Mechanics in Engineering. 2007. Glasgow: Civil-Comp Press.

[39] Orme, J., J. Chapman, and I. Masters. "ASPECTS OF THE PERFORMANCE PREDICTION OF TIDAL STREAM TURBINES IN YAWED FLOW" in NAFEMS World Congress 2007. 2007. Vancouver.
[40] Masters, I., J. Chapman, and J. Orme. "A Three-Dimensional Tidal Stream Turbine Hydrodynamic Performance Model" in World Renewable Energy congress X. 2008. Glasgow.
[41] University of Southampton "Welcome to the Marine Energy website", Online: www.marineenergy.soton.ac.uk, Accessed: 04/05/2006.
[42] Bahaj AS and L. Myers, "Fundamentals applicable to the utilisation of marine current turbines for energy production", Renewable Energy, 2003. 28: p. 2205–2211 .
[43] Molland F, "Measurements and predictions of forces, pressures and cavitation on 2-D sections suitable for marine current turbines", Proceedings of the Institute Mechanical Engineers, 2004. 218 (Part M: J. Engineering for the Maritime Environment).
[44] Drela M at MIT, "XFoil Subsonic Airfoil Development System ".
[45] Bahaj, A., *et al.*, "Power and thrust measurements of marine current turbines under various hydrodynamic flow conditions in a cavitation tunnel and a towing tank." Renewable Energy, 2007. 32: p. 407-426.
[46] Batten, W., *et al.*, "The prediction of the hydrodynamic performance of marine current turbines", Renewable Energy, 2008. 33: p. 1085-1096.
[47] Batten, W., *et al.*, "Experimentally validated numerical method for the hydrodynamic design of horizontal axis tidal turbines", Ocean engineering, 2007.
[48] Batten WMJ, "Hydrodynamics of marine current turbines", Renewable Energy 31, 2006. (Elsevier): p. 249-256.
[49] Myers, L., *et al.* "Flow boundary interaction effects for marine current energy conversion devices" in World Renewable Energy Congress X. 2008. Glasgow.
[50] Bahaj, A., *et al.* "Characterising the wake of horizontal axis marine current turbines" in 7th European Wave and Tidal Energy Conference. 2007.
[51] Bahaj AS, "The Potential of Harnessing Electrical Energy from Marine Currents, "Proceedings of World Renewable Energy Congress, 2005. (Elsevier): p. 257-264.
[52] SUPERGEN Marine "SUPERGEN Marine homepage", Online: www.supergen-marine.org.uk, Accessed: 05/05/2006.
[53] Wang, D., M. Atlar, and R. Sampson, "An experimental investigation on cavitation, noise, and slipstream characteristics of ocean stream turbines", Part A: Journal of power and Energy, 2007. 221.
[54] Myers L, "Wake Studies of a 1/30th Scale Horizontal Axis Marine Current Turbine", Proceedings of World Renewable Energy Congress, 2005. (Elsevier): p. 1205-1210.
[55] Myers L, A.S.B., "Power output performance characteristics of a horizontal axis marine current turbine", Renewable Energy, 2006. 31(Elsevier): p. 197-208.
[56] Garrad Hassan & Partners Ltd, "GH Bladed: Wind Turbine Design Software ",
[57] Hanley Innovations, I, accessed: 05/05/2006., "VisualFoil Plus: Accurate Lift, Drag & Moments for all Airfoil Shapes", [online

http://www.hanleyinnovations.com/air_16.htm] 2006 (accessed 12/07/06).
[58] MCT Ltd, "Marine Current Turbines", [online 2006 www.marineturbines.com] (accessed 12/07/06).
[59] Bryden IG, "Matching Tidal Current Plants To Local Flow Conditions", Energy, 1998. 23 (No.9 Pergamon UK): p. 699–709.
[60] Couch J and I. Bryden, "Numerical Modelling of Energy Extraction in Tidal Flows", Proceedings of World Renewable Energy Congress, 2005. p. 550-555.
[61] Bryden, I. and S. Couch, "ME1-marine energy extraction: tidal resource analysis", Renewable Energy, 2006. 31: p. 133-139.
[62] BERR, "Assessment of performance for tidal energy conversion systems", EMEC, Editor. 2008, Crown Copyright.
[63] Clarke, J., *et al.* "Contra-rotating Marine Current Turbines: Performance in Field Trials and Power Train Developments" in World Renewable Energy Congress X. 2008. Glasgow.
[64] Germain, G., *et al.* "Facilities for marine current energy converter characterisation" in 7th European Wave and Tidal Energy Conference. 2007. Porto, Portugal.
[65] Houghton EL. Brock AE, "Aerodynamics for Engineering Students". Vol. 1 P119,1960: EDWARD ARNOLD.
[66] Moriarty, P.J. and A.C. Hansen, "AeroDyn Theory Manual", NREL, 2005.
[67] Manwell, J.F., J.G. McGowan, and A.L. Rogers, "Wind Energy Explained". 2002, Chichester: John Wiley & Sons Ltd.
[68] Hansen, M., "Aerodynamics of Wind Turbines" Second Edition, 2008, London: Earthscan.
[69] Burton, T., *et al.*, "Wind Energy Handbook". 2001, Chichester: John Wiley & Sons.
[70] Griffiths, R., "Energy from the Wind", University of Wales Swansea internal report, 1974.
[71] Griffiths, R.T. and M.G. Woollard, "Performance of the optimal wind turbine", Applied Energy 4, Applied Science Publishers Ltd 1978.
[72] Badreddine, K., H. Ali, and A. David, "Optimum project for horizontal axis wind turbines 'OPHWT' ", Renewable Energy, 2005. 30: p. 2019–2043.
[73] K. Kishinami *et al.*, "Theoretical and experimental study on the aerodynamic characteristics of a horizontal axis wind turbine", Energy 30, 2005. Elsevier: p. 2089–2100.
[74] Robinson, M.C., *et al.* "Horizontal Axis Wind Turbine Aerodynamics: Three-Dimensional, Unsteady, and Separated Flow Influences" in Proceedings of the 3rd ASME/JSME Joint Fluids Engineering Conference. 1999. San Francisco.
[75] Hu, D., O. Hua, and Z. Du, "A study on stall-delay for horizontal axis wind turbine", Renewable Energy, 2005. Elsevier.
[76] Viterna, L.A. and R.D. Corrigan, "Fixed pitch rotor performance of large horizontal axis wind turbines", DOE/NASA workshop on large horizontal axis wind turbines, 1981. Cleveland, (OH).
[77] Du, Z. and M. Selig, "The effect of rotation on the boundary layer of a wind turbine blade", Renewable Energy, 2000. 20.

[78] Mikkelsen R, "Actuator Disc Methods Applied to Wind Turbines", Dissertation for Technical University of Denmark, Jun 2003.
[79] Shen, W., *et al.*, "Tip loss corrections for wind turbine computations", Wind Energy, 2005. 8: p. 457-475.
[80] Glauert, H., "Airplane propellers", Aerodynamic Theory 4, 1963. Dover & New York: p. 169-269.
[81] Wilson RE, "Applied aerodynamics of wind powered machines", Report NSF/RA/N-74113. Oregon State University, 1974.
[82] De Vries O, "Fluid dynamic aspects of wind energy conversion", AGARD-AG-243, 1979.
[83] Shen WZ, "Evaluation of the Prandtl Tip Correction for Wind Turbine Computations", Proceedings of Global Windpower Conf., 2002. Paris, France.
[84] Maalawi KY, "A direct method for evaluating performance of horizontal axis wind turbines", Renewable and Sustainable Energy Reviews 5, 2001. Pergamon (175-190).
[85] Ebert, P.R. and D.H. Wood, "Observations on the starting behaviour of a small horizontal axis wind turbine", Renewable Energy, 1997. 12(3): p. 245-257.
[86] Wright, A.K. and D.H. Wood, "The starting and low wind speed behaviour of a small horizontal axis wind turbine", Wind Engineering and Industrial Aerodynamics, 2004. 92: p. 1265-1279.
[87] Madsen, H., *et al.*, "A Detailed investigation of the Blade Element Momentum (BEM) model based on analytical and numerical results and proposal for modifications of the BEM model", Journal of Physics: Conference Series, 2007. 75.
[88] Barltrop, N., *et al.*, "Investigation into wave-current interactions in marine current turbines", Proc. IMechE, 2007. 221(Part A: Journal of Power and Energy): p. 233-242.
[89] McCann, G. "Tidal current turbine fatigue loading sensitivity to waves and turbulence - a parametric study" in 7th European Wave and Tidal Energy 2007. Portugal.
[90] Bossanyi, E.A., "GH Tidal Bladed Theory Manual". 2007, Garrad Hassan.
[91] Ahmed, N.A. and R.D. Archer, "Testing of highly loaded horizontal axis wind turbines designed for optimum performance", Renewable Energy, 2002. 25: p. 613-618.
[92] Sanderson, R. and R. Archer, "Optimum propeller wind turbines." Energy, 1983. 7(6): p. 695-701.
[93] Sharpe, D., "A Lifting line Theory for the Determination of Wind Turbine Blade Optimum Performance", EWEA.
[94] Baltazar, J. and J Falçao de Campos. "Hydrodynamic Analysis of a Horizontal Axis Marine Current Turbine with a Boundary Element Method" in OMAE2008. 2008. Estoril, Portugal.
[95] McCombes, T., A. Grant, and C. Johnstone. "Unsteady Hydrodynamic Modelling of Rotor Systems Used in Marine Current Turbines" in World Renewable Energy Congress X. 2008. Glasgow.
[96] Egarr, D.A., *et al.*, "Feasibility Study Using computational Fluid dynamics for the Use of a Turbine for Extracting Energy from the Tide"

in 15th Australasian Fluid Mechanics Conference. 2004. The University of Sydney, Sydney Australia.
[97] Mason-Jones, A., *et al.*, "Characterisation of a HATT using CFD and ADCP site data" in World Renewable Energy Congress X. 2008. Glasgow.
[98] Fabrice, M., *et al.*, "Numerical simulation of the wake of marine current turbines with a particle method" in World Renewable Energy Congress X. 2008. Glasgow.
[99] Kamoun, B., D. Afungchui, and A. Chauvin, "A wind turbine blade profile analysis code based on the singularities method", Renewable Energy, 2005. 30: p. 339-352.
[100] Buhl, M.L., A.D. Wright, and J.L. Tangler. "Wind Turbine Design Codes: A Preliminary Comparison of the Aerodynamics" in 17th ASME Wind Energy Symposium. 1998. Reno.
[101] Buhl, M. "NWTC Design Codes (WT_Perf)", Online: wind.nrel.gov/designcodes/simulators/wtperf, Accessed: 05/05/2006.
[102] Laino, D.J. "NWTC Design Codes (YawDyn)", Online: wind.nrel.gov/designcodes/simulators/yawdyn, Accessed: 05/05/2006.
[103] H J Van Grol, H. Snel, and J. Schepers, "Wind Turbine Benchmark Exercise on Mechanical Loads: A state of the Art Report Volume 1 (Part A)", Netherlands Energy Research Foundation ECN, 1991.
[104] Bossanyi, E.A., "GH Tidal Bladed Version 3.80 User Manual". 2007, Garrad Hassan.
[105] Orme, J., "Dynamic Performance Modelling of Tidal Stream Turbines in Ocean Waves", PhD Thesis, 2006, Civil and Computational Engineering, Swansea University.

Chapter 3: Implementation

In this chapter, the basic theory of the tidal stream turbine model will be presented and discussed. Blade element momentum theory is used to model blade loads and Morison's equation is employed to model loading on other components. Mapping procedures are introduced which allow non-uniform inflows to be modelled, allowing for a more realistic ocean model than uniform inflow.

3.1 Basic Blade Element Momentum Theory

Blade element momentum theory (BEMT) was chosen as a basis for the model due to its low computational demand and reasonable accuracy. Orme [1] has shown that this approach can be utilised for tidal turbine modelling and that wave induced flows may be used as inputs to the BEMT equation. BEMT is well documented for a range of applications, one of the most frequently referenced sources is that of Glauert [2] another clear text on the subject is Griffiths [3] where the derivation of the theory is shown and its application to wind turbines is discussed. BEMT has its origins in one dimensional momentum theory and the development from this to BEMT is well explained in many texts (see [2-8] for examples) but will be repeated here for completeness.

3.1.1 One dimensional momentum theory

This is a highly simplified model for calculating the energy absorption of a wind or tidal turbine. The rotor in this case is modelled as a permeable disc, which is assumed to be frictionless and impart no rotational velocity to the flow, this is often referred to as the 'Actuator Disc'. A control volume (fig 3.1) flows through the actuator disc. The control volume is bounded by a stream tube, with two cross sections far upstream and far downstream of the disc. The stream tube is simplified as not interacting with the fluid outside of the

stream-tube. The actuator disc removes energy from the stream-tube by providing a drag force that produces a pressure drop in the fluid just downstream of the disc. Both upstream and downstream surfaces of the stream-tube are assumed to be at ambient static pressure and so the flow speed must drop downstream to satisfy Bernoulli's equation [9] in the downstream region. It is important to note that Bernoulli's equation is valid in the stream-tube upstream or downstream of the rotor but not across the rotor as energy is extracted there. The variation of pressure and flow speed along the stream-tube is best explained by examination of figure 3.1.

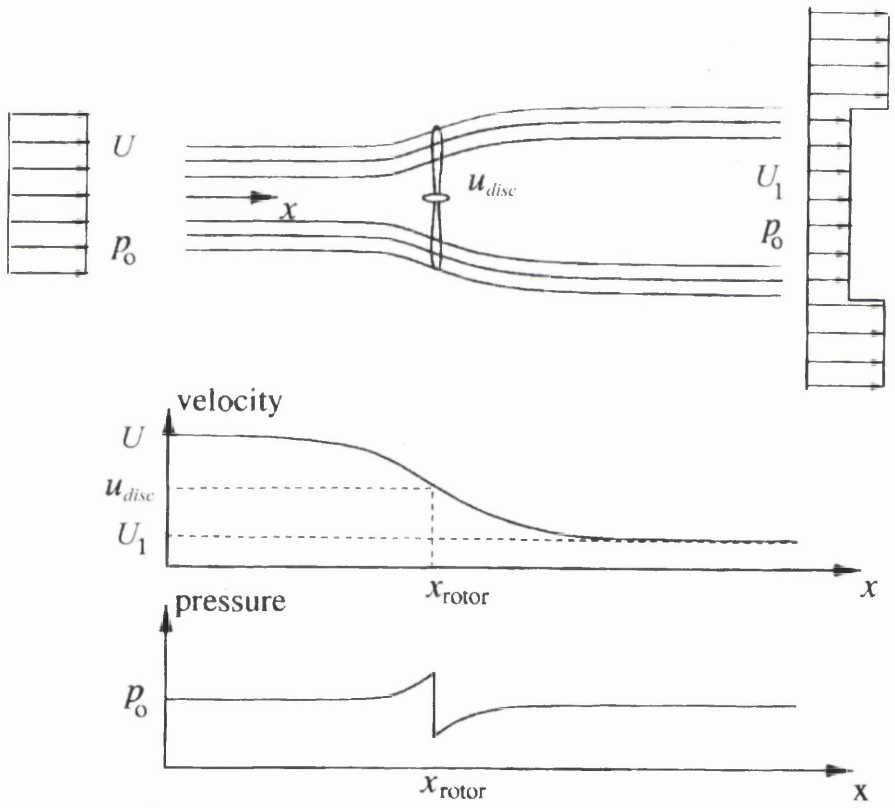

Figure 3.1: Stream tube and plots of velocity and pressure variation in stream-wise direction (Hansen [5]).

The change in momentum of the stream-tube across the actuator disc is due to the drag load put on the fluid by the disc. There is therefore an equal but opposite load applied to the disc by the fluid. This axial force, F_A, applied to the actuator disc can be calculated from the rate of change of momentum of the fluid. If the free-stream flow velocity is equal to U and the downstream

flow velocity is equal to U_1 and the cross sectional areas at the two points are A_0 and A_1 respectively then this may be written as (3.1):

$$F_A = U(\rho A_0 U) - U_1(\rho A_1 U_1)$$

... (3.1)

As mass flow rate is conserved in the stream-tube this can be rewritten as (3.2):

$$F_A = \dot{m}(U - U_1)$$

... (3.2)

F_A can also be defined in terms of the pressure differential immediately upstream and downstream of the actuator disc. $\dot{m}$ is the mass flow rate in (3.2). The static pressures far upstream and far downstream of the actuator disc are equal to the ambient static pressure, p_{amb} as the two points are vertically level with one another. Bernoulli's equation applies separately in the upstream and downstream regions leading to (3.3) and (3.4) respectively.

$$p_{amb} + \frac{1}{2}\rho U^2 = p_{ud} + \frac{1}{2}\rho u_{disc}^2$$

... (3.3)

$$p_{dd} + \frac{1}{2}\rho u_{disc}{}^2 = p_{amb} + \frac{1}{2}\rho U_1^2$$

... (3.4)

Consequently, (3.3) and (3.4) can be used to derive another formula for F_A based on the pressure differential, given in (3.5). The equations are simplified if it is accepted that the cross sectional areas and flow speeds of the stream tubes just upstream and just downstream of the actuator disc are effectively the area of the disc, A_{disc}, and the flow speed at the disc, u_{disc}.

$$F_A = A_{disc}\frac{1}{2}\rho(U^2 - U_1^2)$$

... (3.5)

Calculating the mass flow rate at the actuator disc and equating (3.5) to (3.2) yields (3.6):

$$u_{disc} = \frac{U + U_1}{2} \qquad \ldots (3.6)$$

Therefore, for this model, the flow speed at the rotor disc is the average of the free stream and down stream flow speeds. If the axial induction factor *a*, is now defined as the fractional reduction in flow speed between free-stream and the actuator disc (3.7), relationships for the flow speed downstream (3.8) and at the actuator disc (3.9) may be developed.

$$a = \frac{U - u_{disc}}{U} \qquad \ldots (3.7)$$

$$U_1 = U(1-2a) \qquad \ldots (3.8)$$

$$u_{disc} = U(1-a) \qquad \ldots (3.9)$$

The power, P, removed from the flow can be calculated as the thrust multiplied by the flow velocity at the disc, using (3.5) we can then write the equation for power as (3.10):

$$P = A_{disc}\frac{1}{2}\rho(U^2 - U_1^2)u_{disc} = A_{disc}\frac{1}{2}\rho u_{disc}(U - U_1)(U + U_1) \qquad \ldots (3.10)$$

Using the relationships shown in (3.8) and (3.9) we can then obtain an equation for power produced using only the free-stream flow velocity (3.11):

$$P = A_{disc}\frac{1}{2}\rho U^3 4a(1-a)^2 \qquad \ldots (3.11)$$

The axial force produced (3.5) can be written in the same form (3.12):

$$F_A = A_{disc}\frac{1}{2}\rho U^2 4a(1-a)$$

... (3.12)

Two coefficients are often used to describe the portion of the fluid's power and axial force obtained from the flow, the power coefficient C_P and the axial force coefficient C_{FA}. The definitions of these coefficients are given in (3.13) and (3.14) respectively:

$$C_P = \frac{\text{Rotor power}}{\text{power in streamtube}} = \frac{P}{\frac{1}{2}\rho U^3 A}$$

... (3.13)

$$C_{FA} = \frac{\text{Rotor thrust}}{\text{Available thrust}} = \frac{F_A}{\frac{1}{2}\rho U^2 A}$$

... (3.14)

Placing (3.11) in (3.13) gives (3.15)

$$C_P = 4a(1-a)^2$$

... (3.15)

The maximum power coefficient can be found by differentiating (3.15) with respect to a ((3.16)) to find the stationary point.

$$\frac{dC_P}{da} = 4(1-a)(1-3a) = 0$$

... (3.16)

The two solutions to this are $a=1$ or $a=1/3$. If a is higher than 0.5 it would imply a flow reversal downstream which is not physically possible therefore the theory is only valid up to $a=0.5$ and the peak power coefficient is therefore found at $a=1/3$ and has a value of 16/27. This result is known as the Betz limit and is the peak theoretical efficiency for any un-ducted turbine system.

Before proceeding, it is worth remembering that Actuator disc theory makes the following assumptions:

- There is no frictional drag.

- The flow is incompressible.
- Far upstream and downstream of the rotor the stream-tube is at ambient static pressure.
- There is no rotational velocity imparted to the wake.
- The thrust and change in momentum is uniform over the rotor disc.
- The disc represents a turbine with an infinite number of blades.

3.1.2 Addition of rotational effects

For a single horizontal axis rotor without a hydrodynamic stator, some of the energy lost from the axial flow is converted into rotational momentum of the stream-tube, leaving less power available for energy extraction. This rotational component in the flow is a reaction to the rotational torque imparted to the turbine rotor and is generally assumed to be small in comparison to the rotational speed of the system, Manwell [6] states that this allows the assumption that the ambient pressure far upstream is equal to the pressure far downstream. For the development of a model incorporating rotational effects, the stream tube is divided into annular sections with local radius r and thickness dr as shown at the rotor plane in figure 3.2.

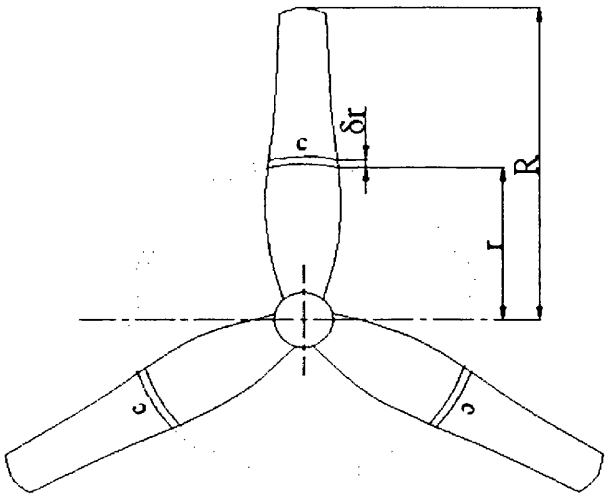

Figure 3.2: Diagram of rotor system showing a blade annulus from Orme [1].

The area of the stream tube annulus is $2\pi r dr$. A control volume rotating at the speed of the rotor, Ω, is employed to solve the problem, a derivation of the pressure differential just downstream and just upstream of the rotor based on Bernoulli's equation is given by Glauert [2]. As the axial flow speed is effectively constant but the rotational flow increases by ω just downstream of the rotor, Manwell [6] states that this pressure change may be written in terms of the imparted rotational momentum as (3.17):

$$p_{ud} - p_{dd} = \rho(\Omega + \frac{1}{2}\omega)r^2\omega$$

... (3.17)

The elemental thrust may then be calculated as the change in pressure multiplied by the annular area as in (3.18).

$$dF_A = \left(\rho(\Omega + \frac{1}{2}\omega)r^2\omega \right) 2\pi r dr$$

... (3.18)

Another induction factor, b, known as the angular induction factor or tangential induction factor is now introduced, its definition is given in (3.19).

$$b = \frac{\omega}{2\Omega}$$

... (3.19)

The annular thrust equation in (3.18) can be re-written using (3.19) to give (3.20):

$$dF_A = \left(4b(1+b)\tfrac{1}{2}\rho\Omega^2 r^2 \right) 2\pi r dr$$

... (3.20)

Alternatively, the equation for axial force obtained in (3.12) remains valid and can be altered to give dF_A by replacing A_{disc} with $2\pi r dr$.

As wake rotation is now included in the equations, it is possible to develop a formula for the torque produced on the rotor annulus, dT, as it must be equal

to the change in angular momentum of the wake. For an annulus this may be written as (3.21)

$$dT = d\dot{m}(\omega r)r = \rho u_{disc} 2\pi r dr(\omega r)r$$

... (3.21)

Using (3.9) and (3.19) in (3.21) an expression for elemental torque is obtained in terms of the upstream flow (3.22)

$$dT_1 = 4b(1-a)\rho U\Omega r^2 \pi r dr$$

... (3.22)

As power is the product of torque and rotational speed, an elemental power formula may be obtained by multiplying (3.22) by Ω. From this, it is possible to derive a formula for peak efficiency that is now dependent on Tip Speed Ratio (*TSR*). *TSR* is a dimensionless measure of the linear speed of the rotor tip against incoming flow speed. It is often used for comparison and its definition is given in (3.23).

$$TSR = \Lambda = \frac{R\Omega}{U}$$

... (3.23)

The derivation of the peak power coefficient is more involved than that for the Betz limit and so is omitted from this text but it is clearly described in Hansen [5] or Buhl [10] amongst others.

3.1.3 The Results of Momentum Theory

By considering the change in axial and rotational fluid momentum upstream and downstream of the idealised rotor, expressions have been derived for the axial thrust and rotational torque produced by an annulus of a turbine rotor. The axial thrust equation is the annular version of (3.12) and is shown in

(3.24). It is the same as (3.12) except that the area can now be calculated as $2\pi r dr$.

$$dF_{A1} = 2\pi r \frac{1}{2} \rho U^2 4a(1-a)dr \quad \ldots (3.24)$$

The annular torque equation is that shown in (3.22). These equations provide a means to calculate torque and axial force of a rotor annulus if the free stream flow, axial induction factor and tangential induction factor are known.

3.1.4 Blade element Theory

Unfortunately, a and b are not known *a priori* and so the equations derived from momentum theory are of little use in isolation. Blade element theory provides an alternative analytical approach to the momentum theory. The principle is based upon dividing the rotor blades into discrete span-wise (along the blade length) elements. It is assumed that there is no fluid interaction between these elements, which allows each element to be modelled as a two-dimensional foil. The loads on the blades can then be assumed to rely purely on the lift and drag characteristics of these foil shapes. The radius of each element is at radial position *r* and it has a width dr, as was used for the annular momentum equations.

Figure 3.3 shows the lift and drag forces acting on one of these 2D elements of a rotor blade. dL is the element lift force and dD is the element drag force. ϕ is the inclination of the resultant flow, V, to the horizontal axis. This resultant flow comes about as the foil is rotating and so experiences the combined vector of the axial in-flow and the rotational induced swirl at the rotor plane as well as its own rotational linear speed.

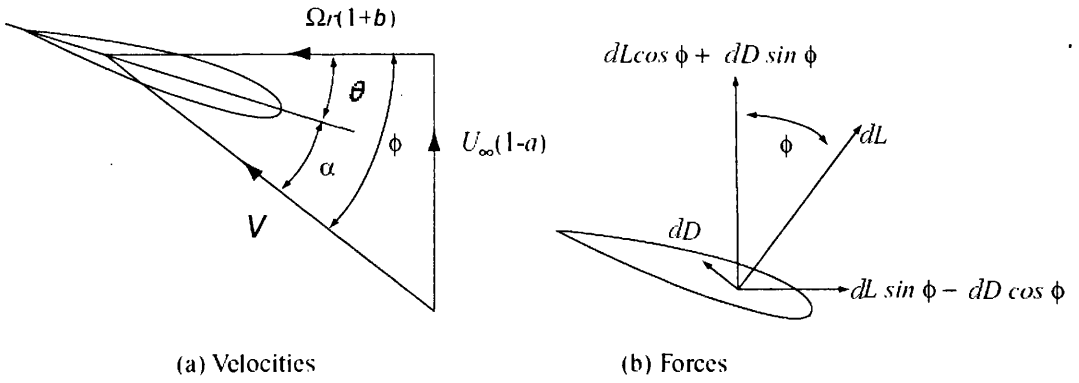

Figure 3.3: Lift and drag diagram for viscous flow. Based on a diagram by Burton [7].

There are three important angles concerned with the flow. These angles are α, ϕ and θ. ϕ is the resultant flow angle of the axial and tangential flow components, α is the angle of attack of the turbine blade from the resultant flow and θ is the combined pitch and twist of the blade. The conventions and calculation of θ and ϕ will be discussed at the end of this subsection.

The axial thrust of the blade element and the torque produced can be found by resolving the lift and drag forces dL and dD : as in (3.25) and (3.26).

$$dF_{A2} = dL\cos\phi + dD\sin\phi \qquad \ldots (3.25)$$

$$dT_2 = r(dL\sin\phi - dD\cos\phi) \qquad \ldots (3.26)$$

In foil theory, the lift and drag performance are often defined in terms of dimensionless variables, C_L and C_D. These lift and drag coefficients are often derived from experimental investigations on standard foil profiles. The coefficients vary with the angle of attack, α, and so data is usually given for a range of flow angles. The definitions of C_L and C_D are given in (3.27) and (3.28) and can be found in any fluids reference text, such as Massey [9].

$$C_L = \frac{L}{\frac{1}{2}\rho V^2 c dr} \quad \ldots (3.27)$$

$$C_D = \frac{D}{\frac{1}{2}\rho V^2 c dr} \quad \ldots (3.28)$$

With the lift and drag coefficients employed and remembering that (3.25) and (3.26) calculate the loads for a single blade element, expressions for dF_{A2} (3.29) and dT_2 (3.30) can now be obtained, N is the number of blades:

$$dF_{A2} = N\frac{1}{2}\rho V^2 c(C_L \cos\phi + C_D \sin\phi)dr \quad \ldots(3.29)$$

$$dT_2 = N\frac{1}{2}\rho V^2 cr(C_L \sin\phi - C_D \cos\phi)dr \quad \ldots(3.30)$$

From Figure 3.3, it can be seen that:

$$\phi = \tan^{-1}\left(\frac{U(1-a)}{r\Omega(1+b)}\right) = \tan^{-1}\left(\frac{(1-a)}{\lambda(1+b)}\right)$$

Where $\lambda = \frac{r\Omega}{U}$, the dimensionless local speed ratio

$\ldots(3.31)$

The definition of ϕ given by Griffiths [3] is in fact different from the majority of other texts [5-7] (as is presented here). It is defined from the rotor normal plane, the general convention is to define this flow angle from the rotor plane as shown in Figure 3.3. The same is true for the definition of the final blade twist, θ. The convention is to define this as the angle of the mean chord line of the foil element from the rotor plane surface. The notation used by Griffiths defines θ_{Grif} as the angle from the rotor plane normal surface. Either definition is valid but awareness of which is being used is vital and $\sin\phi$ must

be swapped for $\cos\phi_{Grif}$ and vice-versa in (3.29) and (3.30) if the Griffiths definitions are employed. (3.31) also changes if the Griffiths definition is to be used. The relationship between the three angles discussed in this chapter also varies depending on the defined relationship. In Griffiths' approach [3] $\theta_{Grif} = \phi_{Grif} + \alpha_{Grif}$ whereas the convention in other texts means that $\theta = \phi - \alpha$. The discussion of Griffiths' flow definitions is present to make the reader aware of the difference. The non-Griffiths definitions will be employed for the rest of this thesis.

V, the resultant fluid flow, can be calculated using Pythagoras' theory:

$$V = [(r\Omega(1+b))^2 + (U(1-a))^2]^{\frac{1}{2}} = U[\lambda^2(1+b)^2 + (1-a)^2]^{\frac{1}{2}} \quad \ldots (3.32)$$

3.1.5 Combination and solution

We now have two separate formulae for axial elemental force and two for elemental torque, these still cannot be solved directly but, with rearrangement, approximate solutions may be found. There are a few subtly different approaches used to solve these equations and these shall now be discussed. Methods one and two are presented in the existing literature (see [4, 6, 7] for examples) and are covered briefly here for completeness. The alternative proposed approach has not been encountered during the review of literature, the basic derivation is somewhat simpler than the other approaches and is presented here.

3.1.5.1 Traditional approaches

The two traditional approaches are to solve the objective equations either for lift coefficient and angle of attack or to solve iteratively for a and b. The starting point for both of these equations is the same.

First, the momentum and blade element equations for torque (3.22 and 3.30) are equated, giving (3.33):

$$N\frac{1}{2}\rho V^2 cr(C_L\sin\phi - C_D\cos\phi)dr = 4b(1-a)\rho U\Omega r^2\pi r dr$$

... (3.33)

Rearrangement of this equality using local solidity ($\sigma = {}^{cN}/_{2\pi r}$) and λ and noting that V may be written as $\frac{U(1-a)}{\sin\phi}$ gives (3.34).

$$\frac{b}{(1-a)} = \frac{\sigma(C_L\sin\phi - C_D\cos\phi)}{4\lambda\sin^2\phi}$$

... (3.34)

Similarly, equating the axial force formulae (3.24) and (3.29) yields (3.35):

$$NV^2 c(C_L\cos\phi + C_D\sin\phi) = 2\pi r U^2 4a(1-a)$$

... (3.35)

Making use of the same relationships employed between (3.33) and (3.34) gives (3.36):

$$\frac{a}{(1-a)} = \frac{\sigma(C_L\cos\phi + C_D\sin\phi)}{4\sin^2\phi}$$

...(3.36)

For method 1, finding C_L and α, these equations must be rearranged further. First, it is assumed that the drag coefficient may be neglected in solving the equation. This is argued by Wilson and Lissaman [11] and will be discussed in more depth (see chapter 4). Using $\tan\phi$ from (3.31) , (3.34) and (3.36) with the drag term neglected, a rearrangement for C_L can be obtained. This is shown in (3.37).

$$C_L = 4\sin\phi\frac{(\cos\phi - \lambda\sin\phi)}{\sigma(\sin\phi + \lambda\cos\phi)}$$

...(3.37)

The two unknowns in this equation are C_L and ϕ but it is known that $\phi = \alpha + \theta$ so the two base unknown variables are in fact C_L and α. These can be found by finding the correct C_L and α combination from empirical foil data. It is important to check that the solution is valid once it is found. It is difficult to incorporate high induction and tip loss corrections (discussed later in chapter 4) and the drag load cannot be incorporated with this approach.

Method 2 solves the equations for a and b rather than C_L and α. To obtain equations for this approach, (3.34) and (3.36) must again be re-arranged to give expressions for b (3.38) and a (3.39) respectively.

$$b = \left[-1 + \frac{4\sin\phi\cos\phi}{\sigma(C_L\sin\phi - C_D\cos\phi)}\right]^{-1}$$

... (3.38)

$$a = \left[1 + \frac{4\sin^2\phi}{\sigma(C_L\cos\phi + C_D\sin\phi)}\right]^{-1}$$

... (3.39)

An iterative procedure can be employed using (3.38) and (3.39) as follows:

1. Guess a starting value for a and b. b is traditionally set to zero, a may be set to zero or approximated using a variety of methods.
2. Calculate ϕ using (3.31).
3. Use this value of ϕ to look up the corresponding lift and drag coefficients from empirical lift and drag data using the relationship $\alpha = \phi - \theta$.
4. Calculate a and b from (3.39) and (3.38).

5. These new values can be fed back in as the starting values and the process can be repeated from step 2 until a converged solution is obtained.

It is possible to neglect drag or keep it in the equation using this approach. This method is suitable for high induction and tip loss correction as will be seen in Chapter 4 and is more suitable for implementation in an automated routine.

3.1.5.2 Alternative proposed approach

The above approaches work well as a simple iterative loop but provide little control on search direction and they are both quite dependent on the selection of a good starting value. They are effectively simple search methods. Additional mathematical constraint of the problem would be possible but an alternative approach is proposed here which can be directly used with a variety of pre-constructed solver routines that benefit from a large degree of development. The particular routine used in this project was Matlab's built in fmincon function [12], which employs sequential quadratic programming to solve the objective. Sequential quadratic programming gives a faster approach to solving an objective function than a line search and is less likely to converge on a local minimum.

The Derivations for the equations for this approach are somewhat simpler than those of method one and two. The torque (3.33) and axial force (3.35) equalities are simply combined into a single minimisation objective function (3.40). Note that ϕ and V are given in (3.31) and (3.32).

$$\text{Minimise } g:$$

$$g=(dF_{A1}-dF_{A2})^2+(dT_1-dT_2)^2$$

$$g=(4\pi rU^2(1-a)a-N\frac{1}{2}V^2c(C_L\cos\phi+C_D\sin\phi))^2+...$$

$$(4\pi\rho r^2U\Omega(1-a)b-N\frac{1}{2}V^2c(C_L\sin\phi-C_D\cos\phi))^2$$

... (3.40)

The lift and drag coefficients in the function are interpolated from a vector of lift data against angle of attack, α.

This can then be implemented as the minimisation objective function in the fmincon routine. Note that the square of both terms is used, this is to avoid the possibility of converging on an incorrect solution where the torque based residual is equal but opposite in sign to the axial based residual.

In this objective function, as in method 2, a and b are the two basic unknown variables on which all other variables depend. The boundary constraints can be input to this routine; b may have any value but will generally be near zero, a has a maximum limit of *0.5*. A value for a over this point would imply that the flow was reversed downstream of the turbine. In true operation, the flow incorporates fluid from the free stream and creates a high degree of turbulence over this limit. Lower bound constraints are also imposed on a and b to prevent excessively negative values of a and b being explored.

3.1.6 Implementation considerations

The implementation approach has been introduced in 3.1.5.2 and was previously described in Chapman [13]. Specific implementation details will be presented here, giving a comprehensive description when combined with 3.1.5.2. The approach used to obtain initial starting values differs slightly to the more common approach that finds a starting value by assuming the rotational interference factor, b, to be zero [4]. This method has a low computational demand but struggles to find properly converged solutions in some cases where tangential induction factors may deviate from their usually low value or where there are multiple local minima. An example of the objective function under conditions where there are multiple local minima is shown in figure 3.4.

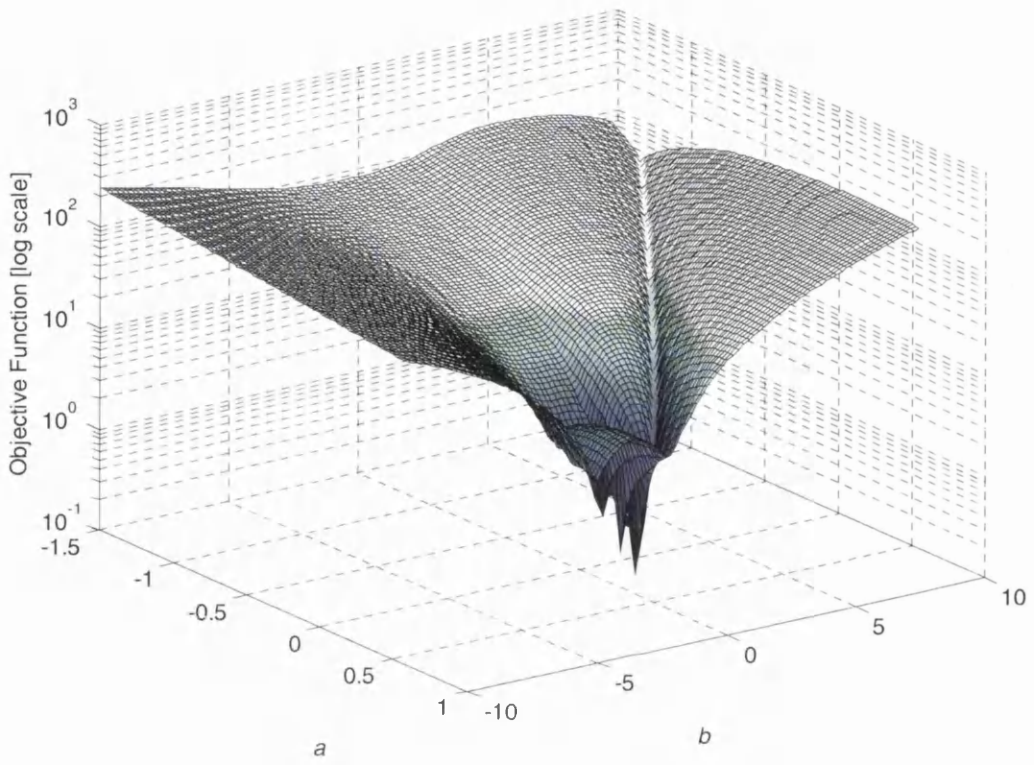

Figure 3.4: Surface of objective function for varying a and b for a case with multiple local minima.

The traditional solver approaches 1 and 2 would be likely to find a local minimum in a case like this. The combination of the robust solver approach and Monte Carlo simulation achieves convergence on the global solution. A Monte Carlo simulation [14] is used to find approximate a and b values before the optimisation routine is run. Although the Monte Carlo routine adds computational demand it can also reduce computational time spent in the solver so has little net increase in processor demand whilst increasing the solution reliability. The Monte Carlo search is operated for the first ten steps of any model run to ensure a reasonable starting solution is found, after this the code employs the solution from the previous model step as the initial solution of the new step. If an element does not converge however the code will revert to the Monte Carlo simulation to find an alternative starting value.

Once values for a and b are found for each blade element, the torque and axial loads can be found for the complete rotor system. The sum of these torques can then be multiplied by the turbine's rotational speed to give the rotor's power production. Post processing can yield axial loads, power coefficients and other information. As previously discussed, there are boundary constraints on the value of a. Unless a high induction correction is employed (see chapter 4) the maximum value of a is 0.5. It is also possible for both a and b to become negative, this implies that the rotor system is acting as a propeller. This can occur at high tip-speed ratios where the tip elements will reach high linear speeds. The outboard elements will produce drag under these conditions but elements of the blade further inboard will continue to produce a generative torque. There is a stage where these two conditions balance out giving no net torque to the generator but also requiring no input torque to continue spinning. It is therefore important that the solution system is capable of solving for all feasible cases. Limits must be placed in the positive *a* region due to the physical limit and negative constraints are placed on both a and b to avoid an excessive search range for Monte Carlo simulation.

Lift and drag data for the foil being modelled must be selected to reflect the operating Reynolds number of the foil. It is common practice to select a fixed characteristic Reynolds number and use a single set of lift and drag data. This gives minimal errors if the Reynolds number operation range does not present massively different lift and drag data. The lift and drag data used in this thesis is that used by Orme in his thesis [1]. The data is for a NACA 4424 foil and data is obtained from foil tests given in Abbot and Von Doenhoff [15] and two-dimensional lifting surface theory from 'Profili' [16]. Profili is a graphical user interface for Drela's XFoil panel method code [17]. Post stall data was calculated using flat plate theory, further information on this is available in Manwell *et al.* [6]. No further development of lift and drag data has been carried out in this thesis although discussions are provided on suitable corrections for stall delay in chapter 4. A good text for further reading on the topic of lift and drag data is provided in Tangler [18].

3.1.7 Tangential Flow inclusion

The basic blade element theory discussed above was initially intended for a uniform upstream flow normal to the rotor plane. In true conditions, flow velocity will vary with time and space. It is relatively simple to include the spatial variations of flow by applying different upstream flow conditions on each blade element (these are found using the mapping procedures displayed later in this chapter). Doing so means that the model is no longer physically correct (different induction factors lead to radial circulation and the wake is no longer uniform) but it is a widely accepted approach and has little impact on the accuracy of results [5]. Time variations can also be taken into account by changing the flow conditions iteratively in a time stepping loop, this assumes an instantaneous steady state flow, which may over-predict the impact of transient flow variations [6] but is an accepted modelling approach [19].

This approach would still only deal with the component of flow normal to the rotor plane. In a three dimensional flow, the blade will also be subject to a tangential flow and a radial flow. As BEMT assumes independent two-dimensional flows for each element, radial flows are not considered. The radial component of inflow is therefore assumed not to interact with the rotor system at present. Induced radial flow due to vortex shedding (see Ch. 4 for description and references) is incorporated with tip loss models and is a factor in stall delay (Chapter 4). It is possible that a similar correction factor could be incorporated into the code at a later stage to allow for the effect of radial inflows. At this stage, an attempt has been made to include tangential flow, this approach will now be outlined:

The incoming flow v for each blade element point is first found and resolved relative to the blade plane using the methods described in the three-dimensional mapping section of this report (giving $v' = \left[v_1' \; v_2' \; v_3' \right]^T$). The tangential component of flow (v_2') must then be included in the blade element and momentum equations. To do this, the tangential flow was assumed a

constant additional term to the tangential fluid velocity. On implementation, this assumption does not affect the core objective function but does alter the angle of incidence (3.41) of the flow and the resultant inflow velocity (3.42). These become:

$$\phi = \tan^{-1}\left(\frac{U(1-a)}{r\Omega(1+b)+v_2'}\right) \qquad \ldots (3.41)$$

And:

$$V = [(r\Omega(1+b)+v_2')^2 + (U(1-a))^2]^{\frac{1}{2}}$$
$$\text{Where } U = v'_1 \qquad \ldots (3.42)$$

These equations may be used in place of (3.31) and (3.32) in the objective function shown in (3.40).

Consultation of existing literature suggests that this approach has not been previously employed. A similar approach is used by Moriarty and Hansen [4] to incorporate the effects of blade vibrations for flexible rotors however.

3.1.8 BEMT Solver Core

At this stage, it is possible to construct a BEMT solver. This can be used to predict hydrodynamic loadings on blade elements given a known inflow velocity, blade chord, twist, radial location and lift drag data for each blade element.

The approach is summarised in figure 3.5. This routine may be used in a loop through rotational speeds with a constant flow velocity to give a performance curve of a rotor system. It may also be used in a time dependent model provided that the rotational speed and inflow velocity can

be calculated. This can be achieved by implementing the mapping and inflow procedures discussed later in this chapter.

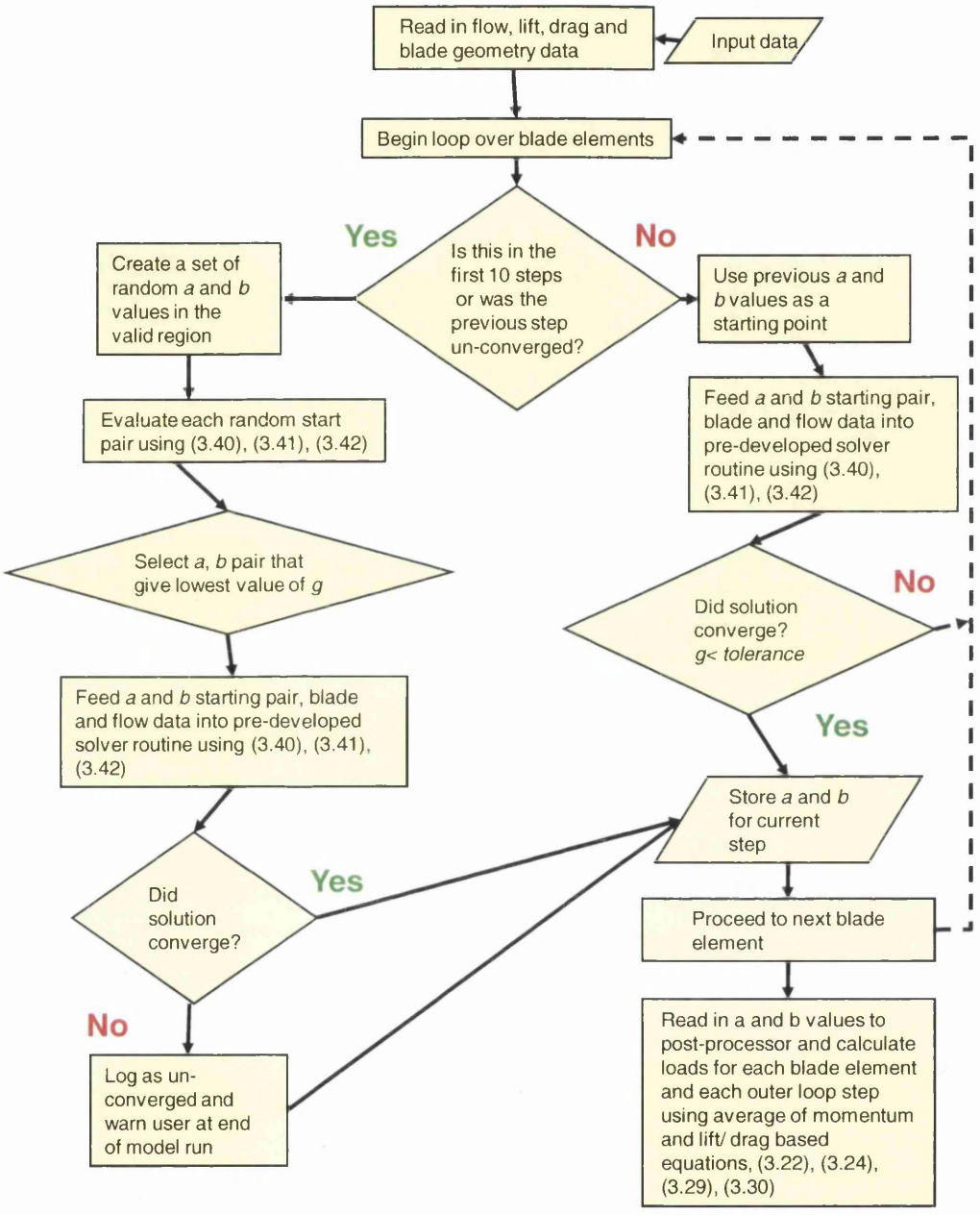

Figure 3.5: Flow chart for BEMT solution routine.

3.1.9 Conclusion

In this section, basic blade element and momentum theory has been reported, the method of implementation of a novel solution approach discussed and a novel adaptation has been suggested to take into account tangential flow velocities, the approach is similar to one used to model blade movement and assumes the wake is independent of this cross flow. A further investigation into the prediction capabilities of the code is seen in Chapter 4.

3.2 Three-Dimensional Mapping

In order to more accurately model the true performance of a marine turbine system, it is necessary to take into account yaw, tilt and rotation of the system relative to a three dimensional, non-uniform flow. For comprehensive modelling, it must therefore be possible to track the position of a blade element in a global coordinate system and resolve the three-dimensional flow field into components relative to the rotor blades. These two operations have a similar basis but the approach taken must differ slightly.

3.2.1 Yaw, Tilt and Rotation

The tracking of a blade element in global coordinates will first be covered. The origin of the global coordinate system is at the base of the supporting structure directly below the tilt and yaw centre of the turbine system with the Z-axis pointing vertically up the support (see fig. 3.6).

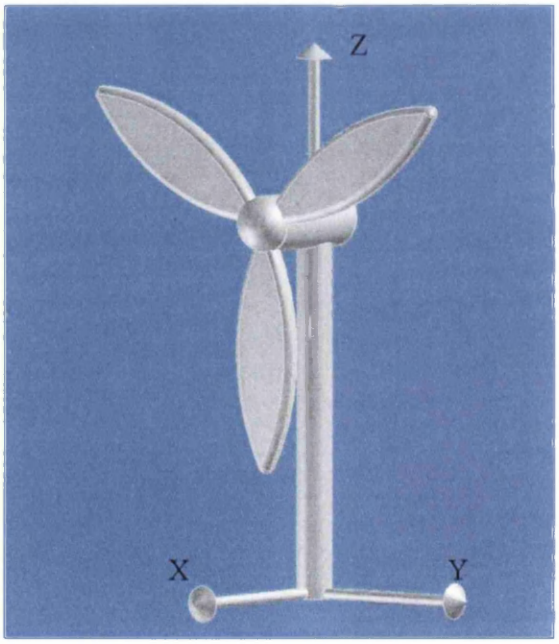

Figure 3.6: Global coordinate system relative to undisturbed turbine

The hub height and distance of the rotor plane from the tilt and yaw centre are taken as being user-defined inputs. It is also assumed that the

orientation of the blades around the hub centre, called the azimuth position (ψ), relative to a prescribed starting position will be input or calculated at each iteration. With this data, it is possible to calculate the position of a blade element in global coordinates.

The undisturbed positions must first be defined. Figure 3.6 shows a rotor system with zero yaw, tilt and azimuth. The centres of rotation of the system must also be defined. The azimuth rotation will always take place around the hub centre and will be in the plane of the rotor system. The Yaw and Tilt centres are assumed to be around the same point in the present approach. This point is horizontally in line with the hub centre and on the Z-axis. Points on the rotor blades can be translated to the origin and rotated around a relevant axis then translated back to calculate their new position [20]. It is important to get the correct order whilst doing this as different orders of rotations and translations will give differing results.

To aid understanding of the procedure, an outline of the process for a general point on a turbine blade is now given:

First, the hub centre must be translated to the Y, Z origin so that it is in the same position as the X-axis. A robust approach for automation is the use of matrices [20]. Defining the yaw centre to hub centre distance as *A* and the distance from hub height to base as *H*, the translation matrix $[S_\psi]$ for the azimuth rotation is (3.43):

$$S_\psi = \begin{bmatrix} 1 & 0 & 0 & -A \\ 0 & 1 & 0 & 0 \\ 0 & 0 & 1 & -H \\ 0 & 0 & 0 & 1 \end{bmatrix}$$

... (3.43)

The corresponding rotation Matrix $[R_\psi]$ (3.44) is:

$$R_{\psi}=\begin{bmatrix}1 & 0 & 0 & 0\\ 0 & Cos(\psi) & -Sin(\psi) & 0\\ 0 & Sin(\psi) & Cos(\psi) & 0\\ 0 & 0 & 0 & 1\end{bmatrix}$$

... (3.44)

Therefore, any point on a rotor blade that has an initial, undisturbed, position **a** in global coordinates has an updated general position **b** (3.45).

$$\mathbf{b} = [S_{\psi}^{-1} \times R_{\psi} \times S_{\psi}] \times \mathbf{a}$$

... (3.45)

For any value of ψ.

The same process may be carried out for tilt and yaw respectively. The Yaw angle is denoted by ς and tilt angle by σ. The translation [S_{σ} and S_{ς}] (3.46) and rotation matrices [R_{σ} and R_{ς}] (3.47), (3.48) for these are:

$$S_{\sigma}=S_{\varsigma}=\begin{bmatrix}1 & 0 & 0 & 0\\ 0 & 1 & 0 & 0\\ 0 & 0 & 1 & -H\\ 0 & 0 & 0 & 1\end{bmatrix}$$

... (3.46)

$$R_{\sigma}=\begin{bmatrix}Cos(\sigma) & 0 & Sin(\sigma) & 0\\ 0 & 1 & 0 & 0\\ -Sin(\sigma) & 0 & Cos(\sigma) & 0\\ 0 & 0 & 0 & 1\end{bmatrix}$$

... (3.47)

$$R_{\varsigma}=\begin{bmatrix}Cos(\varsigma) & -Sin(\varsigma) & 0 & 0\\ Sin(\varsigma) & Cos(\varsigma) & 0 & 0\\ 0 & 0 & 1 & 0\\ 0 & 0 & 0 & 1\end{bmatrix}$$

... (3.48)

Rotation and translation are then combined for each case in the same way as for azimuth rotation. For correct position calculation, the blades must be rotated, then tilted and finally yawed. An effective approach is to combine the matrices and rotate, tilt and yaw the original point in a single operation [20]. To obtain the combined translated rotation matrix $[T_c]$ we use (3.49):

$$T_c = T_\zeta \bullet T_\sigma \bullet T_\psi$$

Where

$$T_\zeta = S_\zeta^{-1} \bullet R_\zeta \bullet S_\zeta \ , \ T_\sigma = S_\sigma^{-1} \bullet R_\sigma \bullet S_\sigma \text{ and } T_\psi = S_\psi^{-1} \bullet R_\psi \bullet S_\psi$$

... (3.49)

Using this matrix, it is possible to calculate the current position, $\mathbf{b}$, of any point on the blade system (3.50):

$$\boldsymbol{b} = T_c \bullet \mathbf{a}$$

... (3.50)

The position of all blade elements can be calculated in global coordinates using the method above. These positions can be used to find the corresponding incoming three-dimensional flows for each blade element. The following step is then to resolve these flows relative to the blade to give normal, tangential and radial flow components.

3.2.2 Mapping

Mapping involves similar matrix operations to the previous section, it is not necessary, however, to apply translations because direction vectors are being dealt with. The incoming flow vector is resolved into blade relative values by transformation into a local coordinate system. This coordinate system tracks a blade, the *x'* axis runs along the blade length, the *y'* axis

points towards the yaw and tilt centre and the *z'* axis is in the plane of the rotor and is 90° anti-clockwise from *x'* when looking downstream (fig. 3.7).

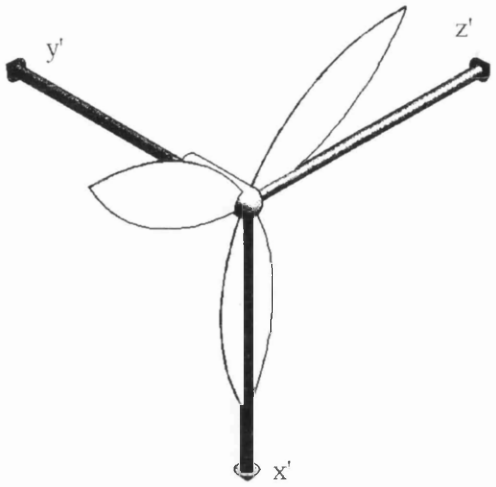

Figure 3.7: Local blade axes for blade pointing vertically downwards

The transformation matrix is obtained by implementation of a generic transformation matrix [21] based on describing the new axis system in terms of the original axis system. Vectors *i'*, *j'*, *k'* describe the axes *x'*, *y'* and *z'* respectively. Likewise *i*, *j*, *k* are direction vectors that represent the global axes *x*, *y*, *z*. The generic form of the transformation matrix $[T_{L/G}]$ (3.51) is:

$$T_{L/G} = \begin{bmatrix} i \cdot i' & j \cdot i' & k \cdot i' \\ i \cdot j' & j \cdot j' & k \cdot j' \\ i \cdot k' & j \cdot k' & k.k' \end{bmatrix}$$

... (3.51)

The local vectors *i'*, *j'*, *k'* can be obtained by first defining the local axis vectors for an undisturbed blade [i.e. No yaw, tilt or rotation] and then applying a rotation matrix to each of these. With reference to figures 3.6 and 3.7, it is possible to define the undisturbed direction vectors i_0', j_0', k_0' and the global axis vectors *i*, *j*, *k* as (3.52):

$$i=\begin{bmatrix}1\\0\\0\end{bmatrix} \qquad j=\begin{bmatrix}0\\1\\0\end{bmatrix} \qquad k=\begin{bmatrix}0\\0\\1\end{bmatrix}$$

$$i_0^{'}=\begin{bmatrix}0\\0\\-1\end{bmatrix} \qquad j_0^{'}=\begin{bmatrix}-1\\0\\0\end{bmatrix} \qquad k_0^{'}=\begin{bmatrix}0\\1\\0\end{bmatrix}$$

... (3.52)

To obtain the rotated, tilted and yawed local blade axis vectors, each of these vectors must be multiplied by a transformation matrix, T_0, given in (3.53), (3.54) which is the product of the first three columns and rows of R_σ, R_ς and R_ψ:

$$T_0=\begin{bmatrix}Cos(\varsigma) & -Sin(\varsigma) & 0\\ Sin(\varsigma) & Cos(\varsigma) & 0\\ 0 & 0 & 1\end{bmatrix}\times\begin{bmatrix}Cos(\sigma) & 0 & Sin(\sigma)\\ 0 & 1 & 0\\ -Sin(\sigma) & 0 & Cos(\sigma)\end{bmatrix}\times\begin{bmatrix}1 & 0 & 0\\ 0 & Cos(\psi) & -Sin(\psi)\\ 0 & Sin(\psi) & Cos(\psi)\end{bmatrix}$$

... (3.53)

$$T_0=\begin{bmatrix}Cos(\varsigma)Cos(\sigma) & Cos(\varsigma)Sin(\sigma)Sin(\psi)-Cos(\psi)Sin(\varsigma) & Cos(\varsigma)Sin(\sigma)Cos(\psi)+Sin(\varsigma)Sin(\psi)\\ Cos(\sigma)Sin(\varsigma) & Cos(\varsigma)Cos(\psi)+Sin(\psi)Sin(\varsigma)Sin(\sigma) & Cos(\psi)Sin(\sigma)Sin(\varsigma)-Cos(\varsigma)Sin(\psi)\\ -Sin(\sigma) & Sin(\psi)Cos(\sigma) & Cos(\psi)Cos(\sigma)\end{bmatrix}$$

... (3.54)

This matrix can be used to find the updated axis vector (3.55), thus:

$$i'=T_0\cdot i_0^{'}\ ,\quad j'=T_0\cdot j_0^{'}\ ,\quad k'=T_0\cdot k_0^{'}$$

... (3.55)

This will give the local axis vectors (3.56):

$$i' = \begin{bmatrix} -\cos(\varsigma)\sin(\sigma)\cos(\psi) - \sin(\varsigma)\sin(\psi) \\ \cos(\varsigma)\sin(\psi) - \cos(\psi)\sin(\varsigma)\sin(\sigma) \\ -\cos(\psi)\cos(\sigma) \end{bmatrix} \quad j' = \begin{bmatrix} -\cos(\varsigma)\cos(\sigma) \\ -\cos(\sigma)\sin(\varsigma) \\ \sin(\sigma) \end{bmatrix} \quad k' = \begin{bmatrix} \cos(\varsigma)\sin(\sigma)\sin(\psi) - \cos(\psi)\sin(\varsigma) \\ \cos(\varsigma)\cos(\psi) + \sin(\varsigma)\sin(\psi)\sin(\sigma) \\ \sin(\psi)\cos(\sigma) \end{bmatrix}$$

... (3.56)

Substituting this into the generic matrix gives the vector-mapping matrix (3.57):

$$T_{L/G} = \begin{bmatrix} -\cos(\varsigma)\sin(\sigma)\cos(\psi) - \sin(\varsigma)\sin(\psi) & \cos(\varsigma)\sin(\psi) - \cos(\psi)\sin(\varsigma)\sin(\sigma) & -\cos(\psi)\cos(\sigma) \\ -\cos(\varsigma)\cos(\sigma) & -\cos(\sigma)\sin(\varsigma) & \sin(\sigma) \\ \cos(\varsigma)\sin(\sigma)\sin(\psi) - \cos(\psi)\sin(\varsigma) & \cos(\varsigma)\cos(\psi) + \sin(\varsigma)\sin(\psi)\sin(\sigma) & \cos(\sigma)\sin(\psi) \end{bmatrix}$$

... (3.57)

Multiplying this matrix by a global velocity vector will give the transformed, local velocity vector. If a flow velocity v is incident on a turbine, the flow velocity relative to the blade element v' is defined as $v' = T_{L/G} v$.

3.2.3 Conclusion

Approaches have been shown in this section to track the position of a blade element during azimuth rotation, tilt and yaw of the rotor. This global coordinate could then be used to find a corresponding three dimensional, global velocity for each blade element. A system to map this velocity vector into a local, blade relative coordinate system has then been described. This resolved velocity can then be used in BEMT (or indeed an alternative flow solver) to predict the performance of the turbine system.

3.3 Wave modelling and non-uniform flows

Now that the basic BEMT model and adaptations to incorporate side-flows as well as a method for mapping a rotor in three-dimensional space and resolving corresponding inflows have been presented, some realistic inflow velocities are needed. A tidal flow model, which is more realistic than a uniform flow assumption, will first be discussed and then wave effects will be incorporated.

3.3.1 Tidal flow profile

The seabed will interact with a tidal flow to give a variation of flow velocity with depth, the water surface will suffer very little drag in comparison and so may be assumed to be a free surface. It is possible to assume therefore that the tide will act as a boundary layer flow (for example Orme [1]). A simple empirical relationship to describe the variation of flow velocity with depth is the power law flow profile (3.58). This is a widely accepted model for many types of boundary layer flow and is presented in many fluids texts such as Schlicting [22].

$$\frac{u}{U_{fs}} = \left(\frac{y}{R}\right)^{\frac{1}{n}} \qquad \ldots (3.58)$$

In this equation, u is the local flow speed and U_{fs} is the free stream flow velocity. The local height above seabed is y and the boundary layer height is R. n is known as the power law exponent and is generally set as seven [23] but is dependent on a specific site's characteristics and $n=10$ has also been recommended for tidal flows [1], the difference in these values is seen in Figure 3.8.

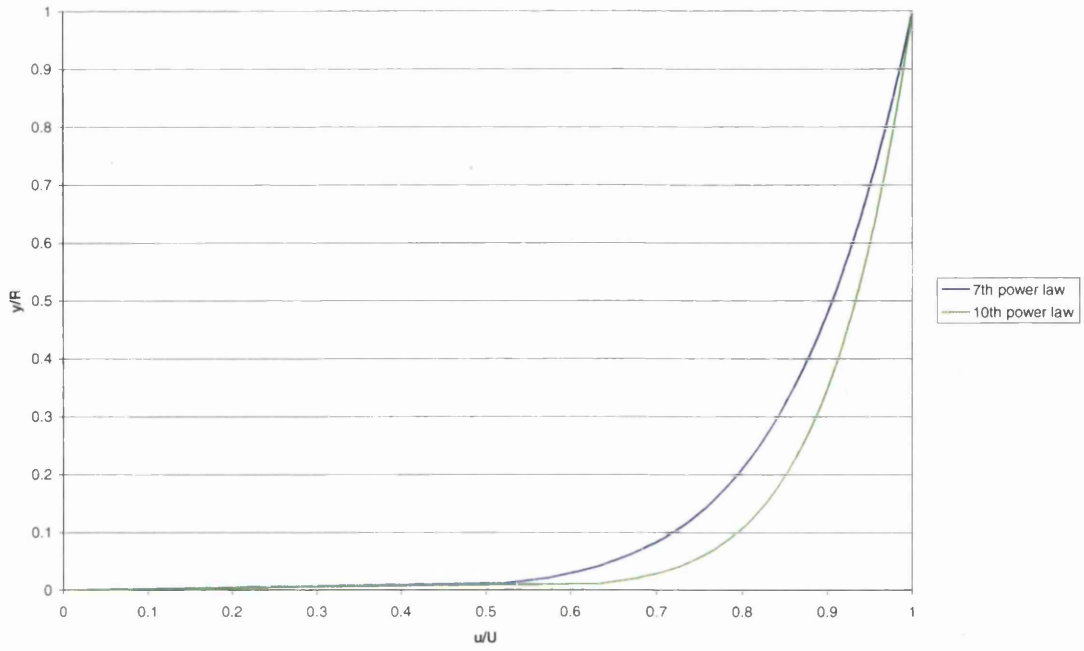

Figure 3.8: 1/7th and 1/10th power law flow profiles. Dimensionless horizontal velocity is plotted against dimensionless water height.

As an initial assumption the boundary layer height may be taken as the water depth, a more flexible approach is discussed in the following section however.

Batten [23] suggests that more precise site-specific logarithmic models that depend on bed roughness may be employed for greater modelling accuracy. Without bed roughness data, the power law approach gives a good approximation to the flow profile and is flexible enough to be calibrated quickly to site-specific flows.

3.3.2 Variable boundary layer height

The simplest implementation of the power law boundary layer assumes that the boundary layer covers the entire depth of the water channel. On studying flow data from specific sites provided by EMEC [24] (Figure 3.9) it is possible to develop a closer approximation of a specific flow profile. This is achieved by having a boundary layer that does not cover the entire depth of the water body and a uniform tidal flow velocity prescribed above this water height. Implementation of this is a relatively simple step in the model. As well as defining water depth in the input data, a boundary height was also defined. The boundary height is used in the power law equation rather than water depth. The simple addition of a conditional 'if' statement in the code that creates the tidal flow profile then allows for the condition of flow above this boundary height to be uniform.

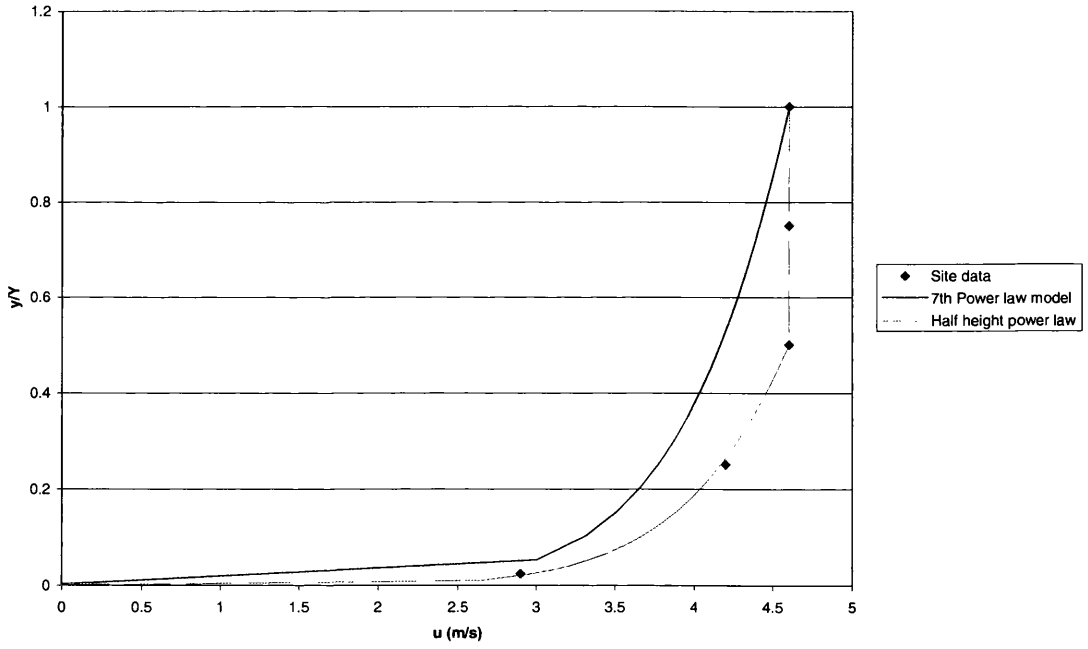

Figure 3.9: local flow velocity variation compared to EMEC data for 59º08'10"N, 002º48'16"W [24].

3.3.3 Wave model

Significant fluctuations in both horizontal and vertical velocity and acceleration are seen in a tidal flow due to the effects of waves. It is therefore important for fatigue load definition and fatigue life assessment as well as control system design that waves are modelled. In reality, sea waves are irregular. They may be approximated as a superposition of several regular waves of different phase, wavelength and period [25], this is known as a sea state [26]. Figure 3.10 represents such a group of waves, known as a wave spectrum.

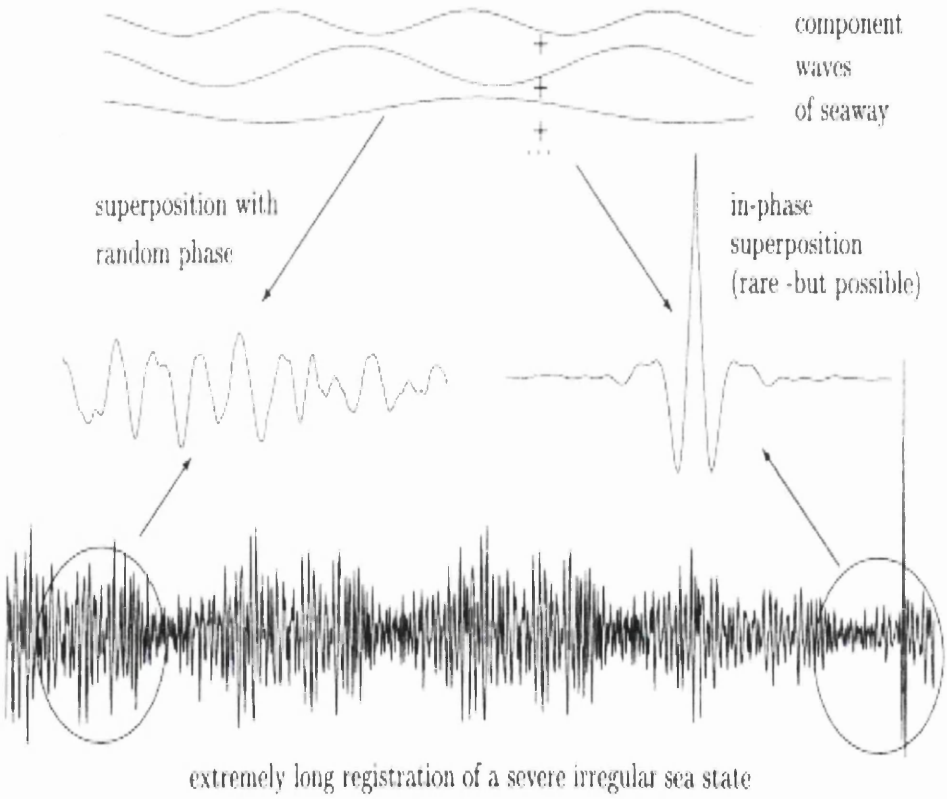

Figure 3.10: Pictorial representation of a sea state taken from Clauss [25].

Sea state modelling is covered in many texts such as Sarpkaya [27], Le Méhauté [26] and Bossanyi [19], the basic approach uses statistics to provide stable variables, which describe the random behaviour of a sea state. Fourier analysis is employed to break down the random sea state in to

harmonic components, these harmonic components are the individual waves of the spectra, which may be modelled using regular wave techniques. Sea state modelling is outside of the scope of this thesis and so shall not be covered in any further detail. The modelling of regular waves, which are also needed for sea state modelling, will now be discussed however.

Le Méhauté [26] presents a clear introduction to regular wave modelling, three important characteristic variables are first defined as follows:

1. Wave height, H, is the vertical distance between peak and trough of the wave.
2. Wavelength, L, is the horizontal distance occupied by a single cycle of a wave.
3. Water depth, d_w, is the undisturbed vertical distance between the seabed and the free surface.

Characteristic ratios are obtained using the variables that are used to define different families of waves. These ratios are $\frac{H}{L}$ (Wave Steepness), $\frac{H}{d_w}$ (Relative Height) and $\frac{L}{d_w}$. In deep water, wave steepness is the defining characteristic as the other two ratios are small, in shallow water relative height is significant.

There are many wave models and Le Méhauté categorises these in to three main families; Linearisation approaches, Power series approaches and numerical methods. Waves of small wave height and wavelength in deep water are modelled using linear small amplitude wave theories (Linearisation approaches), so called because non-linear convective inertia terms are neglected. The free surface elevation is assumed to equal undisturbed surface height, saving the need to determine this variable. This approach is popular due to its low computational demand and has been shown to give

good predictions for waves that are larger than the range assumed in the derivation of these models.

Power series approaches use a solution of the linearised equation as their first term, the non-linear terms are then calculated. This calculation is complex and so Le Méhauté states that solutions are generally limited to two-dimensional periodic waves, which allows elimination of time derivatives of the governing equations.

Exact solutions for certain waves do not always exist and for this type of problem, the differentials of the exact equations are approximated as finite differences.

Orme shows that the significant waves encountered in tidal turbine sites are intermediate to deep water waves and plots the position of a group of example waves (table 3.1) on a plot of the regions of applicability of different wave models from API recommended practice [28] (figure 3.11).

Wave Number	**1**	**2**	**3**	**4**	**5**	**6**	**7**	**8**	**9**	**10**
Wave Height (m)	**0.43**	**0.53**	**0.70**	**0.93**	**1.15**	**1.25**	**1.08**	**1.02**	**1.91**	**6.14**
Wave period (s)	**2**	**3**	**4**	**5**	**6**	**7**	**8**	**9**	**10**	**11**
Water depth (m)	**25**	**25**	**25**	**25**	**25**	**25**	**25**	**25**	**25**	**25**

Table 3.1: Example waves plotted in figure 3.9 (Orme [1]).

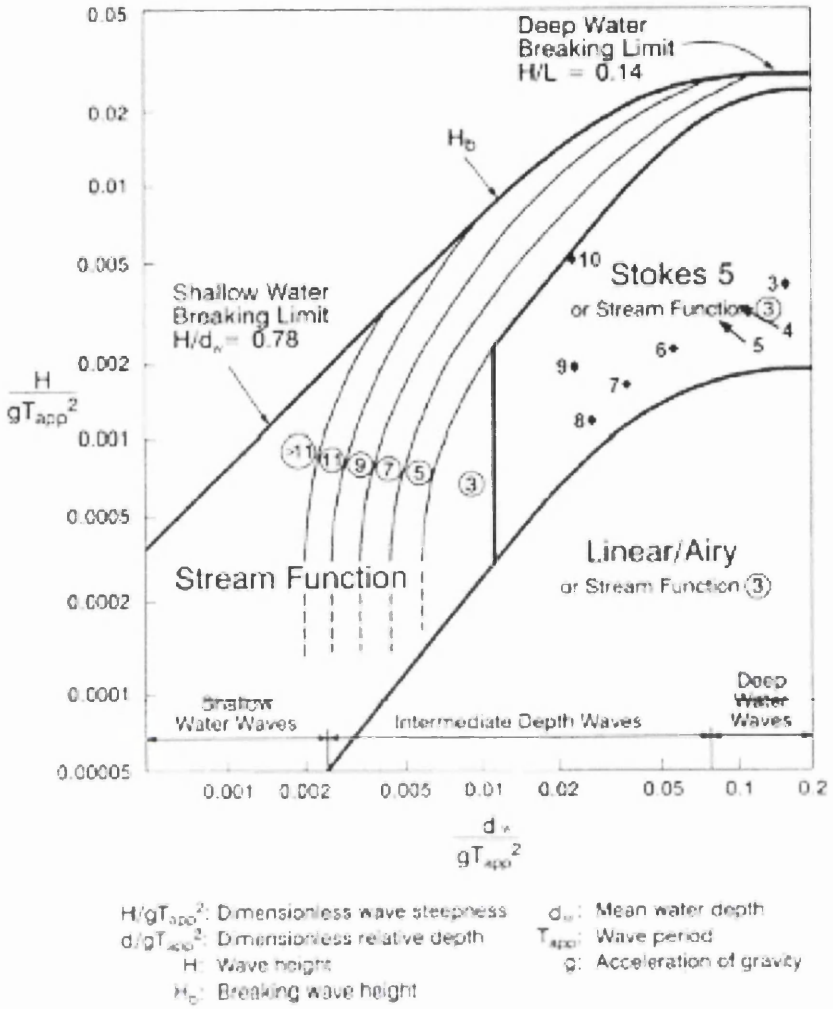

Figure 3.11: Regions of applicability of different wave models from API recommended practice [28] with example waves plotted by Orme [1].

Bossanyi [19] supports this finding to some extent, providing Stream function or Linear Airy wave models for use in Tidal Bladed. Both of these wave models are in the finite amplitude wave family and would appear to be sensible choices for wave modelling in this application. The Airy wave model has a low computational demand but is not accurate for steep waves. As the processing time taken for wave modelling is far smaller than total processing time during a time dependent run, processing demand is not a highly significant issue here and so the approach taken by Orme to use Chaplin's stream function code for all wave modelling is adopted. In the following section, stream function theory will be summarised.

3.3.3.1 Stream function theory

Orme [1] employs an open source FORTRAN stream-function model created by J. Chaplin [29]. This code also forms the basis for GH Bladed's regular wave models [19]. The theory behind this code is described by Chaplin in a Coastal engineering Journal paper [30], this offers a more concise presentation than that of Sarpkaya [27]. Orme uses this description in his thesis [1] and Chaplin's description will again be presented here for completeness.

The stream-function problem is that of a two-dimensional, irrotational periodic wave. H, d_w and the wave period T define the wave conditions and the stream function theory is needed to relate all remaining wave characteristics to these parameters. A reference frame moving horizontally at the same speed as the wave (C) is used to reduce the problem to a steady flow. Figure 3.12 defines the *x*, *y* coordinate axes with origin at mean water level vertically below a crest. The velocity relative to the moving reference frame can be related to a stream function $\psi_{sf}(x, y)$ using $\frac{\partial \psi_{sf}}{\partial y} = u - C$ and $\frac{\partial \psi_{sf}}{\partial x} = -v$ where u and v are the *x* and *y* components of wave induced velocity.

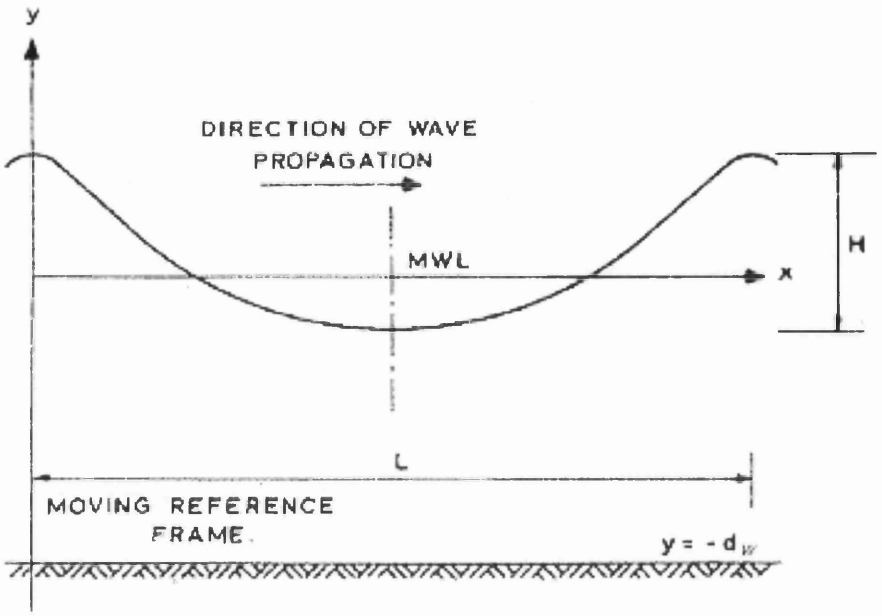

Figure 3.12: Chaplin's [30] definition of wave parameters.

The stream function must satisfy a number of conditions:

1. For irrotationality, $\nabla^2\psi_{sf} = 0$ throughout the water body.
2. The vertical velocity is zero at the seabed, $\frac{\partial \psi_{sf}}{\partial x} = 0$ when $y = -d$.
3. The free surface defined by $y = \eta(x)$ is a flow boundary and the local velocity vector must be tangential to the free surface; $\frac{\partial \eta}{\partial x} = \frac{v}{(u - C)}$. This is the kinematic free-surface boundary condition.
4. Pressure is taken as zero everywhere on the surface so $Q = \frac{\left[(u-C)^2 + v^2\right]}{2g} + \eta$ when $y = \eta(x)$ where Q is the total head, which is a constant for any given wave. This is the dynamic free surface boundary condition.
5. The wave is periodic in x with an interval L and is symmetrical about its crest or trough.

If a stream function equation of the form shown in (3.59) is used, the irrotationality (1.), seabed boundary (2.) and wave symmetry (5.) conditions

are satisfied. This leaves only the two free surface boundary conditions (3. and 4.) to satisfy.

$$\psi_{sf} = -\frac{L}{T}y + \sum_{n=1}^{N} a_n \sinh\frac{2\pi n(d_w + y)}{L}\cos\frac{2\pi nx}{L} \qquad \ldots (3.59)$$

N in (3.59) is the order of the solution, Chaplin's code will automatically alter this until a suitable solution is found. The first term in (3.59) is the mean flow resulting from the choice of a moving reference frame, the summation is the wave-induced disturbance of that flow. The kinematic free surface boundary condition (3.) can be satisfied by imposing the condition that ψ_{sf} is constant along the surface boundary. From (3.59) it can be seen that on the seabed the stream function is equal to $-\frac{L}{T}d_w$. The stream function value at the free surface, ψ_η, is unknown and its value reflects the overall mass transport of fluid caused by the wave. Values for a_1 to a_N must therefore be found as well as L and ψ_η so that the dynamic free surface boundary condition is approximated sufficiently. The wave height and mean water depth must be equal to those specified for the wave in question.

The method used to solve the stream function equations by Chaplin is not trivial and is outside the scope of this thesis. The method may be referred to in Chaplin [30], the approach is to make the problem dimensionless using L as a length scale and ψ_η as a stream function scale. An iterative solution of the sum of square errors of the dynamic free surface boundary condition is then constructed. The particular method employed by Chaplin has advantages over other approaches such as that of Dean [31] because the desired wave height may be defined directly rather than being sought iteratively.

This solution is modelled in the absence of a tidal current, Chaplin's code allows for a uniform current to be added but, as has been shown, this is not a

realistic approximation of the tidal flow. With a non-uniform current, the irrotationality condition on the flow is no longer valid and Laplace's equation is no longer satisfied, making a simple expansion impossible [32]. An alternative formulation is strictly required for this circumstance but this does not lend itself to incorporation in the turbine model presented here. The complexity of such an approach is exemplified in Huang and Mei [33]. A less complex but still non-trivial approach may be seen in the appendix of Swan, Cummins and James [34]. A simple approach is to use the isolated wave (without current) and simply add the tidal flow velocity components to the wave components. Although this is theoretically incorrect as it neglects the flow rotation, Chaplin states it is a good approximation of the true solution in his CS2 [35] documentation. Swan and James [36] warn against simple addition but their main concern is the development of rotation and the effect surface current will have on the dispersive effects of the waves. For the short distances being modelled here, these effects are not a major issue and so the benefits of being able to perform simple addition of wave and tide outweighs the small loss in accuracy. This is therefore the approach taken for the present model.

More complex wave models are the present focus of some degree of research, examples of these are Groeneweg and Battjes [37] and Guinot [38]. These are able to predict the behaviour of waves over a non-uniform seabed but are more complex than is necessary for the present application.

3.3.4 Non-collinear waves and tide

The approach taken to create wave velocity and acceleration data from an existing open source code by Chaplin [29] has just been shown. This is then fed through a three dimensional grid in a single direction with a collinear tidal velocity simply added to it. The assumption of simple addition of tide and velocity has been discussed previously in this chapter and in [39].

The flow grid surrounding the turbine system is designed to be just large enough to cover the turbine under any angle of yaw, tilt and rotation as this minimises storage. To rotate the wave so that it was passing through the grid in a different direction would increase complexity and computational demand. As the turbine system is able to yaw to any angle, it is possible to offset the wave flow relative to the turbine system. It is only necessary therefore to rotate the tide around the yaw centre of the system, the centre of the flow grid. The wave is then fixed as travelling along the global X-axis in the negative X direction. Tide offset and yaw of the turbine can then be defined to achieve any desired offset between system, wave and tide. The tide is offset by taking sine and cosine components of the flow.

3.4 Morison's Equation for blade accelerative and supporting structure loads

The highest hydrodynamic loadings on an horizontal axis tidal turbine system will tend to be those acting on the rotor itself during normal operation, loadings on other components such as the supporting tower, generator housing and nosecone (see figure 3.13) are however expected to be significant in determining lifetime loadings on the system. If yaw errors and non-collinear tide and wave directions are encountered, these loadings may have a more significant impact on the loading of the system and they are of vital importance when modelling yaw behaviour of a system. A procedure for predicting the loads on these structures is presented in this section and results are discussed.

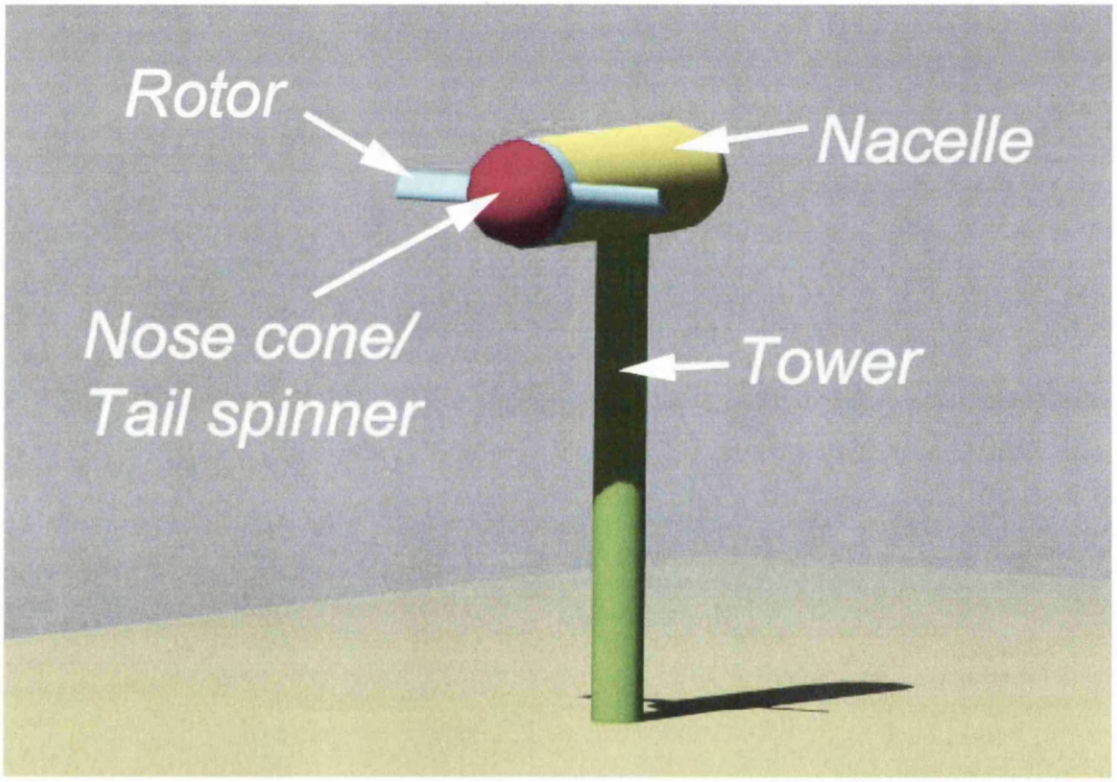

Figure 3.13: Diagram of generic, two bladed, turbine system showing separate components.

3.4.1 Basic approach

The supporting structure of the system has been divided into three components for the purpose of modelling, these are; a supporting tower, a

nacelle (housing the generator and possibly control components) and a nose cone (figure 3.13). To simplify the problem, initially it is assumed that the tower is a vertical cylinder of uniform diameter and reaches from the seabed to the base of the nacelle, it is assumed that the position of this tower is directly below the yaw and tilt centres of the turbine. The nacelle is assumed to be a cylinder whose axis is in line with the axis of rotation of the turbine blades, the nacelle is assumed to reach from the rotor plane towards the yaw centre and has the same yaw and teeter centre as the rotor. The nose cone begins at the rotor plane and stretches out in the opposite direction to the nacelle, this again has the same yaw and teeter centres as the other components. The nose cone is assumed to be a cylinder and so other shapes must be approximated as an equivalent cylinder at present. The cylindrical form assumption greatly reduces the complexity of the problem and allows an efficient approximation of the hydrodynamic loadings on these structures to be calculated.

The incoming flow, including both velocity and acceleration vectors, is already known as these components are inside the flow grid created for the rotor blades described in a previous paper [40] and previously in this chapter. The position of the nacelle and nosecone are tracked using a similar approach to the rotor system, the only difference this time being that these components do not undergo azimuth rotation. The tower is assumed to be fixed and rigid so does not need to be tracked, only specified in the global coordinate field. The global flow may be interpolated to these positions and resolved relative to the components using the same approach as employed for the blades.

To more accurately capture the non-uniformity of the flow and hence loadings on the system, all components are separated into discrete elements, the number of these elements can be defined by the user, increasing the number of elements will improve resolution of the forces but this will increase computational cost. The side loadings on the tower, nacelle and nose cone are calculated in the horizontal and vertical local planes for each element.

The frontal load on the nacelle and nose cone is calculated separately as a single value. To calculate these loads, Morison's equation [27] is used.

3.4.2 Morison's equation

Morison's equation approximates both the inertial and drag components of hydrodynamic loads on submerged structures. It is a widely accepted approximation in the offshore petroleum industry and its use is outlined in the American Petroleum institute recommended practice handbook [28]. The use of the accelerative component of Morison's equation has previously been employed for modelling the loads on marine turbines by Orme [1], in this instance the equation was used to calculate the accelerative loads on the rotor blades due to waves. For the present application, the accelerative and velocity components of the load are calculated. Morison's equation is only an acceptable approximation if the ratio of wavelength to member diameter is larger than five [28]. If the ratio is smaller than this, then the member may significantly modify the incoming wave.

The inertial and drag terms of Morison's equation are displayed in (3.60) [27], in this equation, C_D (drag coefficient) and C_m (inertia coefficient) are assumed constants.

$$F_{Mor} = F_D + F_I = C_D \frac{1}{2} \rho A U |U| + C_m \rho V \frac{\delta U}{\delta t} \quad \ldots (3.60)$$

Where

F_{Mor} = Hydrodynamic force per unit length, F_D = drag force per unit length, F_I = inertia force per unit length, A = Projected area normal to cylinder per unit length (diameter), V = displaced volume per unit length (πr^2), D = effective diameter of member including marine growth, U = component of

water velocity normal to cylinder axis, C_m = inertia coefficient, $\frac{\delta U}{\delta t}$ = component of local acceleration normal to cylinder axis.

Morison's equation is therefore an empirical model whose accuracy is completely dependent on the selection of suitable C_D and C_m values. The drag coefficient of a long cylinder is a reasonably standard and well investigated variable, it is dependent on Reynolds number [9]. In the range of Reynolds numbers experienced by the system in normal operation (up to 8.6×10^6 for a 3m diameter nacelle at 90 degrees to a 4m/s flow using National Physical Laboratory data [41], an extreme case) the variation in drag coefficient is small so a constant C_D value is an acceptable approximation. For consistency, the American Petroleum Institute (API) recommended drag coefficient for a rough cylindrical section of 1.05 [28] may be adopted, this would appear to be towards the high end of the range when compared to values of drag coefficient given in Massey [9] which are between 0.3 and 1.2 for this range of Reynolds numbers. This is to be expected as offshore oil structures will tend to be in slower flows than a tidal energy device. For reporting purposes and to allow standard comparisons to be made, it was decided that keeping the API standard would be preferable. A more accurate drag coefficient should be chosen when modelling any specific device however.

The inertia coefficient is a less commonly discussed value than drag coefficient. It is given by the equation $C_m = (1 + C_a)$ where C_a is the added mass coefficient. Added mass is defined in Sarpkaya as "the quotient of the additional force required to produce the accelerations throughout the fluid divided by acceleration of the body" [27], it can be thought of as an increase in the effective mass of an immersed body due to the effects of the fluid surrounding it. The mass coefficient is multiplied by the displaced volume of the body to give this correction (as seen in (3.60)). Experimental and strip theory values of added mass coefficients are given in Sarpkaya [27] for varying cylinder length (L_{cyl}) to diameter ($2r_{cyl}$) ratios. These values are

attributed to Blevins [42] and are presented here in table 3.2. Strip theory is an approximate numerical approach based on summing two-dimensional elements to give an overall added mass coefficient, the approach strictly only applies to slender cylinders. The highest value for inertia coefficient is given by the API text [28] as 1.6 for a smooth cylinder or 1.2 for a rough cylinder. These values are slightly lower than those given in table 3.2. In the following study, a C_m of two is used as this is the highest value suggested for a cylinder and will therefore show the maximum expected loading. It is recommended that the user selects a suitable C_m based on the aspect ratio of the member being modelled for better accuracy during load modelling.

$L_{cyl}/2r_{cyl}$	Strip theory C_a	Experiment C_a
1.2	1.0	0.62
2.5	1.0	0.78
5.0	1.0	0.90
9.0	1.0	0.96

Table 3.2 Added mass coefficients for finite cylinders (Sarpkaya [27]).

3.4.3 Modelling of the rotor Blade accelerative loads

Velocity loads on the turbine rotor are modelled by BEMT but this neglects local fluid acceleration due to wave action. Orme [1] proposes including these effects by adding the inertial term of Morison's equation to the BEMT solution (3.61), his approach is repeated here.

$$dF_{Atot} = \frac{1}{2N}(dF_{A1} + dF_{A2}) + dF_{Ain}$$

... (3.61)

Where dF_{Atot} is the resulting elemental axial force on a single blade and dF_{Ain} is the elemental axial force due to local acceleration (3.62).

$$dF_{Ain} = C_{ma}\rho V \frac{dU_w}{dt}.dr$$

... (3.62)

C_{ma} is the axial coefficient of inertia and $\frac{dU_w}{dt}$ is the axial local wave acceleration.

Orme calculates the displaced volume per unit length using a relationship provided in his thesis [1] between chord and area for a NACA4424 foil profile (3.63), this would of course require an alternative relationship if another blade profile was to be used.

$$V = 0.1658c^2$$

... (3.63)

The added mass coefficient is then needed so that the inertia coefficient may be calculated. Orme approximates the foil as an ellipse with frontal length dependent on the angle of twist (and pitch) of the blade. The added mass coefficient for an ellipse is shown here in (3.64) and the formula to calculate frontal length is given in (3.65).

$$C_a = \frac{M_a}{\rho V}$$

where

$$M_a = \rho\pi L_F^2$$

... (3.64)

$$L_F = c\cos\theta$$

... (3.65)

Orme takes a similar approach in the vertical rotor plane, this time elemental torque is calculated and so the inertial term (3.66) is slightly altered to account for this.

$$dT_{in} = C_{mv}\rho V \frac{dV_w}{dt} r.dr$$

... (3.66)

$\frac{dV_w}{dt}$ is the vertical acceleration (in plane with the rotor) and C_{mv} is the vertical inertia coefficient. This is calculated in the same way as the axial inertia coefficient except that the frontal area, $L_F = c\sin\theta$.

Using the mapping procedures described earlier in this chapter, the effects of yaw tilt and rotation are taken into account. Only the acceleration normal to the rotor plane is taken into account when modelling frontal inertia effects and only the acceleration normal to the rotor blade but in plane with the rotor is accounted for in the torque based inertial term. This means that inertial terms along the length of the blade are neglected, this is in agreement with the usual approach taken with Morison's equation.

3.4.4 Results

With the supporting structure modelling system incorporated into the Matlab model, it is possible to examine side and heave loads on the nacelle and nose cone as well as side loadings on the tower. The frontal load on the tower and nacelle is only calculated once as it is assumed that one component will always be sheltered by the other in this direction. As the side and heave loads are calculated for a range of elements along the structures, it is also possible to calculate a torque moment around the yaw and tilt centre of rotation.

To give an example of the system's performance, a downstream rotor device has been modelled yawed 90 degrees to the wave and tide flow direction, a 35m depth of water with 1/7th power law tidal flow of 4m/s free stream velocity and an 8.5m high wave with 12.3s period was imposed on the system.

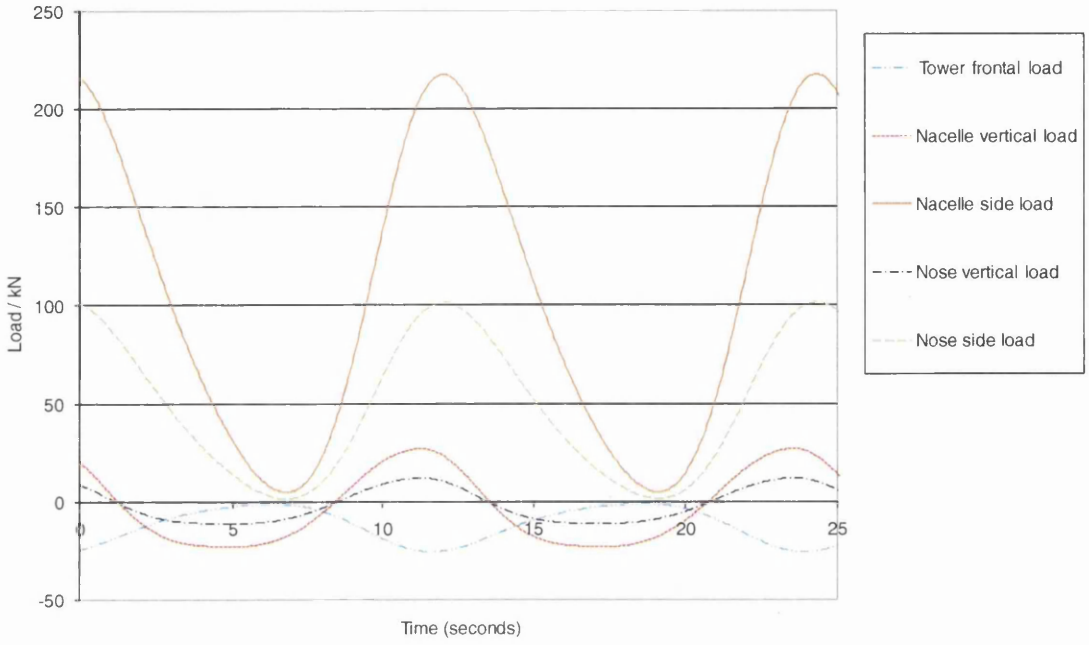

Figure 3.14: Loads acting on supporting structure when system is yawed 90 degrees to flow.

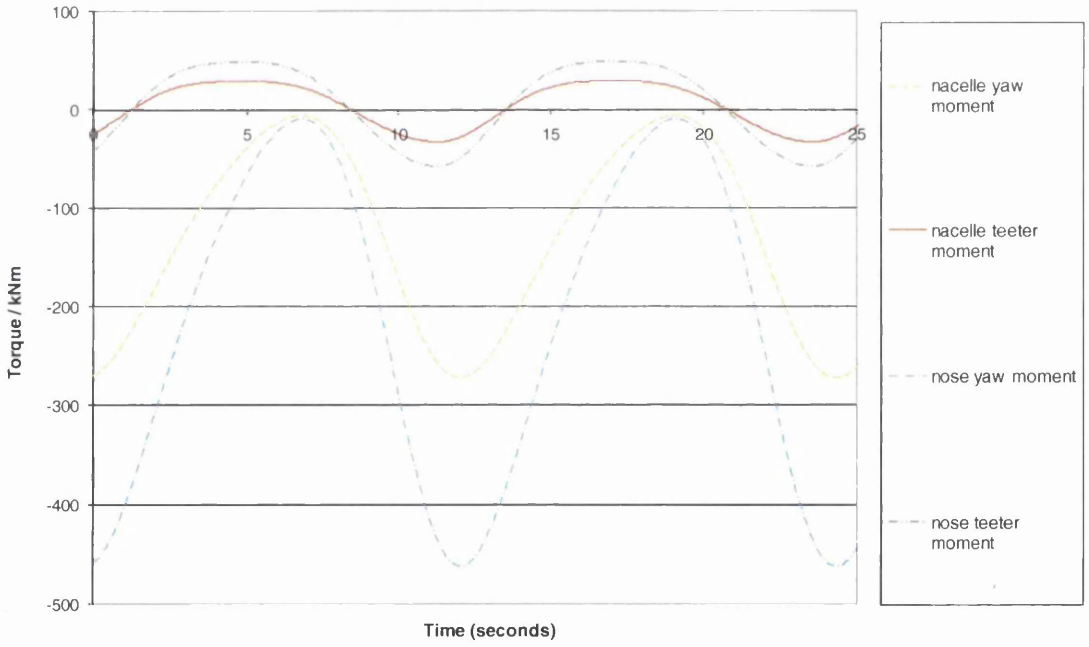

Figure 3.15: Resultant torque loadings around yaw and tilt centre from nacelle and nose hydrodynamic loads.

Another run was taken with a more realistic yaw error for normal operating conditions of 8.3 degrees to the same flow regime as the previous study.

This allowed for comparison of the rotor loadings to the supporting structure loadings.

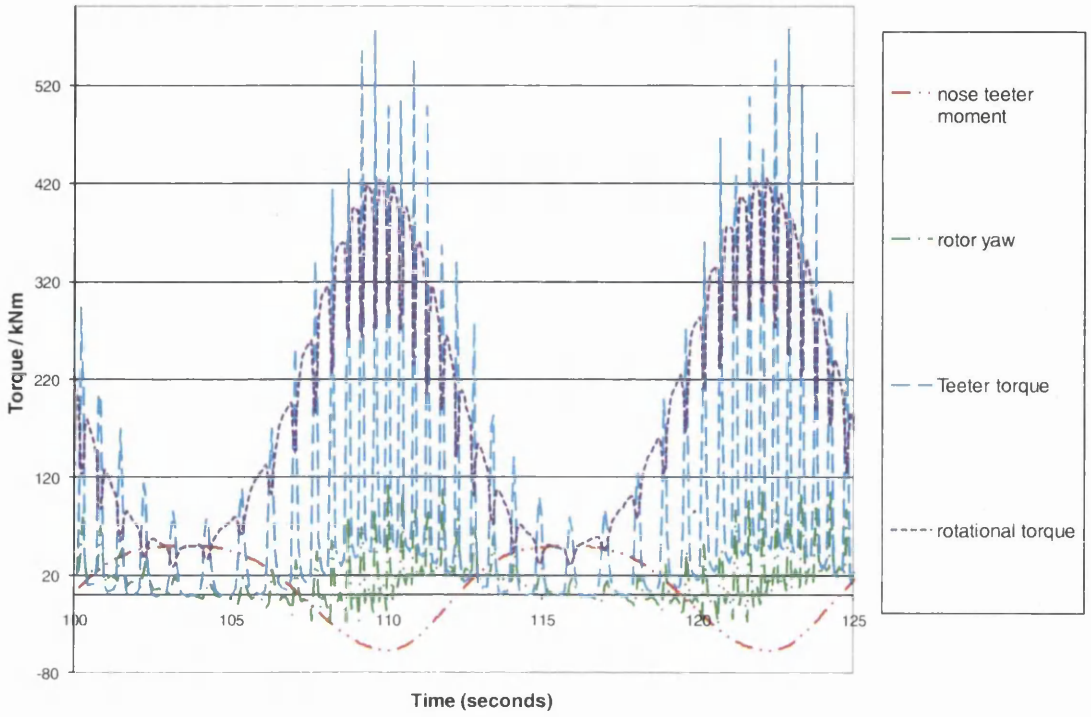

Figure 3.16: Torque loadings from rotor compared to maximum torque loading of supporting structure components.

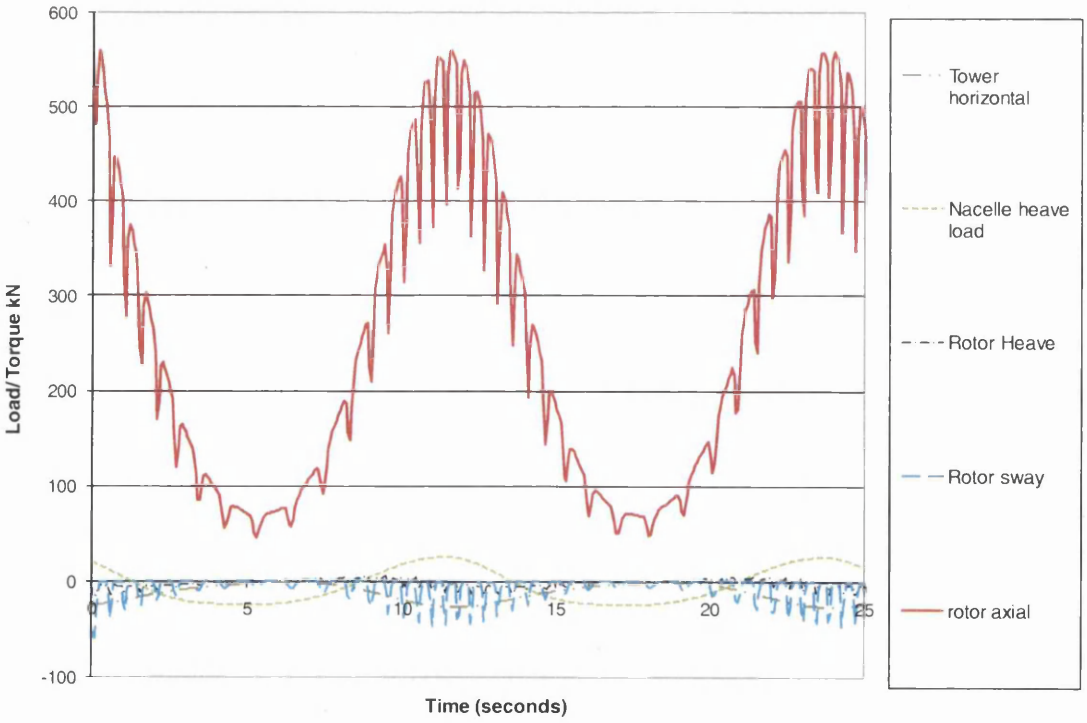

Figure 3.17: Rotor forces compared to largest supporting structure force.

3.4.5 Discussion

Figures 3.14 and 3.15 show the loadings on the supporting structure in the extreme case where the system is yawed 90 degrees to the oncoming flow. It is at this angle that side forces on the nacelle and nose cone will be at their maximum, it is clear that in this case side loads are significant and should certainly be taken into account in the design process of a tidal stream system. It is interesting to note at this stage that the oscillations on the loadings have the same period as the wave passing over the system, this is to be expected as the oscillation in load is due to the wave's changing velocity and acceleration throughout its cycle. It is also interesting to note that the side loads are out of phase with the heave loads, this is as the variation of vertical velocity and acceleration of the wave is not in phase with its horizontal variations of velocity and acceleration.

Figures 3.16 and 3.17 show that, in normal operating conditions, the supporting structure loads are of a far lower magnitude than the peak loadings acting on the rotor system. It is however noteworthy that the supporting structure loads are of a similar magnitude to the smaller rotor loadings such as heave and sway which are more analogous to the supporting structure loads. It is therefore worth the small increase in computational demand to model the loads on the supporting structure to allow a better approximation of the entire system loads for use in the design process. The different nature of load variation between the rotor and support loads is shown well in figures 3.16 and 3.17. The higher frequency oscillations of the rotor pass frequency can be clearly seen over the base oscillation of the wave for the rotor loadings. The lack of this rotor frequency loading on the supporting structure will mean that the supporting structure loads will be far less significant when examining fatigue effects on the system.

3.4.6 Time dependent modelling in three dimensional space

With the mapping procedures and wave modelling approaches discussed, it is now possible to run a time dependent load modelling system using the core BEMT solution approach shown in section 3.1.7. The approach is summarised in figure 3.18. Supporting structure loads may be calculated directly by putting the resolved flow vector values into Morison's equation. The inertial loading on the rotor blades can also be calculated with Morison's equation.

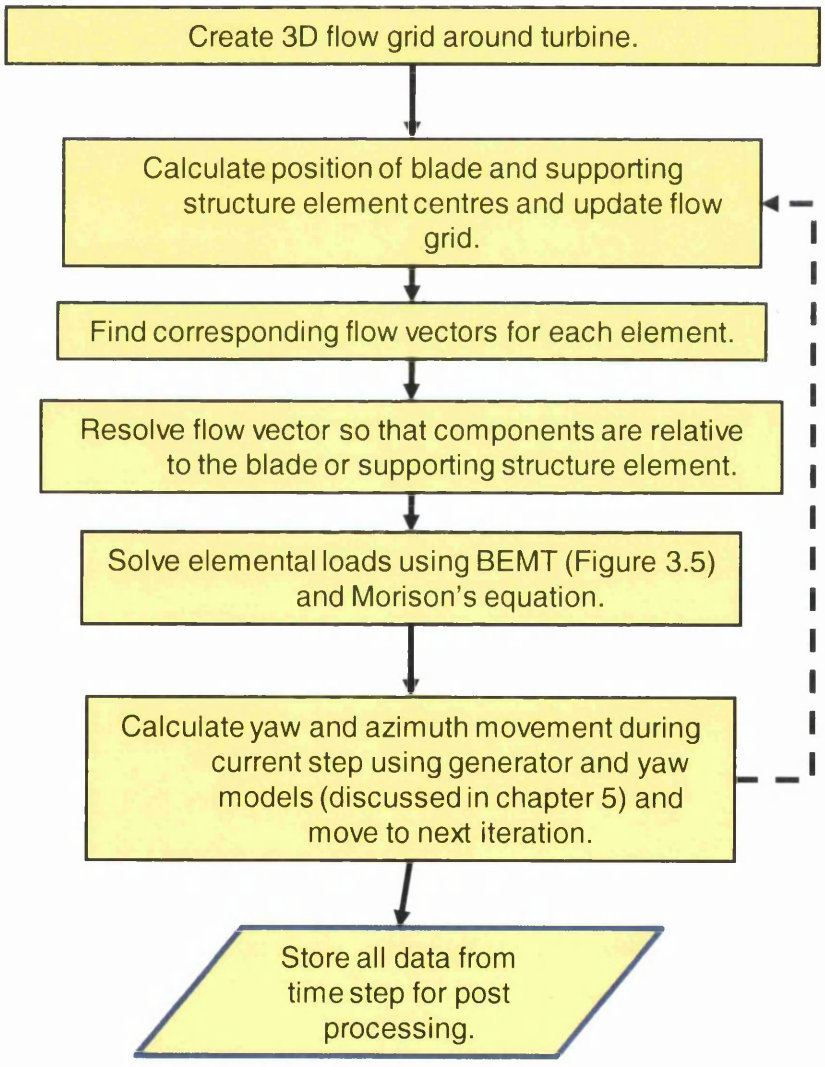

Figure 3.18: Time dependent modelling procedure.

3.4.7 Conclusions and further work

In this section, an approach to model the hydrodynamic loads on the supporting structure of a turbine system has been introduced. The application of Morison's equation has been shown to be relatively simple and hence have a low computational cost. Despite its simplicity, it has been widely accepted by the offshore oil industry as an adequate means of modelling the loading on submerged structures if the wavelength constraint is satisfied.

Two example cases have been shown, in extreme cases it has been seen that the supporting structure loads can be high and are certainly significant from a design point of view. The second case shows that under normal conditions the loadings are less significant yet still large enough to justify the small increase in processing time that modelling of these loads entails. An ability to model more complex geometries than uniform cylinders may be desirable, one simple step towards this could be to incorporate a means for different supporting structure elements to have different diameters and positions. This would then allow cones or domes to be approximated if an adequate number of elements were used and would allow for far more complex supporting structures.

3.5 Visualisation of the model

Visualising the flow and the movement of the turbine system through time is desirable for error checking and validation purposes. A method for animation of the horizontal, vertical and cross velocities through the code's flow grid is described, as is an approach to animate the time varying, three-dimensional position of the blade system with the corresponding inflow vectors for each blade element.

3.5.1 Animation format

Creation of video animation files can be facilitated in Matlab by using existing toolbox functions. The functions used for this were 'avifile' 'getframe' and 'addframe', the use of these is well described in the corresponding Matlab help files [43] so will not be covered here. Typical results include surface plots of velocities for the case of the inflow animation (figure 3.19) and a three dimensional plot of rotor element positions and corresponding quiver plots for the flow vectors at these elements for the rotor animation (figure 3.20).

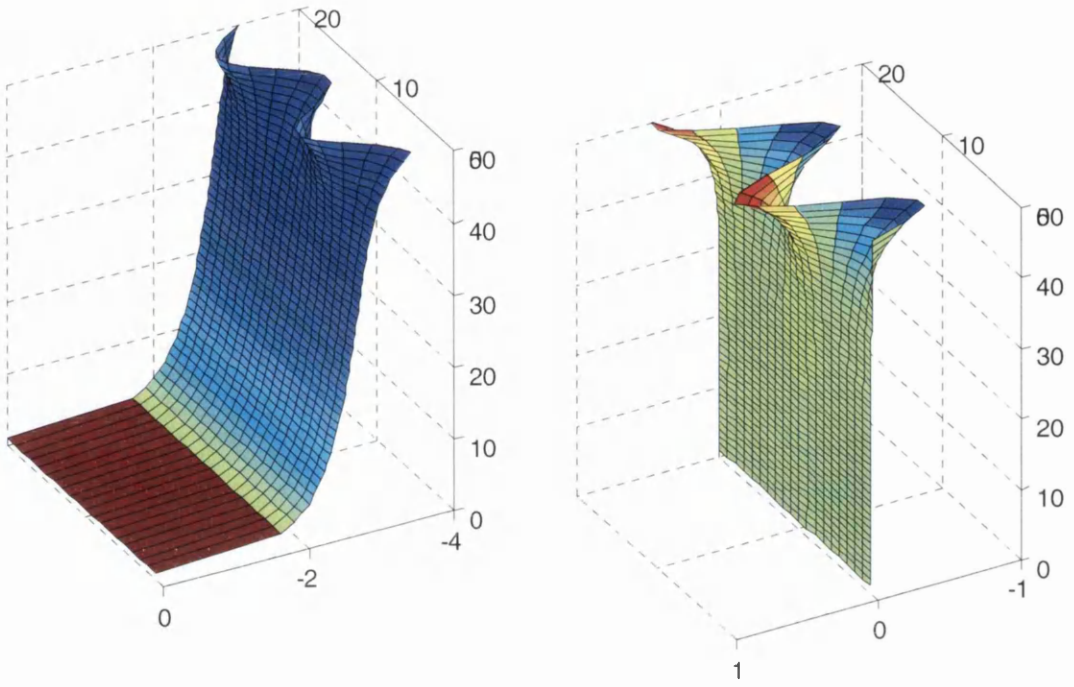

Figure 3.19: Frame from wave plot animation showing horizontal velocity on left and vertical velocity on the right hand plot.

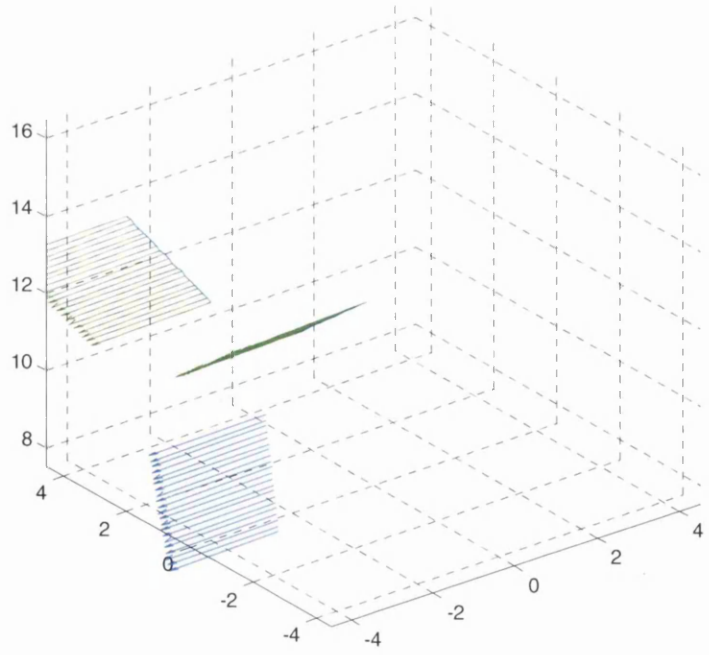

Figure 3.20: Frame from rotor plot animation showing blade position and quiver plots of corresponding inflow vectors.

3.6 Conclusion

In this chapter, the basic theories behind the model have been introduced and discussed. Three-dimensional mapping, BEMT and Morison's equation modelling may be combined with wave and tide inflows to provide a time dependent model, which is able to predict the loading on a complete tidal turbine system. In the following chapter, further corrections to the basic theory will be discussed which allow a more accurate prediction to be made. Chapter 5 then presents situations where this model may be used in realistic operational scenarios.

In this chapter:

- The derivation of traditional BEMT was reported and discussed. The existing solution methods, as displayed in the existing literature were also presented.
- As a novel step, flows tangential to the rotor plane were included in the BEMT equations. This allows non rotor normal flows to be modelled.
- A novel approach to solving the BEMT equations by exploiting pre-developed solver packages was given. This leads to greater control over the solution boundaries and leads to more reliable solution convergence.
- Inertial loadings on the rotor blade were accounted for by the use of Morison's equation as proposed by Orme. The high fluid density of water makes this significant and is not present in alternative modelling codes.
- The three-dimensional mapping procedures employed in the code are presented, these allow for the modelling of non-uniform flow and spatial variations of the turbine system. This was combined with a modular approach to coding to give a flexible code ready to model a variety of different situations.
- The modelling of loads on supporting structures using Morison's equation was presented allowing for full system modelling rather than rotor only capability.

3.7 References:

[1] Orme, J., "Dynamic Performance Modelling of Tidal Stream Turbines in Ocean Waves", PhD Thesis, 2006, Civil and Computational Engineering, Swansea University.

[2] Glauert, H., "Airplane propellers", Aerodynamic Theory 4, 1963. Dover & New York: p. 169-269.

[3] Griffiths, R., "Energy From the Wind", University of Wales Swansea internal report, 1974.

[4] Moriarty, P.J. and A.C. Hansen, "AeroDyn Theory Manual", NREL, 2005.

[5] Hansen, M., "Aerodynamics of Wind Turbines" Second Edition ed. 2008, London: Earthscan.

[6] Manwell, J.F., J.G. McGowan, and A.L. Rogers, "Wind Energy Explained". 2002, Chichester: John Wiley & Sons Ltd.

[7] Burton, T., *et al.*, "Wind Energy Handbook". 2001, Chichester: John Wiley & Sons.

[8] Glauert H, "The Elements of Aerofoil and Airscrew Theory", Cambridge University Press, 1947. p. 201-207.

[9] Massey B, "Mechanics of Fluids" 7th ed, Ed. Ward-Smith J. 1998: Stanley Thornes Ltd.

[10] Buhl, M.L.J., "A New Empirical Relationship between Thrust Coefficient and Induction Factor for the Turbulent Windmill State", NREL, 2005.

[11] Wilson, R.E. and P.B.S. Lissaman, "Applied aerodynamics of wind power machines", Oregon State University Report, 1974.

[12] Mathworks, "Optimisation Toolbox - fmincon".

[13] Chapman, J., I. Masters, and J. Orme, "Rotor Performance Prediction for Tidal Current Turbines", in *A Joint Conference of The Association for Computational Mechanics in Engineering (UK) and The Irish Society for Scientific and Engineering Computation*, C.G. Armstrong, Editor. 2006, Queen's University, Belfast: Queen's University, Belfast. p. 103-106.

[14] D'Errico, J. (2005) "Optimisation Tips and Tricks", Online: http://www.mathworks.com/matlabcentral/fileexchange/loadFile.do?objectId=8553&objectType=FILE, Accessed: 07/08/08.

[15] Abbott, I.H. and A.E. VonDoenhoff, "Theory of Airfoil Sections". 1959, New York: Dover.

[16] Profili Airfoil Analysis Software, [online http://www.profili2.com/ 2006] (accessed 12/07/06).

[17] Drela, M., "XFoil Subsonic Airfoil Development System ", 10/07/07, http://web.mit.edu/drela/Public/web/xfoil/.

[18] Tangler, J.L., "The Nebulous Art of Using Wind Tunnel Aerofoil Data for Predicting Rotor Performance", Wind Energy, 2002. 5: p. 245-257.

[19] Bossanyi, E.A., "GH Tidal Bladed Theory Manual". 2007, Garrad Hassan.

[20] Baker, M.J. "Maths - Rotations" [Website] [cited 2006 11/08/06]; Available

from:http://www.euclideanspace.com/maths/geometry/rotations/index.htm.
[21] Kwon, Y.H. "Transformation Matrix" [cited 2006 11/08/06]; Available from:http://kwon3d.com/theory/transform/transform.html.
[22] Schlichting, H., "Boundary-Layer Theory" 7th ed. 1979, New York: McGraw-Hill.
[23] Batten, W., *et al.*, "The prediction of the hydrodynamic performance of marine current turbines", Renewable Energy, 2008. 33: p. 1085-1096.
[24] EMEC. "Flow characterisation at 59º08'10"N, 002º48'16"W " 2006.
[25] Clauss, G.F., "Task-related wave groups for seakeeping tests or simulation of design storm waves", Applied Ocean Research, 1999. 21: p. 219-234.
[26] Le Mèhautè, B., "An Introduction to Hydrodynamics and Water Waves". 1976, New York: Springer-Verlag.
[27] Sarpkaya T, "Mechanics of Wave Forces on Offshore Structures", Van Nostrand Reinhold Company, 1928.
[28] API, "Recommended Practice for Planning, Designing and Constructing Fixed Offshore Platforms - Load and Resistance Factor Design". 1993, Washington: American Petroleum Institute.
[29] Chaplin J, "Downloadable MS-DOS based software for waves and wave forces", 13/08/08, www.civil.soton.ac.uk/hydraulics/download/downloadtable.htm.
[30] Chaplin, J., "Developments of stream-function wave theory", Coastal Engineering, 1980. 3: p. 179-205.
[31] Dean, R.G., "Stream function representation of non-linear ocean waves." Geophysical Research, 1965. 70(18): p. 4561-4572.
[32] Chaplin, J.R., "CW10 Version 3.2 Software for non-linear waves and currents", Southampton University.
[33] Huang, Z. and C. Mei, "Effects of surface waves on a turbulent current over a smooth or rough seabed", J. Fluid Mech. , 2003. 497: p. 253-287.
[34] Swan, C., I. Cummins, and R. James, "An experimental study of two-dimensional surface water waves propagating on depth-varying currents. Part 1. Regular waves", Journal of Fluid Mechanics, 2001. 428: p. 273-304.
[35] Chaplin, J.R., "CS2 Version 2.0 Simulation of Irregular Waves", Southampton University.
[36] Swan, C. and R. James, "A simple analytical model for surface water waves on a depth-varying current", Applied Ocean Research, 2001. 22: p. 331-347.
[37] Groeneweg, J. and J. Battjes, "Three-dimensional wave effects on a steady current", Journal of Fluid Mechanics, 2003. 478: p. 325-343.
[38] Guinot, F. "Wave-current interaction with Boussinesq approaches" in *8th International conference on hydrodynamics.*
[39] Masters, I., J. Orme, and J. Chapman. "Towards realistic marine flow conditions for tidal stream turbines" in *7th European Wave and Tidal Energy Conference.* 2007. Porto, Portugal.
[40] Chapman, J., J. Orme, and I. Masters. "Velocity Mapping Procedures for Tidal Stream Turbines in an Arbitrary Flow Field and the Implications on Performance Due to Non-Uniform Flow" in *Fifteenth*

UK Conference of the Association of Computational Mechanics in Engineering. 2007. Glasgow: Civil-Comp Press.
[41] Bullard, E., "2.7.9 Physical properties of sea water", 20/09/07, http://www.kayelaby.npl.co.uk/general_physics/2_7/2_7_9.html.
[42] Blevins, R.D., "Flow-induced vibration". 1977, New York: Van Nostrand Reinhold.
[43] Mathworks, "The MathWorks - Online Documentation, R2007b". 2007.

Chapter 4: Losses applied to Tidal Stream Turbines

In this chapter, modifications to the basic Blade Element Momentum Theory are introduced and discussed. These include tip and hub loss corrections, high induction factor corrections and skewed wake correction. The results from implementation of tip, hub and high induction corrections are presented and compared to an alternative BEMT model and a lifting line theory model. Agreement between the two BEMT models is seen to be good and the corrections give an improvement in accuracy over the un-corrected models when compared to the lifting line theory results.

4.1 Tip Losses

In Blade Element Momentum Theory (BEMT) [1], it is assumed that there is no flow along the span of the blade, however, in reality this is not the case. The pressure differential between the suction and pressure sides of the blade creates a situation where fluid will tend to flow around the tip from the pressure side to the suction side, and by implication, there is flow along the span. This flow reduces aerodynamic efficiency near the tip, reducing lift and therefore torque force and ultimately power production near the blade tip (Manwell [2].) The high density of water and the larger resulting load concentration on the blade means that tidal stream turbine (TST) blades will tend to be relatively shorter than wind turbine blades, hence less closely resembling the infinite span length assumed in aerofoil theory. Therefore, tip loss will be even more significant for TSTs than for wind turbines.

With a finite blade, span-wise flow is induced from the upper foil surface to the lower surface due to the pressure differential between the two foil sides. This flow pattern described in the previous paragraph will induce a vortex flow at the tip, this will be shed from the tip in the same way that an aircraft wing will shed a vortex from its tip. This shed vortex will follow the revolution of the rotor blade and so a helical vortex will be produced (Burton [3]), this shed vortex is said to result in a high axial induction factor local to the blade

tip relative to the induction factor in the rest of the annulus. This significant disagreement leads to the need for a correlation to be used in BEMT between local and average induction factor. As an aside, it is interesting to note that much of the noise from wind turbines is attributed to this type of shed vortex [4]. There are a number of equations available to correct BEMT for this effect, all of these are variations on the Prandtl tip loss correction, which will be discussed in the following section.

As with many aspects of tidal turbine performance prediction, much can be learnt from wind turbine research. Hansen and Johansen [4] report on the effects of tip losses on rotating wind turbine blades. In their paper a numerical model was created and the results of this were compared to BEMT combined with Prandtl's tip loss model and an alternative model proposed by Shen *et al.* [5]. Two different tip shapes are investigated, a swept tip and a squarer type of tip. It is stated that the swept tip tends to shed the vortex over a larger span of the blade giving a more diffuse vortex than a square end tip, this is said to be due to the more gradual change in chord forcing the bound circulation to decrease in a more gradual manner. The main concern of the tip vortex in wind turbines is the acoustic noise it creates, this is less of a concern for tidal stream devices where downstream wake effects, cavitation and hydrodynamic efficiency are the primary concerns. In Hansen and Johansen's paper, CFD results for the swept wing show the entire tip operating in stalled conditions and a vortex emanating from the beginning of the sweep, this is in contrast to the standard tip that has attached flow until very close to the end of the blade. The power produced by the swept tip rotor was slightly larger than the standard tip but not by a significant amount.

The agreement between CFD results and the BEMT prediction using the two different tip loss correction factors is seen to be good in the paper with Shen's correction predicting a slightly lower performance than Prandtl's correction factor. This supports the argument for using BEMT with a tip loss correction for load estimation, the load estimate is reasonably accurate with a large saving in modelling time compared to a CFD model.

An alternative explanation of tip loss is available and this shall now be discussed. Basic momentum theory assumes that the number of blades in a turbine system is high enough to affect all fluid particles that pass through the system equally. In reality, the number of blades for a tidal turbine will be low and the flow at different azimuth positions around the rotor will be affected very differently by the blades. As the flow in a single annulus is not affected in the same way, the axial induction factor will not be uniform around the whole annulus. In the Wind Energy Handbook [3], it is argued that, due to this variation, for an average induction factor for the annulus to have a reasonable value, the induction factor near a blade must be high for a rotor with a low number of blades. A high induction factor leads to a small inflow angle which in turn means that the component of lift tangential to the incoming flow will be small, giving a low torque for that blade section. This only occurs near the tip and this explanation accounts for the tip loss effect. The Wind Energy Handbook goes on to explain the behaviour of fluid particles passing through the rotor plane and interacting downstream with a series of shed helical vortex sheets (one for each blade) which are produced when a blade has a non uniform circulation (a is not constant along the blade length or around the annulus). Four particles are considered, the description provided by Burton [3] of these will be summarised here for completeness together with diagrams produced to aid understanding:

Particle one (Figure 4.1) passes just in front of a blade, and leaves the trailing edge after having been accelerated in the tangential direction. It then passes downstream on the 'upwind' side of the blade's vortex sheet. The particle travels radially outwards until it sweeps around the edge of the vortex sheet and then travels inwards on the downwind side of the sheet until it reaches a point where shed vorticity is zero, at this point the particle travels downstream with the same velocity as the vortex sheet.

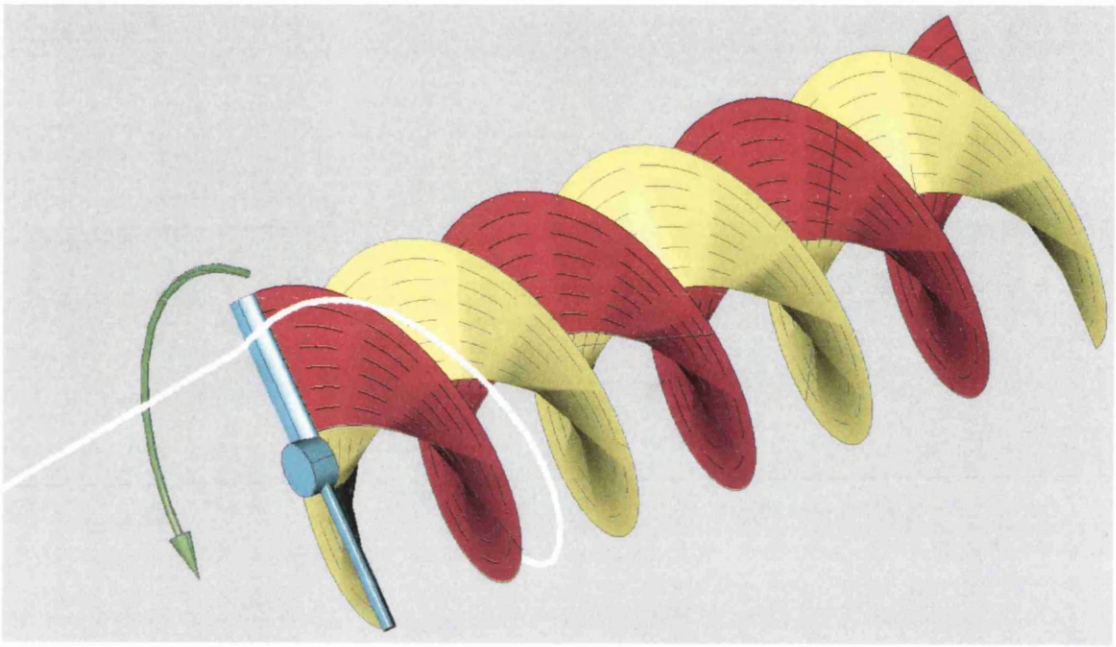

Figure 4.1: Particle one path shown on a two bladed rotor with vortex sheets (particle path shown in white).

Particle two (Figure 4.2) passes close to the downstream side of a blade and is accelerated tangentially in the opposite direction to blade rotation. It then slows down and leaves the trailing edge on the downstream side of the vortex sheet but with the same velocities as particle one so it will, in addition, be travelling radially inwards until its radial velocity reduces to zero.

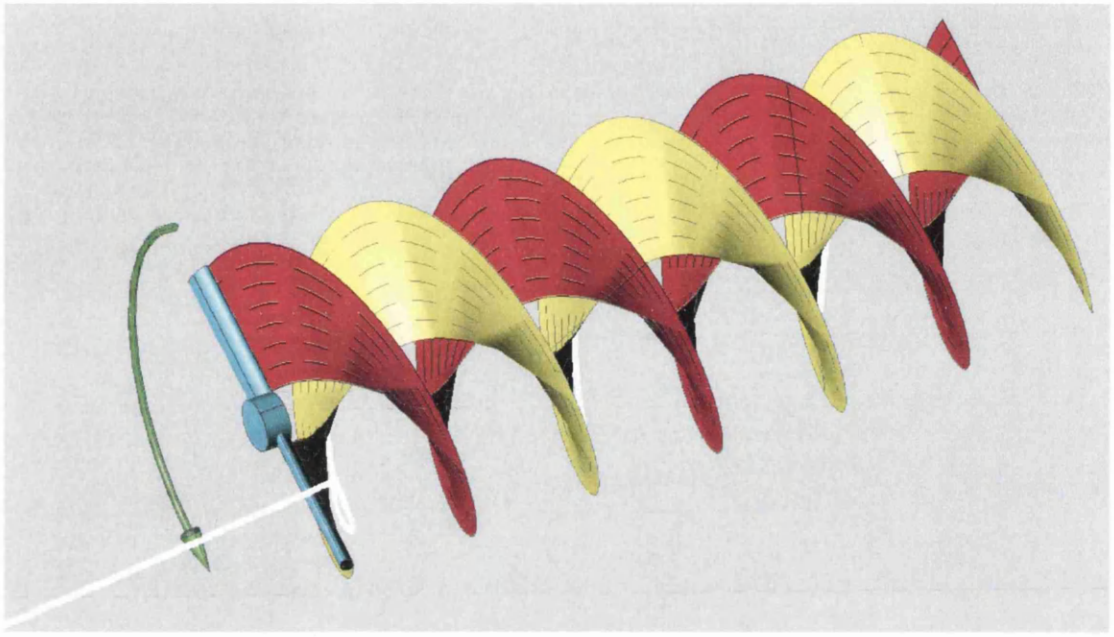

Figure 4.2: Particle two path shown on a two bladed rotor with vortex sheets (particle path shown in white).

Particle three (Figure 4.3) passes between two blades, it is less affected by the blades than particles one and two and so will have a higher velocity. However, the shed vortex sheets effectively present a solid blockage to the flow and so the particle's motion will be deflected into a helical path. The particle will continue moving axially at a speed greater than the vortex sheet and so will 'hop' over each sheet as it reaches it.

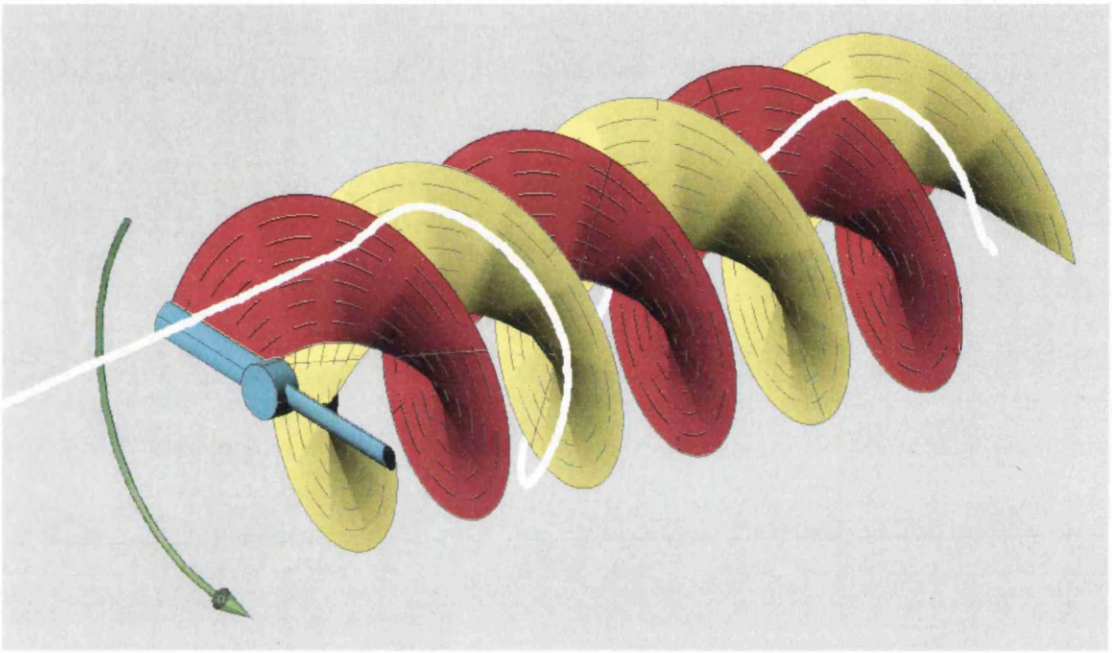

Figure 4.3: Particle three path shown on a two bladed rotor with vortex sheets (particle path shown in white).

Particle 4 (Figure 4.4) again passes between the blades but closer to the rotor centre than particle three. Here the particle's velocity will be the same as that of the vortex sheets and the particle will only move radially enough to account for wake expansion. Particle 4 effectively behaves as a particle in the idealised actuator disc would.

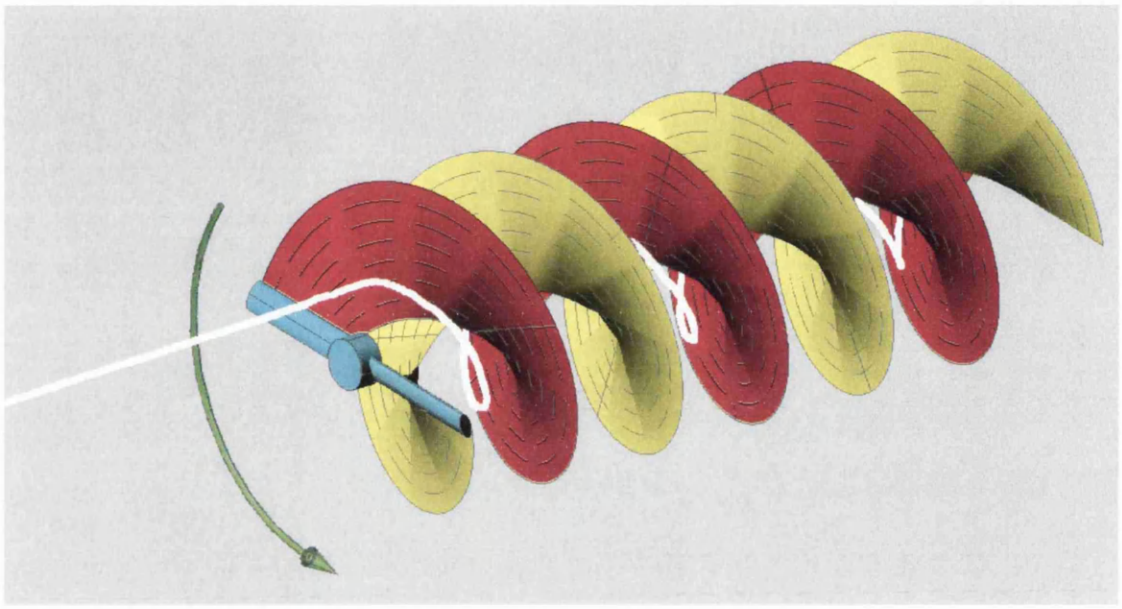

Figure 4.4: Particle four path shown on a two bladed rotor with vortex sheets (particle path shown in white).

Comparison of particle three and particle four explains the tip losses. Nearer the root, the particles will approximate the simple actuator disc theory well and the induction factor will remain effectively uniform for the whole element annulus, whether near a blade or not. Near the tip however, the increased distance between blades allows for a variation of induction factor and leads to the high local induction factors previously discussed. These local induction factors need to be included in the lift based formulae for accurate modelling.

Another field of research that BEMT has been used in is that of marine propellers, although the fluid properties are the same for these devices as TSTs it is important to remember that in terms of scale, function, ambient pressure and Reynolds number these two applications vary greatly. Benini [6] on empirical tip loss and Reynolds number corrections for marine

propellers warns that: "The accuracy of such corrections is doubtful in the majority of cases and leads to erroneous predictions". Benini proceeds to state that this is particularly salient for cavitation prediction as cavitation is highly dependent on blade profile shape and operating conditions, which will not be captured by empirical relationships. The alternative proposed by Benini is the use of a code such as XFoil [7] to predict lift and drag data that takes into account vortex shedding and Reynolds number on the blade profile when predicting lift and drag. This approach does not appear to capture the principle of tip loss on a rotor however, which is subtly different to an isolated finite wing.

4.2 Prandtl Tip loss correction

Although exact solutions of the tip loss behaviour exist such as Goldstein [8] and Biot-Savart [3], they do not lend themselves to inclusion in the BEMT model. Prandtl's approach, summarised in the Wind Energy Handbook [3], approximates tip loss but can be employed with relative ease in BEMT. The principle assumption made to achieve the approximation is that the shed vortex sheets, being impermeable, may be replaced by solid material sheets moving at the speed of the wake and hence have no effect on the wake flow. This theory is only applicable to a fully developed wake. A further approximation made is that rather than a helical wake, Prandtl assumed these vortex sheets resemble a series of discs moving with a uniform wake velocity of $U(1-a)$ and separated by the same distance as the normal distance between vortex sheets. At the wake edge, the free stream flow would notionally be U, this free stream fluid will tend to weave in and out of the gaps between the wake discs. This affects the average velocity of the wake for any given radial position and Glauert set the average fluid velocity to be $U(1-af(r))$ where $f(r)$ is a tip loss function. Near the rotor centre the average flow is unaffected by the free stream and so f is unity, near the tip, however, the impact of this fluid weaving in and out (as described by the particles in section 4.1) is significant and so $f(r)$ reduces with increasing r.

The mathematical derivation of Prandtl's tip loss function is complex but results in a relatively simple closed solution given in (4.0).

$$f(r)=\frac{2}{\pi}\cos^{-1}[e^{-\pi(R_w/d-r/d)}]$$

... (4.0)

Where R_w-r is the distance from the wake edge to the radial blade station and d is the normal distance between the vortex sheets and can be calculated using (4.1).

$$d=\frac{2\pi R_w}{N}\sin\phi_s=\frac{2\pi R_w}{N}\frac{U(1-a)}{W_s}$$

... (4.1)

Although this equation gives a useable formula for tip loss, calculation of the resultant wake velocity (W_s) and wake radius is complicated and time consuming. Glauert [9] argued that values for the wake have the approximate relationships $R_w\approx R$ and $\frac{r}{W}\approx\frac{R_w}{W_s}$ to the rotor values, where $W=\sqrt{(U(1-a))^2+(\Omega r)^2}$. From this, we may obtain (4.2).

$$F_{Tip}=\frac{2}{\pi}\cos^{-1}[\exp(-\left\{\frac{(N/2)[1-(r/R)]}{(r/R)\sin\phi}\right\}]$$

... (4.2)

The energy-based equations are derived from the definition of forces obtained from hydrofoil lift and drag characteristics and so remain unaffected by the tip loss correction, as they will automatically vary so long as the correct flow angle is found. Equating the updated momentum equations in (4.3) and (4.4) and energy-based equations as previously implemented without the correction factor [10], it is possible to solve the equations for axial and tangential induction factors and hence find the torque and axial force experienced by each blade element accounting for the loss in performance.

$$dT=4Fb(1-a)\rho U\pi r^3\Omega dr$$

... (4.3)

$$dF_A=F\rho U^2 4a(1-a)\pi r dr$$

... (4.4)

4.3 Alternative tip loss models

The Prandtl loss factor shown in (4.2) is now one of several tip loss factors, which have been developed. A variety of tip loss correction formulae based on Prandtl's system are discussed by Shen *et al.* [5], the first of these models is Prandtl's tip loss correction with the simplifications of Glauert [11]. A refined model by Wilson and Lissaman [12] where corrections are made on mass flow through the rotor and the induced velocity through the wake is also covered. Wilson and Lissaman's model leads to a system where the induced velocity is not orthogonal to the relative velocity at the blade element [5], which is physically unrealistic. The final correction for BEMT discussed in the paper is that of De Vries [13] this is a further development of the correction proposed by Wilson and Lissaman and corrects for mass flow in the tangential momentum equation as well as the axial momentum equation.

Prandtl's model assumes that there is no wake expansion, this reduces the model's validity for high induction factor conditions where the wake will expand significantly. Glauert [14] also showed that the accuracy of Prandtl's model decreased for blade numbers below three and for high Tip Speed Ratios.

A further modification of the basic Prandtl correction by Xu and Sankar [15] (4.5) is presented in the AeroDyn theory handbook [16]. Xu and Sankar's model is based on Navier-Stokes solutions for a single wind turbine at a single wind speed and the formula results in a physical inconsistency as it predicts a loss factor less than zero at the tip of the blade. Because of these factors, it would not appear to be prudent to apply Xu and Sankar's correction factor for modelling of marine turbine rotors.

$$F_{Xu} = (F_{\text{Prandtl}}^{0.85} + 0.5)/2 \qquad \text{for } 0.7 \le r/R \le 1$$

$$F_{Xu} = 1 - \left(\frac{r}{R}\right)\frac{1 - F_{\text{Prandtl}(r/R=0.7)}}{0.7} \quad \text{for } r/R < 0.7$$

... (4.5)

These equations can be implemented in the same way as detailed in section 4.2. Hansen and Johansen [4] present some correction factors that require further modification to the basic BEMT equations. In Shen *et al.* [5] the Prandtl and Glauert corrections presented above in (4.0) and (4.2) are discussed. Glauert's tip loss equation (4.2) is then investigated and it is noted that for a non-zero lift coefficient the flow angle at the tip will tend to zero and that relative axial velocity will always tend to zero at the tip. It is discussed that although this causes no major mathematical problem it does not realistically model the physical case where axial flow will be non-zero at the tip and a vortex is shed from the tip into the wake. Two further models are then discussed, the first being that of Wilson and Lissaman [12] it is stated that this employed the concept of circulation to create alternative tip loss corrections. As circulation is primarily generated by lift, the tangential induction factor b is neglected. For axial induction, both mass flow and induced velocity are corrected with the formula. Shen *et al.* describe that the zero flow inconsistency at the tip is also present in this model. The second correction system is that proposed by De Vries [13] that attempts to address the issue that Wilson and Lissaman's model gives a non-orthogonal relationship between the velocity at the blade and the induced velocity. Shen *et al.* state that the actual results given by De Vries' model are almost identical to Wilson and Lissaman's and the zero flow condition at the tip still exists. As a solution to this zero flow problem Shen *et al.* propose a further correction, this is shown in (4.6)

$$F_1 = \frac{2}{\pi}\cos^{-1}\left[\exp\left(-g\frac{N(R-r)}{2R\sin\phi}\right)\right]$$

where

$$g = \exp\left[-c_1(N\lambda - c_2)\right]$$

... (4.6)

c_1 and c_2 in the equation are coefficients that are to be determined through experimental data. Using one rotor system for low *TSR* and one rotor system for higher *TSR*, Wilson and Lissaman arrive at values of c_1*=0.125* and c_2*=21*

a small constant is also added to *g* to avoid an instability in the formula when λ tends to infinity. F_1 is then applied to the lift force and drag force in the objective function using the traditional Glauert correction.

4.4 Hub losses

In addition to the tip loss model, AeroDyn [16] suggests the use of a hub loss model. The theory behind this loss model is very similar to the tip loss model. It is utilised to correct the induced velocity that is caused by a vortex being shed near the hub of the rotor. The loss factor (4.7) is applied to the momentum based blade element equations and only the exponential term of the correction factor differs from the tip loss model. The theory that this is based on is the same as the tip loss equation and is simply adjusted to work inwards from the blade root rather than outwards towards the tip.

$$F_{Hub} = \frac{2}{\pi}\cos^{-1} e^{-f}$$

$$where$$

$$f = \frac{N}{2}\frac{r - R_{hub}}{r\sin\phi}$$

... (4.7)

In practice, a blade element will be affected by both tip and hub losses. The combination of these losses can be achieved by multiplying the two loss factors together and using this resultant loss factor in the BEMT model. A comparison of different hub and tip losses is given in fig. 4.5 and the combined tip and hub loss effect is shown in figure 4.6.

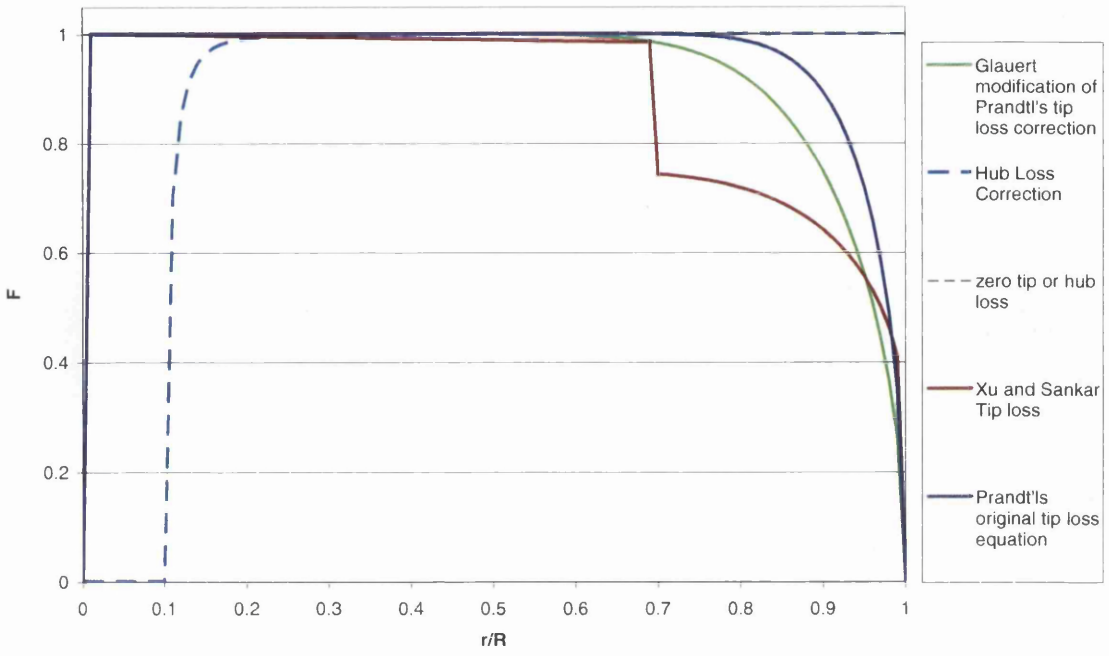

Figure 4.5: A comparison of tip and hub loss equations for a normalised blade radius with root at r/R=0.1 and constant $\phi = 10^{o}$

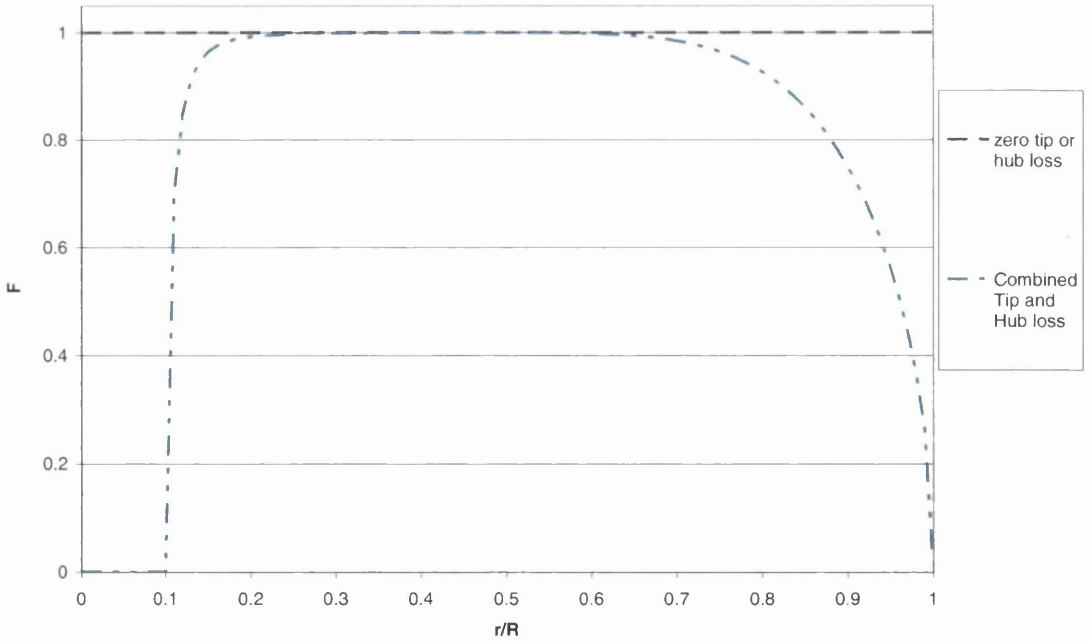

Figure 4.6: Combined tip and hub loss for a normalised blade with root at r/R=0.1 and constant $\phi = 10^{o}$ using Glauert's tip loss formula.

Figure 4.7 shows how the predicted tip and hub loss varies for differing angles of phi, it can be seen that the impact of the loss factors is far smaller for low angles of attack. It is worthwhile noting here that there is a mathematical problem when ϕ=0, the loss equations will both tend to infinity at this point. This case can be avoided by setting ϕ to be a small value if it is calculated to be zero when coding.

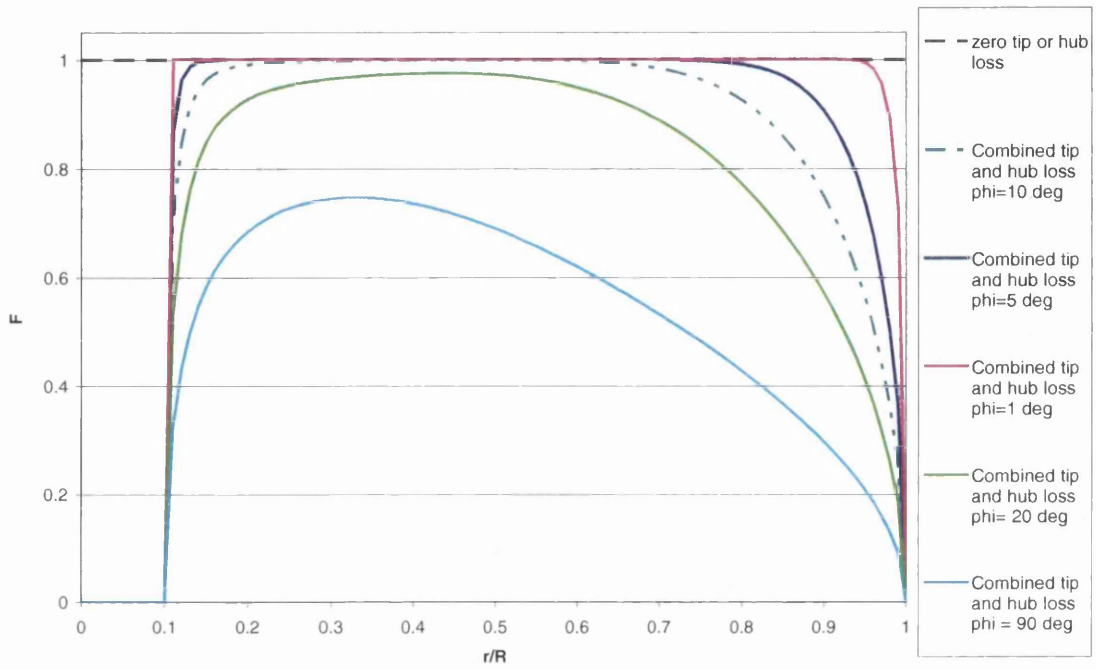

Figure 4.7: Combined tip and hub loss for a normalised blade with root at r/R=0.1 for various values of ϕ. Using Glauert's tip loss formula.

4.5 High induction correction

One further modification of the BEMT model that can be employed is a turbulent wake state correction system. It has been previously discussed in Chapter 3 that at high tip speed ratios the axial induction factor can approach or exceed 0.5, this creates physical inconsistencies in the model as it implies that the flow is reversed downstream of the turbine. For this case, the momentum equations can no longer accurately describe the behaviour of the turbine. In reality, the flow downstream slows and fluid is drawn in from outside of the rotating wake, increasing turbulence. This condition is known

as the turbulent wake state [17]. Validity limits of the BEMT and sketches of the behaviour of the streamlines can be seen in figure 4.8.

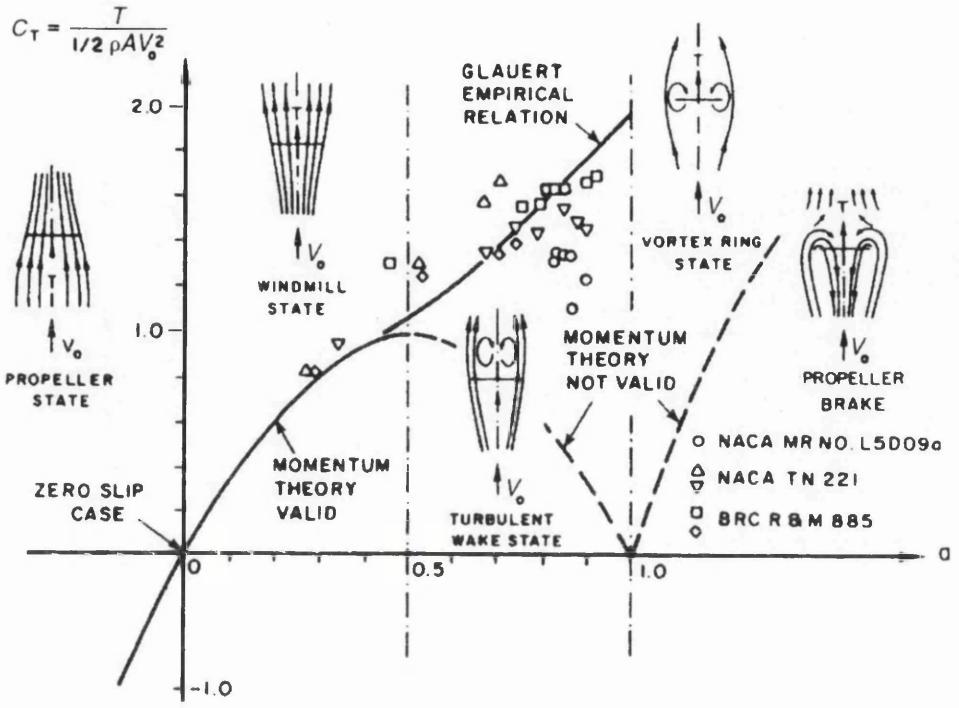

Figure 4.8: Limits of BEMT validity, axial induction against axial force coefficient (from Eggleston and Stoddard [19])

One correction that allows for this is the Glauert thrust coefficient correction [18]. The model is an empirical correction of the axial thrust coefficient and is based on a. The correction is given in (4.8) [3].

$$a = \frac{1}{F}\left[0.143 + \sqrt{0.0203 - 0.6427(0.889 - C_{FA})}\right] \quad \ldots (4.8)$$

This equation is employed when a exceeds *0.4* or when C_{FA} exceeds *0.96F*.

An alternative to this is (4.9), it is attributed to Spera and is discussed in Shen *et al.* and on Strathclyde University's website [5, 20] the critical induction factor is given values of 0.2 to 0.3. This correction system gives a

linear variation of C_{FA} with a, which may over simplify the high induction relationship but lends itself to easier calibration with experimental results. From the plots of this function (Figures 4.9 and 4.10), with a critical induction factor of 0.2 it can be seen that Spera's correction crosses the BEMT induction/ C_{FA} curve at the critical induction factor point and the gradient is well matched at this point. This critical value is rather low to use as the transition point for changing from BEMT to an empirical high induction model however. This is especially true when the system is employed locally to blade elements rather than for the entire rotor plane where average induction factors will be lower than those values at the blade tips.

$$C_{FA} = \begin{cases} 4a(1-a)F & a \le a_c \\ 4(a^2{}_c + (1-2a_c)a)F & a > a_c \end{cases}$$

$$a_c = \text{critical induction factor} \approx 0.2$$

$$a = \frac{1}{2}[2 + K(1-2a_c) - \sqrt{(k(1-2a_c)+2)^2 + 4(ka_c^2 - 1)}]$$

$$K = \frac{4F\sin^2\phi}{\sigma C_l \cos\phi + C_d \sin\phi}$$

... (4.9)

The Glauert formula was originally developed to correct the thrust coefficient for an entire rotor but has since been applied to individual blade elements. Buhl [21] explains that, near the tip, axial induction factors will tend to be high and so tip loss and axial induction correction are dependent on one another. The Glauert correction given in (4.8) introduces a numerical inconsistency when a tip loss is applied as the correction and traditional BEMT no longer agree at the transition stage. This discontinuity can lead to errors in the solution of the objective functions and does not match the physical behaviour of a rotor system at the transition between turbulent and non-turbulent wake. Buhl [21] introduced a modification to Glauert's theory ((4.10)) that incorporated tip and hub losses and addressed the numerical inconsistency in Glauert's model.

$$C_{FA} = \frac{8}{9} + \left(4F - \frac{40}{9}\right)a + \left(\frac{50}{9} - 4F\right)a^2$$

... (4.10)

Buhl treats the correction equation as a mathematical challenge and employs a parabolic curve with constraints to match the value and slope of the BEMT curve at the crossover point (a=0.4) and that crosses C_{FA}=2 when a=1. By imposing these mathematical limits, Buhl's values will always coincide with the BEMT values at the transition point. For a demonstration of this, see Figs. 4.9 and 4.10.

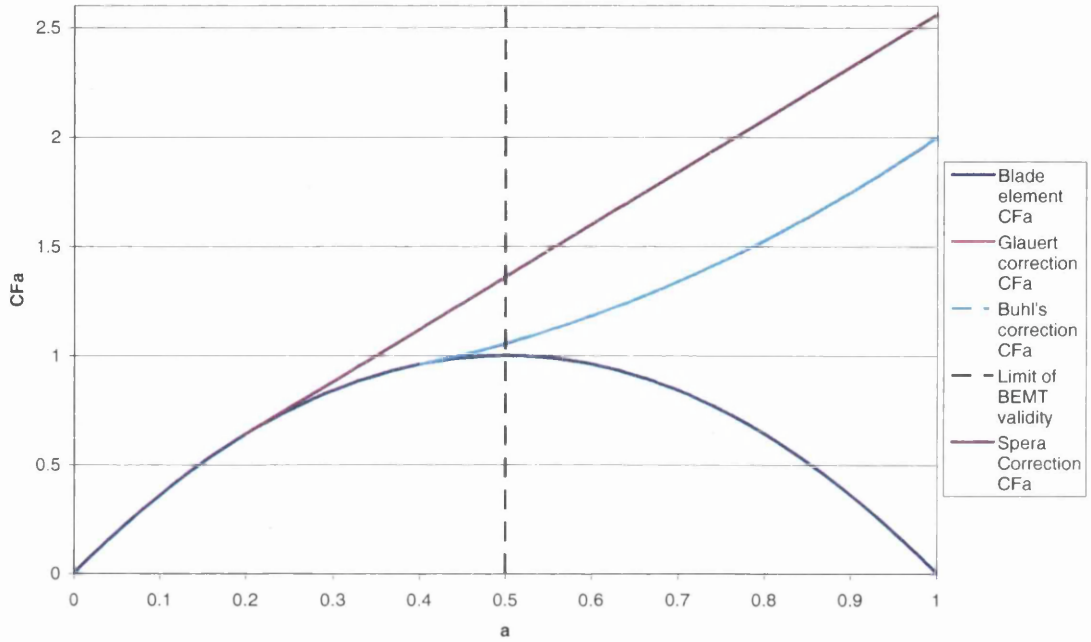

Figure 4.9: Axial Force Coefficient C_{FA} against a for BEMT, Glauert correction and Buhl's correction with zero loss factor F

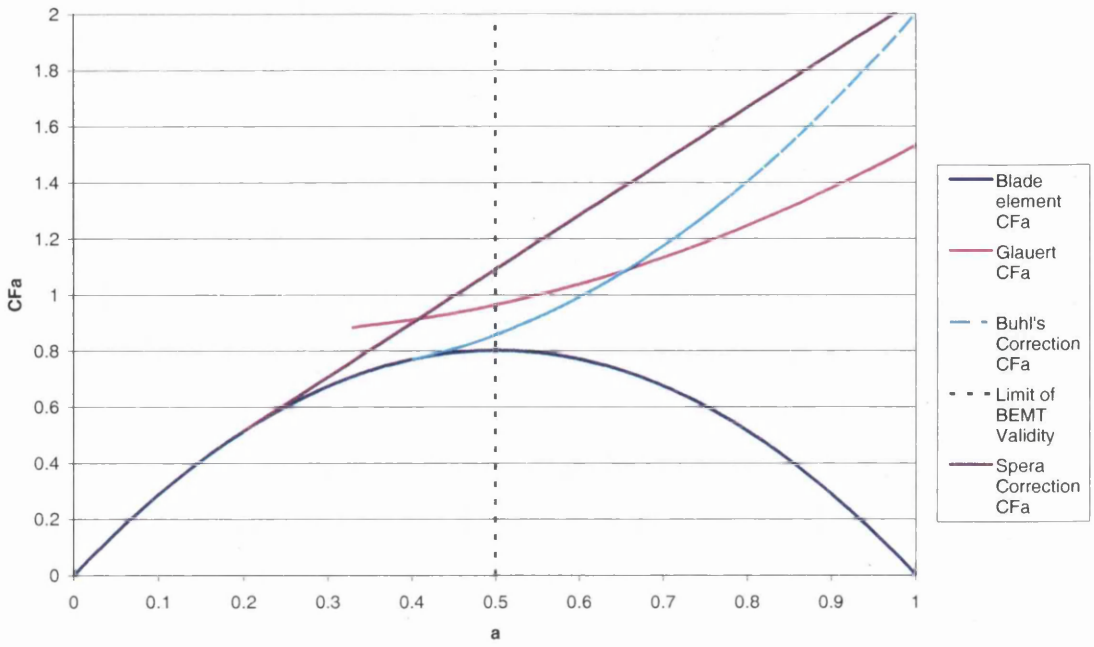

Figure 4.10: Axial Force Coefficient C_{FA} against a for BEMT, Glauert Correction and Buhl's correction with loss factor F = 0.8.

Due to this smooth transition and a reasonably high crossing between BEMT and empirical correction, the Buhl correction was selected for use in the present model. As with all high induction corrections, Buhl's correction is based on empirical data. The Reynolds numbers involved in the test data that the model is based on (fig 4.8) are not published in the reference texts. Most recent discussions on the matter refer back to Eggleston and Stoddard's text [19] which states that the test data is from helicopter rotors in unpowered descent but gives no further information on these tests. The limit of the correction where $a = 1$ gives a $C_{FA} = 2$, this condition is analogous with a flat plate as all flow is stopped at the rotor plane, this therefore gives some degree of confidence on the empirical corrections. It is clear that these empirical corrections should be validated against tidal turbine data when this information becomes available. The fact that a range of data from three rotor systems of differing designs was used to find these trends gives a reasonable degree of confidence in the correction approach as an estimation of high induction performance.

4.6 Other corrections

4.6.1 Skewed wake correction

BEMT is based on the initial assumption that the incoming flow is normal to the rotor plane. In operation the dynamic, non–uniform nature of tidal flows means that maintaining constant zero yaw error is an unrealistic target. During operation therefore, a yaw error will exist, this yaw angle is likely to be relatively small for a well-designed system with an active or passive yaw mechanism but will affect the loading on the system, in particular the fatigue loading. As the rotor blade spins in a yawed flow, the effective angle of attack will vary due to the yaw error. This will give rise to out of balance rotor loads. The wake in a yawed flow no longer shares its axis with the rotor axis (as in un-yawed cases) leading to a skewed wake (see figure 4.11)

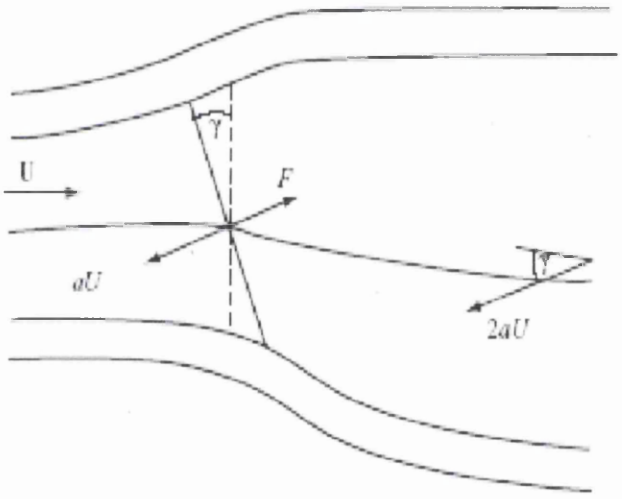

Figure 4.11: Skewed wake for a yawed rotor [3]

The skewed wake problem is covered in significant depth in Burton *et al.* [3], much of the discussion is concerned with presenting models for the new wake structure before using these models to explain several skewed wake correction methods. One such correction, Glauert's momentum theory for a yawed rotor ((4.11)) is described, K is a specific variable dependent on yaw angle.

$$u = u_0(1 + K\frac{r}{R}\sin\psi)$$

... (4.11)

This was originally developed for an autogyro rotor so was derived with high (close to 90°) yaw angles in mind. It is shown in the text [3] that the Glauert yawed rotor momentum equations are valid for any yaw angle. It is important to note that for yawed flows, the axial induction factor will vary (as angle of incidence varies) with azimuth position. The precise variation of the induction factor is complex and an exact solution is not feasible. An approximate relationship for the azimuthal variation of axial induction is used in Glauert's theory but this relationship requires the calculation of a constant for the specific rotor that is dependent on yaw angle.

A development of Glauert's theory, proposed by Pitt and Peters, is employed in AeroDyn [16]. The model is presented in a way that may be used to correct the calculated value of *a* in the solver routine ((4.12)). χ in the equation is the wake skew angle and γ is the rotor yaw angle.

$$a_{skew} = a[1 + \frac{15\pi}{32}\frac{r}{R}\tan\frac{\chi}{2}\cos\psi]$$

where

$$\chi \approx (0.6a + 1)\gamma$$

... (4.12)

Burton *et al.* [3] go on to present a vortex cylinder model for a yawed actuator disc. This theory dictates that the wake is dominated by the vorticity shed from the blade tips by the mean value of circulation. As circulation varies with both radius and azimuth, it is important that this variation is small. It is also assumed that wake expansion is small enough to be neglected. As with Bernoulli's skewed wake correction, a component of axial thrust is obtained from the rotor acting as a circular wing, which does not contribute to rotor torque significantly. Because of this, both theories are thought to overestimate power whereas, under yaw, traditional momentum theory is

likely to under predict axial force but is likely to be more accurate at predicting torque and power than these skewed wake corrections. A comparison of predicted power is seen in figure 4.12. It is important to note that for small angles of yaw error (less than 10^{o}) there is very little difference between all models. It is likely that any yawing TST is unlikely to be operating regularly in yaw errors larger than 20^{o} (where disagreement between the models becomes more significant) although fixed yaw systems may suffer flow misalignments of this magnitude.

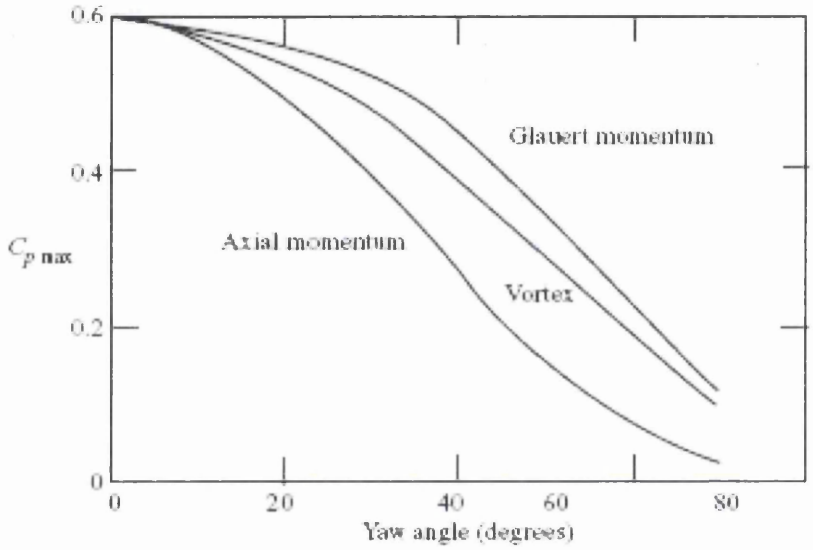

Figure 4.12: Power coefficients for varying yaw angles predicted by alternative momentum theories. [3]

As there is not necessarily a definable yaw error in a non-uniform flow, implementation of a yaw correction in the present code would pose a significant challenge. Mapping of the rotor in three dimensions inherently gives an allowance for the impact of yaw as the blade relative (rather than global upstream) velocities are always employed in the BEMT models and in-plane velocities are incorporated in the model (see chapter 3) allowing their impact on inflow angle to be included. These factors, coupled with the apparent uncertainty that these corrections provide a significant improvement in model accuracy, led to the decision that a skewed wake correction model would not be employed in the code at this stage.

4.6.2 Stall Delay

As a blade rotates, it has been noted that the lift coefficient produced inboard can be far higher than the predicted two-dimensional foil lift coefficient. Hu *et al.* [22] give a brief yet comprehensive review of research into the stall delay process. It appears to be accepted [Burton *et al.* and Hu [3, 22]] that stall delay was first noted by Himmelskamp [23] on propellers and Viterna and Corrigan [24] attributed this to the two dimensional foil data being used. It is stated that the characteristics of stall delay are highly dependent on local solidity, this is presented by Wood [25]. Burton *et al.* [3] state that a full explanation of the physical process of stall delay had not been published but that the adverse pressure gradient on the flow passing over the downwind surface is reduced by the blade's rotation. This pressure gradient slows down the flow towards the trailing edge of the blade and, as it increases, gives rise to flow separation and therefore stall. A reduction in this pressure gradient will maintain attached flow and prevent stall. In the study of Hu [22], there appears to be an explanation for the source of this reduction in pressure gradient. A CFD model boundary layer analysis and a wind tunnel model were used to investigate the phenomenon and in conclusion Hu *et al.* suggest that the stall delay may be attributed to Coriolis and Centrifugal forces which have a significant effect on inboard sections of the blade whereas Reynolds number has a predominant effect on lift characteristics on outboard sections. This would explain why 2D foil data gives a good prediction of outboard loads and not for inboard rotor stations. Viterna and Corrigan [24] propose a correction to the lift and drag data for angles of attack greater than the 2D stall value, the correction is to be used without any Prandtl based tip or hub loss corrections. Viterna's correction is an empirical solution based on 2D lift/drag data and the blade aspect ratio (defined as tip radius divided by chord length at 75% radius), in the report [24] this correction is said to give a good match to measured results. Measurements were only made on two different rotors and so this empirical correction cannot be viewed as a universal solution although application to different systems is possible so long as the equation's constants are calculated for the relevant lift/drag data. A major shortcoming of this correction would appear

to be that it makes no account for radial position. As has been previously discussed, the stall delay phenomenon is prevalent only on inboard sections of the rotor and any model to account for stall delay should reflect this. Snel *et al.* [26] propose a simpler correction to the post-stall lift data that gives improved results over traditional theory and is dependent on local chord and radial position. Snel's correction equation is presented in Burton *et al.* [3] and is repeated here for completeness in (4.13).

$$C_{L3-D} = C_{L2-D} + 3\left(\frac{c}{r}\right)^2 \Delta C_L \qquad \ldots (4.13)$$

Where C_{L3-D} is the corrected lift coefficient, C_{L2-D} is the two-dimensional lift coefficient and ΔC_L is the difference between a linear extension of the two-dimensional lift curve post stall and the two-dimensional values. This correction is employed for post-stall lift coefficients only.

At present, a stall delay model is not implemented in the system as the corrections above do not appear to give a flexible and reliable correction approach due to their reliance on empirical knowledge that does not yet exist for tidal turbines. This means that results at low *TSR* values (post stall) should be treated with caution. If Snel's correction were found to be valid for tidal turbine devices then implementation of this method would be recommended and could be incorporated with relative ease.

4.7 Implementation

4.7.1 Tip and hub loss

Implementation of the correction factors for tip and hub loss differs slightly depending on the solver method and loss factor being employed. If it is considered that only (4.2) and (4.7) are to be used, F_{tip} and F_{hub} are calculated in the same way for either approach. If tip losses are to be neglected then F_{tip} is set to one, likewise if hub losses are not to be modelled F_{hub} is set to one. F, the total loss for the element, is then taken as the product of F_{tip} and F_{hub}.

In the developed model, (4.3) and (4.4) must be equated to the lift and drag based equations for dT and dFa ((3.30) and (3.29)). Rearrangement then produces an objective function as shown in (4.14).

minimise g where:

$$g_1 = ((4\pi\rho r U^2(1-a)aFdr) - (N\frac{1}{2}\rho V^2 c(C_L\cos\phi + C_D\sin\phi)dr))^2$$

$$g_2 = ((4\pi\rho r^3 U\Omega(1-a)bFdr) - (N\frac{1}{2}\rho V^2 cr(C_L\sin\phi - C_D\cos\phi)dr))^2$$

$$g = g_1 + g_2$$

... (4.14)

To reduce processing demand in the solver routine, a number of constants may be cancelled out from (4.14) to give (4.15), values that cannot be removed from both g_1 and g_2 are kept in the objective function as removing them would further bias the solver's solution to either the axial force or torque based objective component.

minimise g where:

$$g_1 = ((4\pi r U^2(1-a)aF) - (N\frac{1}{2}V^2 c(C_L\cos\phi + C_D\sin\phi)))^2$$

$$g_2 = ((4\pi r^3 U\Omega(1-a)bF) - (N\frac{1}{2}V^2 cr(C_L\sin\phi - C_D\cos\phi)))^2$$

$$g = g_1 + g_2$$

... (4.15)

These equations may then be solved using the same approach as presented in chapter 3.1.7. Once these equations have been solved for a and b, the elemental axial force and torque values can be calculated in a post-process using the lift based objective functions, the modified momentum based functions or a mean of the two.

An alternative approach to the solution is provided in several texts including Wind Energy Explained and the AeroDyn manual [2, 16] the momentum and lift/drag based equations are again combined for axial force and rotational torque with the loss correction factor included, these are then rearranged to give equations for a and b. Wind Energy Explained presents a simplified case where drag coefficient is neglected. Wilson and Lissaman [27] argue that this should be the case as drag is produced by skin friction only in attached flow and this does not affect the pressure drop across the rotor. If the flow is stalled, the drag is predominantly caused by pressure variations and so should be included. As drag coefficients are generally low in attached flow it would appear prudent to include the effects of drag coefficient to allow the model to better capture both stalled and un-stalled flows. Deriving equations for a and b as presented in Chapter 3 but using (4.3) and (4.4) gives us (4.16) [16]:

$$a = \left[1 + \frac{4F\sin^2\phi}{\sigma(C_L\cos\phi + C_D\sin\phi)}\right]^{-1}$$
$$b = \left[1 + \frac{4F\sin\phi\cos\phi}{\sigma(C_L\sin\phi - C_D\cos\phi)}\right]^{-1} \quad \ldots (4.16)$$

These can then be employed in the same manner as was presented in Chapter 3.

4.7.2 High induction correction

If the approach to solving for a and b presented in most texts is used, it is relatively simple to incorporate the Buhl high induction correction. A conditional switch in the solver loop can be added that employs an alternative calculation for a if $C_{FA} > 0.96F$ or if the previous value for a >0.4. Equation (4.9) may be used or alternatively (4.10) can be rearranged (using the quadratic formula) to give (4.17) [16]. The approach simply employs a condition switch based on either axial induction factor or axial force coefficient BEMT validity limits and (4.17) is employed to calculate a if the limit is exceeded.

$$a = \frac{18F - 20 - 3\sqrt{C_{Fa}(50 - 36F) + 12F(3F - 4)}}{36F - 50} \quad \ldots (4.17)$$

Implementation in the novel approach presented in this text requires one more step as an objective function to minimise axial force disagreement is required. Hansen [17] rearranges the lift based axial force equation using the axial force coefficient formula to give a C_{FA} formula (4.18) to equate to Spera's correction (4.9) which is then rearranged to give an equation for a.

$$C_{FA} = \frac{(1-a)^2 \sigma (C_l \cos\phi + C_d \sin\phi)}{\sin^2\phi} \quad \ldots (4.18)$$

Using axial force coefficient formulae in the model developed in this thesis would lead to problems in solution as the axial force based equation solution would have a far smaller weighting than the torque based equation. An alternative approach is therefore employed using Buhl's correction to give a smooth transition. The high induction factor formula for C_{FA} ((4.10)) is substituted into the definition of thrust coefficient, (3.15), where the reference area is taken as the area of the annulus ($2\pi r dr$) and the reference velocity is

the elemental blade normal inflow component. The resulting formula may be equated to the lift / drag equation for axial force and rearranged to give the axial force based component (4.19) of the minimisation objective function.

$$g_{1Buhl} = ((\frac{8}{9} + (4F - \frac{40}{9})a + (\frac{50}{9} - 4F)a^2)U^2\pi r - \frac{N}{2}V^2c(C_L\cos\phi + C_D\sin\phi))^2 \quad \ldots (4.19)$$

This can then be solved to find *a* and *b* as previously described. An "if" condition may be added to the minimisation objective function. This allows switching between BEMT and Buhl formulae at the $a=0.4$ border. The minimisation objective is then (4.20).

$$\begin{aligned} &\text{if } a < 0.4 \\ &\text{minimise } g = g_1 + g_2 \\ &\text{else if } a \geq 0.4 \\ &\text{minimise } g = g_{1Buhl} + g_2 \end{aligned} \quad \ldots (4.20)$$

Consulting the literature suggests that this approach has not been previously employed. Care must be taken during the implementation that the different axial force objective functions are evenly weighted at the border between traditional BEMT and the high induction correction. An uneven weighting here will lead to a tendency for the solver to prefer one or other set of equations and will prevent a smooth transition between the traditional solution and Buhl's induction correction. This will show up as a problem if a smooth curve is not seen at the transition stage in a plot of a values against *TSR*. If a smooth transition were not found then a weighting value would have to be added to the terms to encourage transition. With a reasonably robust solver algorithm, this becomes less of a problem and it was not found to be an issue with the model developed here.

4.8 Results

4.8.1 Tip loss and hub loss performance against *TSR*

To assess the performance of the tip and hub loss correction factors, the predictions of blade performance made by the code with and without the corrections were compared to models from Garrad Hassan's Bladed program [28] and to a Lifting line theory model by David Sharpe [29]. The results of this are shown in figures 4.13 to 4.16

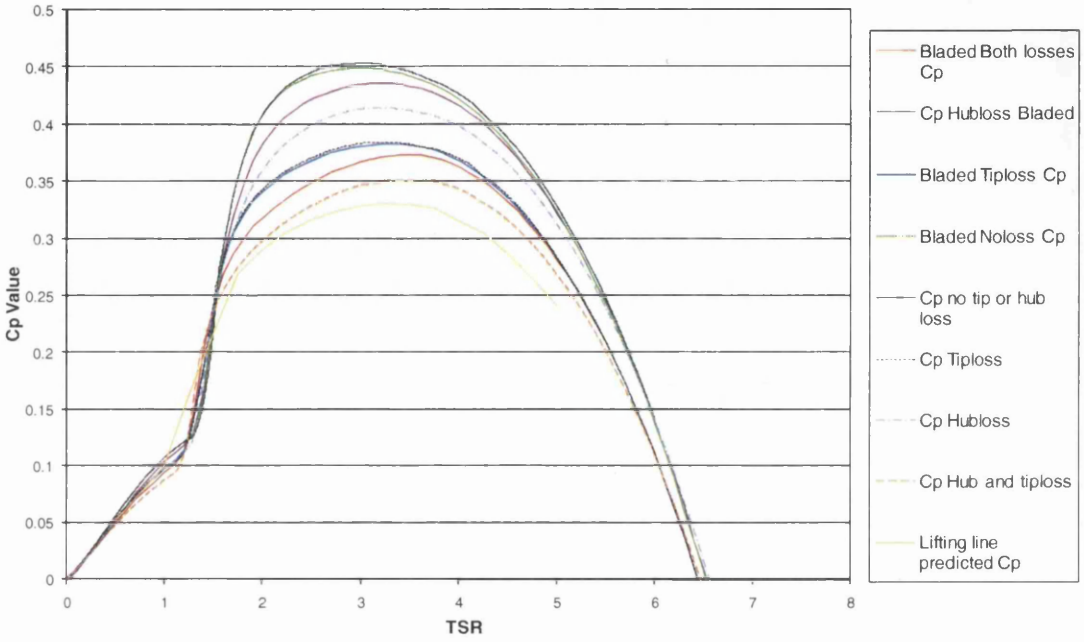

Figure 4.13: Comparison of power coefficient against predictions from GH Bladed and D. Sharpe's lifting line theory code.

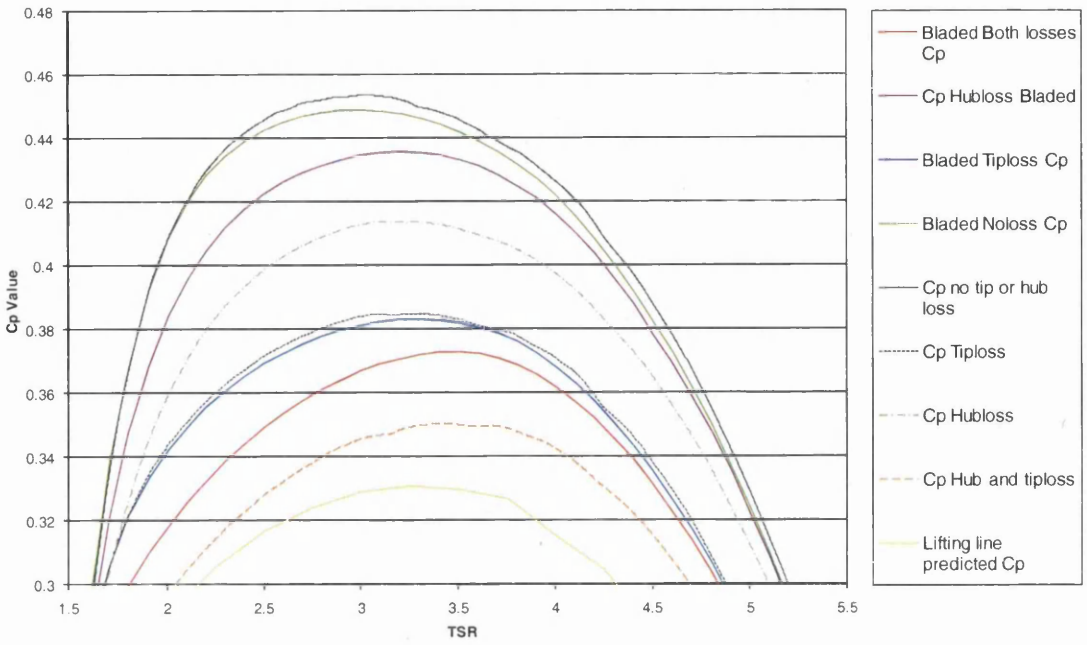

Figure 4.14: Detail view of Power coefficient curve for BEMT model with combinations of tip and hub loss models.

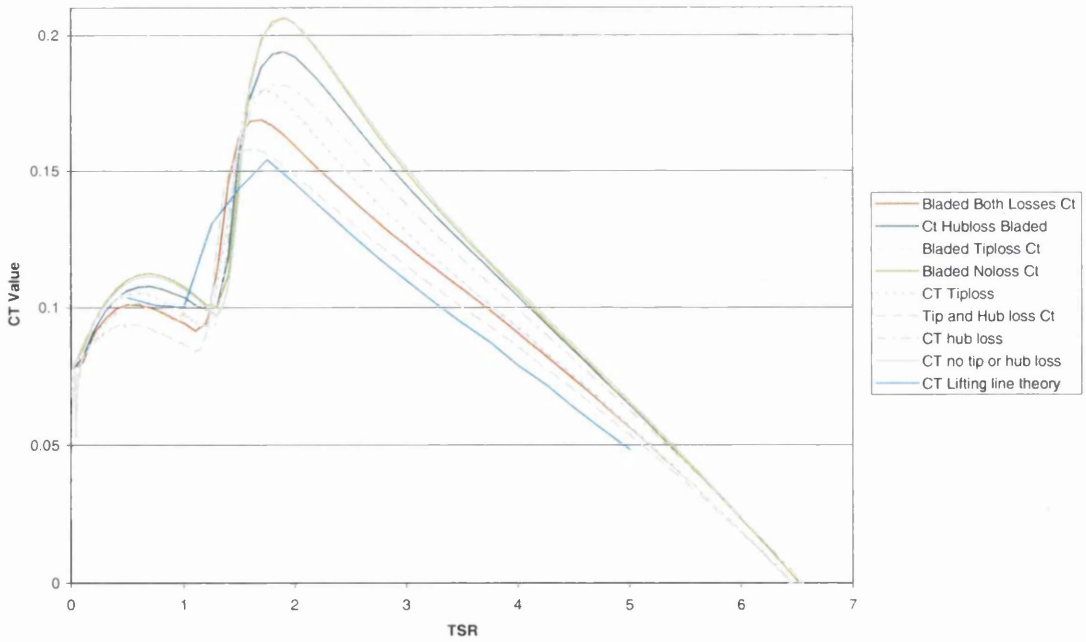

Figure 4.15: Comparison of Torque coefficient against predictions from GH Bladed and D. Sharpe's lifting line theory code.

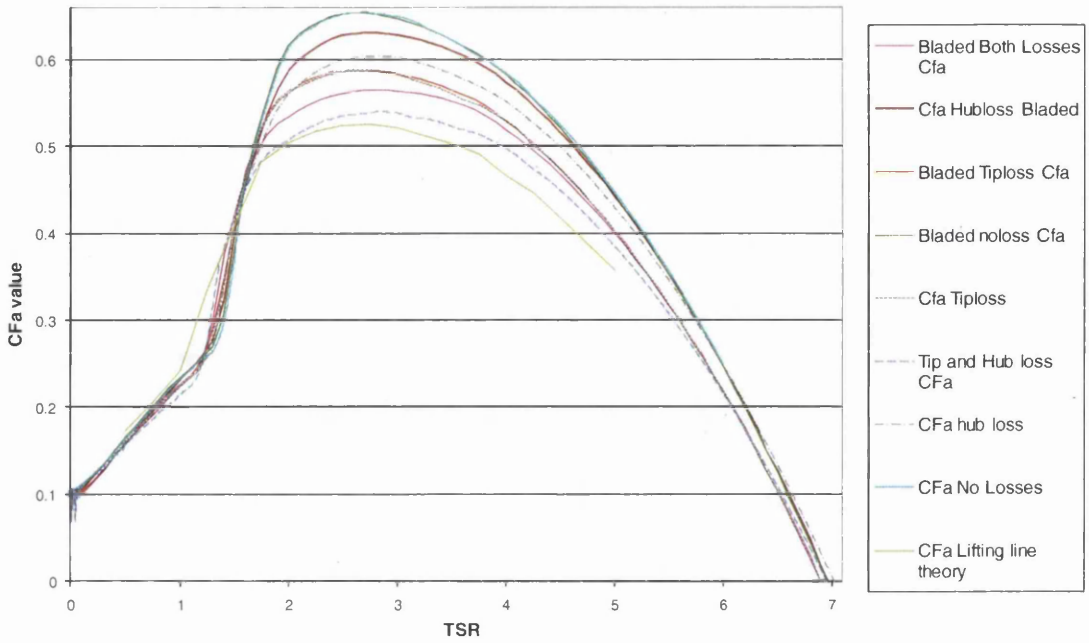

Figure 4.16: Comparison of thrust coefficient with predictions from GH Bladed and D. Sharpe's lifting line model.

It can be seen that the lossless solution compares very well between GH Bladed and the developed model with disagreement between predicted values lower than one percent. The predicted tip loss only curves also agree well, again with a disagreement of similar magnitude. The small disagreements in predicted values for these runs are expected to be primarily due to the different methods of blade geometry definition. In GH Bladed, the geometry is defined at element ends whereas with the developed model the blade geometry at the element centre is defined, this leads to the slight disagreement in calculated performance even with a similar number of elements for each model. As Bladed is Germanischer Lloyd certified, this gives a good confidence in the results from the developed code.

Disagreement between the two models for the hub loss only run is significant (up to around 7% for C_P). The specific hub loss model employed in GH Bladed is not divulged in the user manual [30] or theory manual [31] and so a rigorous examination of the source of this disagreement is not possible. As the total loss factor for any point on the blade is the product of tip and hub loss for that point, a similar disagreement is seen for the combined loss

model runs. This disagreement is larger than can be attributed to differences in geometry definition and is most likely due to a different hub loss formula being employed by the two models. Although a definitive conclusion cannot be made without more information on the Bladed hub-loss model, the losses predicted by the developed model appear to give a prediction closer to Sharpe's lifting line predictions.

Comparison to the lifting line theory model shows that both the developed model and Bladed predict higher torque, axial force and power coefficients than the lifting line theory. This disagreement between the theories is discussed by Badreddinne, Ali and David [32] and is attributed to the fact that BEMT does not account for three dimensional flow effects induced on the rotor disc by the shed tip vortex or the induced radial flow created by rotation of the blades.

4.8.2 High induction performance against *TSR*

The topic of high induction correction is not discussed by any of the Bladed literature [30, 31] it is not therefore known what correction is used or indeed if one is employed at all. Because of this, comparison to Bladed results would offer no improvement in understanding. Results from D. Sharpe's model do not include results from a blade design that runs into the high induction region and so likewise cannot be used for comparison. An assessment of the performance of the axial induction correction is therefore made against the developed model's performance without the induction correction and the resulting induction factors across the blade are discussed.

Figure 4.17 shows the results for the blade design used in the previous tip loss study with the blades pitched by an extra 5 degrees towards the rotor plane. In this case, high induction values are encountered but these values do not become excessive (see Figures 4.18 and 4.19). It can be seen that, at low *TSR*, there is no disagreement between the results with and without induction correction. This is as expected, in this region the axial induction

factor is below 0.4 and so traditional BEMT is used in both models. With increasing *TSR*, high induction factors are encountered near the tip and the operation of the correction factor is evident in the axial force coefficient curve and to a lesser extent in the power coefficient curve. The code has been allowed to exceed the theoretical limit of $a=0.5$ for the cases with and without high induction correction.

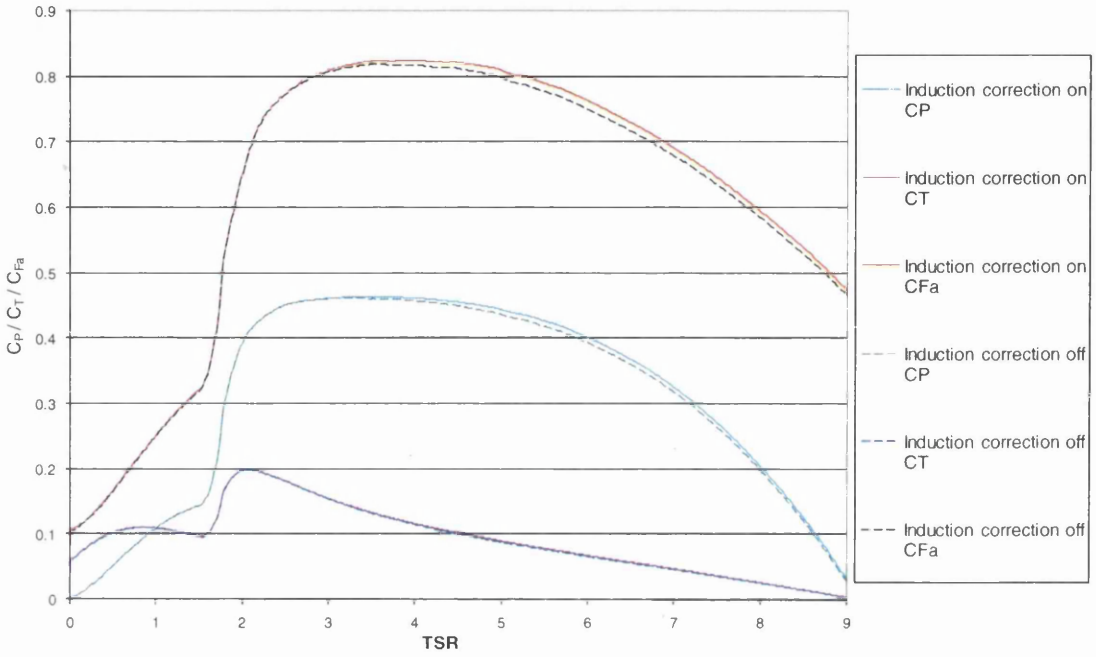

Figure 4.17: Performance curve with blade pitched by 5° towards rotor plane to initiate high induction values. Results with and without Buhl's correction displayed.

Figure 4.18 shows that a mathematical solution continues in excess of this physical constraint, this explains why there is only a small disagreement between the results in fig. 4.17.

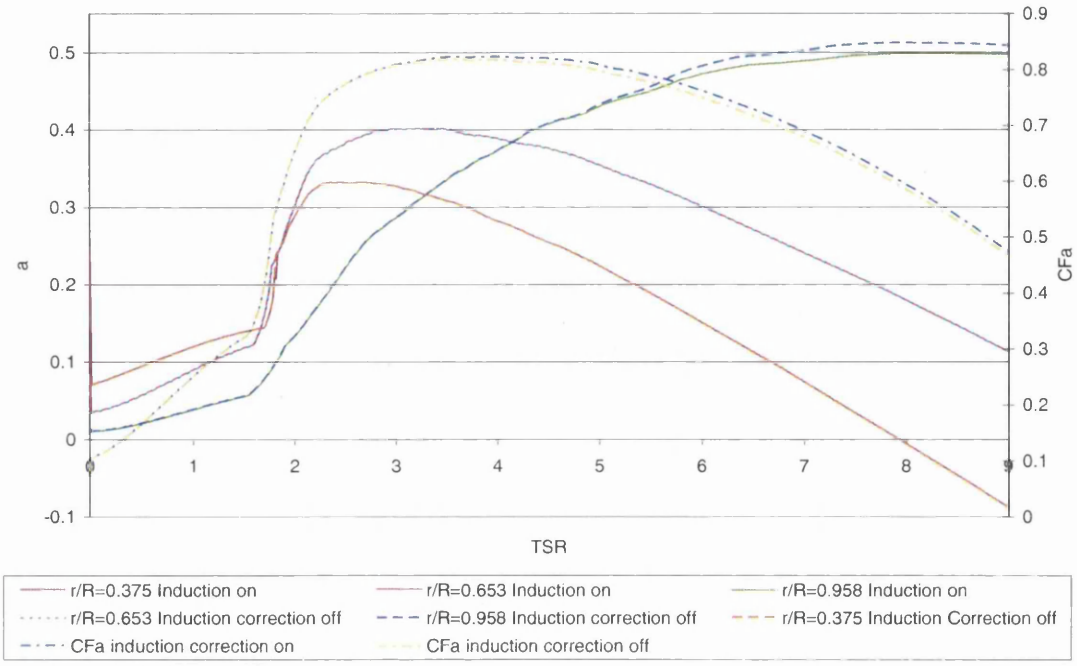

Figure 4.18: Induction factors at different radial stations and axial force coefficient for rotor blade pitched 5° towards rotor plane. Results with and without Buhl's correction.

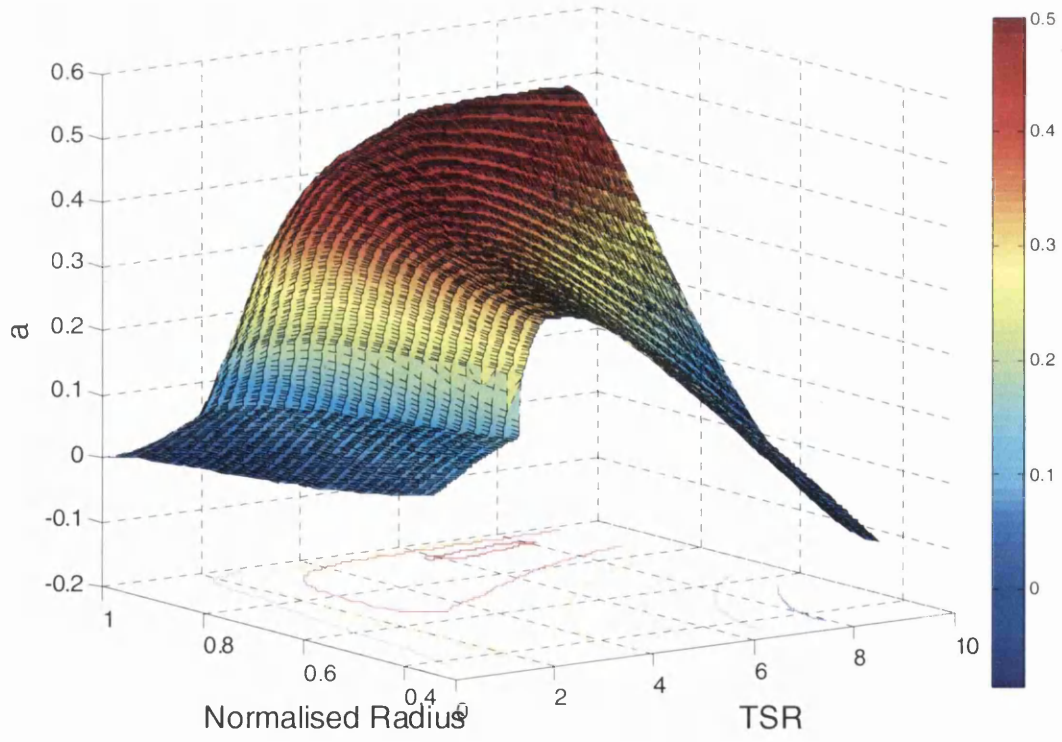

Figure 4.19: Surface and contour plot of axial induction factor for all blade elements at varying TSRs for high induction correction results shown in Fig 4.17.

Figure 4.20 demonstrates a more extreme case where the blade is pitched by 10 degrees towards the rotor plane. This gives a far greater proportion of high induction elements and it can be seen in figure 4.20 that under these conditions (*TSR>2*) the traditional BEMT model struggles to find a valid solution and the majority of elements fail to converge on a solution.

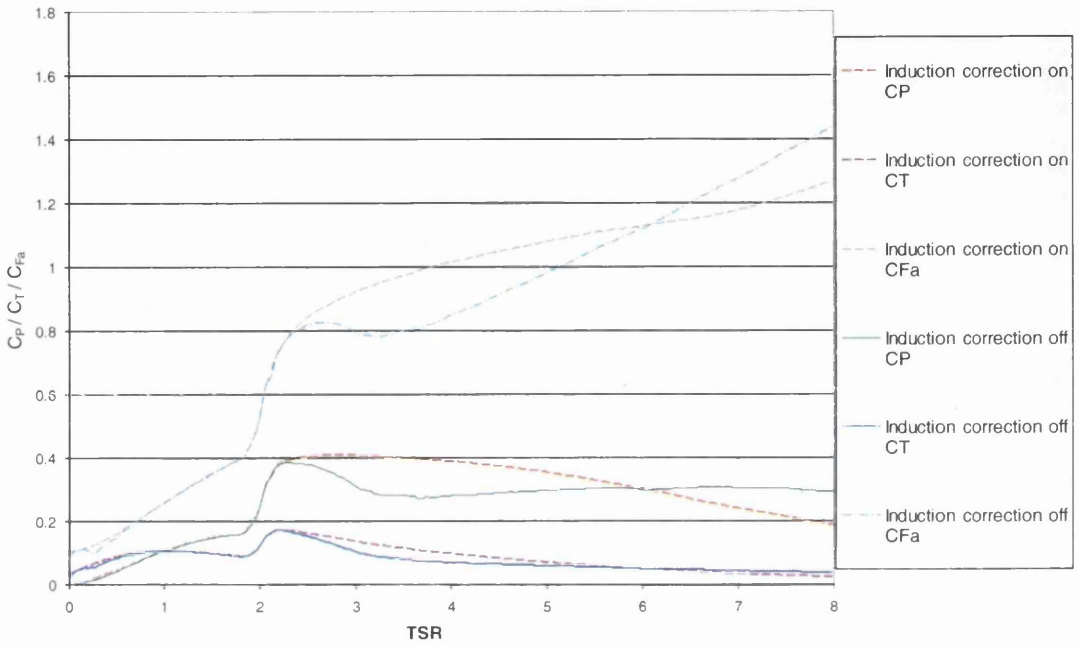

Figure 4.20: Performance curve with blade pitched by 10 degrees towards rotor plane to increase occurrence of high induction values. Results with and without Buhl's correction.

Using Buhl's correction, the system is able to function and produces converged solutions for axial induction factors in excess of one (the BEMT limit). The system without high induction correction is still seen to predict axial force coefficients greater than one (not possible in traditional blade element theory). This is because the lift and drag based equations are used in the postprocessor. This means that even if an element has converged to an incorrect solution or has reached the upper or lower bound constraints of the induction factors, the axial force and elemental torque will be calculated for this element and using the lift and drag based equations there is no $C_{FA}=1$ limit. From a practical point of view, it is vital that the operator is warned about this case and a warning statement is issued by the code together with a list of non-converged elements at each step.

4.8.3 Combined tip, hub and high induction corrections against *TSR*

Because tip (and hub) losses lead to high local induction factors, it is important that tip, hub and high induction correction factors function in combination. It has been shown in section 4.8.1 that the tip and hub loss models function well in combination so it only remains to test these in combination with the high induction correction.

In figures 4.21 to 4.23, the high induction correction can be seen to have a more marked effect on the C_{FA} curve with losses turned on than with the losses neglected. This is because the tip and hub losses lead to higher induction factors at the tip and root as can be seen by comparing figure 4.19 with figure 4.24. Combination of tip, hub and axial induction causes little problem using the implementation presented in this thesis. The objective function becomes more complex and so processing time is increased slightly but the employed solver routine is still able to solve the equations reliably.

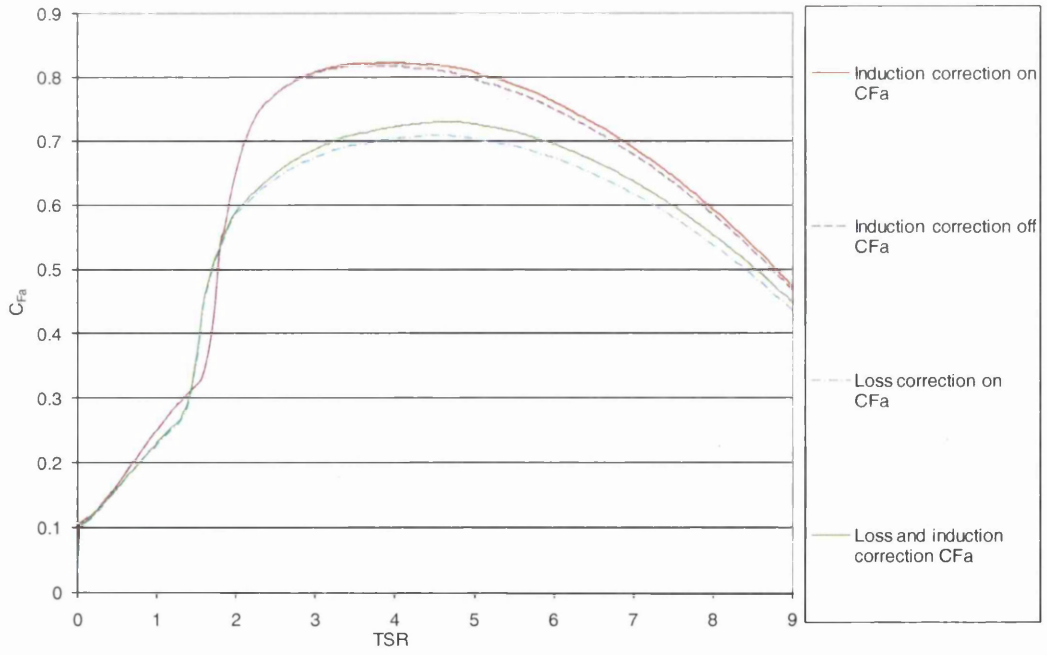

Figure 4.21: Axial force coefficients with losses (tip and hub) and induction corrections turned on and off

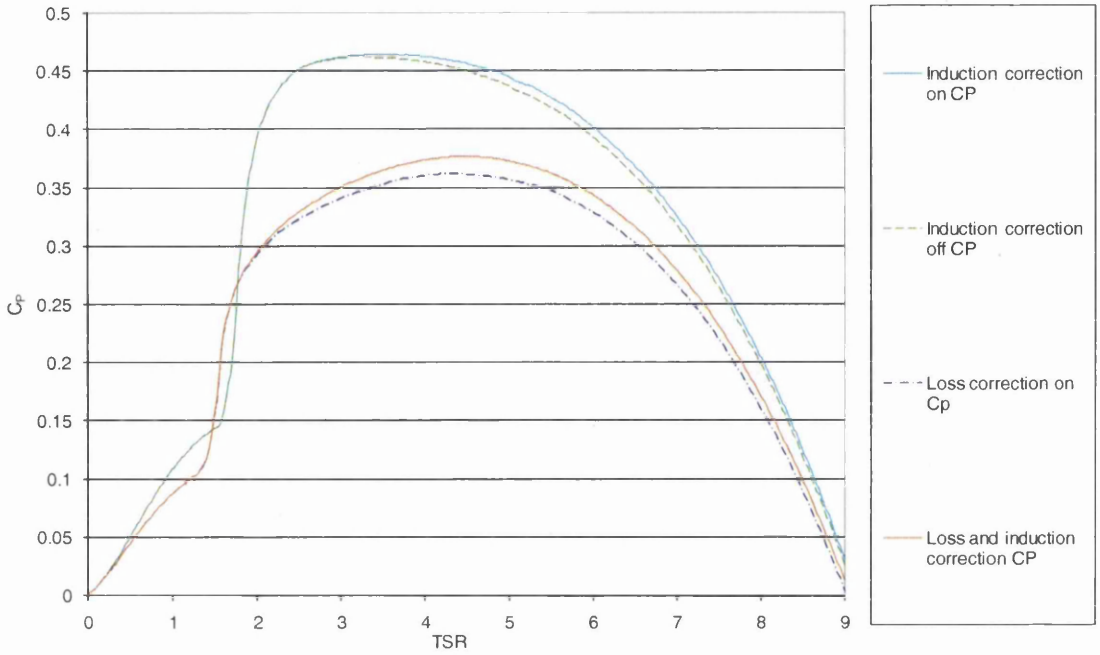

Figure 4.22: Power coefficients with losses and induction factors turned on and off.

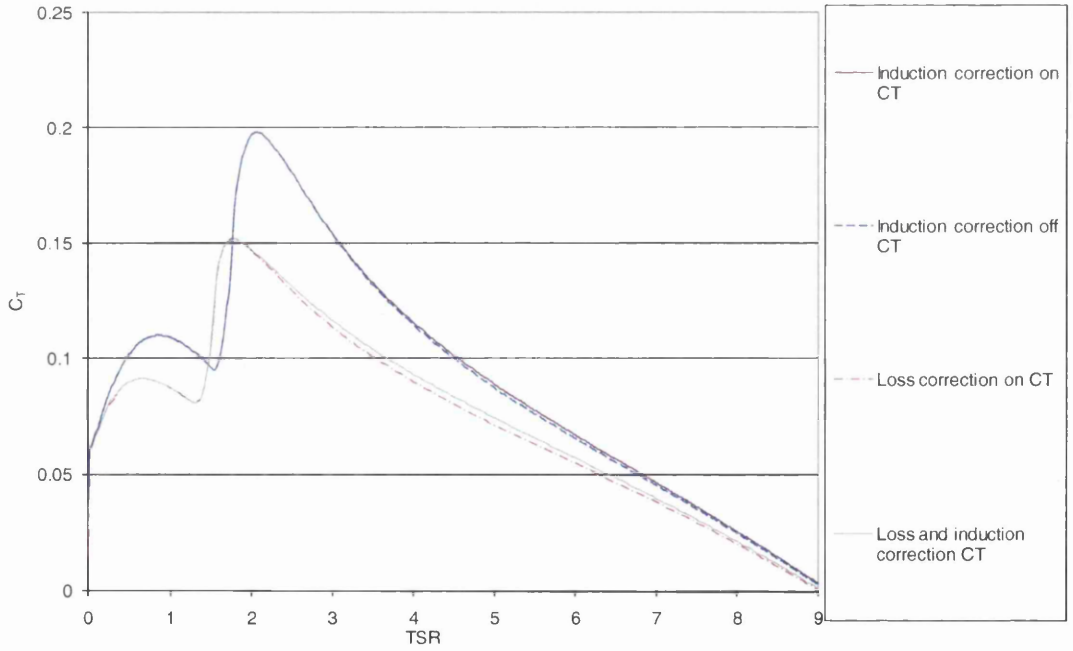

Figure 4.23: Torque coefficients with losses and induction factors turned on and off.

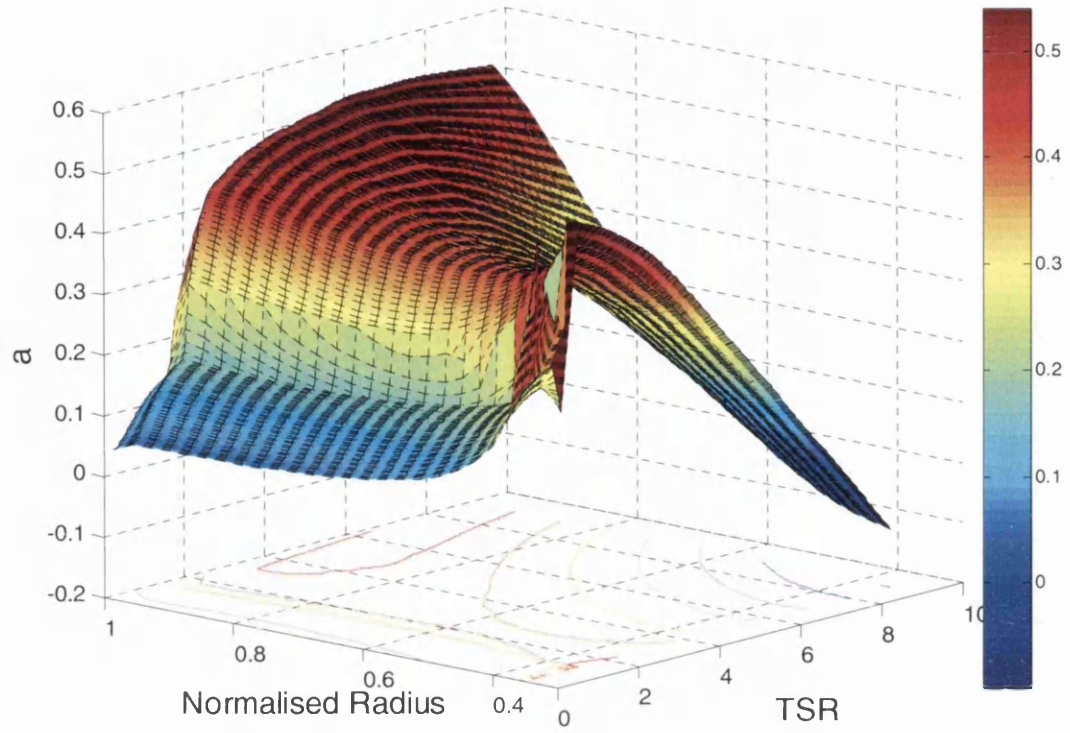

Figure 4.24: Surface and contour plot of axial induction factor for all blade elements at varying TSRs for high induction and loss correction results shown in Fig 4.15.

4.9 Conclusion

In this chapter:

- The Prandtl based tip and hub loss corrections were presented and were seen to improve accuracy when compared to a lifting line theory model. There is only a small computational cost of employing these corrections and so inclusion proves to be beneficial. The Prandtl based corrections were selected as they do not rely on empirical data.
- A high induction correction proposed by Buhl was implemented using a novel approach and results are discussed. A smooth and therefore reliable transition between the BEMT equations and this correction has been demonstrated. The uncertainty of applicability of the empirical data this correction is based on was discussed and a need for future investigation highlighted.
- Novel rearrangements of the high induction, hub and tip loss corrections were presented that allowed them to function in combination with the novel solution approach presented in chapter 3.
- The output of the model using these corrections was compared with GH Bladed and a lifting line theory model. The results showed a good correlation with the existing codes. The developed approach has the advantage of being able to account for cross flows and inertial loadings.

4.10 References

[1] Griffiths RT and Woollard MG, "Performance of the optimal wind turbine", Applied Energy 4, 1978. Applied Science Publishers Ltd.

[2] Manwell, J.F., J.G. McGowan, and A.L. Rogers, "Wind Energy Explained". 2002, Chichester: John Wiley & Sons Ltd.

[3] Burton, T., *et al.*, "Wind Energy Handbook". 2001, Chichester: John Wiley & Sons.

[4] Hansen, M. and J. Johansen, "Tip Studies Using CFD and Comparison with Tip Loss Models", Wind Energy, 2004. 7: p. 343-356.

[5] Shen, W., *et al.*, "Tip loss corrections for wind turbine computations", Wind Energy, 2005. 8: p. 457-475.

[6] Benini, E., "Significance of blade element theory in performance prediction of marine propellers", Ocean Engineering, 2004. 31: p. 957-974.

[7] Drela M at MIT, "XFoil Subsonic Airfoil Development System ".

[8] Goldstein, S., "On Vortex theory of screw propeller", Proc. Roy. Soc., 1929. 123: p. 440.

[9] Glauert, H., "Airplane Propellers", Aerodynamic Theory, 1963. p. 169-360.

[10] Chapman, J., I. Masters, and J. Orme, "Rotor Performance Prediction for Tidal Current Turbines", in A Joint Conference of The Association for Computational Mechanics in Engineering (UK) and The Irish Society for Scientific and Engineering Computation, C.G. Armstrong, Editor. 2006, Queen's University, Belfast: Queen's University, Belfast. p. 103-106.

[11] Glauert, H., "Airplane propellers", Aerodynamic Theory 4, 1963. Dover & New York: p. 169-269.

[12] Wilson, R. and P. Lissaman, "Applied aerodynamics of wind power machines", Oregon State University Report, 1974. (NSF/RA/N-74113).

[13] DeVries, O., "Fluid dynamic aspects of wind energy conversion", AGARD Report, 1979.

[14] H, G., "Airplane propellers", Aerodynamic Theory 4, 1963. Dover & New York: p. 169-269.

[15] Xu, G. and L. Sankar. "Application of a Viscous Flow Methodology to the NREL Phase VI rotor" in ASME Wind Energy Symposium. 2002.

[16] Moriarty, P.J. and A.C. Hansen, "AeroDyn Theory Manual", NREL, 2005.

[17] Hansen, M., "Aerodynamics of Wind Turbines" Second Edition ed. 2008, London: Earthscan.

[18] Glauert, H., "A General Theory of the Autogyro". 1926.

[19] Eggleston, D.M. and F. Stoddard, "Wind Turbine Engineering Design". 1987, New York: Van Nostrand Reinhold.

[20] Strathclyde University, "Tidal Power Case Studies".

[21] Buhl, M.L.J., "A New Empirical Relationship between Thrust Coefficient and Induction Factor for the Turbulent Windmill State", NREL, 2005.

[22] Hu D, "A study on stall-delay for horizontal axis wind turbine", Renewable Energy, 2005. Elsevier.
[23] Himmelskamp, "Profile investigations on a rotating airscrew", PhD Thesis, 1945, Gottingen University, Germany.
[24] Viterna, L.A. and R.D. Corrigan, "Fixed pitch rotor performance of large horizontal axis wind turbines", DOE/NASA workshop on large horizontal axis wind turbines, 1981. Cleveland, (OH).
[25] Wood, D., "Three-dimensional analysis of stall-delay on a horizontal axis wind turbine", J Wind Eng Ind AeroDyn, 1992. 37: p. 1-14.
[26] Snel, H. "Sectional prediction of three-dimensional effects for stalled flow on rotating blades and comparison with measurements." in EWEC. 1993.
[27] Wilson, R.E. and P.B.S. Lissaman, "Applied aerodynamics of wind power machines", Oregon State University Report, 1974.
[28] Garrad Hassan & Partners Ltd, "GH Bladed: Wind Turbine Design Software ".
[29] Sharpe, D., "Lifting line theory model results". 2007.
[30] Bossanyi, E.A., "GH Tidal Bladed Version 3.80 User Manual". 2007, Garrad Hassan.
[31] Bossanyi, E.A., "GH Tidal Bladed Theory Manual". 2007, Garrad Hassan.
[32] Badreddine, K., H. Ali, and A. David, "Optimum project for horizontal axis wind turbines 'OPHWT' ", Renewable Energy, 2005. 30: p. 2019–2043.

Chapter 5: Specific features – system level extension

In this chapter, specific aspects of the model are introduced which enable more accurate modelling of system specific features. These include tower shadow effects, yawing models, brake and generator models. These aspects are demonstrated using time dependent model runs.

5.1 Blade off model

5.1.1 Development of theory

A severe case of failure of a tidal turbine is for one blade to become detached from the hub. The modelling case for this is not the same as a simple reduction in blade number as the remaining blades will not be evenly spaced. This will affect the flow characteristics through the rotor plane, as the section of the rotor missing the blade will present a lower blockage to the flow than that of the portion of the rotor with blades still intact. This would result in a lower local induction factor in the 'blade off' region and a higher induction factor (when compared to a rotor with the same number of evenly spaced blades) in the region near the remaining blades. If it is assumed that, despite this localised change in induction, the average induced velocity is unaffected and that the induced velocity at the rotor blades is largely unchanged compared to an equal number of evenly spaced blades then it is possible to employ BEMT to model the remaining blades. Although this is unlikely to be the true case, it will give a satisfactory initial approximation of this failure case.

If this induction assumption is accepted, the problem is reduced to one of correctly mapping the remaining blades and correct resolution of the calculated loads. For this model, the number of blades is reduced by the number of detached blades. The remaining blades are positioned as they would be for a rotor with the original number of blades. This positioning is a

relatively straightforward problem that requires the addition of another variable in the model. The original number of blades in the rotor system needs to be defined in addition to the number of blades to be modelled. The initial azimuthal position of the remaining blades can then be calculated using the algorithm in (5.1).

$$\psi_{0nb} = \psi_{spacing} \times (nb - 1)$$

$$where$$

$$\psi_{spacing} = \frac{2\pi}{N_{full}}$$

... (5.1)

Once these initial blade azimuth positions are calculated, the global position at any step can be found using the mapping approach presented in chapter 3. If the number of blades is low, the resulting out of balance mass loading of the rotor system will become highly significant. Centripetal out of balance loads are not accounted for in the model but if the correct rotational moment of inertia is used then the rotational speed calculated by the time dependent code will be correct. A simple calculation can then be performed to assess the magnitude of centripetal force due to the missing blade so long as the centre of mass is known for the rotating system.

5.1.2 Example

To demonstrate the impact of a missing blade on the hydrodynamic loads of a three-blade downstream rotor design, a brief study is now reported. A model of the three bladed rotor was run in a 4.5m/s free stream power law flow and the same flow case was then modelled using the same rotor design but with one turbine blade missing. A fixed rotational speed was defined to allow a direct comparison of the loadings produced. As can be seen in Figure 5.1 torque is not simply reduced by the proportion of remaining blades to existing blades (blade off torque is on average 89% of 3 bladed rotor torque) and a similar result can be seen for axial force which is reduced to 81% of the undamaged rotor's values.

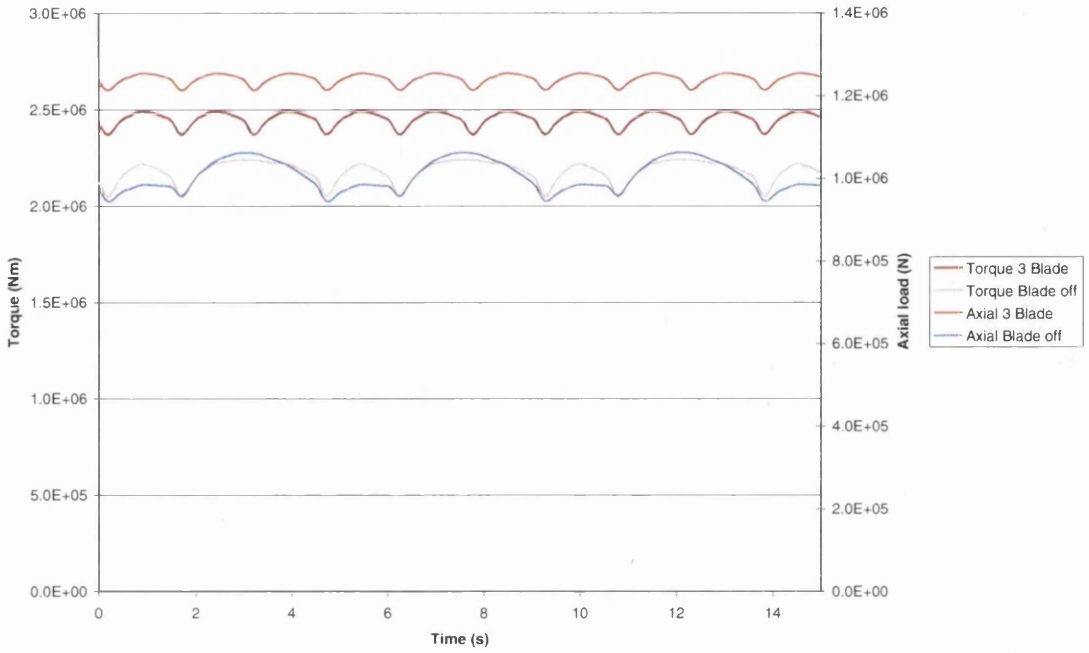

Figure 5.1: Axial force and Torque for a three bladed rotor compared to the same design with one blade missing.

A plot of axial induction factor for these runs at different radial stations can be seen in Figure 5.2. The induction factor is reduced to approximately 75% of the three bladed values with the blade removed. The frequency of oscillation of these loads has also changed, the lack of blade pass effects from the missing blade can clearly be seen in figure 5.1 by comparison of the three bladed rotor and blade off results. The driving factor for these changes in load and induction factor values is the fact that rotor solidity (local solidity, $\sigma = \frac{Nc}{2\pi r}$) is two thirds of the original value when one blade is removed. This change in solidity, when placed in to the BEMT equation brings about the variations in induction factor and loads presented here.

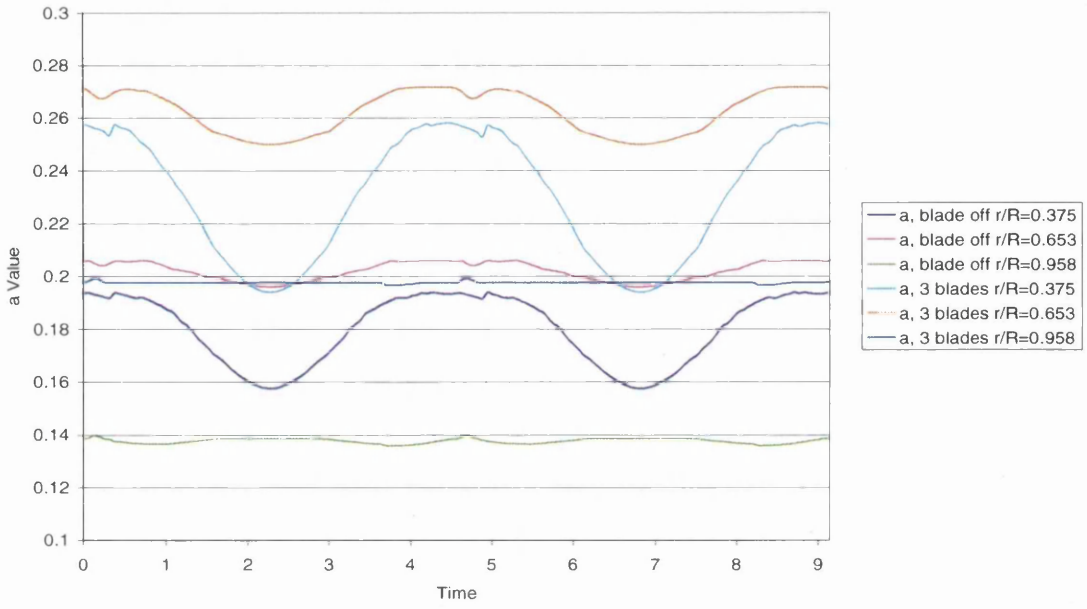

Figure 5.2: Axial induction factors for blade 1 of a three bladed turbine and the same design with one blade removed.

The impact on the out of balance loadings with one rotor blade missing is clearly demonstrated by the yaw and teeter moments displayed in Figure 5.3. There is a 560% increase in teeter moment and a 2900% increase in yaw moment. These loads demonstrate the catastrophic effects a failure such as this would have on the turbine system if allowed to continue running.

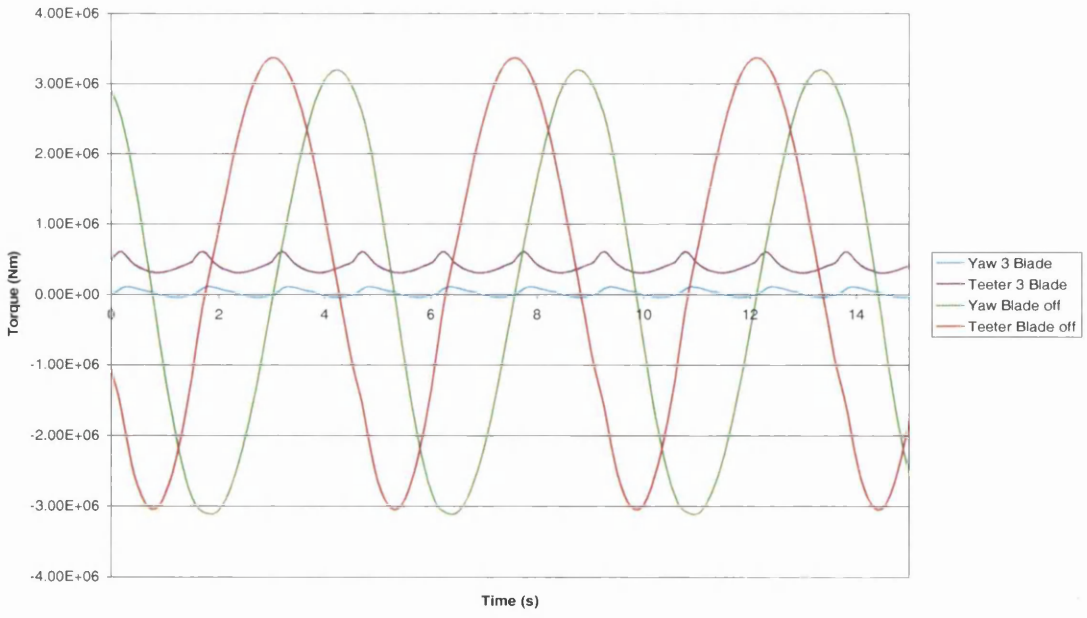

Figure 5.3: Yaw and teeter moments about hub centre for a three bladed rotor compared to the same design with one blade missing.

5.2 Free yawing model

As a further addition to the model, a yaw control facility was developed. A yaw model reads in the rotor hydrodynamic loads or flow data and calculates the system's updated azimuth position and speed, this then forms part of the modelling procedure shown in figure 3.18. To demonstrate this ability a free yawing system model was developed. It would be relatively trivial to replace this with an active yaw model in the code. This free yaw model allows the system to pivot around its yaw centre so that the hydrodynamic loads of the system find an equilibrium yaw position in any given flow.

5.2.1 Modelling parameters

As the nacelle and tail spinner or nose cone are now able to move, they have an associated rotational velocity (Ω_{yaw}) and acceleration ($\dot{\Omega}_{yaw}$) about the yaw axis. These rotational values can be used to calculate the linear velocity and acceleration of nacelle and tail spinner elements by multiplying the rotational values by the radial position ($r_{yaw\ elem}$) of the element from the yaw centre.

Once these accelerations and velocities are known, it is possible to calculate a relative fluid velocity and acceleration for each nacelle and tail spinner or nose cone element. This is achieved by subtraction of the local body velocity and acceleration from the local fluid velocity and acceleration. This is displayed in (5.2) for resulting local side velocity and (5.3) for resulting side fluid acceleration.

$$u_{elem} = u_{flow} - r_{yaw\ elem}\Omega_{yaw} \qquad \ldots (5.2)$$

$$\frac{du_{elem}}{dt} = \frac{du_{flow}}{dt} - r_{yaw\ elem}\dot{\Omega}_{yaw} \qquad \ldots (5.3)$$

These velocity and acceleration values are then used in the Morison's equation formulae (see Chapter 3) to calculate loads on each tail spinner or nosecone and nacelle element. These loads are then summed and the resulting moment about the yaw centre can be calculated for the nacelle (M_{Nac}) and nose cone (M_{Nose}). These can then be fed into a moment balance equation together with bearing friction torque ($M_{Bearing}$), rotor yawing moment (M_{Rot_Yaw}) and the moment resulting from rotor sway loads ($F_{Rot\_side} \times X_{Hub\_to\_yaw}$). F_{Rot_side} is the rotor sway (side) load and $X_{Hub\_to\_yaw}$ is the distance from rotor hub centre to yaw centre.

The bearing friction model must be based on a specific design of yaw mechanism. For a typical free yawing model, the radial and thrust loads from the whole system, including hydrodynamic (calculated for each time-step), weight and buoyancy loads (which are calculated and input by the operator) are resolved to the yaw bearings (radius and position are defined for each specific design). Using a friction coefficient and bearing contact radius (again user defined), a resistive torque is calculated. When all these loads are known, they may be resolved into a sum of moments around the yaw centre using (5.4):

$$\sum M_{ZN} = M_{Nac} + M_{Nose} + M_{Rot\_Yaw} - F_{Rot\_side} \times X_{Hub\_to\_yaw} - M_{Bearing} \times sign(\Omega_{yaw}) \quad \ldots (5.4)$$

If the yaw friction is greater than the sum of other moments and the yaw velocity is small, the frictional torque will allow the system to come to rest but would not reverse the yaw velocity. To account for this, a logical condition statement (5.5) is included in the code which calculates the new yaw position using half of the previous yaw velocity (the average for that time step) and sets the new yaw velocity and acceleration to zero for the following time step.

$$
\begin{aligned}
&if\ \text{abs}(M_{Nac} + M_{Nose} + M_{Rot\_Yaw} - F_{Rot\_side} \times X_{Hub\_to\_yaw}) \leq abs(M_{Bearing}) \\
&and\ abs(\Omega^i) < 0.001 \\
&\dot{\Omega}_{Yaw}^{i+1} = -\frac{\Omega^i}{dt} \\
&\Omega_{Yaw}^{i+1} = 0 \\
&else \\
&\dot{\Omega}_{Yaw}^{i+1} = \frac{\sum M_{ZN}}{I_{Yaw}} \\
&\Omega_{Yaw}^{i+1} = \Omega_{Yaw}^{i} + \dot{\Omega}_{Yaw}^{i+1} dt
\end{aligned}
$$

... (5.5)

In this case, i represents the present time step.

5.2.2 Calculation of yaw acceleration

A straightforward approach may be adopted to model the yaw acceleration and hence update the yaw velocity at each time step. $\sum M_{ZN}$ can be used as a resultant torque to calculate yaw acceleration, which is then employed to update the yaw velocity and position for the following time step as shown in (5.5). For this, I_{Yaw}, the yaw moment of inertia, must be calculated for a specific turbine design and used as an input to the model.

Using the calculated acceleration directly leads to an unsteady model, the assumption that the acceleration is constant throughout the time step produces an overestimation of the yaw velocity for the following step. At the following time step the resistive loads are therefore over-predicted leading to a large deceleration force. This results in an unstable, divergent model. To correct the instability a successive over relaxation approach (SOR) was adopted, this effectively gives a weighted average of acceleration using the previous acceleration value and the predicted acceleration for the following step to create a smoothed value. The SOR algorithm is widely reported [1] and is presented here in (5.6).

$$\dot{\Omega}^{i+1}_{Yaw\_SOR} = \dot{\Omega}^{i+1}_{Yaw} \times \omega + (1-\omega)\dot{\Omega}^{i}_{Yaw} \quad \ldots (5.6)$$

In this equation, ω is known as the extrapolation factor. A value of 0.5 is found to create a steady system in the present application. Using this relaxed acceleration instead of the instantaneous acceleration in the load calculations for the following time step avoids the previous instability in the model.

5.2.3 Sample case

To demonstrate the function of the free-yawing model, a test case was run with the nacelle initially yawed at 30° to a power law flow with a regular wave. The yaw position is shown in figure 5.4 where it can be seen that the system quickly reaches an equilibrium state with small oscillations after an initial overshoot of the equilibrium position. The equilibrium position is non-zero for several reasons; the sway load produced by a rotor operating in a boundary layer flow is non-zero as the blades experience a higher flow in the top region (travelling in one direction) than on their return through the lower region. Tower shadow effects add to this sway load. Even if this sway load was not present, a zero yaw error would not exist with this free-yawing model as bearing friction will prevent the system yawing to the completely aligned position and would instead come to rest close to where the nacelle side loads balance with this bearing friction. It is worth noting at this point that the overshoot is due to the high starting yaw misalignment and that this is unlikely to occur in true life situations where tide speed increases gradually and will yaw the turbine slowly to a small yaw misalignment. The case studied here would only occur if the yaw bearing was to seize in the starting yaw position then suddenly become free.

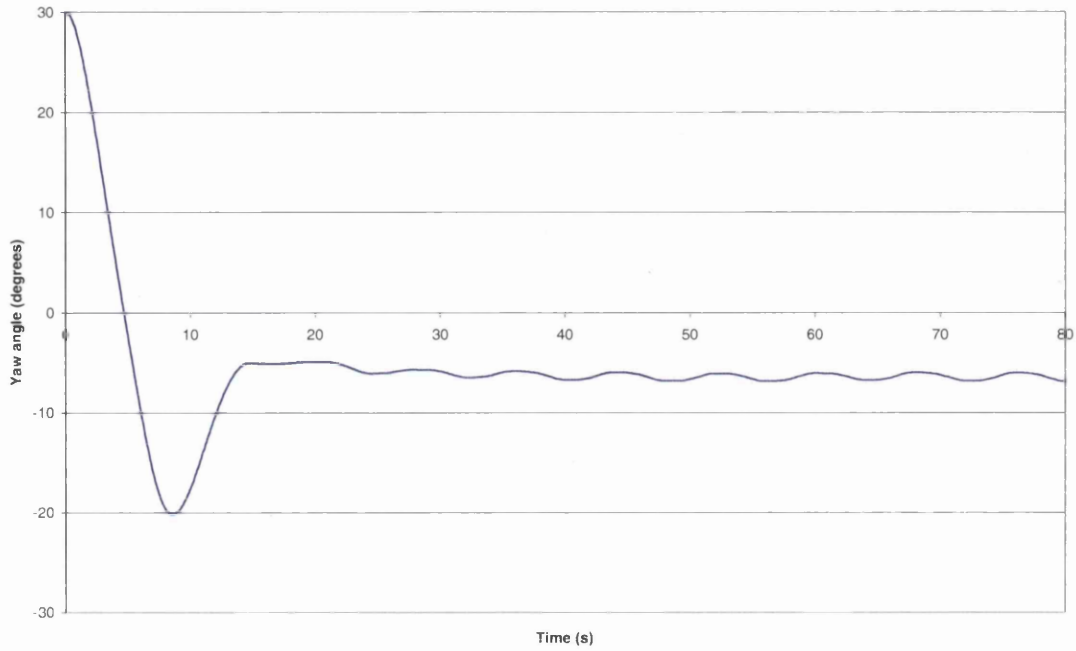

Figure 5.4: Yaw position of rotor in free yaw model run.

Figure 5.5 shows the yaw velocity of the rotor system, it can be clearly seen in this plot that there are regular time intervals where the yaw velocity is zero due to the bearing friction limit not being exceeded by the yawing moments.

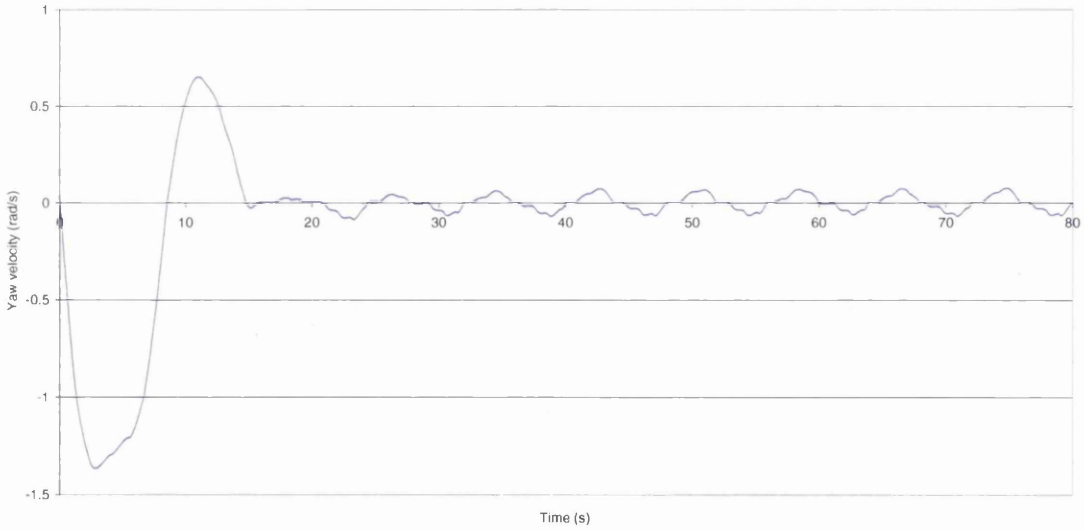

Figure 5.5: Yaw Velocities of the rotor system in free yaw model run.

Figure 5.6 gives the yaw acceleration of the system, spikes of acceleration exist but with the successive over relaxation method applied, these spikes are stabilised by the system rather than being allowed to grow in an unsteady and unrealistic fashion.

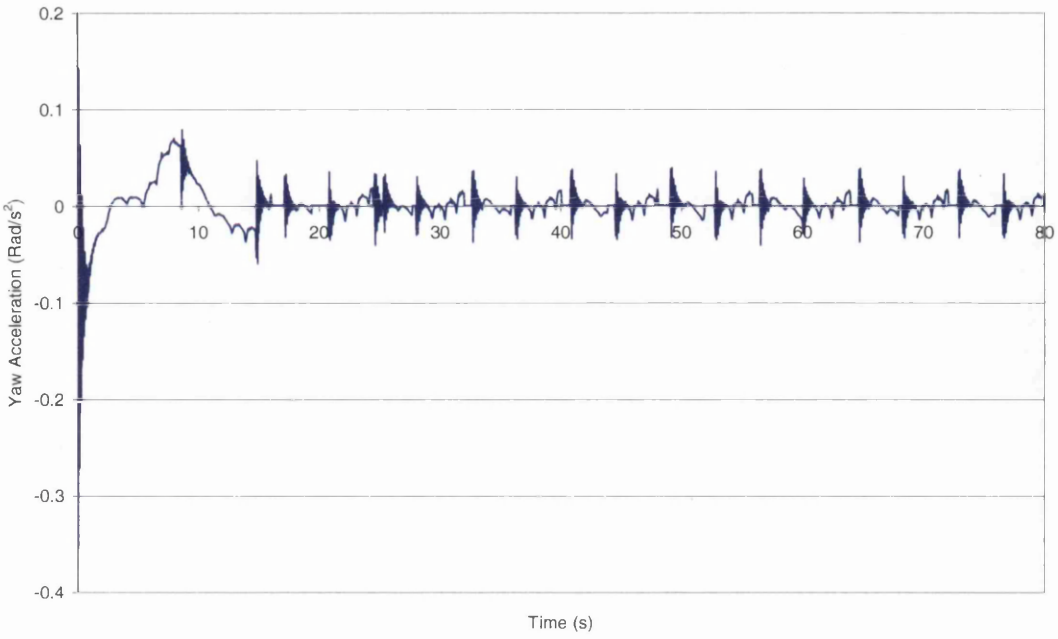

Figure 5.6: Yaw acceleration for the rotor system in free yaw model run.

Figure 5.7 shows a breakdown of yawing moments for the rotor system. The magnitude of bearing friction is shown in this plot. Bearing friction will always act in the opposite direction to yaw velocity or in the opposite direction to the sum of all other moments when the yaw system is stationary. It can be seen from this break down that, for this specific example, all moments are of a similar magnitude but that bearing friction and rotor sway moment are the largest contributors to the yawing motion. The small, high frequency oscillations in nacelle and tail spinner moments are primarily due to the oscillation in yaw acceleration. The oscillation can be reduced by employing increasingly smaller time steps or a smaller extrapolation factor on the SOR, this oscillation is not a major concern however as the resulting yaw behaviour is not highly sensitive to these small, high frequency variations. These oscillations should be filtered before defining fatigue loads.

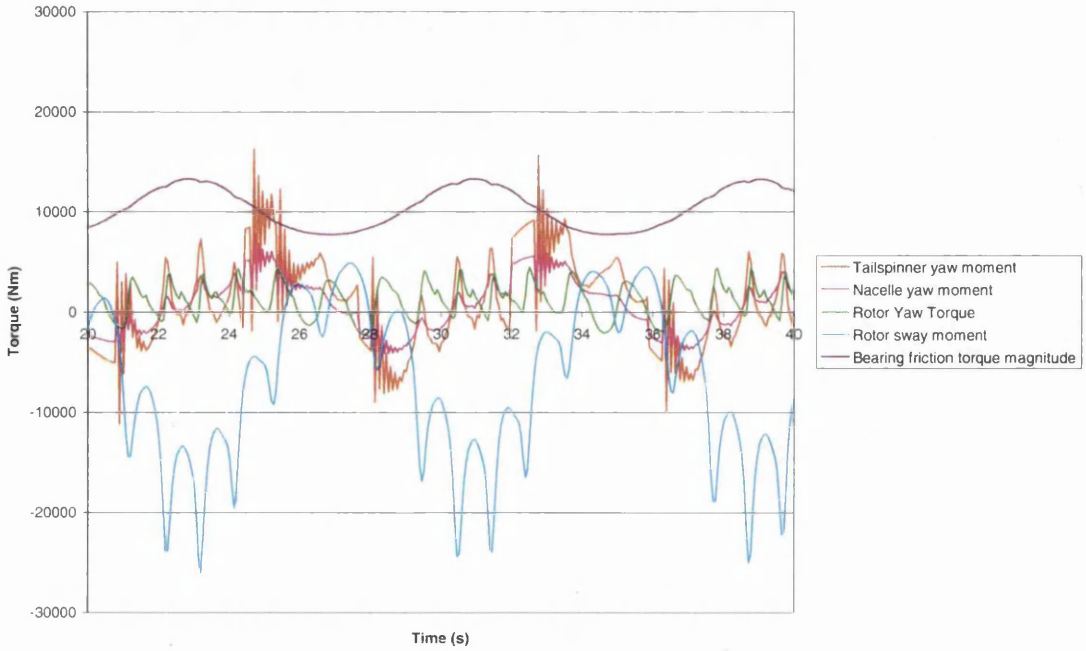

Figure 5.7: Components of yaw moments for rotor system in free yaw model run.

Figure 5.8 shows the net yaw torque acting on the system, the oscillations of the tail spinner and nacelle can be seen clearly, at the shorter time scale it is possible to see that these impulses occur as the yaw torque increases to a level that overcomes the system's static friction. Once this static friction is overcome, the system accelerates and due to the size of the time step, an overshoot in acceleration is seen, giving the first spike in yawing torque. This is then controlled by the SOR approach. Using this approach is preferable to shortening the time step as this would lead to a very slow model.

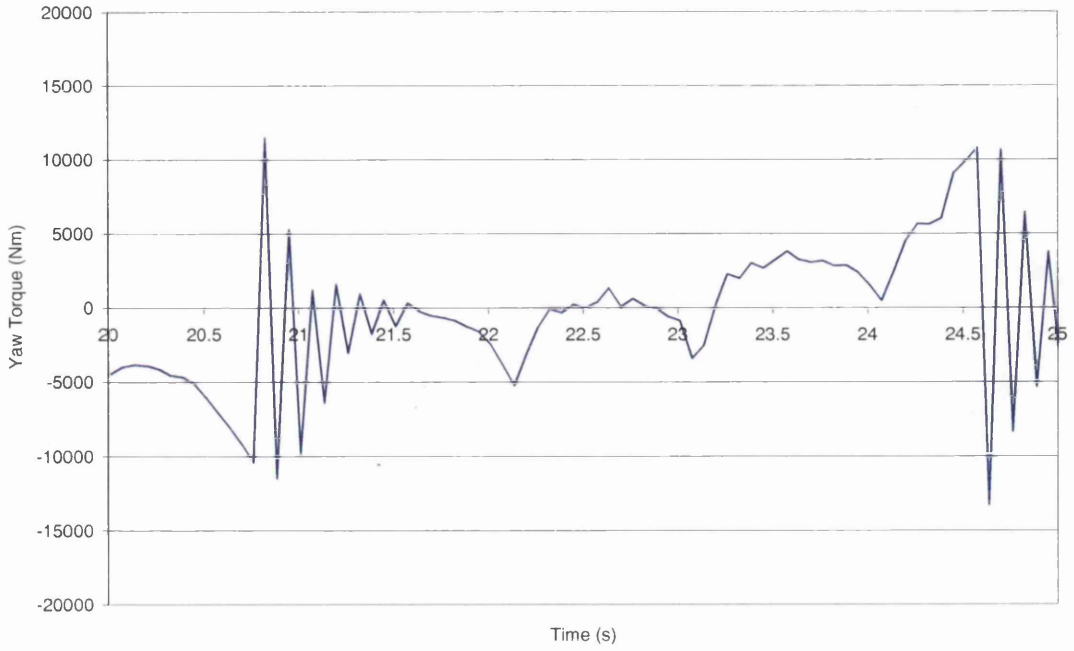

Figure 5.8: Total yawing torque for rotor system in free yaw model run.

5.3 Generator models

A generator model may read in the rotor hydrodynamic loads and calculate the rotor's updated position and speed to be calculated, this then forms part of the modelling procedure shown earlier in figure 3.18. A simple model for modelling generator torque was developed by Orme [2] which used a target *TSR* and corresponding power coefficient to calculate the desired load to keep the rotor operating close to the target *TSR* in an over speed controlled device. The formula is displayed in (5.7) and is effectively a rearrangement of the definition for power coefficient to give a torque load with the target *TSR* used to give an equivalent inflow velocity.

$$T_{Gen} = C_{P\text{target}} \frac{1}{2\Omega} \rho \pi R^2 \left(\frac{\Omega R}{TSR_{\text{target}}}\right)^3 \quad \ldots (5.7)$$

Although this implies a rudimentary control system, this does not accurately model any 'real life' control and generator system. This control will also only

work for rotors in over speed. Running in over speed, the turbine system has a natural level of control because, as rotational speed increases, rotor torque reduces and vice versa. This means that a constant generator load may be applied and the system will self-regulate. For simple comparisons, a fixed rotational speed model is also incorporated into the code. A set rotational speed is defined for the system, which is unrealistic as any real control system will have some degree of 'slip' involved [3]. This fixed rotational speed model is very useful for direct comparisons however.

A facility was added to the code to allow a system specific control module to be employed. An example model was developed by N. Lawrence in Excel [4], which has been translated into a Matlab script. The sample control system incorporates a loading model based on the electrical properties of the generator and a logic based, time filtered control system. The control system uses calculated voltage and electrical current values of the generator to approximate torque and rotational speed of the turbine. Load resistance is then varied to control the turbine to run at target *TSR*. The friction in the shaft bearings is also modelled, this part of the script was based on work by T. Oakes [5] and is a more complex calculation than that assumed by Lawrence. The friction is added to the generator load to give an overall resistive torque of the system. With a reasonable length time filter in place, the example control system effectively provides a constant generator resistance for a set flow speed and wave type and will only change if the mean flow speed alters. This allows the system to speed up or slow down slightly with wave variations if the system is operated in the over speed region. Switching loads for transient changes in wave velocity is avoided as frequent generator load switching would lead to wear problems in electrical and mechanical systems.

Figure 5.9 displays the rotational speed of the blade system in a 3m/s free stream, power law flow with a 2.3m wave. The three different control systems are displayed, the fixed speed control can be seen to keep the rotational speed exactly constant whereas the basic control system allows for an oscillation in rotational speed with wave variation, keeping close to a fixed

TSR as flow speed varies. The developed model is initially greatly different to the other models, this is the period when the filter is inoperative and the system reverts to a low generator load. Once the filter has a sufficient buffer, a load closer to the target is switched to. At this stage, the oscillation in rotational speed is larger than the basic model, this is due to a fixed loading being used rather than one that varies with inflow speed as in the basic model. There is one final small step change in generator load before the system becomes steady.

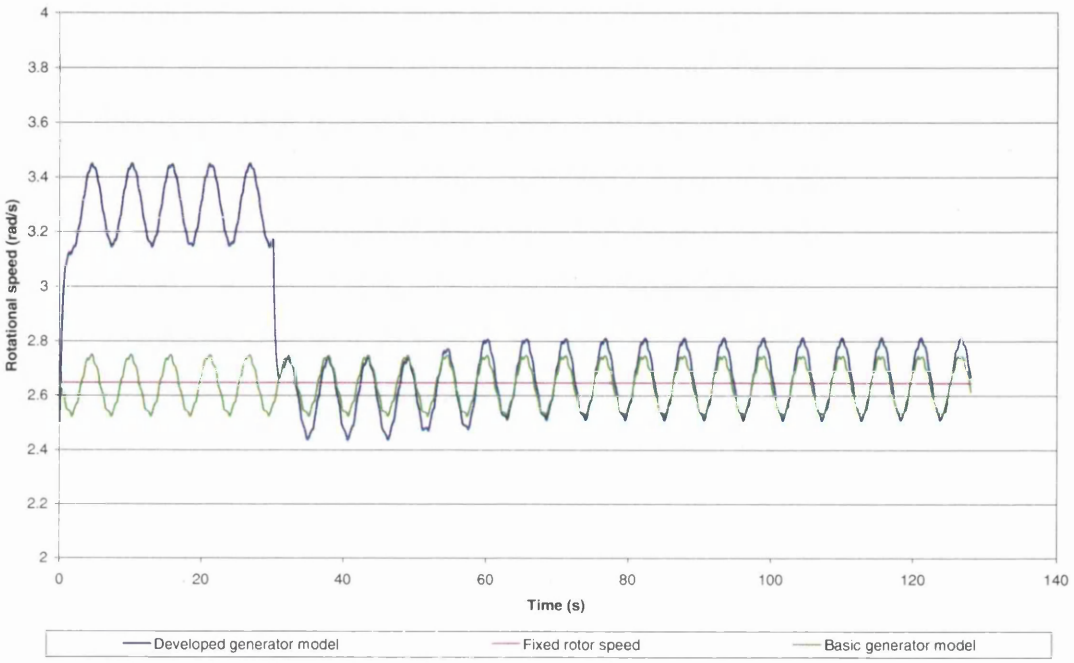

Figure 5.9: Comparison of turbine rotational speed in a 3m/s free stream power law flow with 2.3m, 5.55s wave using different control models.

Figure 5.10 shows the rotor torque produced in the same runs as displayed in figure 5.9. The fixed rotor speed model can be seen to give higher load oscillations than the other two models that display little disagreement between one another once the developed generator's model has enough time-averaged data for its filter to operate. It is important to note that, during normal operation, flow speed will generally increase very gradually and so the filter would have time to fill its buffer and select an appropriate load without the step effect seen from imposing a relatively high flow speed at the initial operation stage. These plots clearly show that the control system

being employed can have a significant effect on the loadings being produced by the rotor system, making the facility for user defined generator models vital for accurate modelling of system designs. The inclusion of generator modelling therefore shows a large step towards realistic operational load characterisation.

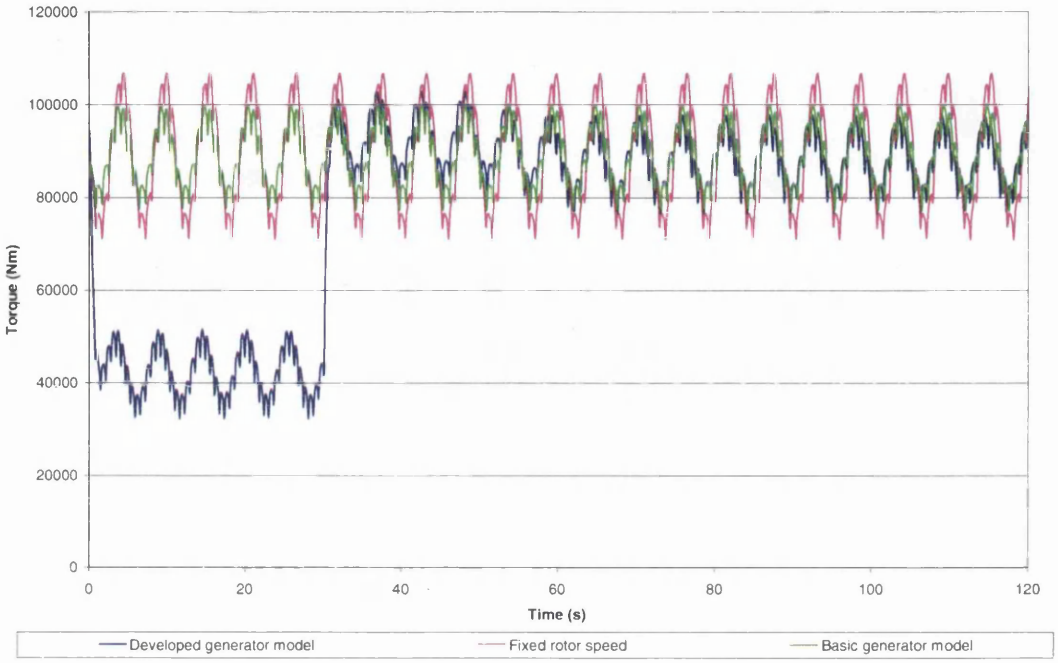

Figure 5.10: Torque produced by rotor in a 3m/s free stream power law flow with 2.3m, 5.55s wave using different generator models.

5.4 Brake model

A specific case of interest to design engineers will be the system shutdown scenario. To investigate the loadings produced during such an operation the generator model must be replaced by a brake model. This model must incorporate variation of braking load over time as well as rotational inertia of the system. In the braking scenario presented here, all loading from the generator is removed before the braking system is applied. A linear lead-in of braking torque is assumed over a defined time up to a maximum defined braking torque. The most interesting case to investigate is the braking of a system that has been allowed to run into over speed (Past peak C_T). This means that the hydrodynamic torque coefficient will increase as the rotational speed of the system reduces (see figure 4.15 for C_T variation with *TSR*) and the brake must exceed peak rotor torque to be able to stop the device.

The addition of a braking model to the code is facilitated by the modular structure of the code. A flag was added to the input script to act as a switch for the braking model. Also defined in the input script is a variable for peak braking torque, a time during the run at which the brake starts and the lead-in time needed for the braking system to reach maximum braking torque. At the defined time- step, the generator load is then replaced with a calculated brake load. The model uses this load to calculate rotor acceleration and rotational speed for the following time step. The brake load is updated at each time step using the specified linear ramp data.

To demonstrate the function of the braking system model, a run was conducted in a uniform flow, the system was allowed to reach a steady state before the brake was applied. Figure 5.11 shows the rotational speed of the rotor system. The rapid jump in rotational speed as the generator load is removed is apparent. Following this jump is a gradual reduction in rotor speed as the brake ramps up to full power. A sudden drop off in rotor speed is then witnessed, this occurs when the peak C_T value is passed, at this point

the torque produced by the rotor blades rapidly decreases whilst the braking torque supplied continues to increase towards its maximum value.

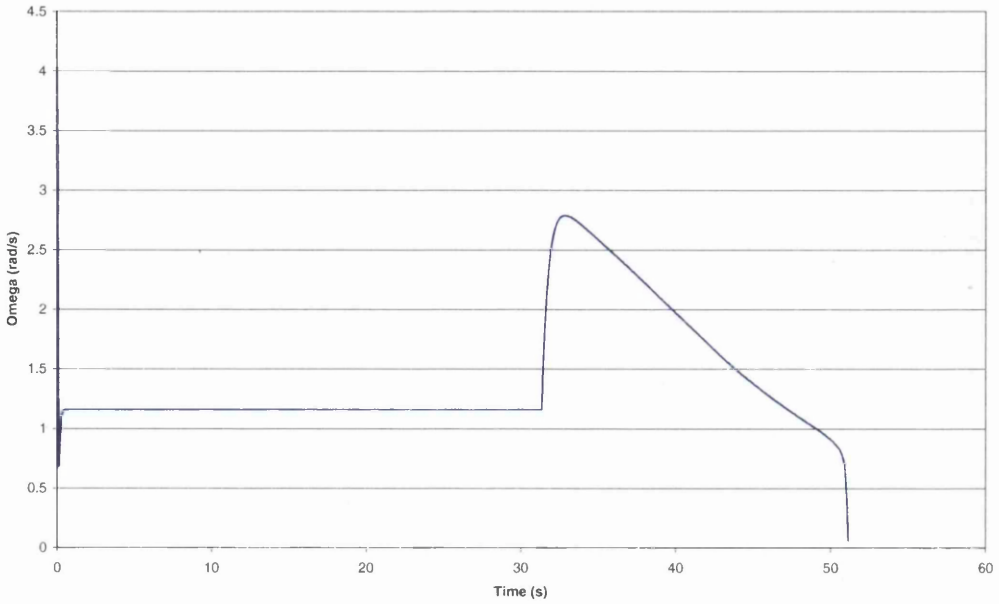

Figure 5.11: Rotational speed of turbine system during braking in a 4m/s uniform flow.

Figure 5.12 shows the torque supplied by the brake and the torque produced by the rotor system. Initially the rotor torque drops significantly as the rotor speeds up towards the zero torque brake state. As the torque value of the brake ramps up, the rotor and brake torque become matched (a characteristic of operation at over speed) until the aforementioned peak C_T point is reached and rotor torque trails off rapidly.

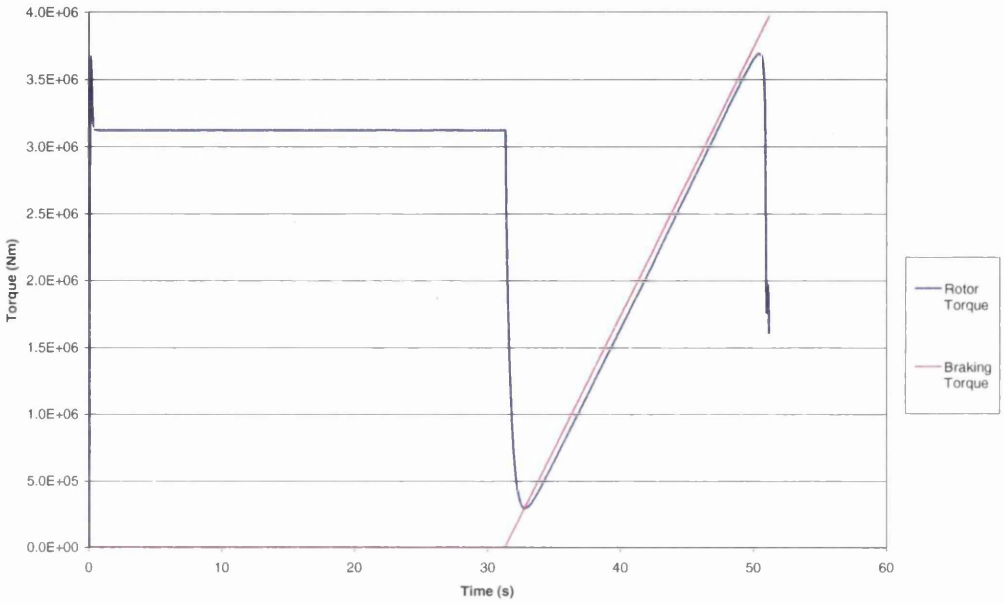

Figure 5.12: Rotor torque and braking torque of system during braking in a 4m/s uniform flow.

Figure 5.13 shows that, for the demonstration rotor design, axial force loading is unlikely to cause significant problems during this braking operation apart from the rapid initial variation in axial load. The power produced during braking presents a vital piece of data for design engineers. The area under the power curve during the braking period represents the work done by the braking system, in this case the value is approximately 56MJ, this will be dissipated as heat and it is important that the components in the system are able to withstand this heating effect.

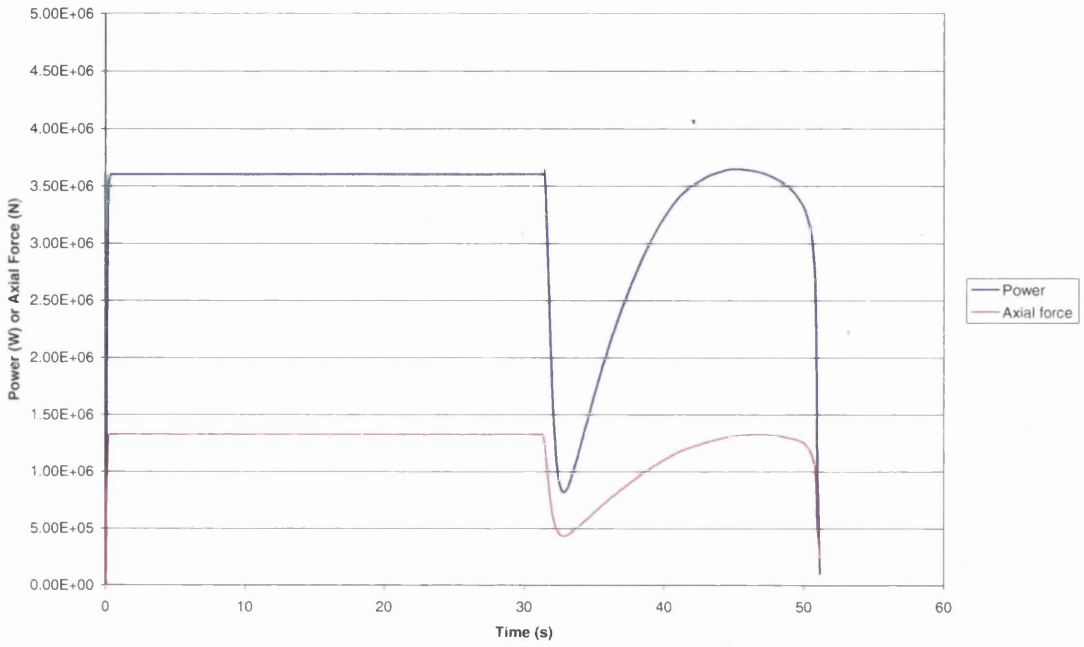

Figure 5.13: Rotor Power and axial load during braking in a 4m/s uniform flow.

Figure 5.14 shows the same system in the same underlying flow but with wave action. In this case, the wave action aids the braking system as, although the wave increases mean flow power, it also provides periods of lower flow speeds that enable the brake to overcome the peak torque coefficient at a lower torque value. The wave selected for this demonstration was an extreme wave, in normal operational conditions it is unlikely such a large wave would be experienced (even as a 50 year return wave) but this wave was used to clearly demonstrate the effects that waves have on the braking requirements.

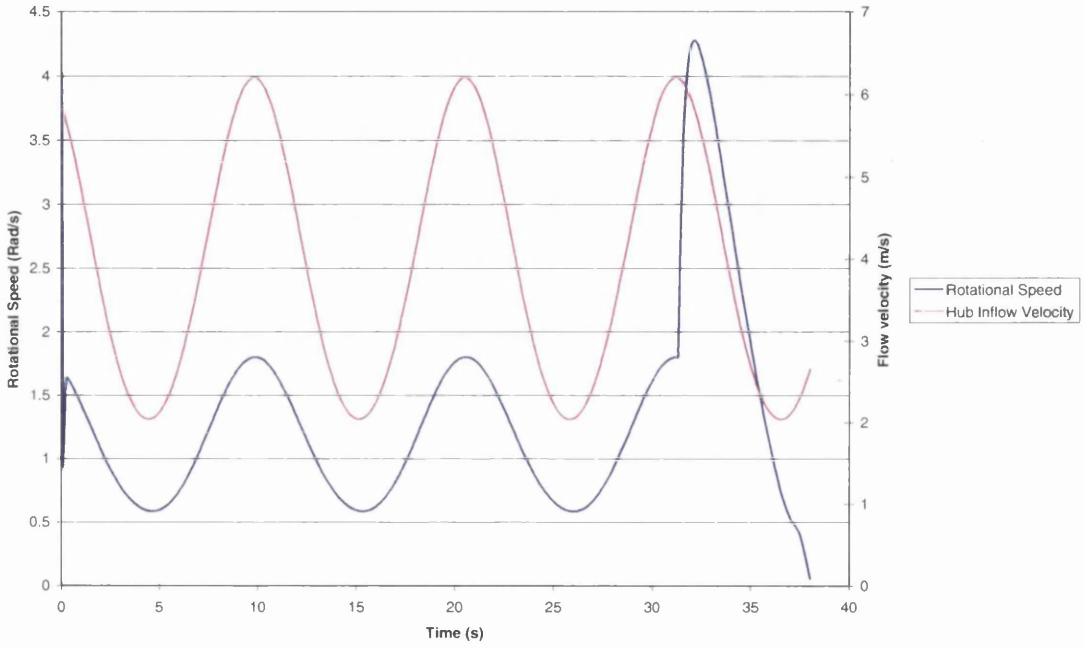

Figure 5.14: Rotational speed and hub inflow velocity in an extreme 4m/s free stream flow with 11.7m, 10.7s wave during braking.

Figure 5.15 is another plot from the wave run giving rotor and braking torque. It demonstrates that, although the peak torque during operation is greatly increased by the large wave, the braking torque required to stop the system is significantly reduced. If this type of wave were employed as a design case, it would be the brake's ability to hold the blades stationary at peak flow velocity rather than the braking system's ability to stop the rotor. For the case given here, the braking torque required to do this would be approximately 3.3MNm, a factor of 3 greater than the braking torque required to halt the system.

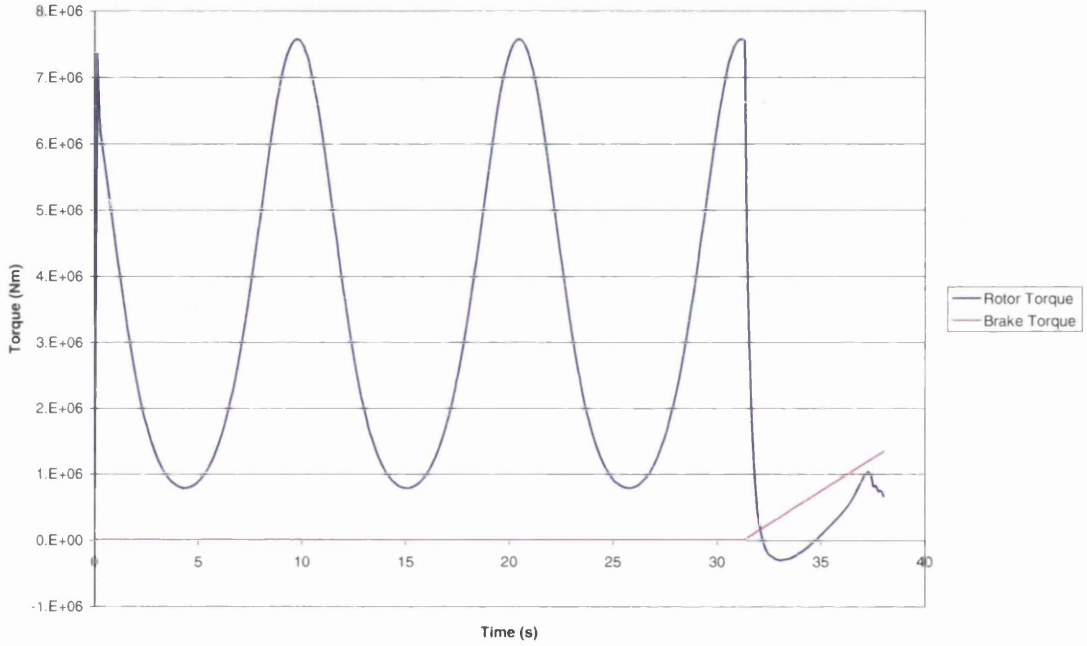

Figure 5.15: Rotor torque and brake torque during braking in a flow with an extreme 4m/s free stream flow with 11.7m, 10.7s wave during braking.

The behaviour of the system during the brake run is summarised in table 5.1.

Time	Event	Torque
0s	Model is started and left to reach a steady state.	0 to 3.67MNm
2s	Steady state operation reached.	3.12MNm
31.3s	Generator fails, brake lead in begins.	3.12MNm
31.3s-32.9s	Rotor speeds up and approaches propeller brake state. Braking torque increases linearly.	3.12MNm-0.9MNm
32.9-50.5s	Braking torque reduces rotor speed, increasing C_T.	0.9MNm-3.7MNm
50.5s	Applied braking torque exceeds maximum rotor torque.	3.7MNm
50.5s-51.2s	Rotor speed drops rapidly until stationary.	3.7MNm-1.6MNm

Table 5.1: Summary of brake run results describing each stage of the variation.

5.5 Tower shadow model

5.5.1 Introduction

The tower of a tidal stream turbine will interact with the rotor blades in a similar way to the tower and blades of a wind turbine. There has been a large amount of research into tower shadow effects in the wind industry, which can be drawn upon.

There are two main cases for tower effects, these depend on whether the rotor blades are upstream or downstream of the tower. If the blades are upstream of the tower, the impact of tower shadow is far smaller than in the downstream case. The upstream blades will experience tower effects as a slight reduction in the local fluid velocity in line with the tower and a slight increase of the fluid velocity around the sides of the tower. A similar but far larger velocity variation is seen for the downstream rotor case due to the wake of the tower. As well as this impact on velocity, the tower will increase turbulence in the downstream fluid and introduce additional unsteady effects due to vortex shedding from the tower [6]. Wang and Coton [6] state that the turbulence and vortex shedding effects are less significant than the local velocity deficit.

The tower shadow leads to a number of challenges for system design and operation. The fluid velocity varies over a small azimuth rotation, this leads to rapid variations in effective blade angle of attack, which in turn will produce a high frequency oscillatory load on the blade. For wind turbines, it has been stated that, for downwind systems, tower shadow can produce a fluctuation in torque of 10% of peak torque [7]. It is expected that the effect on tidal stream turbines will be more significant than wind turbines as the tower is likely to be larger in proportion to rotor diameter and suffer from bio fouling and corrosion, causing a larger flow disturbance. This will influence the fatigue life of the rotor blade and can lead to a flicker effect in power generated [8]. Each blade will pass through the wake of the tower once per revolution, it will experience a slight increase in fluid speed, followed by a

more significant decrease then a slight increase again as the blade passes through the shadow region. There is a significant amount of research available on tower shadow wakes for wind turbines, the existing literature will be reviewed in the following section.

5.5.2 Existing Tower Shadow Research

Wang and Coton [6] use a prescribed wake vortex model combined with a near wake dynamic model of the vorticity trailed from the blade and a semi-empirical tower-shadow velocity deficit model. This approach is said to give a high-resolution result for downstream rotors. The implementation of the model is more complex than the BEMT approach but the velocity deficit model is relatively simple. The deficit model requires local blade radius and azimuth position to calculate the wake profile. This arrangement does not lend itself to incorporation into the developed model as it cannot be directly applied to the mapping procedure, it could however be rearranged to yield an equation for dimensionless distances from the tower centre which would be suitable. Lifting line theory models such as this could be considered for a more complex model in the future.

Maalawi and Badr [9] present the same wake model as Wang and Coton and cite Thresher [10] for this correction. There is little additional discussion of the deficit model in this paper and the majority of the work is concerned with the selection of an optimal blade profile. The correction as presented by Maalawi and Badr [9] is repeated below in (5.8) to (5.10).

$$B(\psi) = 1 - T_s(\psi) \text{ for } (\pi - \psi_0) \leq \psi \leq (\pi + \psi_0) \quad \ldots (5.8)$$

Otherwise

$$B(\psi) = 1 \quad \ldots (5.9)$$

$B(\psi)$ is known as the tower shadow blockage factor and is multiplied by the free flow velocity to give an estimation of the flow velocity including tower blockage effects. ψ_0 is the tower shadow half angle and T_s is the tower shadow coefficient, which for a cylindrical mono-pile is:

$$T_s(\psi) = \frac{A_s}{2}[1 + \cos\frac{\pi}{\psi_0}(\psi - \pi)] \ldots (5.10)$$

The tower shadow is represented by a $2\psi_0$ angular sector of the rotor plane centred at $\psi = \pi$ (with the rotor blade pointing straight down in the coordinate system used in the paper) for the maximum decrease in velocity, represented by the factor A_s. A_s is not defined in the paper and so would have to be defined from an empirical relationship or alternative source. ψ_0 and A_s would need to vary with both distance from tower centre and local blade radius to give a realistic model. The use of this correction is limited to downwind turbines only. This is an empirical shadow model and several variations of this set of equations are presented in other papers, some examples of these will be shown.

Powles [11] presents a similar tower shadow model to (5.10), this is displayed in (5.11). The principal of this equation is the same as that presented in Maalawi and Badr with the advantage that, in Powles' paper, a variety of test data is provided so that suitable empirical variables may be substituted into the equation if a similar tower to that tested in the paper is employed.

$$S(\theta, x) = 1 - D\cos^2(\frac{\pi}{2W} x_p \sin\psi \cos\beta)$$

... (5.11)

Where

$x_p = r / R$ fractional distance along blade span

ψ = rotational position, β = cone angle,

D = wake depth, W = Wake width

This system still relies on the selection of suitable empirical data and an expected increase in velocity at the edges of the tower wake is not incorporated. The significance of this velocity increase may not be great however. The equation again only models the wake downstream of a tower.

Hansen [12] suggests the use of a potential flow model for tower shadow modelling effects using a source-sink doublet. The background to potential flow theory is described in Massey [13] amongst other texts. A diagram of the streamlines in such a flow as well as a representation of the nomenclature used by Hansen [12] is reproduced in Figure 5.16.

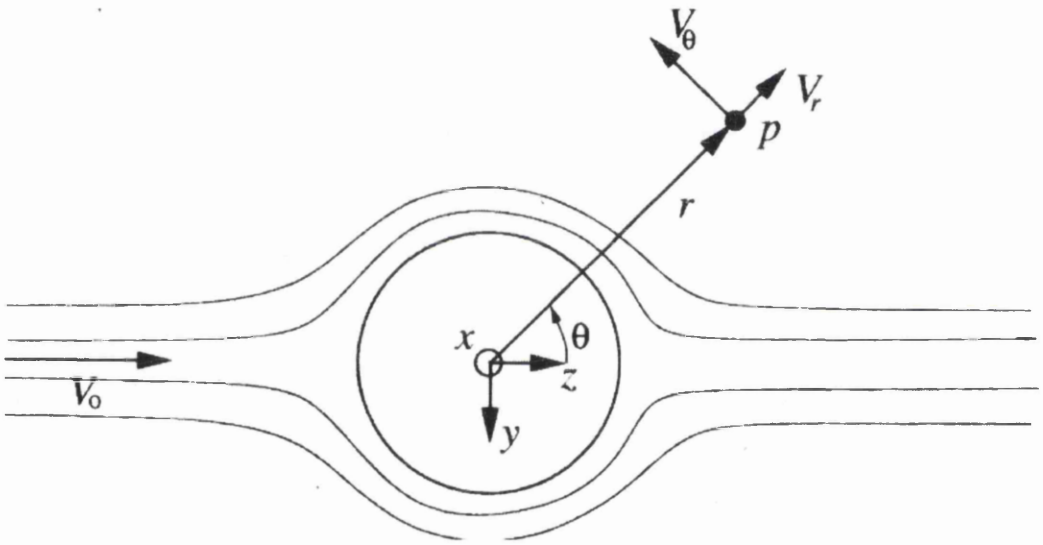

Figure 5.16: Potential flow model for a tower (Hansen [12]).

The potential flow is described initially in terms of polar coordinates ((5.12) and (5.13)).

$$V_r = V_0(1-\left(\frac{a}{r}\right)^2)\cos\theta \qquad \ldots (5.12)$$

$$V_\theta = -V_0(1+\left(\frac{a}{r}\right)^2)\sin\theta \qquad \ldots (5.13)$$

These equations are then resolved into the *z*, *y* coordinate system and aligned with the oncoming flow giving (5.14) and (5.15). a is not displayed in the diagram of figure 5.16 but denotes the radius of the tower in this case.

$$V_z = V_r \frac{z}{r} - V_\theta (-\frac{y}{r}) \quad \ldots (5.14)$$

$$V_y = V_r (\frac{y}{r}) - V_\theta \frac{z}{r} \quad \ldots (5.15)$$

After presenting these formulae, Hansen proceeds with a warning that the potential flow solution is a bad approximation of the tower shadow effect for a downstream rotor system. This is because the potential flow model does not predict flow separation so would only be valid downstream for very low Reynolds number flows. The approach would appear to provide a sufficient model for an upwind device.

In Burton [14], the potential flow solution is again recommended for the modelling of upstream rotor systems but its inability to model downstream tower shadow is again commented upon. An empirical cosine model is presented to approximate the downstream flow. The empirical model is of a similar form to Powles [11] and Thresher [10] and requires a width of the wake deficit region to be defined. The slight increase in flow speed either side of the wake region is neglected in this model.

Yoshida and Kiyoki [15] report excessive load variations using an isolated tower wake model and proceed to propose an improved model that corrects the wake using results from a three-dimensional rotor and tower CFD model for a downstream wind turbine (see Figure 5.17). Their research is based on a 2MW downwind wind turbine with a tower at $Re \approx 2.6 \times 10^6$ and a drag coefficient of 0.36. The tower is 2.5m in diameter, leading to this more analogous Re value than Powles [11], the cylinder is smooth in this case

however. Yoshida and Kiyoki's model is shown to predict far smaller and more diffuse variations in performance as the blade passes through the tower shadow. The reduction in variation is attributed to the blade and tower interaction, this appears logical as the rotor blade will tend to disrupt the wake of the tower, dispersing the tower wake. This would create a wake quite different to that of an isolated tower. The resources to conduct a similar correction procedure are not available at present as a complex CFD model of both tower and blades would be required.

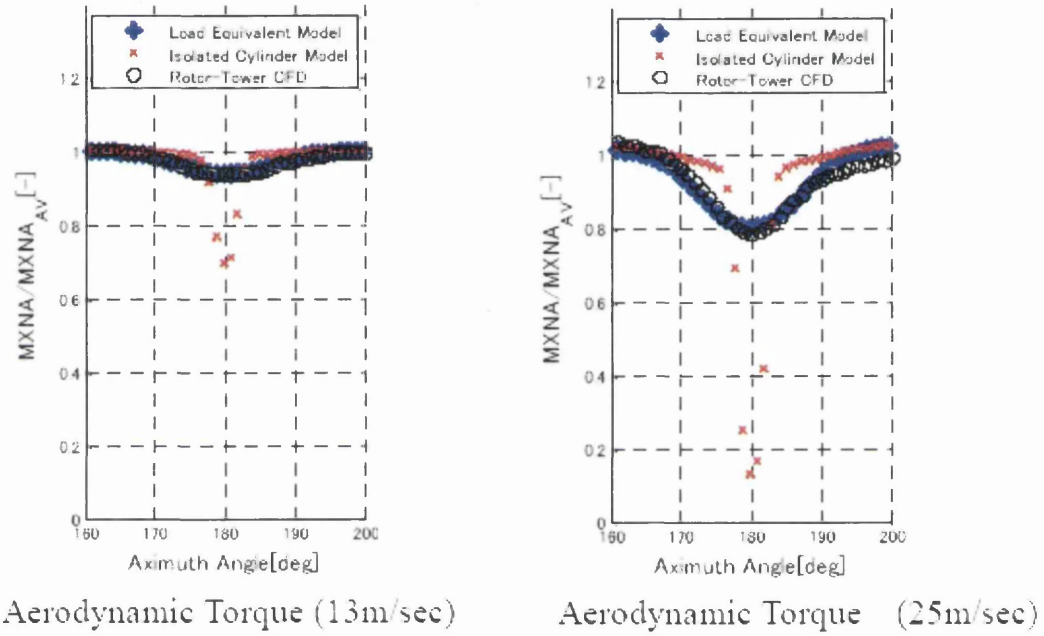

Figure 5.17: Predicted rotational torque (M_{XN}) by Yoshida and Kiyoki [15] for a downstream wind turbine.

The AeroDyn theory manual [16] provides a promising approach to tower shadow modelling. A potential flow based solution around a cylinder by Bak *et al.* [17] is used as the base flow field near the tower and is coupled with an empirical downstream wake model for flow effects downstream of the tower.

The equations for the influence of the wake on the nearby velocity field are shown in (5.16) and (5.17). These equations are adjustments of the potential flow formula and were proposed by Bak *et al.* [17] to account for the influence of cylinder drag. The intended operating range for these formulae

is $1\times10^6 < \mathrm{Re} < 3\times10^6$. The 0.1 value is present to calibrate the solution with a more complex model by Parkinson and Jandali [18].

$$u = 1 - \frac{(x+0.1)^2 - y^2}{((x+0.1)^2 + y^2)^2} + \frac{C_D}{2\pi}\frac{x+0.1}{(x+0.1)^2 + y^2} \quad \ldots (5.16)$$

$$v = 2\frac{(x+0.1)y}{((x+0.1)^2 + y^2)^2} + \frac{C_D}{2\pi}\frac{y}{(x+0.1)^2 + y^2} \quad \ldots (5.17)$$

Where u and v are components of horizontal inflow in the x and y direction normalised by the free stream horizontal flow speed at the point of interest. x and y are in-stream and cross-stream distances from the tower centre normalized by tower radius. C_D should be specified for each particular case and has a significant impact on the resulting shadow model, this will be discussed in a following section. Equations (5.16) and (5.17) are used directly as the upstream tower dam effect on the rotor blades for an upstream device.

For downstream rotor modelling, the tower influence is modelled with an additional tower wake model based on Powles [11], this wake factor algorithm is repeated here in (5.18) to (5.20).

$$u_{wake} = \frac{C_D}{\sqrt{d}}\cos^2\left(\frac{\pi}{2}\frac{y}{\sqrt{d}}\right) \text{ for } |y| \le \sqrt{d} \quad \ldots (5.18)$$

$$u_{wake} = 0 \text{ for } |y| > \sqrt{d} \quad \ldots (5.19)$$

Where

$$d = \sqrt{x^2 + y^2} \quad \ldots (5.20)$$

d is the dimensionless radial distance of the point from tower centre. Fig 5.18 by Moriarty and Hansen [16] illustrates these dimensions. For consistency in the u_{wake} equation, d is normalised by the tower section radius.

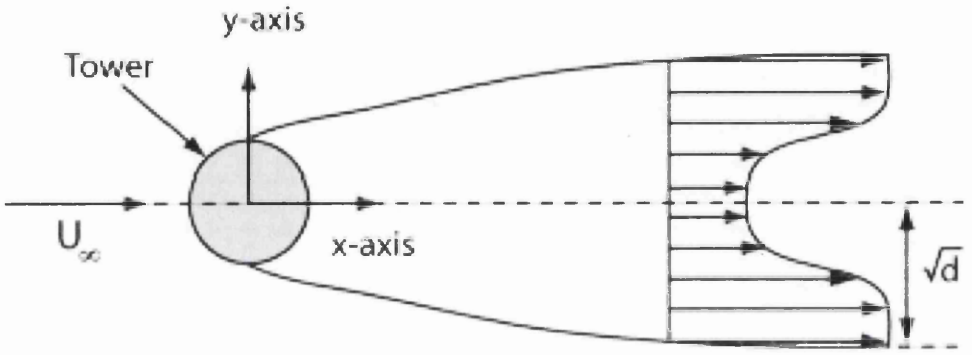

Figure 5.18: A schematic of tower shadow with parameters illustrated from AeroDyn theory manual [16]

The composite local flow velocity is determined by Moriarty and Hansen [16] by combining (5.16) to (5.19) as shown in (5.21):

$$U_{local} = (u - u_{wake})U_{\infty}$$
$$V_{local} = (v - u_{wake})U_{\infty}$$

... (5.21)

In the AeroDyn model, the wake is assumed to align with the instantaneous horizontal wind vector, in reality, the theory book suggests alignment with a time averaged wind direction could be more realistic and this is specified as a field for further development in the document. Another assumption made in the model is that the wake grows with the square root of dimensionless distance from tower centre, this is not validated but is stated to be consistent with previous models employed in the AeroDyn code.

The approach described above provides the most complete solution that is applicable to the present model, the computational cost of employing this

solution is minimal. For compatibility with the three-dimensional mapping procedure, the wake model is employed in the blade normal direction with the blade normal flow component being taken as the in stream flow. A plot of the in stream flow velocity around the tower is given in figure 5.19, the fact that this system models wake expansion is clear from this plot.

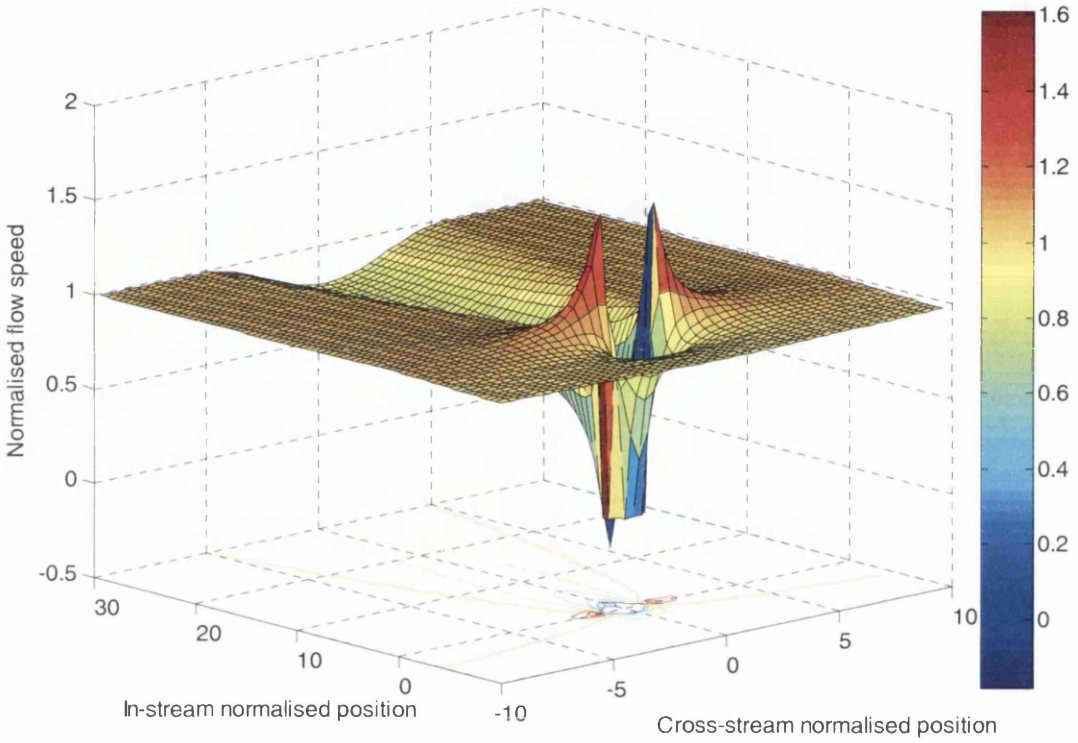

Figure 5.19: in stream flow velocity normalised to uniform inflow against position normalised to tower radius for AeroDyn wake model with $C_D = 1.05$

The V_{local} equation (5.21) was found to give unrealistic flow in the downstream wake. Figure 5.20 displays the downstream wake, and it can be clearly seen that the flow is reduced in the same direction either side of the tower, in practice the flow will travel towards the tower centre line.

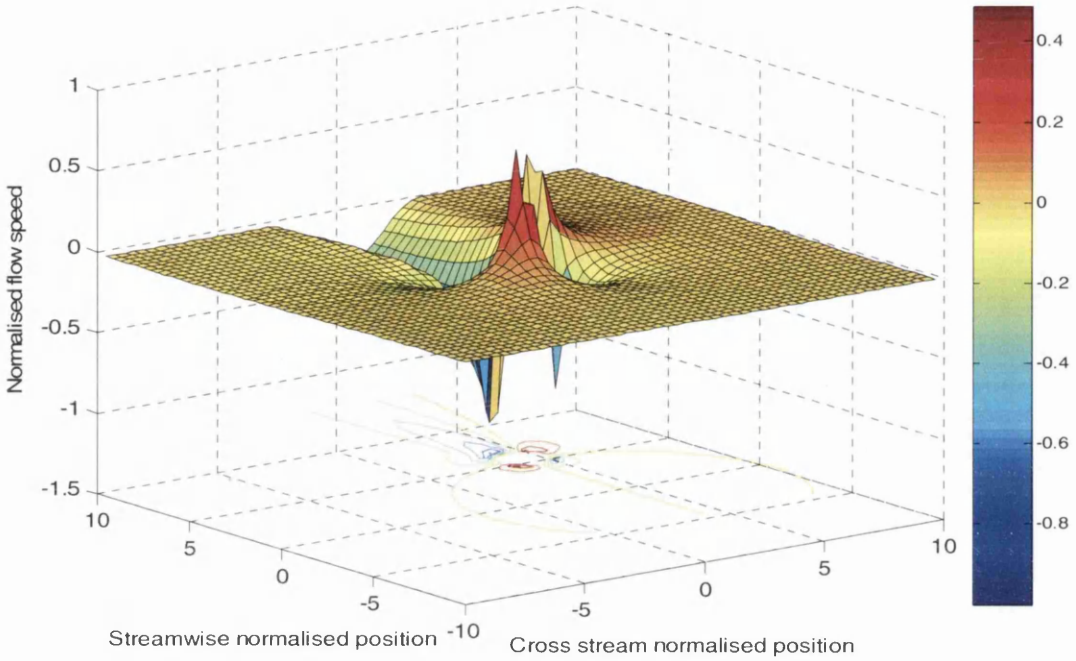

Figure 5.20: cross-stream flow velocity normalised to uniform inflow against position normalised to tower radius for AeroDyn wake model (5.19) with C_D = 1.05

u_{wake} was therefore removed from the V_{local} equation in (5.21) modifying the equations to those in (5.22) and giving the cross-stream flow profile in figure 5.21. This neglects the small cross-stream component downstream of the tower but this will have a lower impact on accuracy than continuing to use the equations in the form of (5.21).

$$U_{local} = (u - u_{wake})U_{\infty}$$
$$V_{local} = (v)U_{\infty}$$

... (5.22)

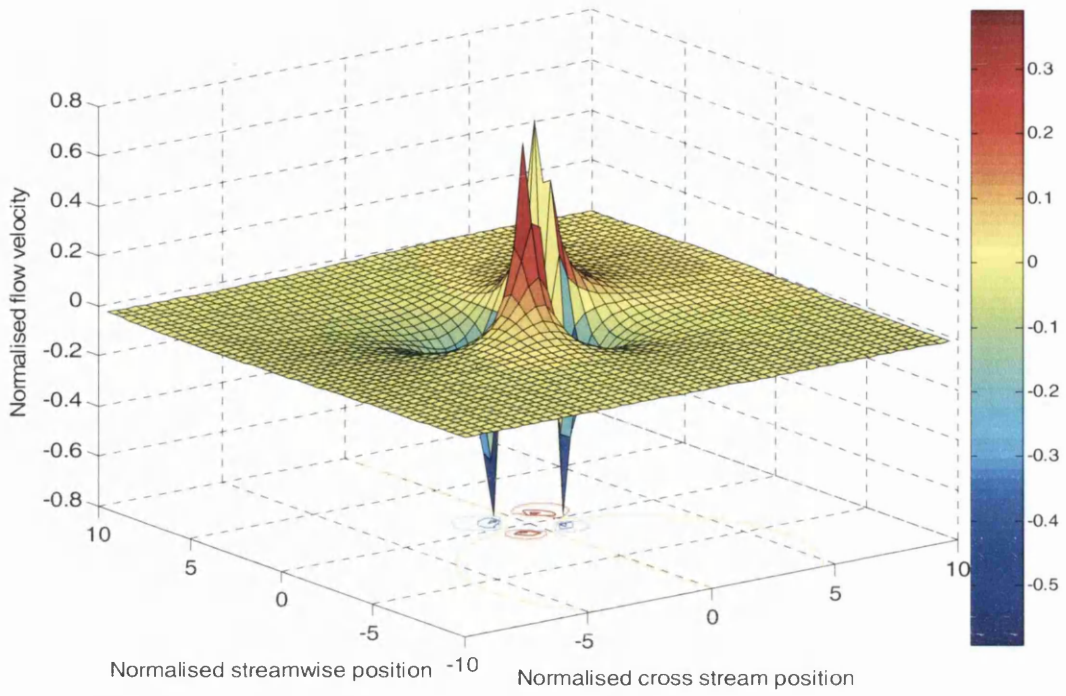

Figure 5.21: cross-stream flow velocity normalised to uniform inflow against position normalised to tower radius for modified AeroDyn (5.20) wake model with C_D = 1.05

5.5.3 Results arising from a tower shadow model with API recommended drag co-efficient

With the tower shadow model described by Moriarty and Hansen [16] employed using the alteration given in (5.21) and a tower drag coefficient of 1.05 from API recommended practice [19] selected, a large and sudden dip in both rotational torque and axial force is experienced once per revolution on each blade (see Figure 5.22). The magnitude of this variation as well as its pulsing nature would cause large problems in terms of fatigue for the device and the predicted impact of this appears to be excessive. Calibration of a tower shadow model to reflect more accurately the tidal turbine case is now presented. A comparison of existing literature is discussed in the following section. A wake model calibrated for tidal turbines will then be presented.

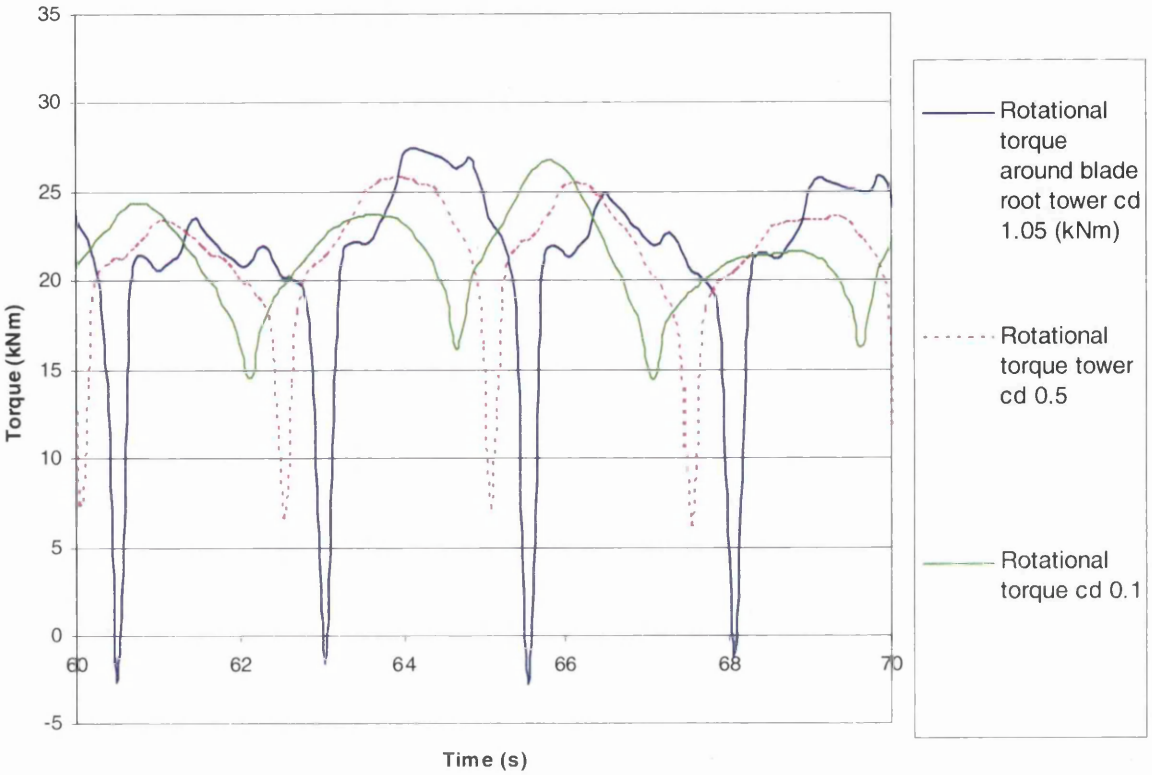

Figure 5.22: Rotational torque around blade root (M_{XB}) for different tower drag coefficients against time.

5.5.4 Comparison to relevant literature

A simple check on the recommended drag coefficient may be made. The value of 1.05 appears unrealistically high. For a Reynolds number of 2.1 x 10^6 (corresponding to a flow of 3m/s, kinematic viscosity 1.4 x 10^{-6} m^2/s [20] and tower diameter 1m) the drag coefficient of a cylinder is approximately 0.4 and that of a streamlined strut is 0.06 [13]. The drag coefficient given in the API standards book would be intended for areas of sea with lower flow speeds hence lower Reynolds numbers as the values are intended for offshore oilrigs rather than for a tidal stream turbine support. It is therefore suggested that a lower drag coefficient than the API practice recommendation would be more suitable.

Further to the high drag coefficient taken from API practice, it would appear that the type of wake model used [16] is likely to overestimate the effect that the tower has on the flow (based on an isolated tower, ignoring blade interaction). It is possible to compare the relative disagreement of the basic wake model results, test results and the proposed model results in Yoshida and Kiyoki's paper [15].

Figure 5.23 shows the Matlab model's predicted performance in a format analogous with that in figure 5.17 for drag coefficients of 1.05, 0.5 and 0.1, the local oscillations in values can be attributed to wave effects. It can be seen that a similar effect to the correction used in Yoshida and Kiyoki's paper can be achieved by reducing the drag coefficient.

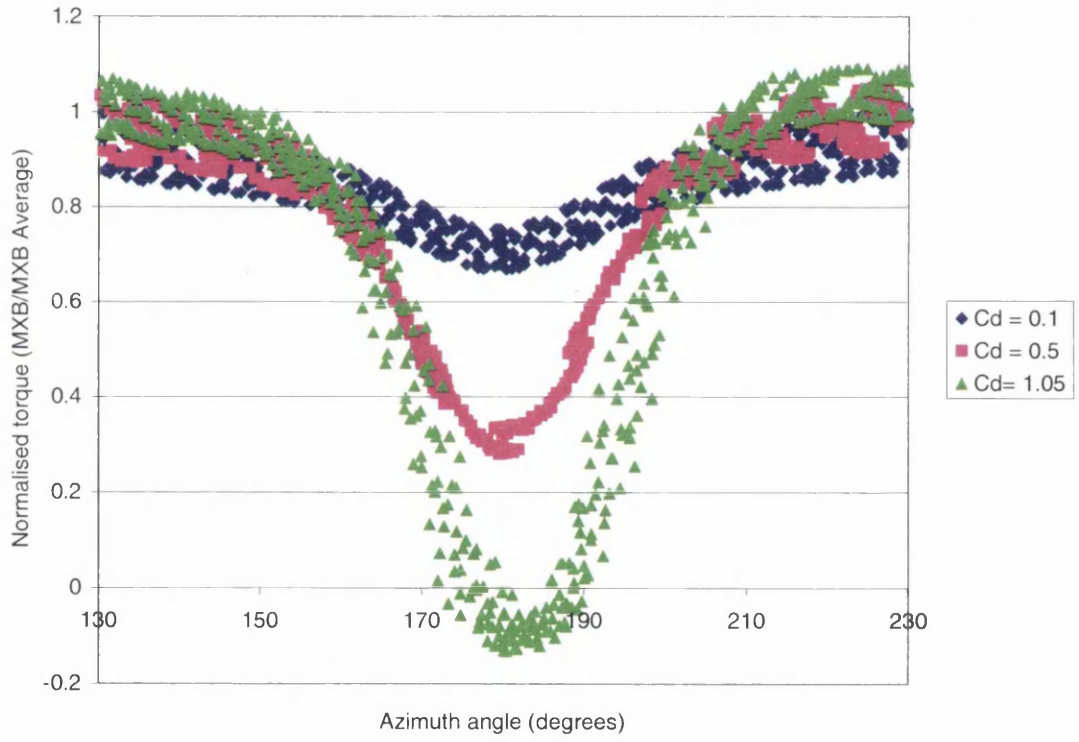

Figure 5.23: Predicted blade root rotational torque (M_{XB}) from Matlab code using different drag coefficients in the tower shadow model.

5.5.5 Calibration of model against 2D CFD results

Consultation with literature can only progress so far as there would appear to be no data on tower shadow effects specific to tidal turbine systems. The previous section shows clearly however that selection of suitable wake variables is vital for an accurate tower shadow model and that this greatly affects the out of balance system loadings. It also demonstrates that the actual effect of tower shadow is less than that predicted using an isolated cylinder wake model. Data from Powles [11] gives results for Reynolds number flows of approximately 7.5×10^4, far lower than those predicted for the tidal turbine case. In Powles' paper, a slender tower is used, further reducing the Reynolds number. The kinematic viscosity of air being an order of magnitude larger than that of seawater will mean that this Re disagreement between wind and tidal models will be the general case.

Another factor, which is less of an issue for wind devices, is that of surface roughness. Marine growth and corrosion could lead to a significant roughening of the tower that will influence the wake structure. The tower examined in Powles [11] is octagonal rather than cylindrical and so in this respect will mimic a rough tower to some extent. There appears to be little specific data on corrections for a rough tower.

Due to these discrepancies, a new study is now presented on the wake behind a tidal turbine tower. As a first stage, an isolated tower is considered despite the aforementioned shortcomings of this. The isolated tower investigation was chosen due to the complexity of modelling and the unsteady nature of incorporating blade-tower interaction. The isolated tower model will be a conservative approximation, giving load fluctuations larger than in the true case.

CFD models were provided for a cylinder with a surface roughness height of 5mm and of a hydrodynamic strut (with the aim of reducing wake effects) by Carswell [21]. These models were run in "Fluent" [22], the cylinder was 1m diameter and the hydrodynamic strut had a thickness of 1m. Steady state,

2D models were created for flow speeds of two and 4 m/s, corresponding to Reynolds numbers of the approximate range $1.6\times10^{6} < \mathrm{Re} < 3.3\times10^{6}$. The resulting horizontal velocity flow fields are displayed in Figures 5.24 and 5.25 with the hydrodynamic strut displayed in figure 5.26. The flow from the CFD analysis as displayed in these figures may be used to assess and calibrate upstream and downstream tower shadow models.

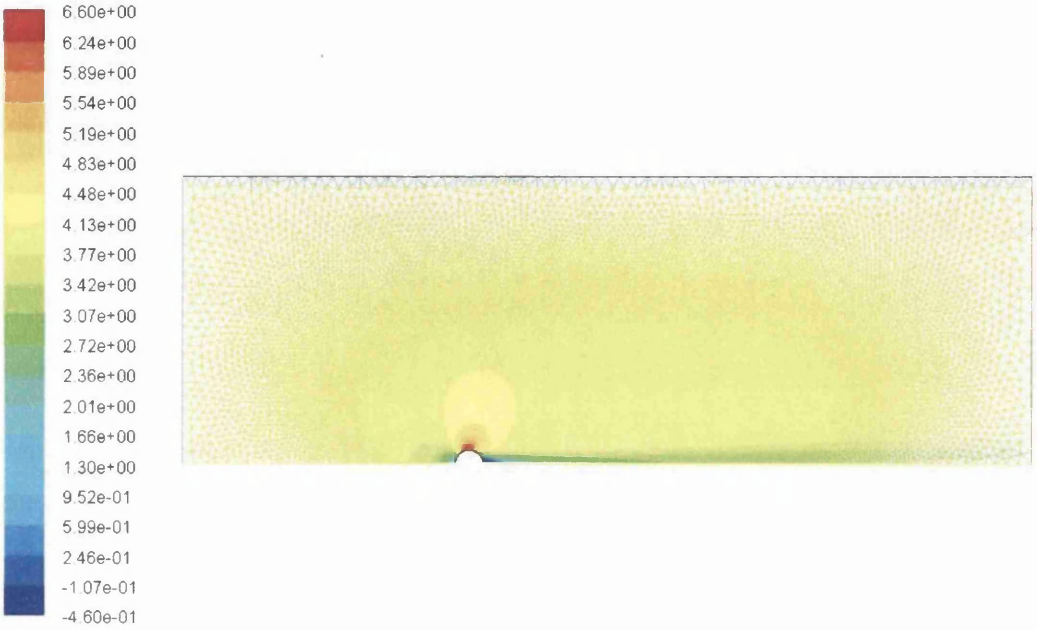

Figure 5.24: In-stream flow velocity plot of a 1m diameter rough cylinder in 4m/s flow (Carswell [21]).

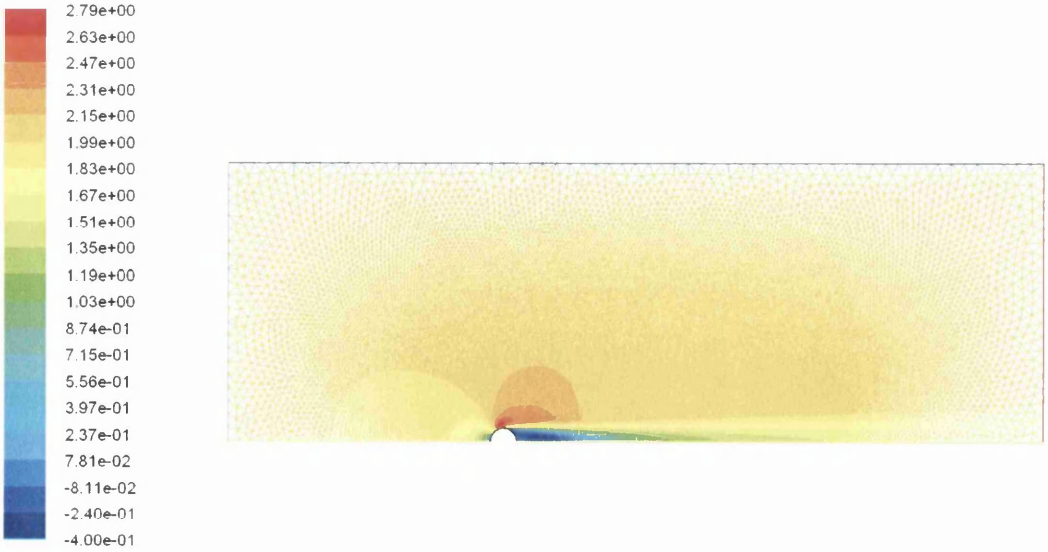

Figure 5.25: In-stream flow velocity plot of a 1m diameter rough cylinder in 2m/s flow (Carswell [21]).

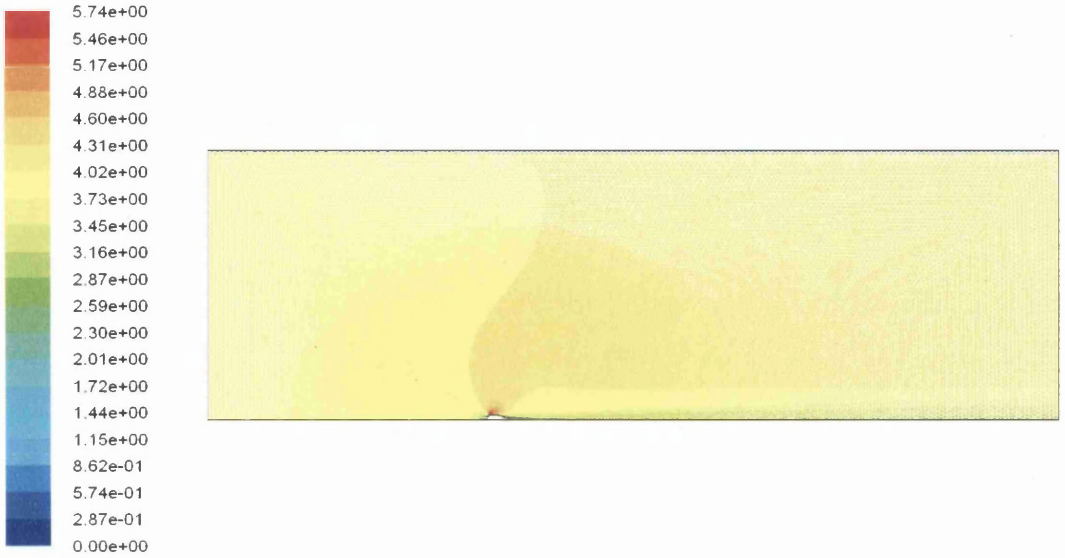

Figure 5.26: In-stream flow velocity plot of a 1m thick hydrodynamic strut in 4m/s flow (Carswell [21]).

Figure 5.27 shows the fluent prediction [21] at 2m/s flow ($\mathrm{Re} \approx 1.6 \times 10^6$) with Powles' [11] results ($\mathrm{Re} \approx 7.5 \times 10^4$) overlaid. The difference in wake is clear, Powles' results showing a wider wake pattern with more significant wake expansion than the results for the higher Reynolds number flow. The two results do however, display similar characteristics, supporting the assumption made that Powles' octagonal tower resembles a rough cylindrical tower.

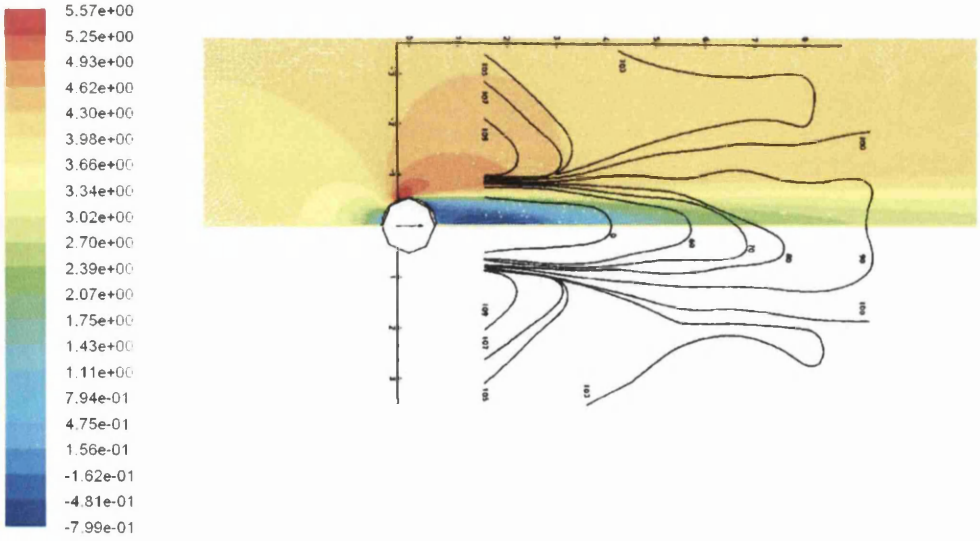

Figure 5.27: Comparison of 2m/s CFD [21] predicted flow with Powles [11] results for an approximate Re 7.6E4 superimposed. Powles results given as line plots.

Figures 5.28 and 5.29 display transects of the CFD flow at different in stream positions for the 2m/s and 4m/s flow, it is useful to note that the change in flow speed has very little impact on the dimensionless flow in this range. These data transects may be used directly for comparison and calibration.

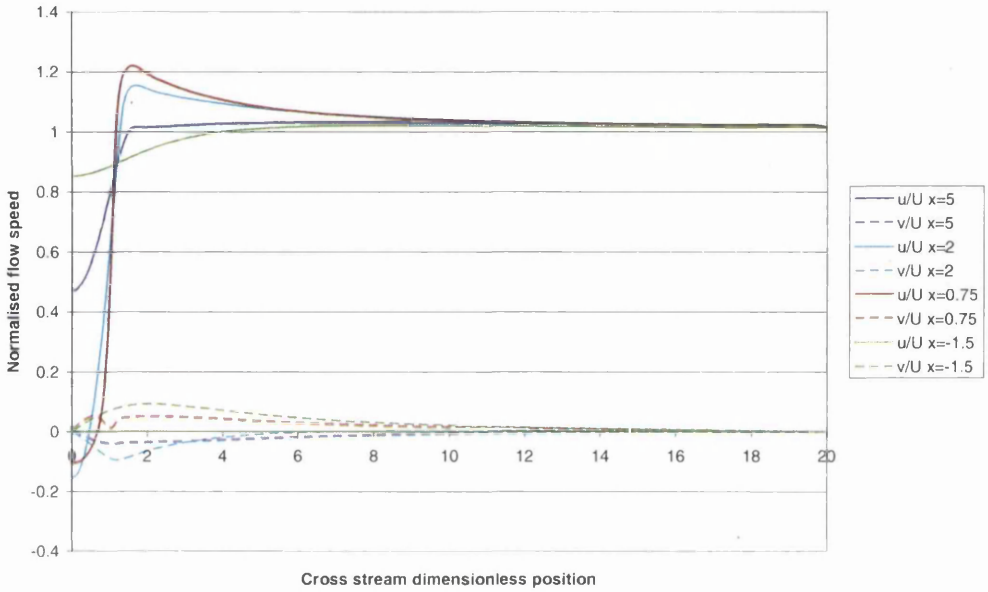

Figure 5.28: Fluent predicted in-stream flow velocities for cross-stream traverses at different upstream and downstream positions. The model is the rough cylinder model with a free stream flow of 2m/s.

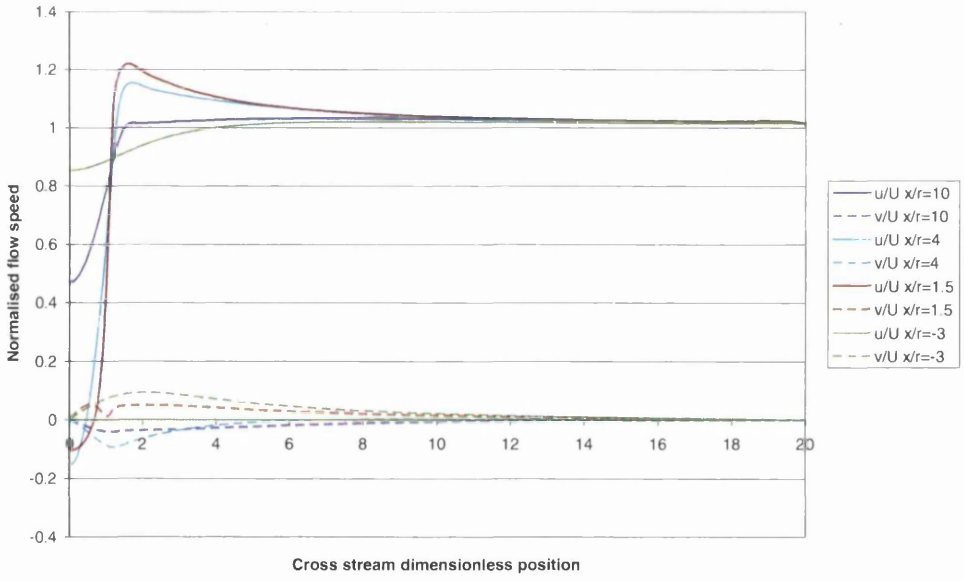

Figure 5.29: Fluent predicted in-stream flow velocities for cross-stream traverses at different upstream and downstream positions. Based on the rough cylinder model with a free stream flow of 4m/s.

It can be seen in the plots that wake expansion is minimal and that flow recovery is far more rapid in the case of the hydrodynamic strut than that of the cylinder. The assumption by Moriarty and Hansen [16] that wake expands with the square root of distance from tower centre appears invalid for this case. Using this data, an attempt was made to match the fluent predictions with (5.22) for the cylindrical tower. The results of this are shown in figures 5.30 to 5.37.

The agreement between predicted and modelled upstream flows (see figures 5.30 to 5.33) show that there is little need to adjust the formulae for upstream modelling and that a drag coefficient of approximately 0.5 for a rough cylinder is recommended for use in the equations upstream from this study.

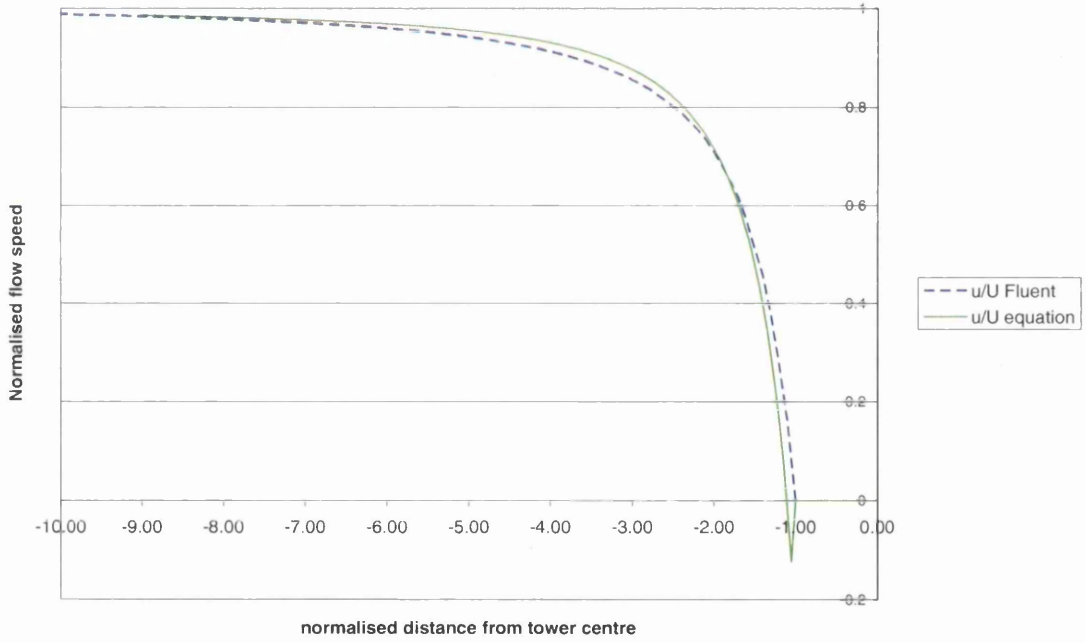

Figure 5.30: Comparison of predicted upstream-normalised flow velocity along axis centreline against normalised stream-wise position between fluent model for a rough cylinder and AeroDyn based equation with a $C_D = 0.5$.

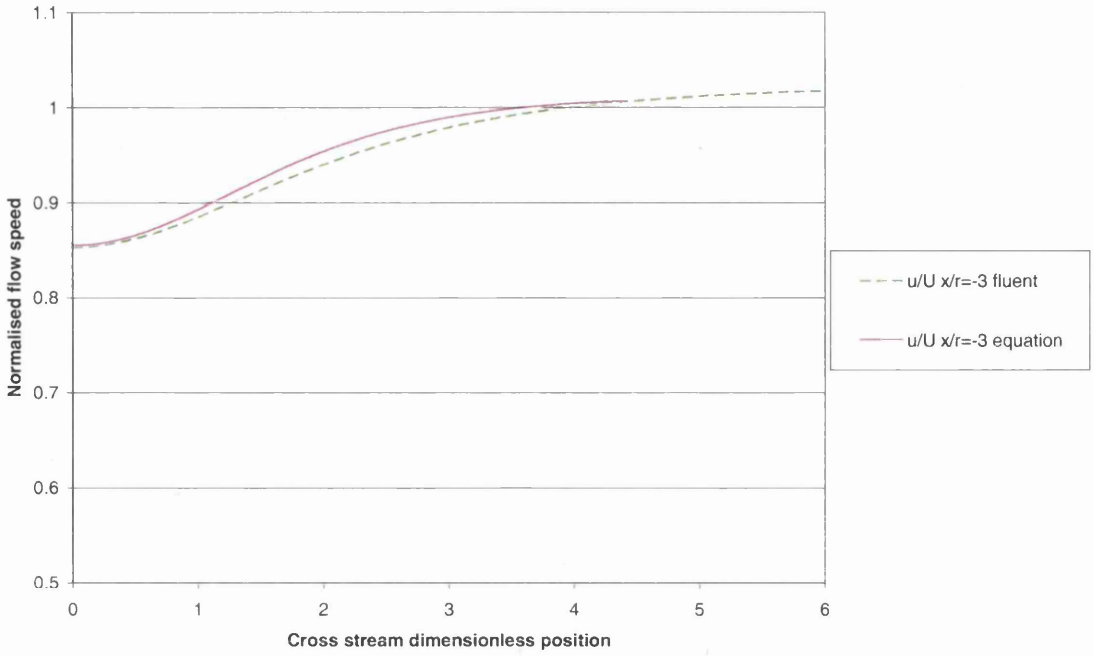

Figure 5.31: Comparison of predicted normalised in-stream flow velocities across normalised cross stream position at 3 tower radii upstream between fluent model for a rough cylinder and AeroDyn based equation with a C_D = 0.5.

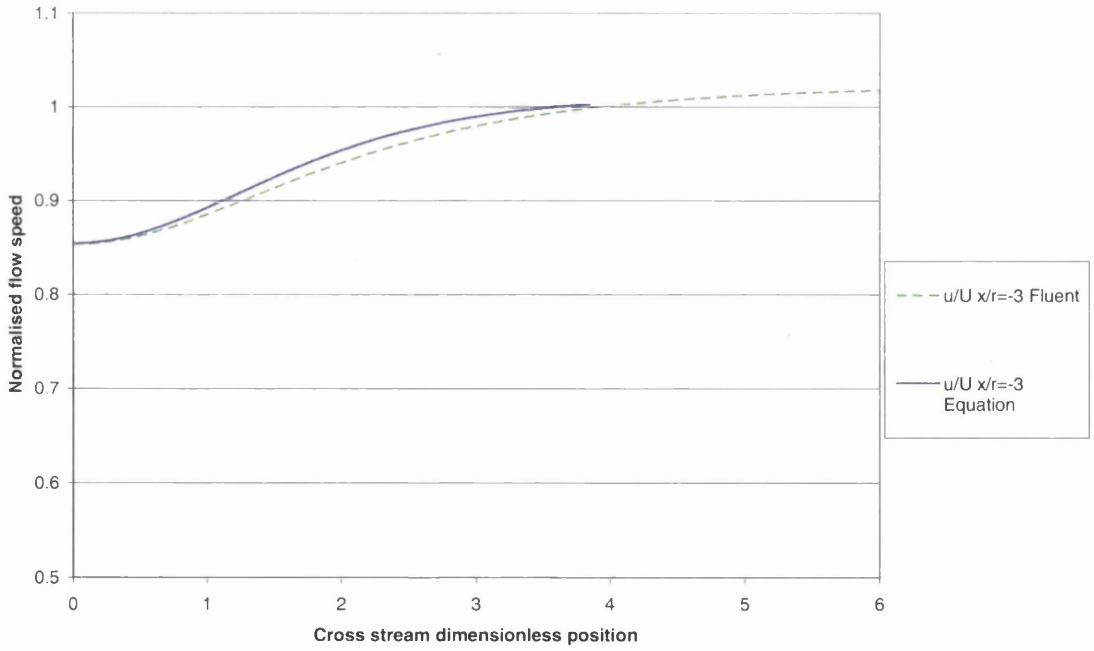

Figure 5.32: Comparison of predicted normalised in-stream flow velocities across normalised cross stream position at 3 tower radii upstream between fluent model for a rough cylinder and AeroDyn based equation with a C_D = 0.5.

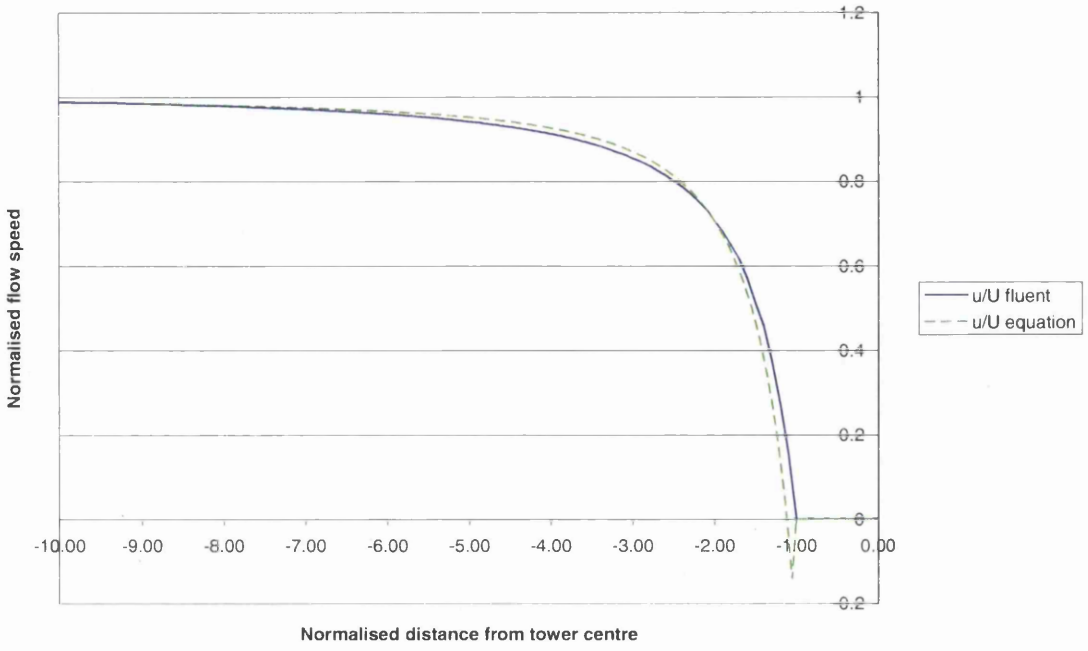

Figure 5.33: Comparison of predicted upstream-normalised flow velocity along axis centreline against normalised stream-wise position between fluent model for a rough cylinder and AeroDyn based equation with a C_D = 0.5.

In the Reynolds number range studied, it can be seen that the solution is effectively independent of changes in *Re* (flow speed or tower size). This result is to be expected as Massey [13] explains that, in this range, viscous effects are relatively small and so C_D is practically independent of *Re*. The C_D value of 0.5 also correlates well with suggested values for a cylinder in Massey [13] at this Reynolds number range. This suggests that, upstream, the C_D value in the equation reflects the physical C_D value well.

Downstream of the tower, the empirical model correction performs less well than the potential flow based upstream equation and a different approach could be desirable. Figures 5.34 to 5.37 demonstrate the inability to fit the equation to the CFD solutions. In the figures, the drag coefficient giving lowest disagreement for stream-wise maximum wake deficit is displayed. Cross-stream transects at certain points downstream are also presented.

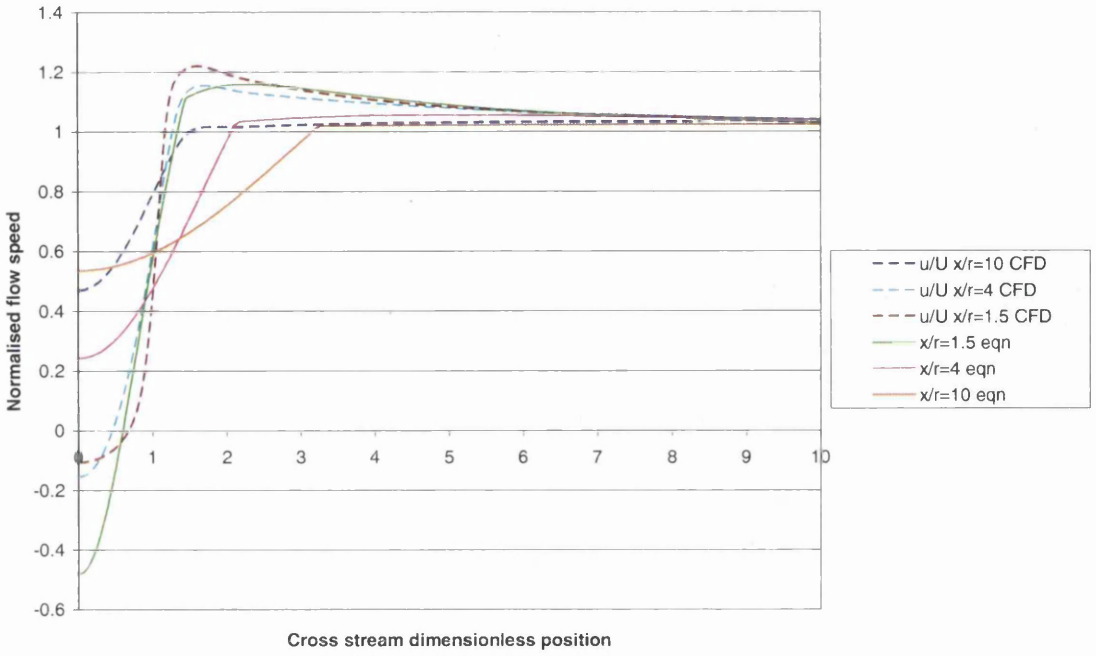

Figure 5.34: Comparison of predicted normalised in-stream flow velocities between fluent model for a rough cylinder and AeroDyn based equation with a C_D = 1.52 for different in-stream positions.

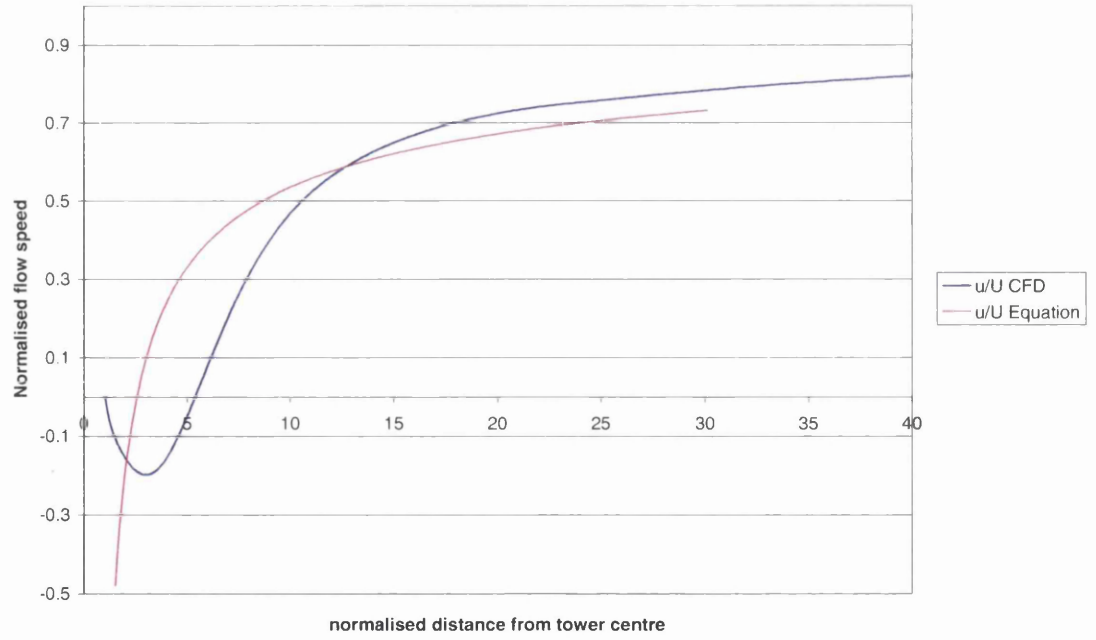

Figure 5.35: Comparison of predicted normalised in-stream flow velocities between fluent model for a rough cylinder and AeroDyn based equation with a C_D = 1.52 along in-stream direction. Flow velocity normalised to free-stream and position normalised to tower radius for 2m/s flow.

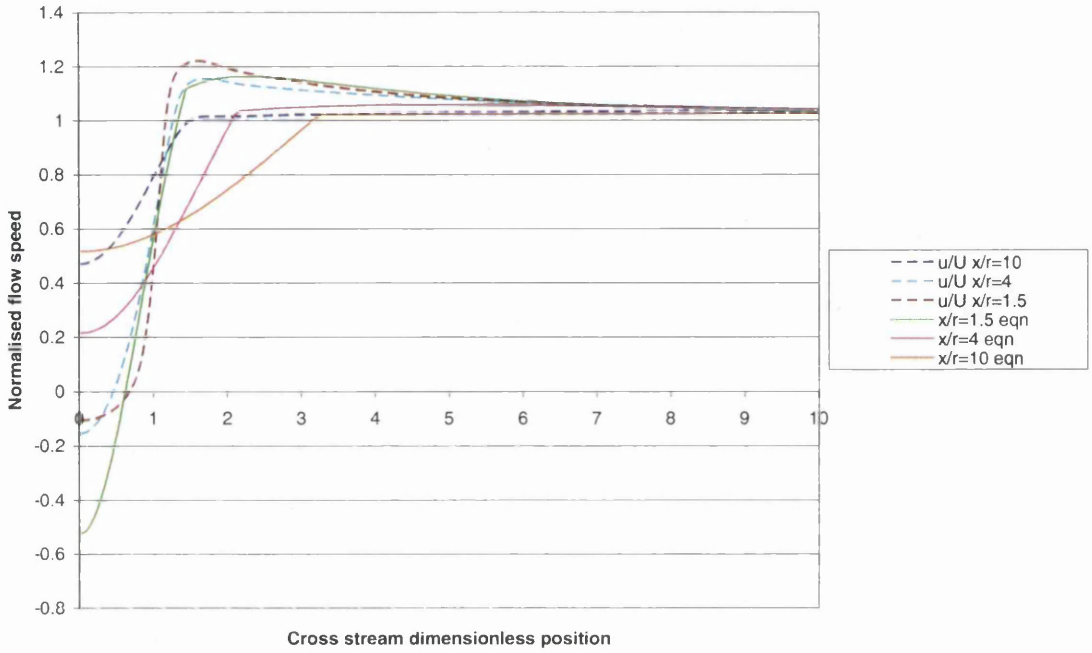

Figure 5.36: Comparison of predicted normalised in-stream flow velocities between fluent model for a rough cylinder and AeroDyn based equation with a C_D = 1.52 for different in-stream positions.

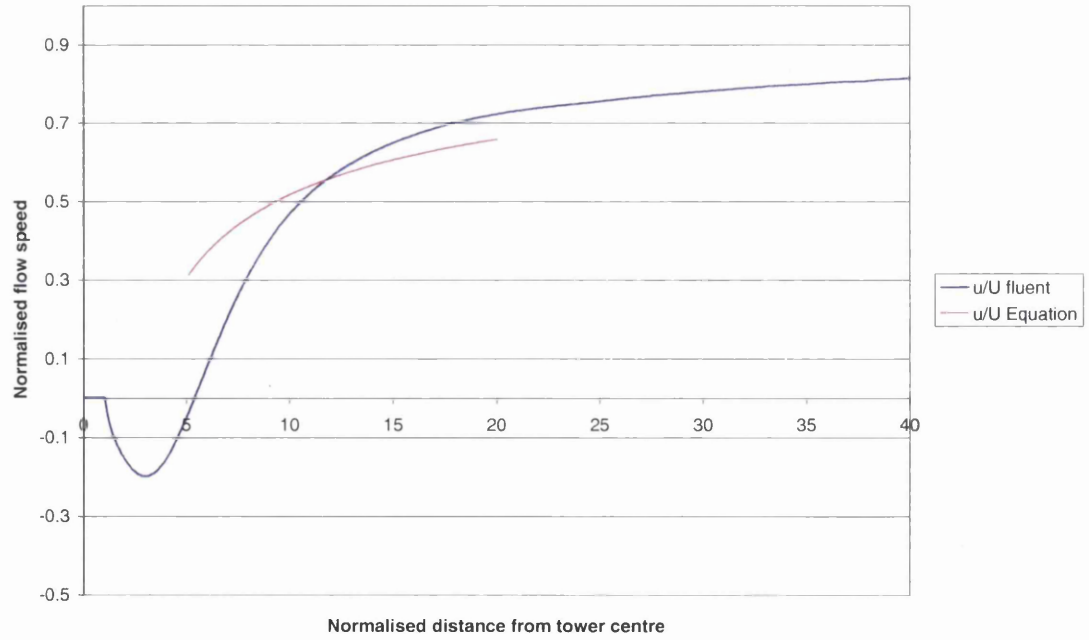

Figure 5.37: Comparison of predicted normalised in-stream flow velocities between fluent model for a rough cylinder and AeroDyn based equation with a C_D = 1.52 along in-stream direction.

Despite adjusting the $C_{D'}$ solution to a small feasible region, a good fit could not be obtained and the $C_{D'}$ value that the approach yielded was not a close match to the expected value or that found suitable for upstream predictions. One possibility for gaining a better match is to alter $C_{D'}$ with downstream distance, this would mean that the $C_{D'}$ term would no longer reflect the drag coefficient of the cylinder and would become a function based on distance from tower centre, effectively reverting to Powles' [11] formula. Alternatively, a lower drag coefficient than this minimisation solution could be applied, this would give a lower minimum flow value than the CFD results and will tend to also produce a broader wake, this would be in-keeping with the effects of blade-tower interaction but this relationship cannot be easily quantified using a single $C_{D'}$ value. Although a model based on true $C_{D'}$ offers much in terms of flexibility and ease of use, it is clear from this study that it is not accurate and so must be discarded at this point.

It appears preferable at this stage to employ the empirical correction model presented in Powles [11] with a wake depth dependent on dimensionless stream-wise distance from the tower centre and a similarly varying shadow width. This can be used in conjunction with the near tower formula of Bak *et al.* [17] to give a complete model for upstream and downstream tower effects.

5.5.6 Implementation of full tower shadow model

First, Powles' [11] formula is rearranged in to the form of u_{wake} presented by Moriarty and Hansen [16] and the dependency on blade azimuth is removed (5.23).

$$u_{wake} = D\cos^2\left(\frac{\pi y}{2W}\right)$$

... (5.23)

This facilitates incorporation into the mapping procedures of the developed generator model. To apply the wake deficit to the model, a reference flow is used. As an approximation the blade element local flow is employed rather than the tower flow speed. This gives a local flow that is reduced by the presence of a tower which may be used as an input to the BEMT solver routine.

Suitable values for D and W must now be found, to do this the CFD predicted wake deficit at *y=0* was taken and the predicted deficit of the near wake equation (5.16) was subtracted, the remaining deficit was then plotted in Microsoft Excel and the "trendline" feature was used to fit a polynomial curve to the deficit. The deficit shape meant that two separate polynomial equations were needed, one for the near range of *1<x<7* (in-stream dimensionless distance) displayed in (5.24) and a further polynomial (5.25) for the far range *7<x<40*.

$$D = -0.0041060900(x)^4 + 0.0821749613(x)^3 - 0.6169348560(x)^2 + 1.9644692675(x) - 1.0876723621$$

... (5.24)

$$D = -0.0000001130x^5 + 0.0000157011x^4 - 0.0008622883x^3 + 0.0236004023x^2 - 0.3300575567x + 2.1909219910$$

... (5.25)

At the border between these two polynomials, it is important for the case of a flexible blade that no discontinuity exists, to achieve this, the crossover

region should take a weighted average of the formulae. The 4m/s CFD results were used to tune the deficit values but the fit is also very good with the 2m/s results as can be seen in figure 5.38. Unfortunately, these polynomials are not as concise as the previous wake models and are sensitive to rounding. Using these formulae, the fit to the wake deficit curve for the tower in question over the relevant range of Reynolds numbers is greatly improved. These results are valid for any size of pile with an accordingly scaled surface roughness but should only be used for the Reynolds number range discussed.

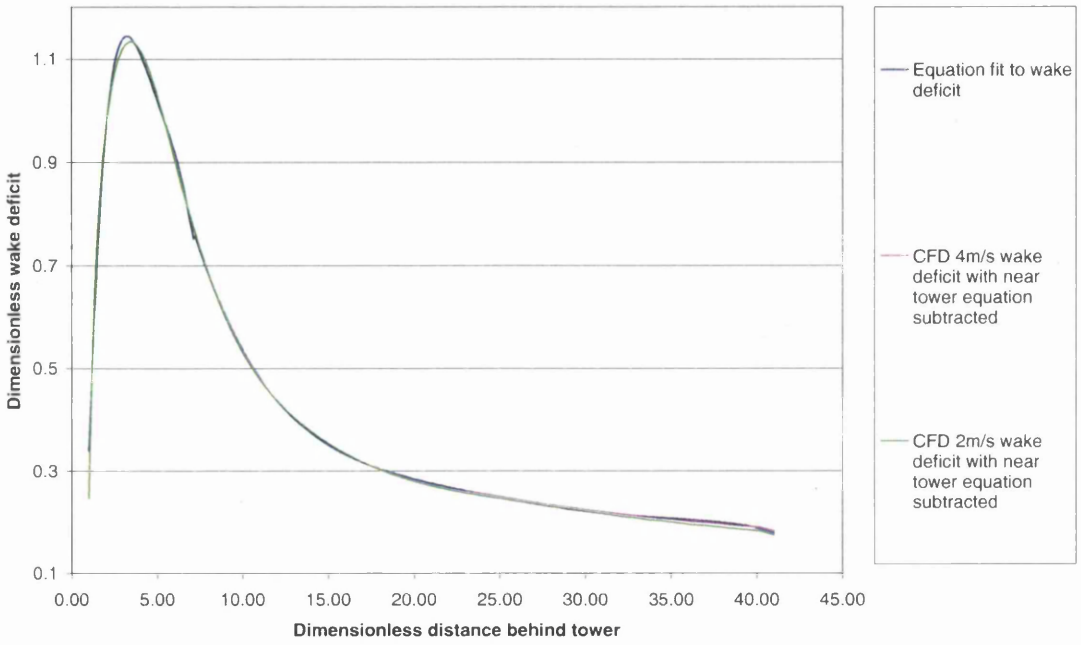

Figure 5.38: Comparison of y=0 wake deficit for 2m/s and 4m/s CFD results (with potential flow based equation deficit deducted) compared to the new empirical wake deficit polynomial equations.

A formula to define the width of the wake, W, with respect to stream-wise distance is needed. A similar approach is taken to determining the wake depth, the width of the wake was estimated from CFD data and a curve was fitted using the trend line feature in Excel. Figure 5.39 shows the plot of data points used to calculate the width formula given in (5.26).

$$W = -0.00044255\left(\frac{x}{r}\right)^2 + 0.04451284\left(\frac{x}{r}\right) + 1.27034543 \quad \ldots (5.26)$$

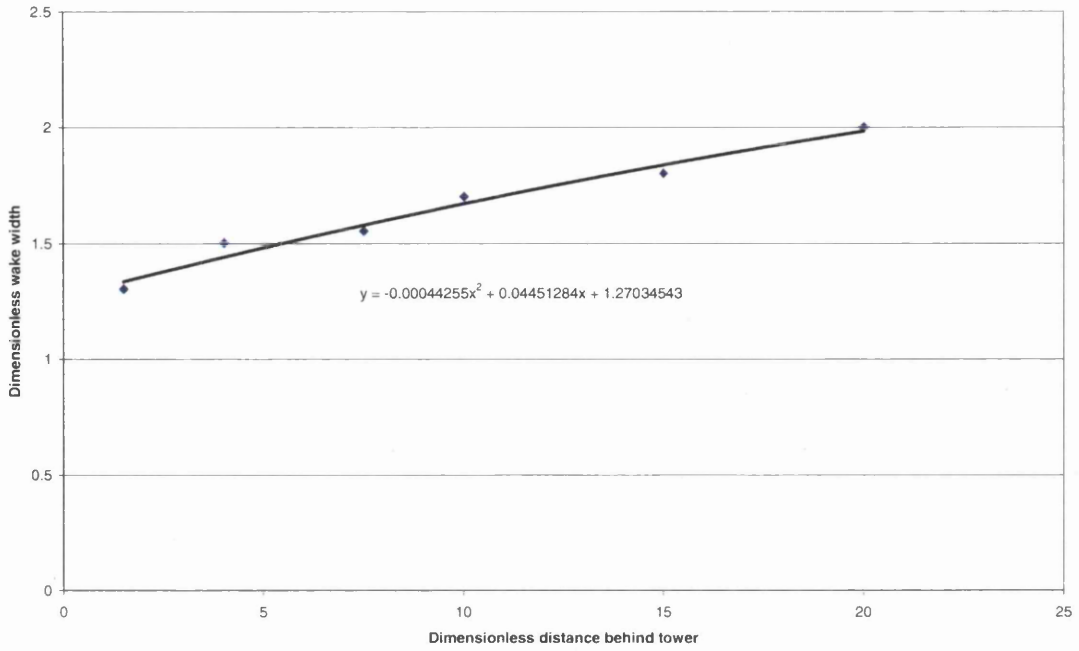

Figure 5.39: wake width for cylindrical tower in 4m/s flow with quadratic curve fitted to data points.

This gives a complete formula for wake deficit behind the cylindrical tower. As discussed previously, this does not take into account blade/tower interaction and so is likely to be an overestimate of the flow reduction. With further research, a correction could be made to the depth and width formulae to account for the effect of the blades. A plot of the resulting dimensionless flow velocity behind the tower is displayed in figure 5.40. A good correlation can now be seen between the model displayed in Figure 5.40 and the CFD results shown in Figures 5.24 and 5.25.

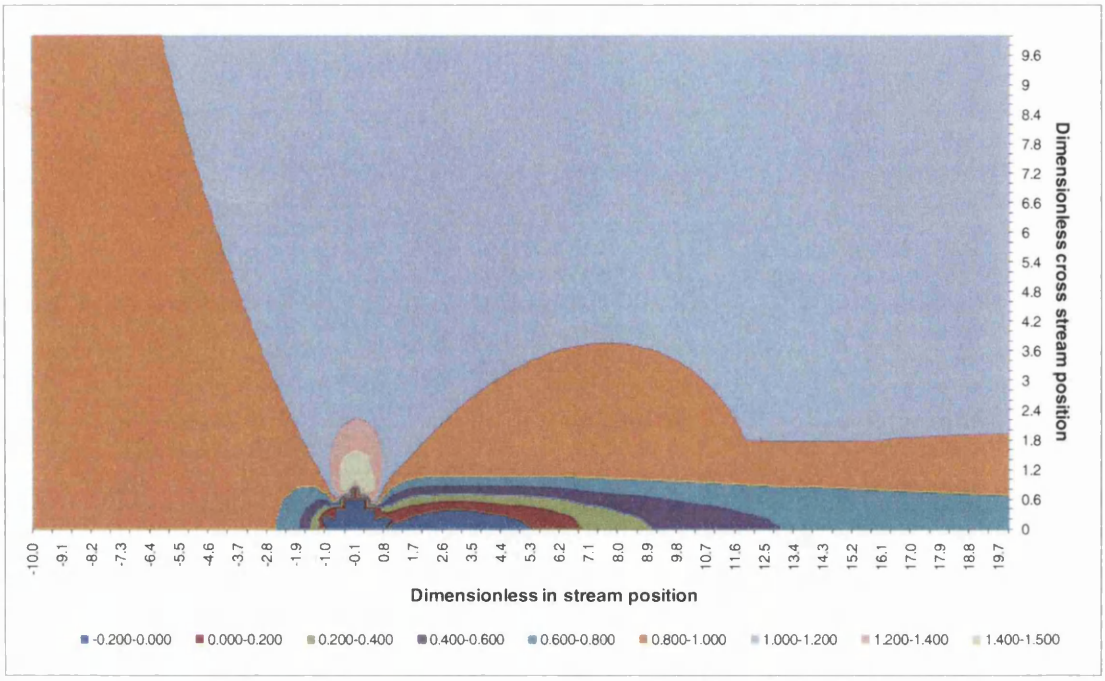

Figure 5.40: Half plot of dimensionless in-stream velocities predicted by wake model with developed empirical formulae for rough cylinder

The wake produced by the tower is significant and mitigation of this flow reduction may be required for downstream turbine systems. To this end, the foil shaped hydrodynamic tower strut will be investigated.

5.5.7 Tower shadow model for a streamlined strut

A similar approach to the modelling of the cylindrical strut may be taken to produce a wake model for a hydrofoil shaped strut. Upstream, the flow is very similar to the cylindrical tower and the near wake potential flow based formulae of Bak *et al.* [17] remains sufficiently accurate in this region. Although a potential flow solution based on a foil shape should be employed here, assumption that the flow is sufficiently similar to the flow over a cylinder allows for increased flexibility of the model whilst maintaining sufficient accuracy. A drag coefficient of 0.06-0.08 is suggested for streamlined struts by Massey [13] and figure 5.41 demonstrates that selection of a C_D=*0.08* gives a good correlation upstream with CFD results for the near wake formula.

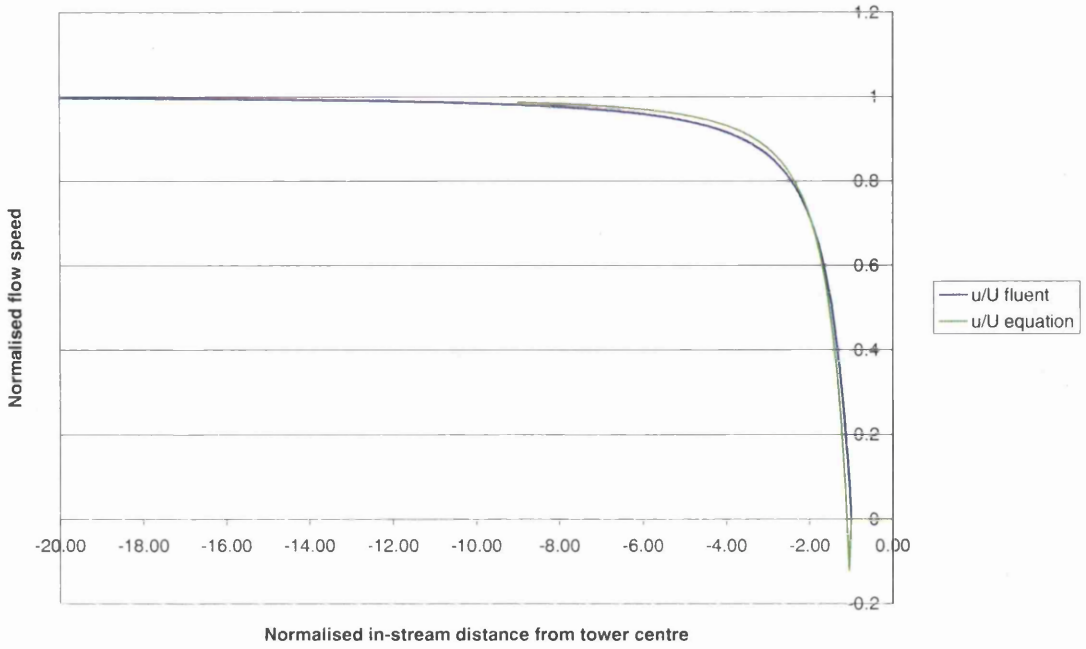

Figure 5.41: Upstream flow speed for hydrodynamic strut from CFD results compared with Bak et al.'s model with C_D=0.08.

The downstream wake differs from the cylinder case more significantly and a new set of formulae for D and W are needed to calibrate Powles' wake model. A CFD model run at 3m/s was used for this but, as with the cylinder, the result is not highly sensitive to variations in *Re* within the studied range.

D is again split into two polynomial functions, (5.27) is for *3.9<x<12* and (5.28) is for *x>12*.

$$D = 0.0001041779x^6 - 0.0052163285x^5 + 0.1071032428x^4 - 1.1542146513x^3 + 6.8921352129x^2 - 21.6919029642x + 28.5999208880 \quad \ldots (5.27)$$

$$D = 0.00011097x^2 - 0.00599767x + 0.28871276 \quad \ldots (5.28)$$

The wake width formula was again found by minimising the disagreement between CFD results and equation prediction for in-stream flow velocity at

several transects across the downstream flow. The resulting formula for W is presented in (5.29).

$$W = -0.0033x^2 + 0.1898x + 0.2939 \quad \ldots (5.29)$$

The resulting in-stream flow velocities for the hydrodynamic tower model are plotted in figure 5.42, again a good correlation can now be seen when compared to the CFD results displayed in figure 5.26.

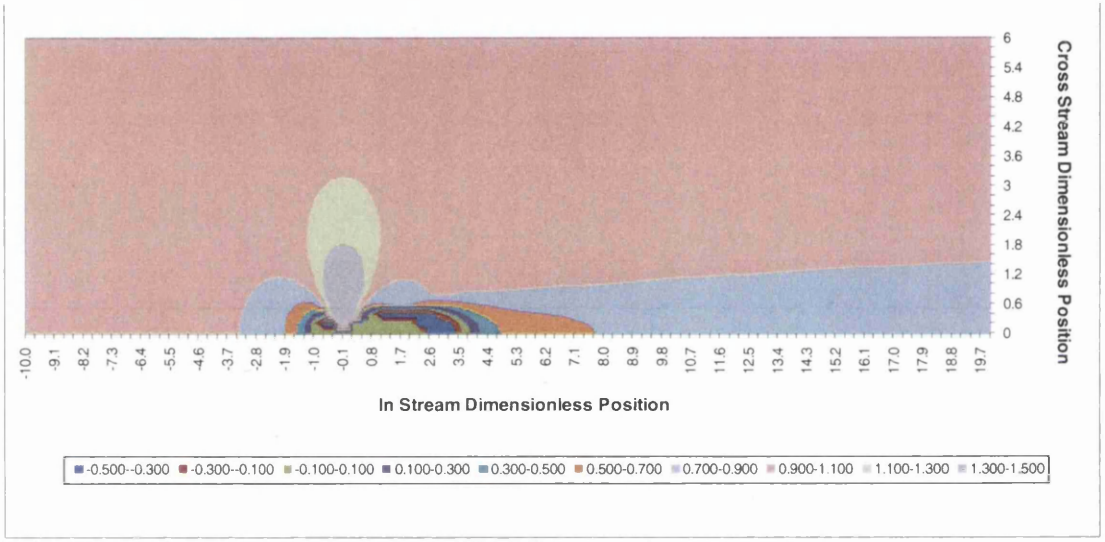

Figure 5.42: Half plot of dimensionless in-stream velocities predicted by wake model with developed empirical formulae for hydrodynamic strut.

5.5.8 Discussion of derived wake models

The studies in 5.5.6 and 5.5.7 provide formulae for an isolated tower of streamlined or cylindrical form. In the absence of a specific blade/tower interaction model it may be considered prudent to incorporate these wake models 'as is'. The high increase in out of balance loads that this results in however could lead to over-engineered systems and therefore higher costs. A tentative adjustment of the developed isolated tower models may be made using the work of Yoshida and Kiyoki [15]. Their investigation found that the

effective flow deficit is 0.16 of the depth of that predicted by the isolated tower model when interaction is incorporated and that effective wake width is a factor of three larger than the isolated model. These may be employed as a blanket correction where D and W are replaced by D_c and W_c given the relationships in (5.30) and (5.31). This approach uses the isolated tower model but adjusts its impact by the proportion experienced by Yoshida and Kiyoki. The actual relationship of blade/ tower interaction will depend on the specific system design and so a CFD investigation would ideally be carried out for each new design and a new relationship tailored for this.

$$D_c = 0.16D \quad \ldots (5.30)$$

$$W_c = 3W \quad \ldots (5.31)$$

5.5.9 Conclusions

Tower shadow is an important factor and is particularly significant in downstream turbines. An isolated tower wake model has been calibrated to CFD solutions of isolated towers, which are more realistic for tidal devices than the existing wind calibrated models. Considering that blade and tower interaction has been reported to reduce the impact of downstream wake, a correction based on Yoshida and Kiyoki's findings has been proposed. This correction would benefit from further research as it will depend on the specific turbine system design and flow conditions but should give a more realistic initial estimate of wake impact than using the un-corrected isolated tower models. This correction requires either three-dimensional CFD or model testing results for verification before being used in the design stage. A cautious approach of using the 2D calibrated wake models may be preferable at the load definition stage.

As tower shadow is likely to have a significant impact on the fatigue life of downstream devices, it is advised that an attempt be made to employ hydrodynamic tower sections for such devices. It is expected that the increased cost of such a structure will be outweighed by the saving of fatigue stresses in other components and their resulting increased life span.

5.6 Discussion

In this chapter:

- A new blade failure model was presented, this utilised the assumption that the mean induction factors of an *N* bladed rotor with a blade removed would be equal to that of an *N-1* bladed rotor. Using this assumption, initial estimates of the resulting loadings of this type of failure were produced and the potentially catastrophic impact this would have on out of balance loadings was discussed.
- A bespoke generator model was presented and discussed. The importance of such a facility was demonstrated in the variation of loading resulting from different control models in the same flow.
- A yawing model was then presented, this allowed for user-defined yaw systems to be written into the model and a free-yawing system was used to demonstrate this. The response to both velocity and accelerative hydrodynamic loading was modelled, the inertial capabilities of this code, absent in all but Orme's code enabled this.
- A braking system model was presented. It was seen that wave effects aided the braking of the rotor system.
- The need for a tidal specific tower shadow model at an appropriate Reynold's number range was highlighted.
- A new tower shadow model was presented which was calibrated against CFD data to give a valid shadow model.
- A correction based on Yoshida and Kiyoki's work was presented as a possible correction of the isolated tower models. This requires validation before using for load modelling.

The yaw and generator model developed in this chapter, together with the three-dimensional mapping presented in chapter 3 and the corrections of chapter 4, enable the model to capture realistic operational conditions in a realistic environment. This allows the system to model far more than the basic BEMT result of a performance curve and provides a useful design tool. These developments lead to a system somewhat more complex than the flow charts presented in chapter 3. To allow the reader a more detailed view of the developed system layout, a pseudo code outlining the time dependent modelling process is presented in Appendix 1.

With the system now ready to model most characteristics of a real life tidal power generation device, the next chapter will concentrate on the application of the developed modelling system to real data and demonstrate its ability to provide useful data for design and performance assessment of tidal stream turbines.

5.7 References

[1] James, G., "Modern Engineering Mathematics" 3rd ed. 2001, Harlow: Prentice Hall.

[2] Orme, J., "Dynamic Performance Modelling of Tidal Stream Turbines in Ocean Waves", PhD Thesis, 2006, Civil and Computational Engineering, Swansea University.

[3] Bossanyi, E.A., "GH Tidal Bladed Theory Manual". 2007, Garrad Hassan.

[4] Lawrence, N., "Control model internal communications", 2007,

[5] Oakes, T., "Yaw bearing friction model -Internal company document". 2007, Swanturbines.

[6] Wang, T. and F.N. Coton, "A high resolution tower shadow model for downwind wind turbines", Journal of Wind Engineering and Industrial Aerodynamics, 2001. 89: p. 873-892.

[7] Dolan, D.S.L. and P.W. Lehn. "Real-Time Wind Turbine Emulator suitable for Power Quality and Dynamic Control Studies" in International Conference on Power Systems Transients. 2005. Montreal, Canada.

[8] Vilar, C., J. Usaola, and H. Amaris, "A Frequency Domain Approach to Wind Turbines for Flicker Analysis", IEEE Transactions on Energy Conversion, 2003. 18(2): p. 335- 341.

[9] Maalawi, K.Y. and M.A. Badr, "A practical approach for selecting optimum wind rotors", Renewable Energy, 2003. 28: p. 803-822.

[10] Thresher, R., E.L. Hershberg, and A.D. Wright. "Computer analysis of wind turbine blade dynamic loads". 1984. United States.

[11] Powles, S.J.R., "The Effects of Tower Shadow on the Dynamics of a Horizontal-Axis Wind Turbine", Wind Engineering, Official Journal of the EWEA, 1983. 7(1): p. 26-42.

[12] Hansen, M., "Aerodynamics of Wind Turbines" Second Edition ed. 2008, London: Earthscan.

[13] Massey B, "Mechanics of Fluids" 7th ed, Ed. Ward-Smith J. 1998: Stanley Thornes Ltd.

[14] Burton, T., *et al.*, "Wind Energy Handbook". 2001, Chichester: John Wiley & Sons.

[15] Yoshida, S. and S. Kiyoki. "Load Equivalent Tower Shadow Modelling for Downwind Turbines" in European Wind Energy Conference. 2007.

[16] Moriarty, P.J. and A.C. Hansen, "AeroDyn Theory Manual", NREL, 2005.

[17] Bak, C., H.A. Madsen, and J. Johansen. "Influence from blade-tower interaction on fatigue loads and dynamics (poster)" in 2001 European wind energy conference and exhibition. 2001. Copenhagen.

[18] Parkinson and Jandali, "A wake source model for bluff body potential flow", J. Fluid Mech., 1970. 40(3): p. 577-594.

[19] API, "Recommended Practice for Planning, Designing and Constructing Fixed Offshore Platforms - Load and Resistance Factor Design". 1993, Washington: American Petroleum Institute.

[20] Bullard, E., "2.7.9 Physical properties of sea water", 20/09/07, http://www.kayelaby.npl.co.uk/general_physics/2_7/2_7_9.html.

[21] Carswell, D., "Personal communication", 2008.

[22] "Fluent", ANSYS: Lebanon, New Hampshire.

Chapter 6: Real data application

This chapter presents examples of the application of the developed model. In the first section, the time dependent code will be used to produce a fatigue load regime for a sample site. An approach to assess the relative performance of different design concepts is then presented before an approach to use measured flow data directly is introduced.

6.1 Fatigue load analysis

In this section, an example of the load assessment of a system at a specific site is presented. This will demonstrate the function of all aspects of the developed code and demonstrate how the results are post-processed to provide the design engineer with a variety of detailed load data.

6.1.1 Site description

For this study, site data compiled by T. Baker [1] for the Alderney race is used to demonstrate the model. The occurrences of different waves and flow speeds for this site are shown in figures 6.1 and 6.2 respectively. Baker organised these probabilities into bins of flow speed and wave height giving table 6.1. This gives a number of different flow cases that may be modelled by the code presented in this thesis. The bin sizes were increased to reduce the number of model cases, giving table 6.2. The modelling parameters were taken as the maximum flow speed and wave height from each occurrence bin, giving an optimistic prediction in terms of power production but a conservative estimate of loads. This gives 24 different combinations of wave and tide to be modelled.

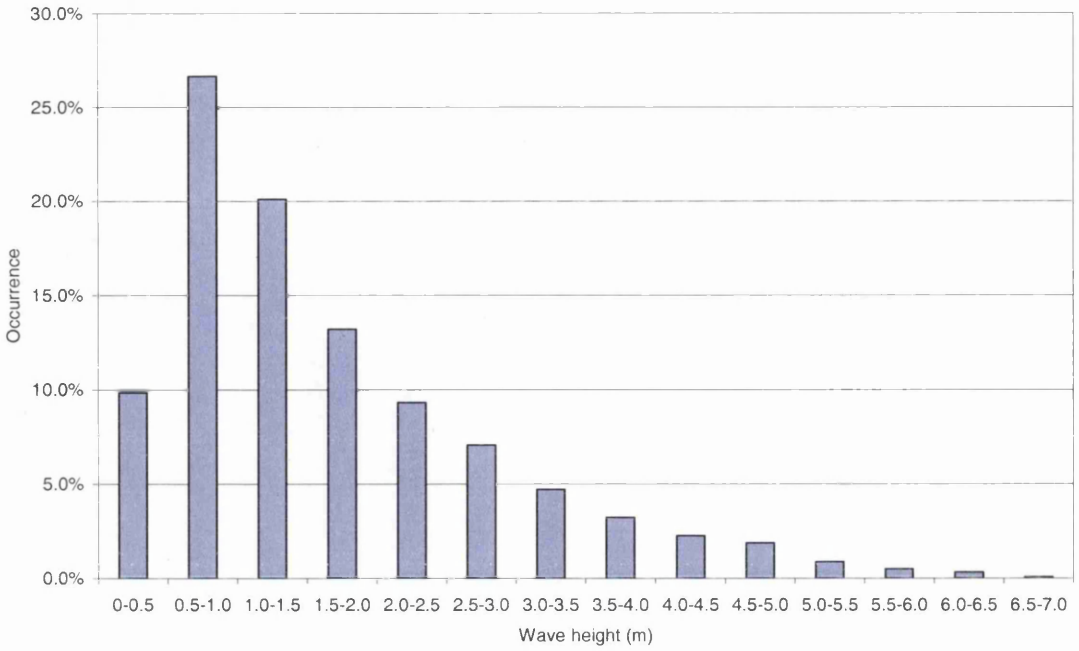

Figure 6.1: Occurrence of wave heights at Alderney race from Baker [1].

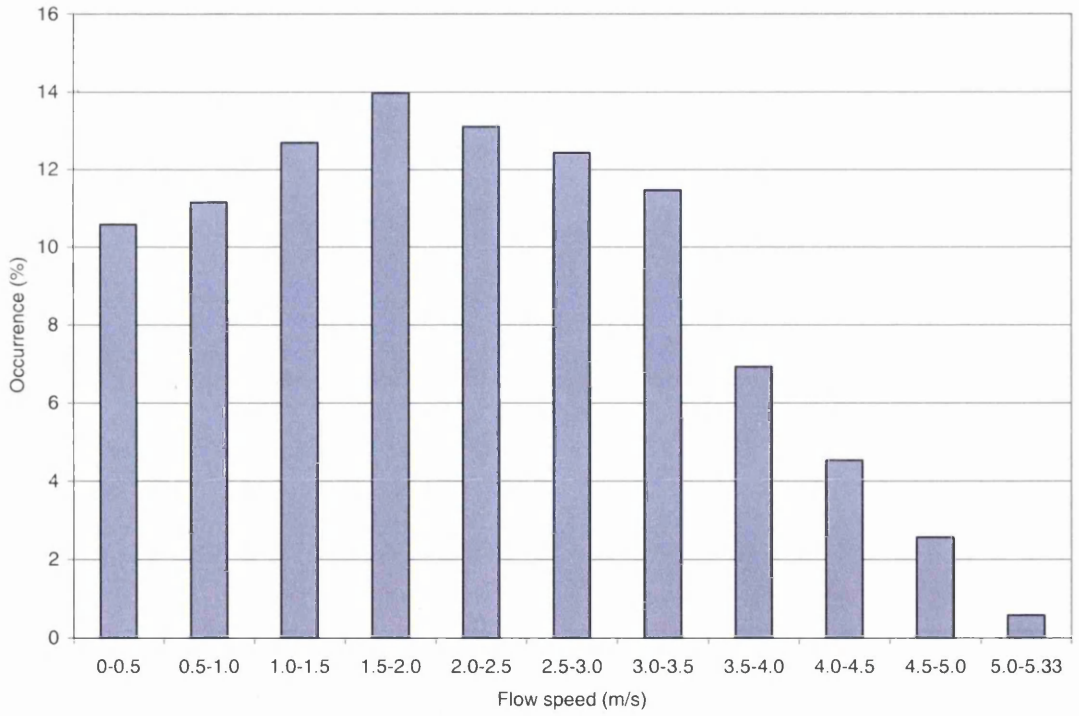

Figure 6.2: Occurrence of flow speeds at Alderney race from Baker [1].

	Flow speed	0-0.5	0.5-1.0	1.0-1.5	1.5-2.0	2.0-2.5	2.5-3.0	3.0-3.5	3.5-4.0	4.0-4.5	4.5-5.0	5.0-5.33
Wave height	**Percentage occurrence**	10.6	11.2	12.7	14.0	13.1	12.4	11.5	6.9	4.5	2.6	0.6
0-0.5	9.8	1.04	1.10	1.25	1.38	1.29	1.22	1.13	0.68	0.45	0.25	0.06
0.5-1.0	26.7	2.82	2.97	3.38	3.72	3.49	3.31	3.05	1.85	1.21	0.68	0.16
1.0-1.5	20.1	2.13	2.24	2.55	2.81	2.63	2.50	2.30	1.39	0.91	0.52	0.12
1.5-2.0	13.2	1.40	1.47	1.68	1.85	1.73	1.64	1.51	0.92	0.60	0.34	0.08
2.0-2.5	9.3	0.99	1.04	1.18	1.30	1.22	1.16	1.07	0.65	0.42	0.24	0.05
2.5-3.0	7.1	0.75	0.79	0.90	0.99	0.93	0.88	0.81	0.49	0.32	0.18	0.04
3.0-3.5	4.7	0.50	0.53	0.60	0.66	0.62	0.59	0.54	0.33	0.21	0.12	0.03
3.5-4.0	3.2	0.34	0.36	0.41	0.45	0.42	0.40	0.37	0.22	0.15	0.08	0.02

Table 6.1: Combined probabilities of flow speed and wave height, from Baker [1].

		Flow speed	0-1	1-2	2-3	3-4	4-5	5-5.33
Wave period	Wave height							
4.9901	1		7.93%	9.73%	9.32%	6.71%	2.59%	0.21%
5.8367	2		7.24%	8.88%	8.51%	6.13%	2.37%	0.19%
6.6833	3		3.56%	4.37%	4.19%	3.02%	1.16%	0.10%
7.5299	4		1.73%	2.12%	2.03%	1.46%	0.56%	0.05%

Table 6.2: Reduced version of table 6.1.

Once each case has been defined as in table 6.2, it is given a case number to allow quick reference to the source of any output data. The case numbers for this run are shown in table 6.3. The reader may note that certain wave cases have been excluded from the fatigue assessment. It is assumed that for these extreme waves, the rotor system would shut down, requiring a separate assessment of these load cases which is not included here.

		Flow speed (m/s)	1	2	3	4	5	5.33
Wave period (s)	Wave height (m)	TSR	4.5	4.5	4.5	4.5	5.54	5.75
		Loadcase No.						
4.9901	1		32_2	33_2	34_2	35_2	36_2	37_2
5.8367	2		38_2	39_2	40_2	41_2	42_2	43_2
6.6833	3		44_2	45_2	46_2	47_2	48_2	49_2
7.5299	4		50_2	51_2	52_2	53_2	54_2	55_2

Table 6.3: Case numbers for system assessment.

6.1.2 Running the model in batch mode

To model a variety of site cases, such as those in section 6.1.1, setting individual models running is time consuming and setting up batches and running the models without the operator present is preferable. The batch system also allows for a more consistent and structured approach to setting up cases and saving results, giving a more structured archive system and reducing overall set-up time and probability of user error. The process adopted in the code will now be described.

6.1.2.1 Site case set-up

The input files for each site case are stored in a site-specific folder that is assigned a site case number, the details of key input variables of each case are then noted in a list of site cases. In each of these created batch folders, the wave input file, 'input.dat', containing inputs for the open source wave model, the Matlab input script, 'inputvalues.m', and the Matlab variables stored in 'inputdata.mat' are created and modified for the particular site case. Also stored in the batch folder is a template for a sanity check, this will be discussed in a following section.

6.1.2.2 Running

With a group of these site case folders set up, a list of the directory paths of the folders is entered in the Matlab 'site_cases.m' script. It is a limitation of the current code that all of these paths must contain the same number of characters. It is therefore advisable to employ a standardised folder naming system and an existing 'site_cases.m' file is used as a template. To run these site cases, a controlling script 'Batchrun.m' was created. When this script is called, Matlab reads in the data for each site case using the 'load' command [2]. To allow the open source wave code to run, the 'input.dat' file is copied from the relevant site case folder to the current directory path, the open source code then reads this file as it would for a single run case.

6.1.2.3 Outputting

Summary data from the code is likely to be used regularly so it is transferred from the Matlab workspace to a csv file for broader compatibility. The Matlab function 'csvwrite' [2] does not lend itself to this operation as it is difficult to write a combination of text strings and numerical values, meaning that title headers could not be created using 'csvwrite'. To write the title line, the C style operators of fopen, fprintf and fclose are employed and to add the numerical values to the script, the Matlab operator 'dlmwrite' was used. The output file created by the open source wave code is then moved to the relevant folder by using the 'movefile' command. The script also outputs error logging data and writes useful data to a 'sanity check' template for validation of the results. These operations are covered in the following section.

6.1.2.4 Error logging and validation template

In its single run structure, the code is able to handle errors in three different ways. Large errors create a flag that make the system halt and return an error message. Less serious errors allow the system to continue running but warn the operator and log the errors in the workspace. The lowest level of error logging suppresses any warning and simply logs the message and details in the workspace.

When running in batch mode, it was decided that if one of the cases failed, it would be best that the batch continued running. The system was therefore altered so that all errors are logged and some print a warning to screen but none halt the process. The workspace for each case is written to its relevant folder at the end of a run. Contained in the workspace are the error messages and data outputs, it is therefore possible for the user to interrogate these after the batch run has completed. A special case is convergence of the BEMT solution, the high dependence of reliable results on convergence meant that this information was important enough to be output to the

aforementioned .csv file to allow for quick reference when using the data in the .csv file.

The error checking enables the user to ensure the code has run correctly but does not guarantee that the model has realistically captured the physical case. This is of increased importance during extreme flow cases and during validation of the code or validation of a new generator or yawing model. To accelerate the verification process, the code has been set up to write certain relevant data such as maxima and minima of loads and torques as well as their average values to a single document for the user to check. Input values and un-converged steps are also written for error checking. These values are written straight to an excel file using the Matlab command 'xlswrite'. It is then possible for the operator to open this file and examine the values, comparing against hand calculations where applicable to verify that a realistic solution has been produced by the model.

6.1.2.5 Batch structure conclusions

In this section, a means of running site cases in a batch system has been presented, the benefits from the structured input and output system and the reduction in operator time required using this system were highlighted. Using this approach, the model data given in 6.1.1 may now be input to the model and run.

6.1.3 Further model parameters

With the flow cases defined and the batch system available, it only remains to define the additional flow parameters and turbine system parameters. A downstream turbine system with an 18m diameter rotor, aligned to the flow direction was chosen for this study. Lift and drag data of the foil is the same as was used for the model runs in previous chapters, it was provided by Orme and was used in his thesis [3]. It was assumed that the flow follows a

$1/7^{th}$ power law profile throughout the constant water depth taken as 36m for all model runs. The basic over-speed generator model developed by Orme [3] and discussed in chapter 5 was used in this case, for the higher speed flow cases the target *TSR* was allowed to increase, shedding power. This represents a control system that flat rates the power production of the system for flow speeds above 4 m/s.

6.1.4 Results

The amount of data produced by this model for 24 time dependent runs is large. To aid the engineer, these values may be summarised in a number of ways. Elemental rotor loads are automatically resolved to forces and moments about the rotor hub but can also be interrogated on an element-wise level if desired. Maximum and minimum loads may easily be found from the stored matrices of data in Matlab or by exporting to an alternative format. A summary of maximum loadings about the hub is given in table 6.4.

	Hub centre load:	Heave	Sway	Axial	Yaw	Teeter	Torque
Loadcase		kN	kN	kN	kNm	kNm	kNm
32_2		1.5	-3.1	63.0	-12.0	69.5	93.4
33_2		2.2	-10.4	229.0	-28.8	228.6	336.5
34_2		3.3	-22.0	503.1	-53.3	481.5	734.3
35_2		4.7	-37.9	885.2	-84.6	827.6	1288.6
36_2		6.1	-52.7	915.9	-138.4	1385.2	1020.8
37_2		6.6	-58.6	905.2	-153.5	1592.0	915.8
38_2		3.8	-6.3	82.7	-21.1	125.5	129.9
39_2		4.9	-14.1	259.5	-45.3	310.3	390.1
40_2		6.6	-27.3	545.0	-78.0	600.2	804.0
41_2		8.6	-44.8	939.1	-117.6	982.8	1375.1
42_2		10.7	-60.3	963.7	-196.0	1593.0	1089.8
43_2		11.6	-66.7	951.5	-221.2	1820.5	981.6
44_2		-6.6	-10.0	112.5	33.8	184.4	187.8
45_2		7.8	-19.2	307.0	62.6	410.8	470.2
46_2		10.2	-33.6	611.0	-101.4	743.0	907.9
47_2		13.1	-53.0	1024.2	-148.5	1168.5	1505.7
48_2		16.3	-69.5	1033.7	-254.8	1831.8	1187.4
49_2		17.4	-75.0	1019.7	-295.5	2043.5	1071.1
50_2		-9.3	-13.6	152.9	182.6	260.2	262.9
51_2		-11.0	-24.0	370.8	93.9	512.2	571.6
52_2		13.5	-40.1	698.0	137.8	882.8	1042.6
53_2		17.4	-60.9	1136.5	188.0	1344.7	1674.8
54_2		21.8	-78.3	1129.7	345.1	2065.6	1305.5
55_2		23.8	-85.4	1107.0	392.3	2329.3	1178.1

Table 6.4: Summary of rotor loads and moments resolved to hub centre.

The maximum magnitude of loads is given in table 6.4. Some values appear to turn negative without following the general trend (such as the heave value for 44_2), this is because the values are oscillatory around a value close to zero. This means that the maximum positive value is of similar magnitude to the maximum negative value. This is an important design consideration, which is not apparent from a tabulation of maxima alone, showing the need for a more comprehensive approach to summarising the time varying loads.

A plot of the rotor torque shown in table 6.4 is given in figure 6.3, it can be seen that up to a flow speed of 4 m/s, maximum torque increases with both flow speed and wave height, this is as expected because the maximum torque is effectively increasing with flow speed for a fixed *TSR*. At flow speeds above 4m/s it can be seen that the rotor torque decreases, this is due to the flat rating of the generator mentioned in section 6.1.3, rotor torque decreases but rotor speed increases so that rotor power is kept constant above this flow speed.

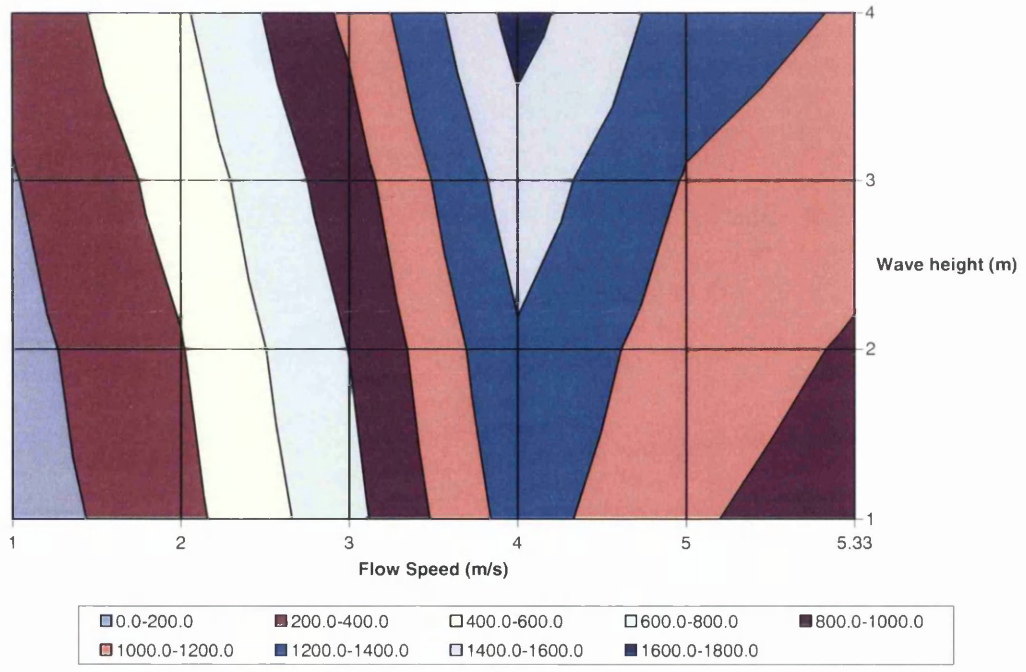

Figure 6.3: Maximum rotor torque value in kNm for flow speeds and wave heights modelled for Alderney race.

Further information may be given to the design engineer by summarising maximum, minimum and mean loads. A demonstration of this is given for the moment around a single blade root due to the axial force on that blade in tables 6.5 to 6.7.

		Flow speed (m/s)	1	2	3	4	5	5.33
Wave period	Wave height	TSR	4.5	4.5	4.5	4.5	5.54	5.75
		Peak Myb (kNm)						
4.9901	1		100	346	748	1300	1786	1997
5.8367	2		144	423	855	1440	1973	2180
6.6833	3		201	521	994	1617	2184	2398
7.5299	4		273	636	1148	1814	2408	2629

Table 6.5: Peak moment around blade root due to axial load on the corresponding blade.

		Flow speed (m/s)	1	2	3	4	5	5.33
Wave period	Wave height	TSR	4.5	4.5	4.5	4.5	5.54	5.75
		Min Myb (kNm)						
4.9901	1		47	189	428	759	927	993
5.8367	2		19	183	421	753	915	983
6.6833	3		-13	133	390	715	908	981
7.5299	4		-70	76	329	645	845	924

Table 6.6: Minimum moment around blade root due to axial load on the corresponding blade.

		Flow speed (m/s)	1	2	3	4	5	5.33
Wave period	Wave height	TSR	4.5	4.5	4.5	4.5	5.54	5.75
		Mean Myb (kNm)						
4.9901	1		66	265	595	1057	1427	1576
5.8367	2		66	266	598	1057	1429	1578
6.6833	3		68	275	601	1064	1435	1582
7.5299	4		71	283	607	1071	1439	1587

Table 6.7: Mean moment around blade root due to axial load on the corresponding blade.

The results are displayed graphically in figures 6.4 to 6.6. These plots show the variation of loadings in relation to wave height and flow speed. It can be seen that the mean and minimum values do not follow the same trend as the peak values. Peak moment increases with both flow speed and wave height but the minimum value decreases with increasing wave height. This is explained by the cyclic nature of the wave-induced flow. As the wave acts in the direction of the tide, the resultant flow speed is increased, giving a larger maximum rotor thrust (resulting in the larger peak torques of figure 6.4) but as the wave acts against the tide, the flow speed is reduced by the wave action, resulting in the lower minimum power for larger waves. Increasing wave height increases the amplitude of oscillation of the loads. Reference to

table 6.7 and figure 6.6 shows that the mean blade root axial torque is largely unaffected by wave height, this can also be attributed to the oscillatory nature of the wave induced flow.

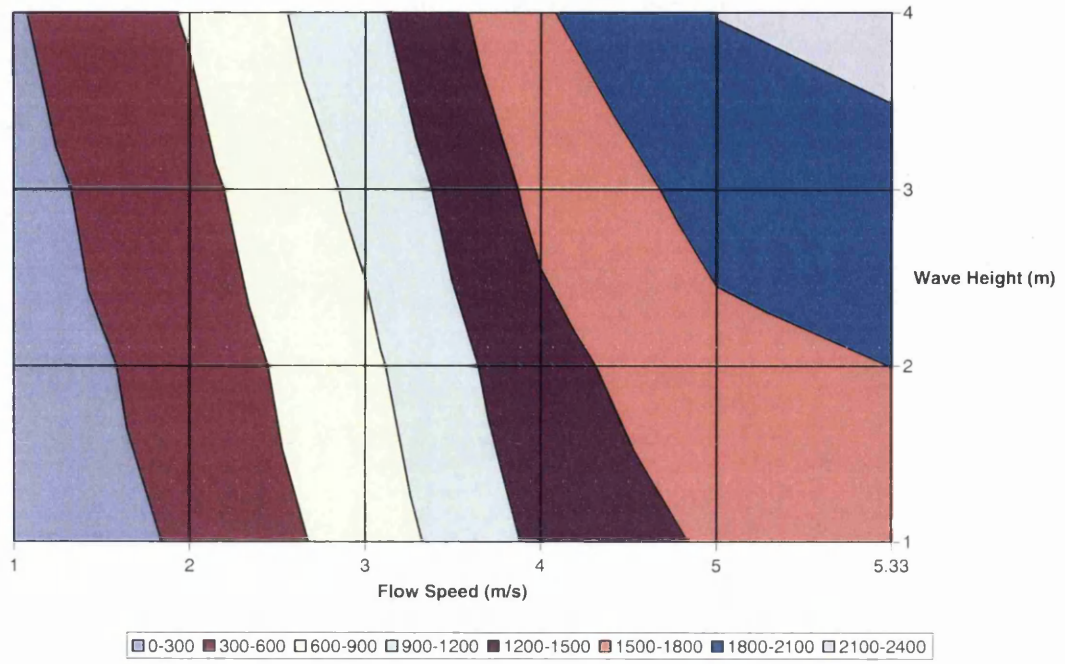

Figure 6.4: Peak moment (kNm) around blade root due to axial load on the corresponding blade.

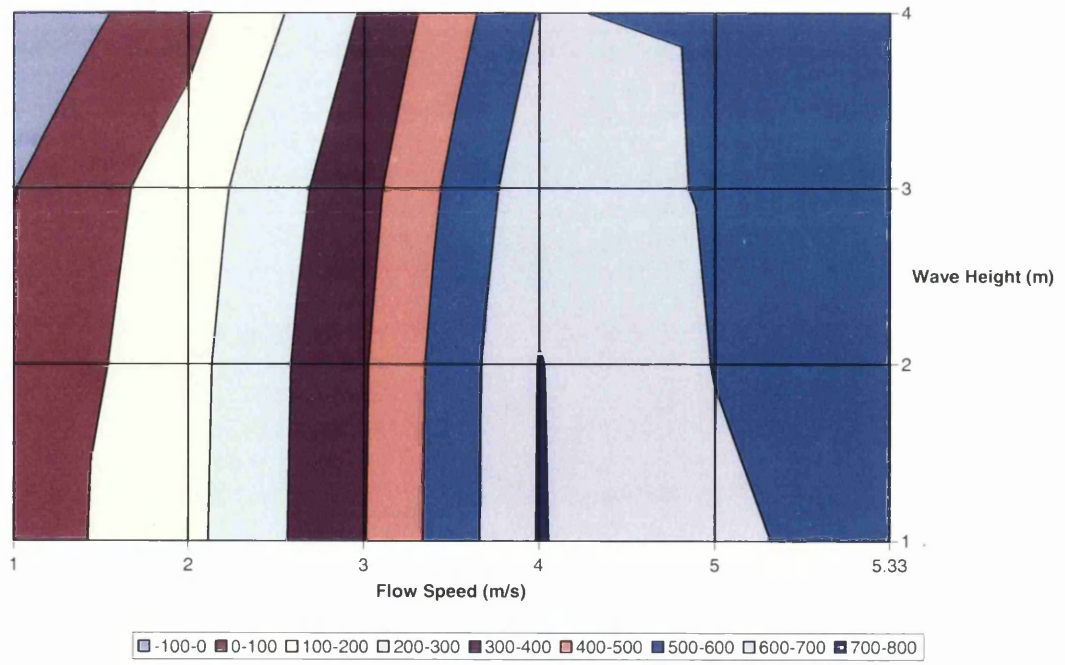

Figure 6.5: Minimum moment (kNm) around blade root due to axial load on the corresponding blade.

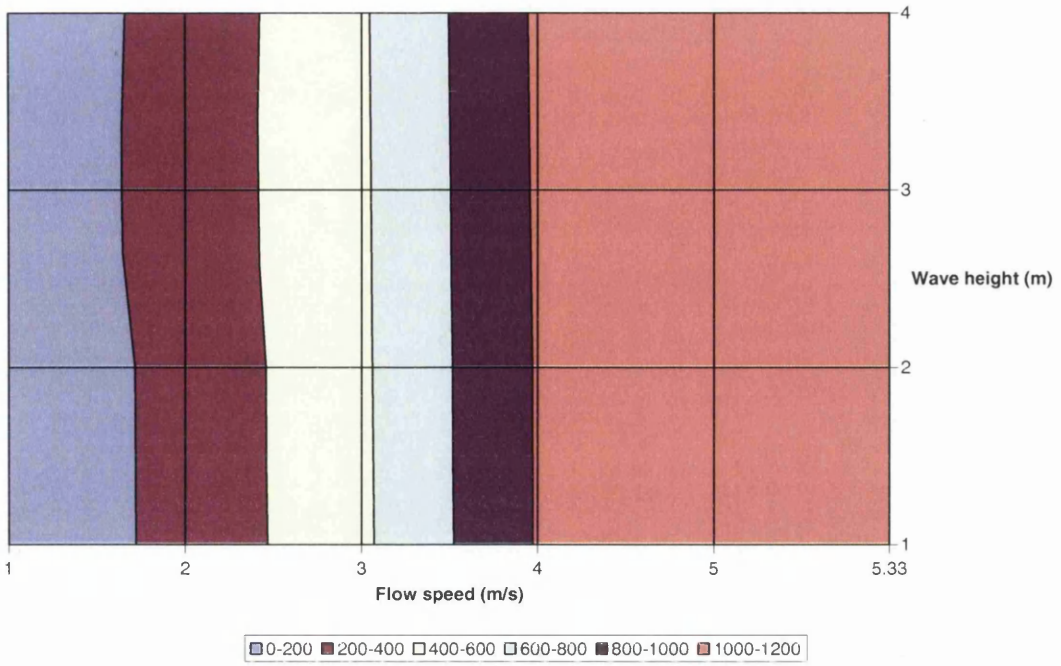

Figure 6.6: Mean moment (kNm) around blade root due to axial load on the corresponding blade.

Although the study of maxima, minima and mean values gives a better understanding of the loadings on a system, it still does not yield sufficient information for assessment of the fatigue regime on the system. To convert the time series data into information for fatigue assessment, Rainflow analysis may be used. This approach has a wide popularity in the wind turbine industry, reflected by its inclusion in the texts of Burton [4], Hansen [5] and Manwell [6]. Paraphrasing from Manwell *et al.* [6]; 'Rainflow analysis is a cycle counting technique to identify alternating stress cycles and mean stresses from a time series of randomly applied loads'. In his thesis, Johannesson [7] attributes the approach to Matsuishi [8] and Endo *et al.* [9]. The implementation of the Rainflow cycle counting method has not been conducted in this work, an open source Matlab script by Nieslony [10] has instead been employed. Nieslony developed the script according to the ASTM standard E 1049-85 [11] which uses an algorithm presented by Downing and Socie [12]. A detailed description of the algorithm will not be included here but the summary given by Manwell [6] is reiterated. Local maxima and minima are identified as peaks and valleys, the range between a peak and valley is considered as a half cycle. Each half cycle is compared to

sum complete cycles, which is associated with a mean. The reason this approach is termed Rainflow cycle counting is the graphical representation of the approach. The time series of peaks and valleys is turned 90° clockwise so that time is on the vertical axis, increasing downwards. Lines drawn between peaks and troughs are considered as roofs, rain travels down the roof and trickles off the peak, here it travels vertically downwards. A half cycle is counted when this runoff merges with the flow along another gradient, when it reaches the point of a peak of greater magnitude than the one it ran off or when it reaches the end of the time series.

The results of Rainflow analysis of the blade root moment from axial load will now be presented. Each load case must be analysed using the Rainflow approach. The results of the Rainflow analysis may be arranged in to bins of oscillation amplitude and mean using Nieslony's [10] script. In this case, 10 bins have been selected for both mean and amplitude, the number of bins may be varied however depending on the desired trade off between precision and data volume. To facilitate post processing, a further Matlab script was created to assess each load case and tabulate the results into an excel file. Samples of these results are presented for three of the twenty-four cases in Tables 6.8 to 6.10 and figure 6.7.

Oscillation Amplitude (kNm)	1	4	7	10	12	15	18	20	23	26
Oscillation Mean (kNm)	No. of cycles in 118s									
50	0	0.5	0	0	0	0	0	0	0	0
52	0	0	0	0	0	0	0	0	0	0
54	0	0	0	0	0	0	0	0	0	0
56	0	0	0	0	0	0	0	0	0	0
59	5	0	0	0	0	0	0	0	0	0
61	1	3	2	0	0	0	0	0	0	0
63	0	0	0	1	1	0	0	0	0	0
65	0	0	0	0	1	1	0	1	0	0
67	0	0	0	0	0	0	0	1	2	0
70	0	0	0	0	0	0	0	0	0	4.5

Table 6.8: Rainflow cycles for case 32_2 for blade root moment due to axial force.

Oscillation Amplitude (kNm)	13	35	57	79	101	122	144	166	188	210
Oscillation Mean (kNm)	No. of cycles in 118s									
456	0	0.5	0	0	0	0	0	0	0	0
480	0	0	0	1	0	0	0	0	0	0
504	0	0	0	1	3	0	0	0	0	0
527	6	0	0	0	0	4	0.5	0	0	0
551	0	0	0	0	0	0	2.5	2	0	0
575	0	0	0	0	0	0	0	1	1.5	0
598	0	0	0	0	0	0	0	0	1	5
622	0	0	0	0	0	0	0	0	0	3
646	0	0	0	0	0	0	0	0	0	0
670	0	0	0	0.5	0	0	0	0	0	0

Table 6.9: Rainflow cycles for case 40_2 for blade root moment due to axial force.

Oscillation Amplitude (kNm)	49	133	217	300	384	468	552	636	720	804
Oscillation Mean (kNm)	No. of cycles in 118s									
766	0	0.5	1	0	0	0	0	0	0	0
873	0	0	11	3	0	0	0	0	0	0
981	12	0	0	4	4	0	0	0	0	0
1088	0	0	0	0	4	1	3	0	0	0
1196	0	0	0	0	0	0	4	4	0	0
1304	0	0	0	0	0	0	0	1	4.5	7.5
1411	0	0	0	0	0	0	0	0	0	6.5
1519	0	0	0	0	0	0	0	0	0	0
1626	0	0	0	0	0	0	0	0	0	0
1734	0	0	0	0.5	0	0	0	0	0	0

Table 6.10: Rainflow cycles for case 55_2 for blade root moment due to axial force.

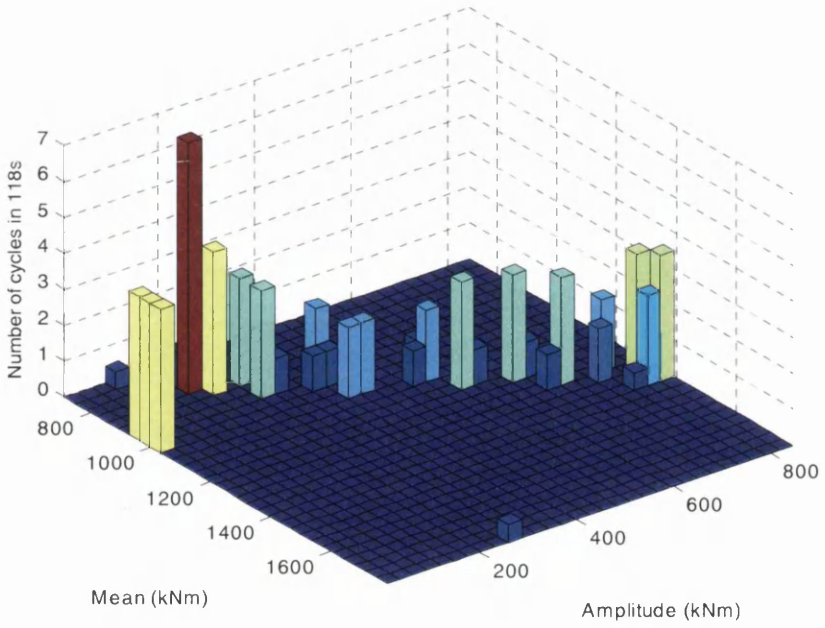

Figure 6.7: Rainflow plot for case 55_2 for blade root moment due to axial force.

The amount of data produced here highlights the need to automate the analysis as much as possible and demonstrates why the data was reduced from the original set of flow probability data for the case of this example. The results in Tables 6.8 to 6.10 relate to a 118-second modelling period. For the lifetime of the system, the number of cycles must therefore be multiplied by their probability of occurrence and scaled to the total operational lifetime to give the total number of load cycles. Once this has been carried out for the loading of a particular component (in terms of load, stress or strain), a cumulative fatigue assessment of the component may be carried out. It is generally suggested that Miner's rule [13] should be used for this [6]. The basic principle of Miner's rule is explained in Burton [4], it relates the number of strain cycles of a particular mean and amplitude to the number of permissible strain cycles. Each resulting damage value is summed to give the equivalent cumulative damage of the strain regime. The result should be below one for a component that is unlikely to fail. Figure 6.8 gives a Fourier transform of a single blade loading moment from load case 40_2. The two distinct peaks of wave action (at 0.77 of the rotor pass frequency) and tower shadow (once per rotor pass) can be seen.

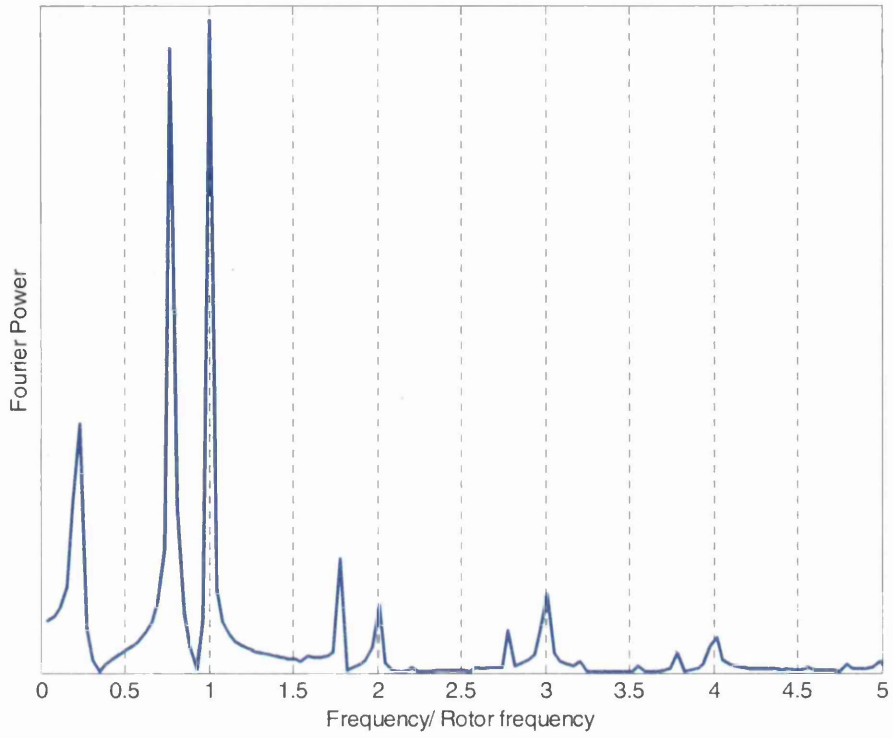

Figure 6.8: Fourier transform for case 40_2 for blade root moment due to axial force.

6.1.5 Discussion

The capabilities of the model to estimate the loading regime of a potential tidal site have been demonstrated in this section. Approximations of the site flow must be made to reduce the flow regime to a set of tidal flow cases with regular waves. This then allows time based loading results to be produced, which may be post-processed to give fatigue loading information, which is of vital importance to the design engineer. An irregular wave model, discussed in the previous chapter and in section 6.3 as well as a turbulence model would allow for a further increase in load prediction accuracy if reliable measurements could be obtained for the flow regime, this would further increase the volume of data. At the time of writing, this data is sparse but increasing as ADCP measurements of sites are made available by organisations such as EMEC [14]. The structure of the code allows incorporation of more complex flow models as discussed in section 6.3.

6.2 System design selection study

6.2.1 Modelling approach

A tidal stream rotor may have a variety of different yawing system concepts. The most effective approach will depend on the cost of manufacture and maintenance of the turbine system and the lifetime energy it produces. Although the ebb tide in a tidal regime is often approximately 180^{o} from the flood tide, this is not always the case so if a design is to be employed in multiple sites, it is important that all tide regimes are taken into consideration.

It was shown in Chapter 5 that the developed model is able to predict rotor performance at varying degrees of yaw misalignment. Power coefficients relative to the full tidal flow may be tabulated for a range of yaw misalignment angles and for a variety of rotor designs and layouts. If a group of tidal sites is selected it is possible to assess the relative energy produced by different system designs. A procedure to achieve this is presented in figure 6.9.

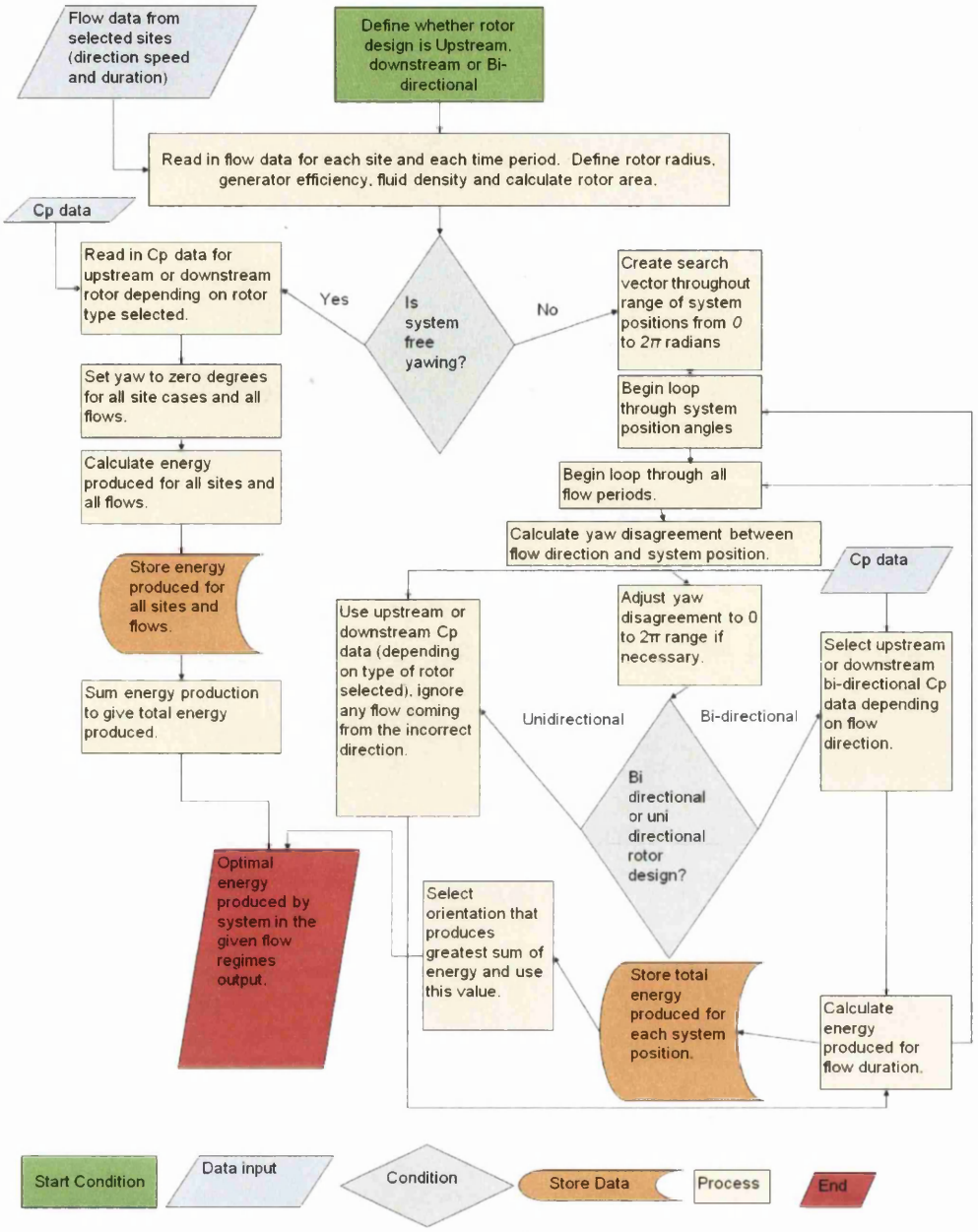

Figure 6.9: Rotor study Flow chart.

The model shown in figure 6.9 takes a yaw performance curve for each device type and a set of tide magnitudes and directions from a number of flow sites as inputs. The yaw performance curve is predicted using the code presented in the previous chapters. For a correct performance map from the code, it is important to note that performance varies with azimuth rotation when the rotor is yawed and when a depth varying flow is present. An average C_P at each *TSR* and yaw angle must therefore be taken after modelling performance throughout a full $2\pi/N$ revolution (taking advantage

of symmetry). It is vital here that the model's ability to account for losses in power due to tower shadow effects and flow misalignment is exploited. Depending on the type of control system envisaged, the operating C_P for each yaw orientation may be reduced to either the peak C_P, the C_P at a specific *TSR* or the C_P at a specific rotational speed for that yaw angle.

For a fixed yaw system, a positional optimisation can then be conducted. This uses the C_P data and seeks to maximise the power output from the system over all the sites by adjusting the installed angular orientation of the device. To achieve this optimisation, a simple search procedure with angular intervals of 1° is carried out and the best performing positioning angle for each site is used.

6.2.2 Example

To demonstrate the operation of this assessment tool, an example case study is now presented:
A study was conducted in order to assess the relative performance of four different types of system; upstream fully yawing, downstream fully yawing, two position yaw and a fixed position bi-directional device. The results of this lifetime energy study allow comparison of the performance of the different systems, this can then be factored into a cost benefit decision-making process for system selection.

For comparison purposes, the radius of the turbine rotor was fixed at 4.5m and a fixed generator efficiency of 0.92 was assumed. The flow data was collected from a number of sources and was provided by M. Willis in an internal communication [15]. The flow data covers tidal regimes from sites at Anglesey, Barry, the Solent, the Pentland Firth and Orkney area and a number of sites around the Scottish coast. The flow data consists of tide speed and direction data for a number of time intervals for each site. This data is summarised in table 6.11. The flow data is converted to SI units and

placed as input matrices into the system shown in figure 6.9. The more comprehensive this data is, the more precise the comparison of the different devices will be.

Group	Location	No. Data groups	Total time of samples (h)
Anglesey			
	Anglesey 1	26	24
	Anglesey 2	26	24
Barry			
	Barry 1	26	24
	Barry 2	26	24
Scottish			
	Orkney 1	6	36
	Orkney 2	6	36
	Orkney 3	6	36
	Orkney 4	6	36
	Orkney 5	6	36
	Orkney 6	6	36
	Pentland Firth 1	6	36
	Pentland Firth 2	6	36
	Pentland Firth 3	6	36
	Pentland Firth 4	6	36
	Pentland Firth 5	6	36
	Pentland Firth 6	6	36
	Pentland Firth 7	6	36
	Pentland Firth 8	6	36
	Pentland Firth 9	6	36
	West Scotland 1	6	36
	West Scotland 2	6	36
	West Scotland 3	6	36
	West Scotland 4	6	36
	West Scotland 5	6	36
	West Scotland 6	6	36
	West Scotland 7	6	36
	Kintyre 1	6	36
	Kintyre 2	6	36
	Galloway 1	6	36
	Galloway 2	6	36
Solent			
	Solent	26	24
Fall of Wareness			
	Fall of Wareness	26	24

Table 6.11: Summary of sites used in flow analysis for system concept comparison.

The yaw misalignment to flow is calculated for the different devices for each tidal period, for the fully yawing systems this is zero. For the two-position

yaw device and the fixed position system, optimisation of the positioning of the turbine must be conducted. For the two-position yaw system, the data was divided into flood and ebb tides and the code was run for both data sets, the sum of both runs was then used as the output for this case.

The calculation of yaw error allows the performance coefficient for each of the tide cases at each site to be interpolated from the provided performance curve for the device type being assessed. The performance coefficient is taken at a constant operational Tip Speed Ratio (the operating *TSR*) in this example. The interpolated performance coefficient, which takes account of yaw error, can then be used with the flow speed, fluid density, rotor area and time period of the related tide case to give the energy produced for each tide case and site. These values are summed to give a result for the system's expected 'lifetime' output. Either this lifetime output may then be used directly to provide a figure of energy produced during the modelled period or the values may be normalised to the maximum energy obtained by any approach to allow simple comparison between the device concepts.

6.2.3 Results and discussion

The normalised results are displayed in Table 6.12. The input data for Scottish sites had a large time interval, this meant that directional data was not very precise, so a study was run without these sites included. Some sites had compass directions for the flow directions rather than a more accurate bearing, as these give a lower accuracy of the tidal direction, a study was also conducted ignoring these sites.

In table 6.12, it is clear to see that, using this study, a free yawing upstream device gives the largest lifetime energy output of all systems. In the selection of a system though, cost implications of this type of device must also be considered. System availability has not been factored into these results either and a more complex system is more likely to be offline due to system faults than a simpler one. The two-position yaw system also performed well,

this is because the majority of tides are primarily bi-directional and so the small yaw error encountered by a two-position yaw system is not highly significant in terms of power production.

Device type	Normalised output	Normalised output excluding Scottish sites	Normalised output excluding compass direction sites
Free yaw - upstream	1	1	1
2 position yaw	0.9997	0.989	0.997
Free yaw - downstream	0.941	0.941	0.941
fixed elliptical	0.832	0.967	0.931

Table 6.12: Relative lifetime power outputs of different yaw systems.

A downstream infinite yaw device was seen to be almost as effective as the two-position device, the loss of energy compared to the upstream devices is due to tower shadow effects suffered by the downstream rotor. The free yawing downstream device shows a performance lower than what may be expected, this is explained by the fact that a large tower and hence large tower shadow were modelled in generation of the performance data. This demonstrates the importance of considerate hydrodynamic design of the supporting structure if downstream devices are to be used, performance could be significantly increased by careful design of the supporting structure. The bi-directional, fixed yaw and pitch system has a less efficient blade design because it must operate in two directions, this is reflected in its relative performance. This system is the simplest of all meaning that initial cost should be low and reliability should be high but the increased loadings from yaw error and tower shadow effects need consideration.

It is not possible to draw a definitive conclusion on the most suitable of the design concepts displayed here as reliability, cost and maintenance requirements must also be considered. The aim of this study was to demonstrate an application for yaw performance data produced by the model described in this thesis and to demonstrate the function of the system presented in this section. The combination of these approaches results in a useful analytical tool for the initial concept selection process of a tidal stream device.

6.3 ADCP data modelling

6.3.1 Methodology

In order to assess the true performance of a system in a specific site, it is desirable to be able to run the model subjected to realistic flow data. To achieve this, Acoustic Doppler Current Profiling [ADCP] data may be used.

For a specific site, data should ideally always be from a fixed reference point, seabed mounted devices are therefore the most likely systems to be used. A high sample frequency (ping rate) data set is desirable as this will allow short-term flow fluctuations to be captured, ideally a sampling period of a similar time scale to the modelling step would be used but this is an unrealistic target as equipment, physical and storage constraints mean a typical maximum ping rate is 2Hz [16].

One problem with using ADCP data directly is its form, the data will be for the entire water depth but for a fixed point in space over time. As the inflow data for the model must be at least three-dimensional (depth, length and time), several assumptions must be made to allow this data to be used directly. Firstly, it is assumed that the flow values are uniform in the *y*-direction, this allows the data to be used at a specific *x* value for any value of *y* and happens to be in accordance with recommendations in the recent BERR assessment guidelines [17]. It is also assumed that the flow velocities move through the inflow grid at a mean flow rate in the *x*-direction. Using this assumption, it is possible to space the time dependent data by making the distance between samples equal to the product of the mean flow speed and time between samples. With the data in this form, it is then possible to interpolate or map velocity values onto the global flow grid and update them at each time step.

Although the assumptions made mean that this procedure does not fully capture the real flow it is a close approximation and allows for simulation of a turbine system operating in the marine environment.

ADCP data does not contain information on the acceleration of the fluid so accelerative loads cannot be calculated using this data. If the time between flow samples was sufficiently small, the instantaneous acceleration could be approximated by the change in flow speed at each step, using the present ADCP technology this level of resolution is unlikely however. Figures 6.10 and 6.11 show that whilst the effect of neglecting accelerative loads is significant, the difference in results is not excessive and so may be neglected for initial appraisals of performance.

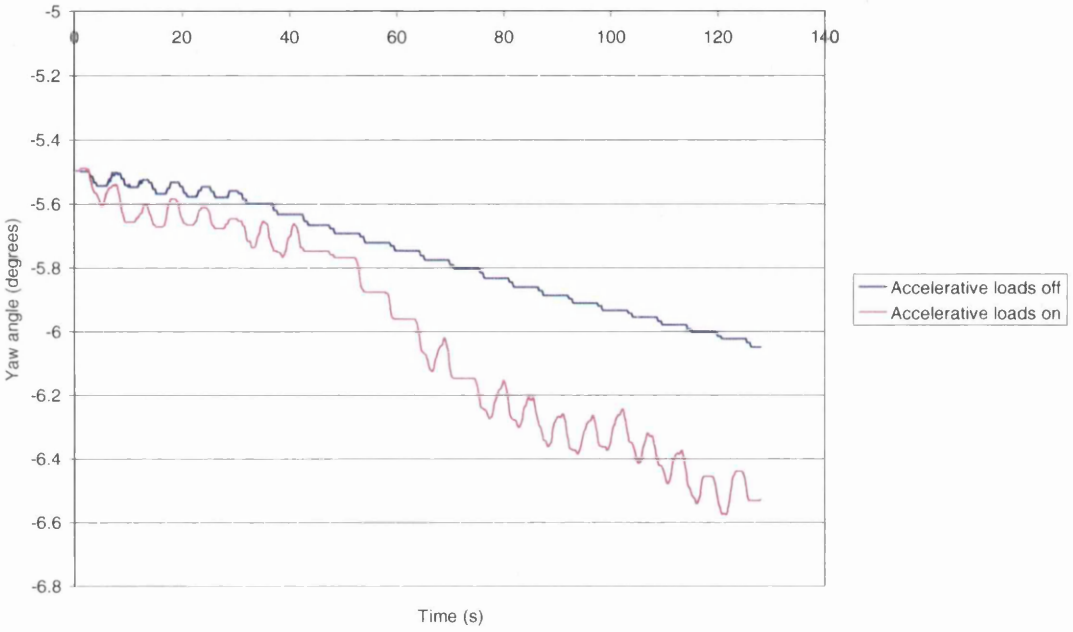

Figure 6.10: Yaw angle comparison of free yawing device with and without accelerative modelling in a 3m/s free stream flow with regular 5.55s 2.3m wave in 35m water.

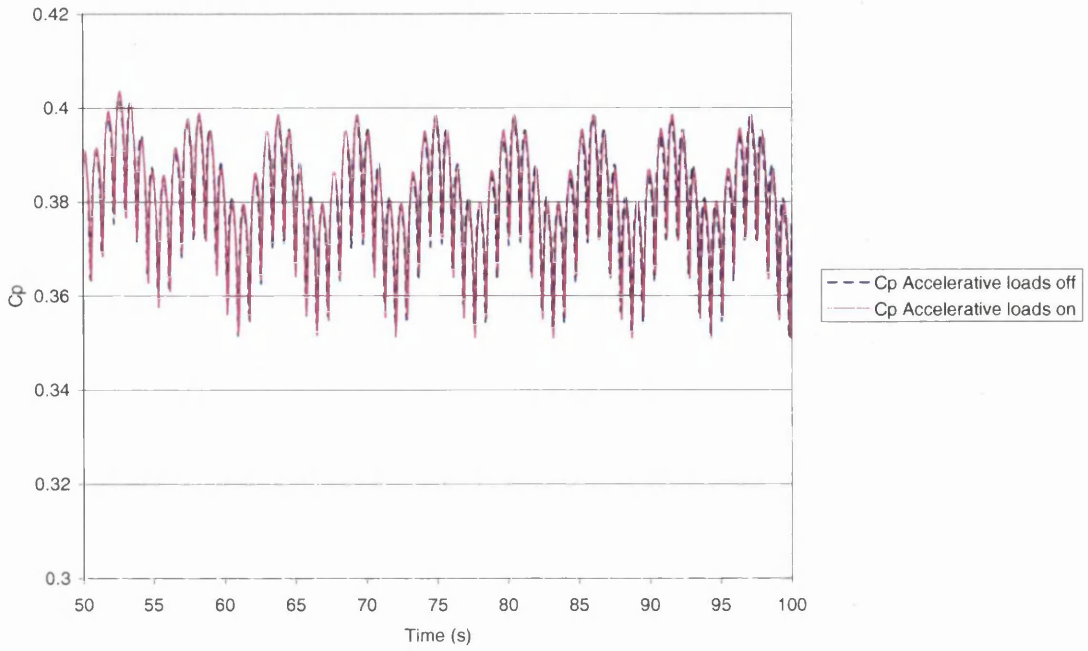

Figure 6.11: C_P comparison of free yawing device with and without accelerative modelling in a 3m/s free stream flow with regular 5.55s 2.3m wave in 35m water.

Determination of the resultant flow direction of the ADCP data and hence the correct yaw angle for the device can be challenging as it varies with time and position. It is therefore preferable to allow the model to calculate the correct yaw using a yaw model, as the system would in operation. The free-yawing model described in Chapter 5 has been used in this case.

6.3.2 Calculation of time span requirement of data set

ADCP data was provided by EMEC (see Norris [14]) for a variety of sites [24]. An example period was taken from one of these sites to demonstrate the procedure for transporting raw ADCP data into the time dependent turbine model.

From the full ADCP data, a manageable period of flow (figure 6.12) was selected. North, east and vertical velocities were output for each ping during this period.

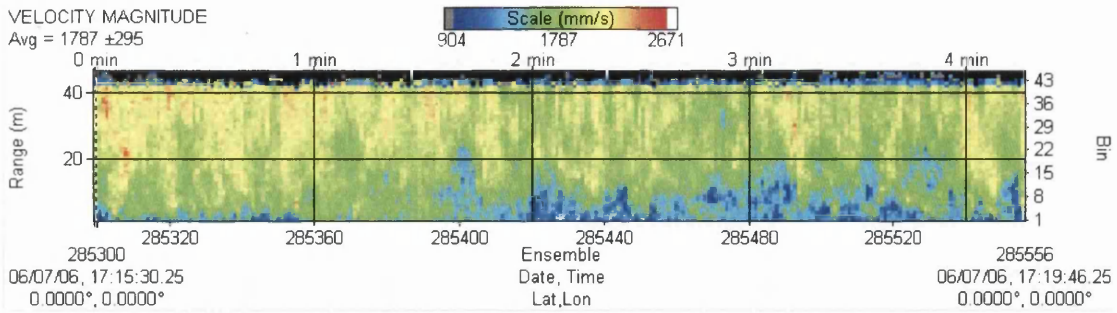

Figure 6.12: Velocity magnitude for sample period plotted by WinADCP [21].

The flow data is fed through the three dimensional grid much as the wave data is handled in Chapter 3. Whereas the wave data had a known wavelength and period, which could be used to space the data correctly in the flow grid, the non-uniformity of ADCP data requires a different approach. The bulk flow rate is calculated by taking the mean flow velocity throughout the modelling period for the north velocity, the direction that the data is fed through the modelling system. This then gives a reference flow speed and, as step frequency is defined, it is possible to correctly space the flow data to ensure that the flow is updated in real time (i.e. a set point will experience the same change in flow as was measured by the ADCP in the same time frame). It is important that sufficient flow data is used for the desired time span. The flow data must run for longer than the desired modelling time span as it must always be possible to fill the flow grid with data. The time span of data required may be calculated using the simple equation given in (6.1).

$$T_{ADCP} = \frac{T_{Model} \times \dot{M} + L_{Grid}}{\dot{M}} \qquad \ldots (6.1)$$

T_{ADCP} is the required time length of ADCP data, T_{Model} is the desired modelling time span, $\dot{M}$ is the bulk flow rate of the ADCP data and L_{Grid} is the length of the flow grid. In practice, the bulk flow rate is dependent on the time span selected, complicating (6.1). It is therefore preferable to approximate a bulk flow rate from an estimated time span and to use (6.1) as a guide, a time

span in excess of the resulting solution can then be taken to ensure the grid will be filled for the entire model time span. This approach reduces operator time and leads to an acceptably low increase in storage demand.

6.3.3 Interface Requirements

The output ADCP velocity data must be pre-processed by a developed Matlab script to interface with the turbine model. The steps involved are:

- The velocities are converted from mm/s to m/s.
- Erroneous data is found by checking through an iterative loop of data points and excessive flow values are set to zero.
- A time scale vector in seconds is created starting at zero for the first ping in the data set and spaced at the ping rate.
- A vector of water height above the seabed is created.
- Data below the ADCP is created by adding the seabed boundary constraint of zero velocity at the bed.
- Data is stored in structures to facilitate interrogation of the data.

The data after this stage is shown in figure 6.13. A more accurate approach is to create an interpolated value of erroneous flow speed rather than simply setting to zero. It is important that flow values above the free surface are not created if this is done however.

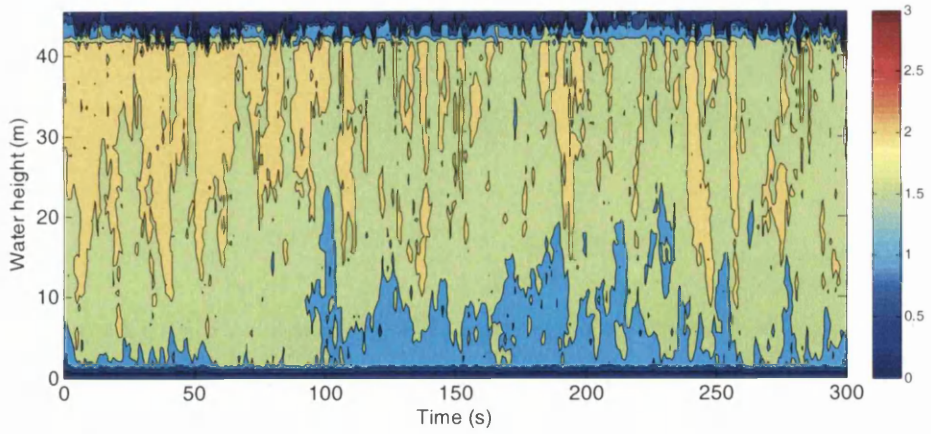

Figure 6.13: Sample of flow magnitude (m/s) after processing and reading in to Matlab.

6.3.4 Demonstration of ADCP data use

To demonstrate the operation of a turbine system in the converted ADCP flow, a model was run of a downstream, free yawing turbine system. Hub, tip and high induction corrections were turned on, as was tower shadow. The user defined generator model based on the work of Lawrence was employed [25].

Figure 6.14 shows the resulting variation in yaw angle of the system. It can be seen from the plot that the system is almost constantly yawing with the exception of a few stationary periods such as between 175 to 180 seconds. This is partially due to the lack of the additional damping provided by accelerative loads but is primarily a result of the constantly varying inflow velocities. This highlights the importance of including non-uniformities of flow in system modelling at the design stage as this yawing motion will be highly important when wear of the yawing system is considered.

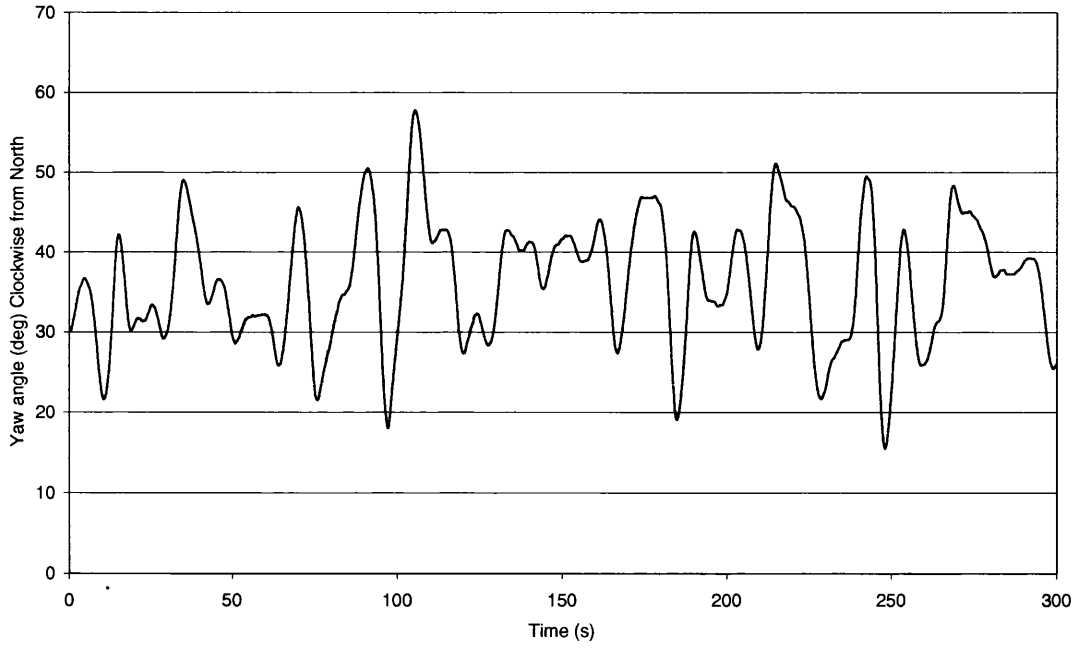

Figure 6.14: Yaw angle of rotor system, clockwise from North.

Figure 6.15 shows a compass plot of horizontal flow direction and magnitude, a quick comparison between this and the values in figure 6.14 show that the

yawing system is working reasonably well but a direct measure of yaw error as in figure 6.16 gives a more precise evaluation of this.

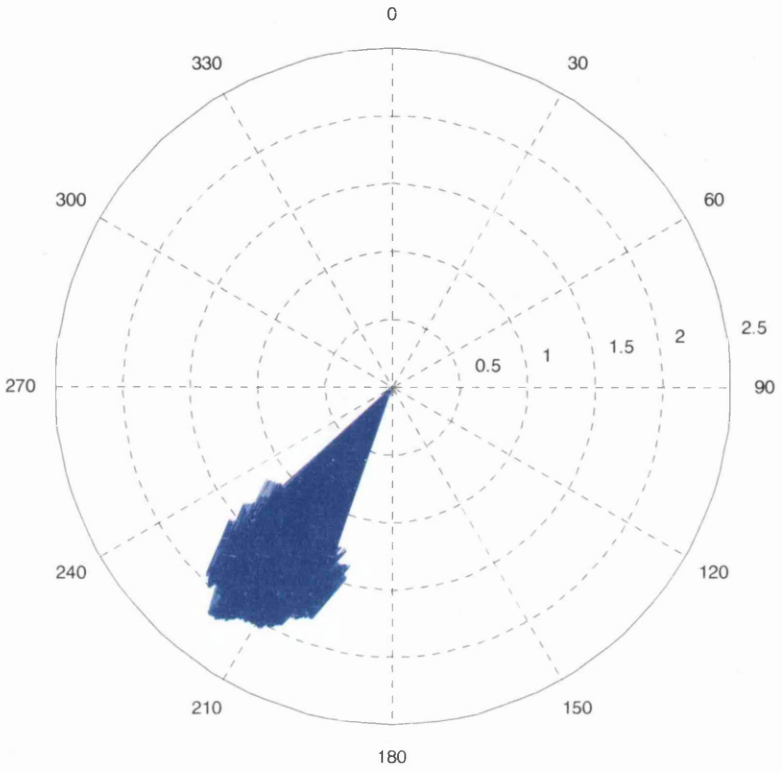

Figure 6.15: Horizontal flow direction (degrees) and magnitude (m/s) at rotor hub during modelling period.

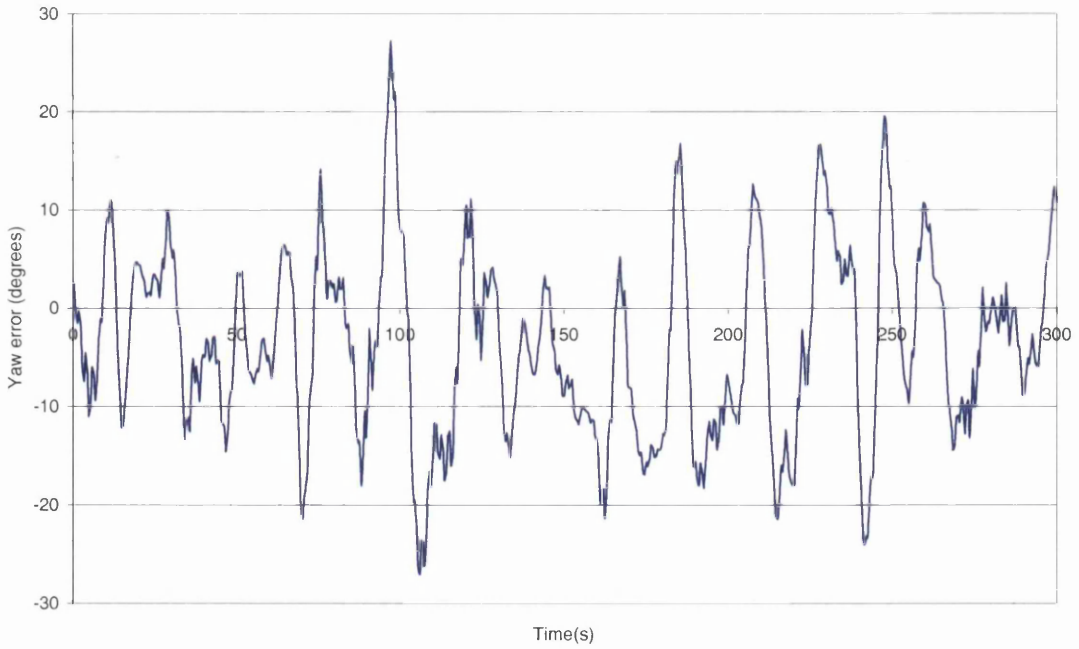

Figure 6.16: Yaw error measured against horizontal hub flow velocity.

Unfortunately, even the plot of yaw error in figure 6.16 does not give an exact indication of yaw misalignment. The flow, being non-uniform, has no single direction. Hub flow has been used here as a reference and whilst this provides a useful and easily comprehensible reference it does not necessarily reflect the nature of the flow across the whole of the rotor plane. Figure 6.17 shows a comparison of the hub flow magnitude and the mean flow velocity across the rotor plane, normal to the rotor plane. It can be seen that hub velocity does give a reasonable measure of whole rotor flow velocity in this case. It is important to remember however that flow velocity has a cubic relationship to power and that rotor torque and thrust are proportional to the square of flow speed, errors in flow speed share this relationship when carried through to torque, thrust or power coefficient measurements.

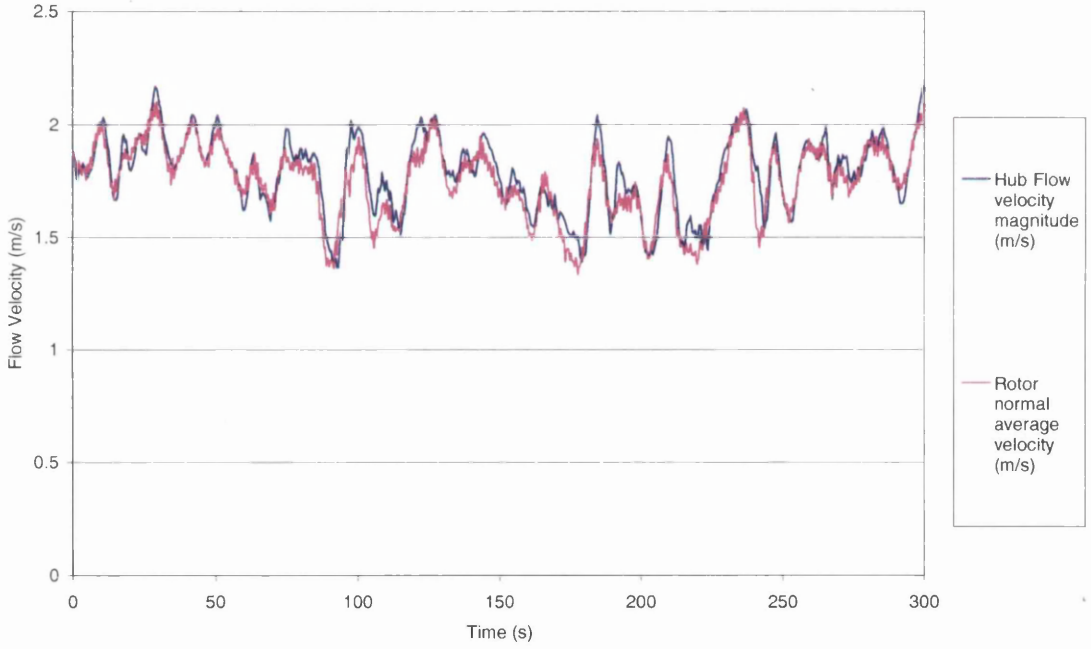

Figure 6.17: Comparison of hub flow velocity with average rotor normal velocity.

Tables 6.13, 6.14 and 6.15 give summaries of the data run. Table 6.14 shows that the standard deviation of the whole rotor average flow speed is the same as the standard deviation of the hub flow speed, this again suggests that hub flow speed is a reasonable parameter for comparison in this case.

	Yaw Speed	Yaw Speed	Yaw clockwise from North	Flow angle	Yaw error	abs yaw error
	Rad/s	Deg/s	Degrees	Degrees	Degrees	Degrees
Average	0.000	0.013	36.119	32.298	-3.821	8.232
Standard deviation	0.054	3.101	7.705	4.703	9.285	5.748
Max	0.210	12.049	57.660	48.033	27.129	27.129
Min	-0.142	-8.147	15.471	19.116	-27.098	0.005

Table 6.13: Summary of yaw measurements from ADCP model run.

	HubU	HubV	Flow magnitude	Mean rotor flow velocity
	m/s	m/s	m/s	m/s
Average	-1.50	0.95	1.78	1.75
Standard deviation	0.15	0.16	0.16	0.16
Max	-0.96	1.38	2.17	2.09
Min	-1.79	0.55	1.36	1.33

Table 6.14: Summary of Flow characteristics from ADCP model run.

	Power Kw	Cp hub	Cp mean rotor flow	Hub normal power/ power in flow
	kW	-	-	-
Average	65.668	0.357	0.376	0.949
Standard deviation	16.046	0.059	0.035	0.111
Max	112.370	0.673	0.468	1.514
Min	29.587	0.202	0.214	0.573

Table 6.15: Summary of power performance from model run.

Figure 6.18 provides plots of C_P using both hub flow velocity magnitude and average flow speed normal to the rotor plane as reference flow speeds. Accepting the inaccuracies of using both reference flows mentioned in the previous paragraph, these two power coefficients give a measure of the performance of the system incorporating yaw error in the case of the hub velocity and neglecting yaw error in the case of the mean normal flow speed. The plot clearly suggests that yaw error accounts for a degree of efficiency loss as, for the majority of the run, the hub flow C_P value is below the rotor normal flow C_P value. The exceptions to this, such as the spike just before 100s, may be attributed to local turbulence at hub height, which is not reflected in the rotor-averaged values. Comparison of the mean C_P values

given in table 6.15 suggest that the reduction in performance due to yaw error is low, the difference shown between hub and mean rotor values being only 1.9%.

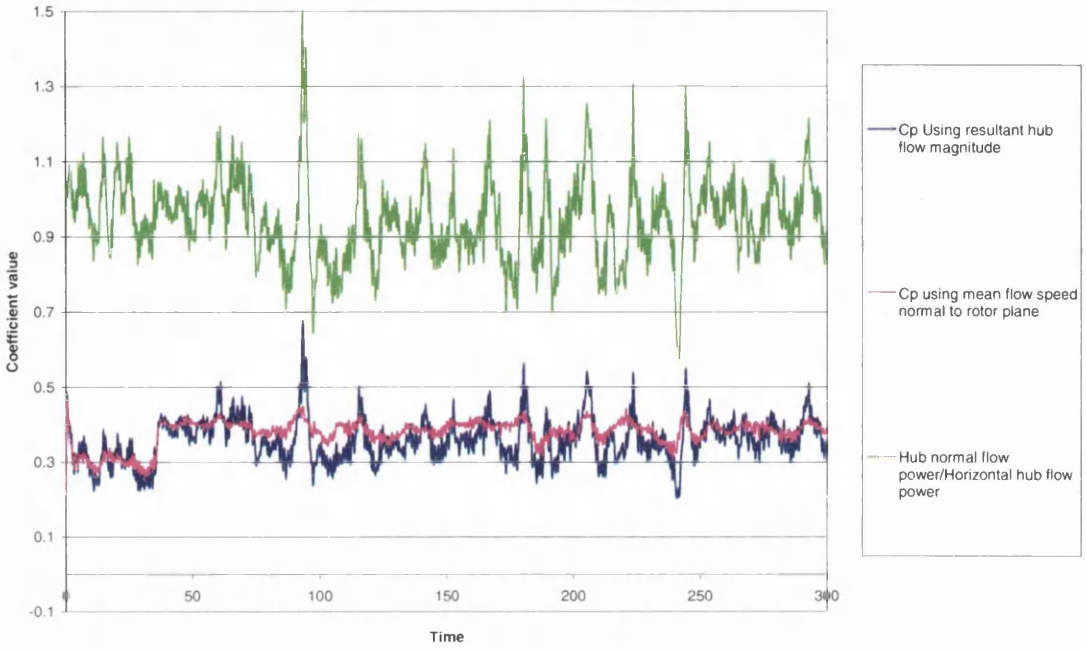

Figure 6.18: Comparison of C_P using Hub flow velocity magnitude as reference and using Rotor normal average speed as reference. Ratio of rotor averaged flow speed to hub flow speed also plotted.

Despite the ADCP data showing distinct non-uniformity, rain flow analysis of the resulting rotor loads still gives distinct trends of cycle mean and amplitude values. Examples of these analyses are given in figures 6.19 and 6.20. It can be seen in both of these plots that there is no longer the single distinct load band created by wave and rotor pass cycles as seen in Fig. 6.7.

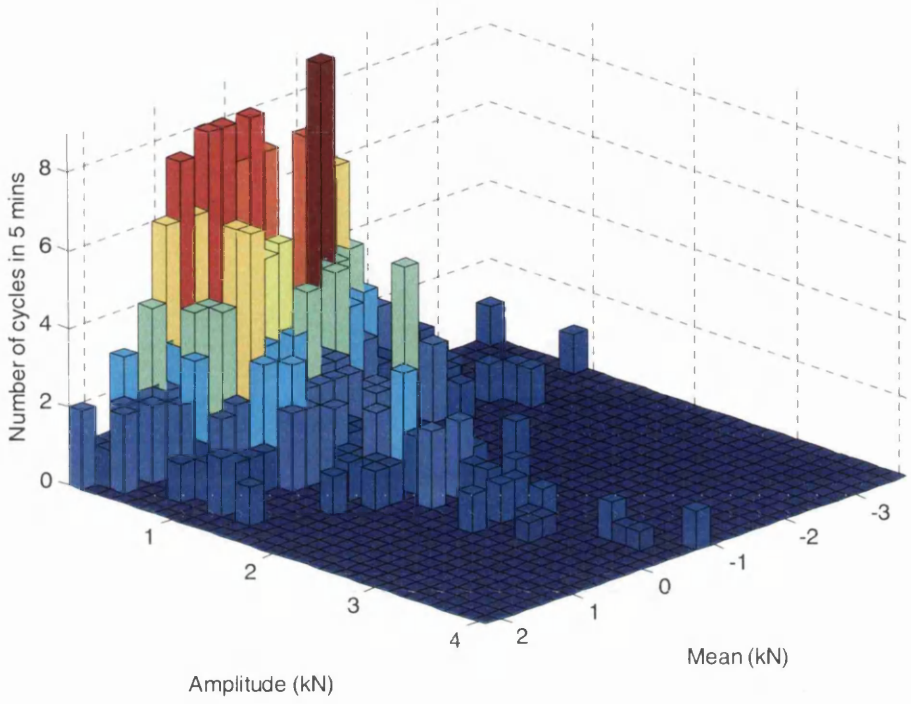

Figure 6.19: Rain flow analysis of heave force produced by rotor in ADCP data run.

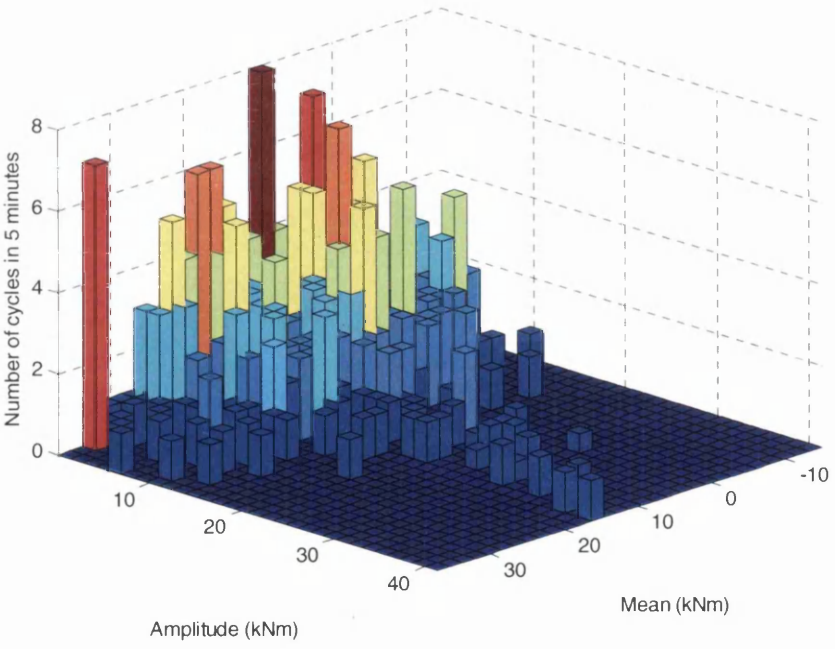

Figure 6.20: Rain flow analysis of teeter torque around hub produced by rotor in ADCP data run.

There is however still a general trend in the data. In all cases, the number of cycles is of a similar order to the number of blade pass oscillations that would be expected. The mean rotor speed is 17rpm during this run and so in the 5-minute period this could be expected to count for 255 cycles (17*5min*3 blades). The six rotor load and torque outputs (heave, sway, axial load, yaw torque, teeter torque, rotor torque) showed between 359 and 401 cycles each during the 5 minute period. It is therefore clear that rotor pass is responsible for over half of the oscillations seen. In this case, tower shadow is a significant contributing factor to load oscillations of rotor pass frequency, this demonstrates how important minimisation of shadow effects is on the fatigue life of the system.

A Fourier transform of teeter torque (Figure 6.21) shows that there is indeed a concentration of oscillation around blade pass frequency (3 on the x-axis of figure 6.21). There also appears to be a distinct oscillation with a frequency slightly less than that of the rotor pass (just below unity on the x-axis). It is not clear why this is but study of figure 6.22 suggests that this oscillation could be due to flow variations, this is far from conclusive however.

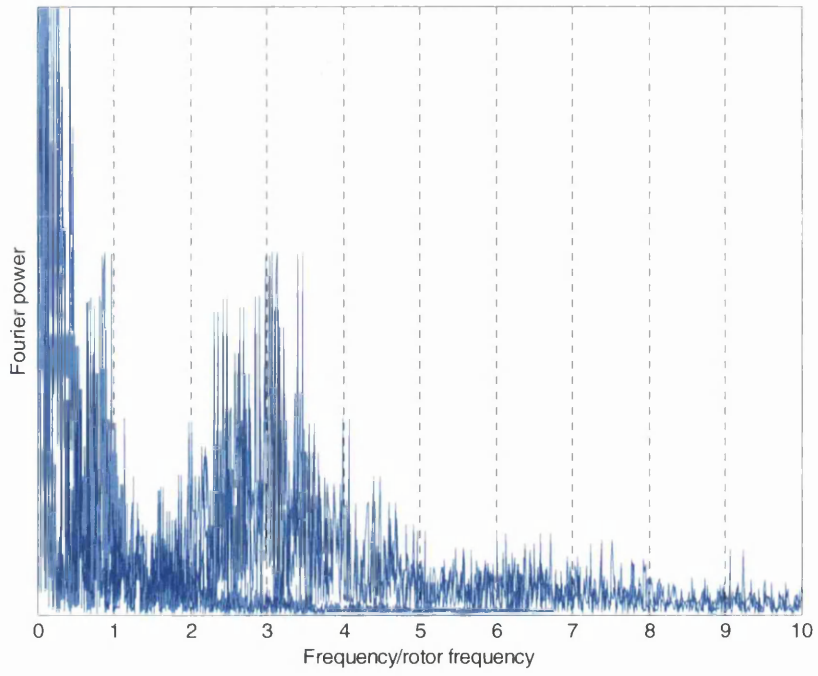

Figure 6.21: Fourier transform of teeter torque produced by rotor in ADCP data run.

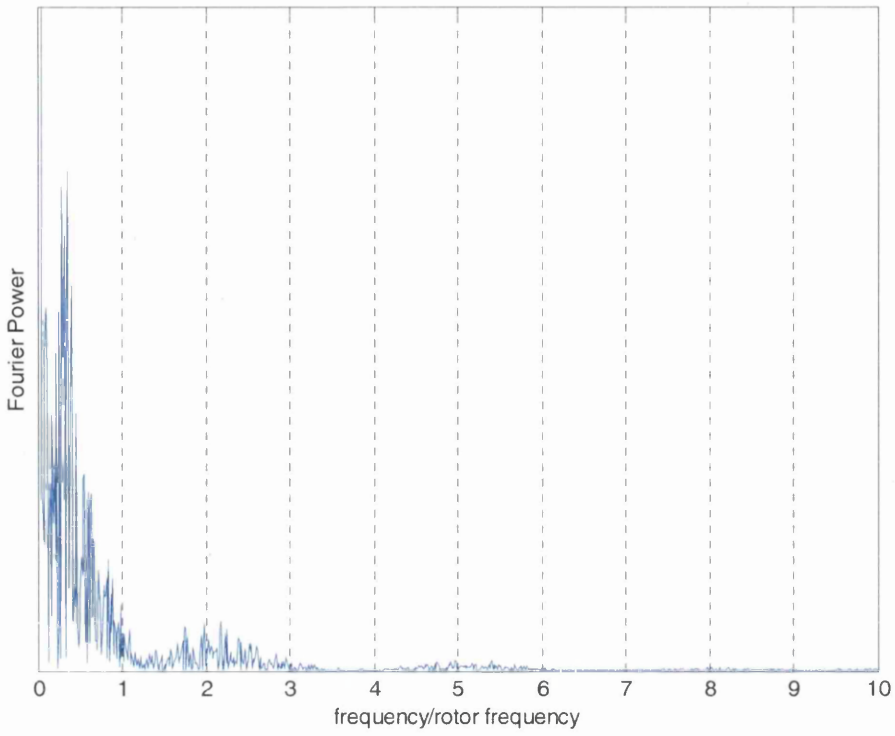

Figure 6.22: Fourier transform of horizontal flow magnitude from ADCP data run.

6.4 Conclusions

In this chapter:

- The application of the theory of all previous chapters was shown. The practical use of the developed code has been demonstrated by producing lifetime fatigue loading data for an example site.
- Basic blade performance data output by the BEMT code was employed in a novel approach to compare the performance alternative design concepts in a range of sites. This could be used in a cost/ benefit analysis of alternative design concepts.
- In section 6.3, a novel approach to using ADCP data as a direct input to the model was discussed and an example given. The significance this non-uniform flow has on operation has been demonstrated with the aid of Rainflow and Fourier analysis. The results demonstrate

both the function of the system model and the non-uniformity of real sea flows.

- The advantage of using data measured from the true environment is clearly demonstrated by the results of the case study. The flexibility of the code has been demonstrated by giving different examples of its use.

As an area of further work, a more accurate system than using ADCP data directly could be developed. Either by the use of ADCP arrays, giving flow values for three-dimensional grid points or by analysing ADCP data and modelling it as tidal, wave and turbulent flow components. A number of papers document the latter approach, for examples see Rørbæk [18], Strong [19] and Terray [20]. It can be facilitated by the use of available programs such as WinADCP [21], WavesMon [22] and WavesView [23] which allow the raw ADCP data to be converted into North, East and vertical velocities before being post-processed to filter wave spectra and current profiles. If a sea state model is available, the resulting spectrum may then be modelled to give a time dependent output. This approach has two distinct advantages, accelerative flow terms may be modelled and modelling parameters may be extrapolated to approximate extreme seas and rare flow occurrences, which may not have been captured in the ADCP measurement period. Sea state modelling of this complexity is out of the scope of this thesis and warrants separate in depth development. Either of these approaches would be more costly, financially or in terms of time compared to the present, direct data usage approach but would lead to an even closer understanding of the sea conditions at a site and therefore the performance of turbine systems in real cases. The model is capable of taking such inflows and predicting the performance directly because of its three-dimensional mapping capabilities. The direct inputting approach presented in this section could be used to check the validity of a developed sea state.

6.5 References

[1] Baker, T., "Alderney race wave and tide data", Swanturbines, 2008.

[2] MathWorks, "The MathWorks - Online Documentation, R2007b". 2007.

[3] Orme, J., "Dynamic Performance Modelling of Tidal Stream Turbines in Ocean Waves", PhD Thesis, 2006, Civil and Computational Engineering, Swansea University.

[4] Burton, T., *et al.*, "Wind Energy Handbook". 2001, Chichester: John Wiley & Sons.

[5] Hansen, M., "Aerodynamics of Wind Turbines" Second Edition ed. 2008, London: Earthscan.

[6] Manwell, J.F., J.G. McGowan, and A.L. Rogers, "Wind Energy Explained". 2002, Chichester: John Wiley & Sons Ltd.

[7] Johannesson, P., "Rainflow Analysis of Switching Markov Loads", PhD Thesis, 1999, Centre for Mathematical Sciences, Lund University

[8] Matsuishi, M. and T. Endo, "Fatigue of metals subjected to varying stress", JSME, 1968.

[9] Endo, T., K. Mitsunaga, and H. Nakagawa. "Fatigue of metals subjected to varying stress" in Chugoku-Shikoku District Meeting. 1967: JSME.

[10] Nieslony, A., "Rain flow for MATLAB". 2005, Matlab Central File Exchange http://www.mathworks.com/matlabcentral/fileexchange/loadFile.do?objectId=3026.

[11] ASTM, "ASTM E 1049-85 (Reapproved 2005), Standard practices for cycle counting in fatigue analysis", Annual Book of ASTM Standards, 1999. 03.01: p. 710-718.

[12] Downing, S. and D. Socie, "Simple rainflow counting algorithms", International Journal of Fatigue, 1982. 4(1): p. 31-40.

[13] Miner, M.A., "Cumulative damage in fatigue", Journal of Applied Mechanics, 1945.

[14] Norris, J. and E. Droniou, "Update on EMEC activities, resource description, and characterisation of wave-induced velocities in a tidal flow".

[15] Willis, M., "Flow directions of top UK sites", 2007, Spreadsheet.

[16] Instruments", T.R. "Workhorse Sentinel self-contained 1200,600,300 kHz ADCP, The Global Leader", 2 Online: http://www.comm-tec.com/Prods/mfgs/RDI/brochures/wh_sentinel.pdf, Accessed: 22/08/08.

[17] BERR, "Assessment of performance for tidal energy conversion systems", EMEC, Editor. 2008, Crown Copyright.

[18] K. Rørbæk and H. Andersen, "Evaluation of wave measurements with an Acoustic Doppler Current Profiler", IEEE, 2000.

[19] Strong, B., B. Brumley, and G. Stone, "The Performance of ADCP-Derived Directional Wave Spectra and Comparison with Other Independent Measurements", IEEE, 2000.

[20] Terray, E., B. Brumley, and B. Strong, "Measuring Waves and Currents with an Upward-Looking ADCP", IEEE, 1999.

[21] RD Instruments, "WinADCP". 2003 http://www.rdinstruments.com/cc_software.html.
[22] Strong, B., "WavesMon". 1998, RD Instruments, http://www.comm-tec.com/Prods/mfgs/RDI_Prods.html.
[23] Strong, B., "WaveView". 1998, RD Instruments, http://www.rdinstruments.com/cc_software.html.
[24] EMEC, "ADCP dataset for tidal test sites." 2007, Computer files supplied to Swanturbines Ltd.
[25] Lawrence, N., "Control model internal communications", 2007.

Chapter 7: Conclusions and Further Work

7.1 Discussion and conclusions

In this thesis, a novel tidal turbine hydrodynamic model has been developed. The implementation of a three dimensional system has been introduced and various hydrodynamic improvements were added. A new means to incorporate tangential blade flows into BEMT has been introduced and a novel solution approach for the BEMT functions has been presented. Specific abilities of the code include a novel approach to modelling a rotor system with blades removed. Bespoke yawing, generator control and braking models were presented to demonstrate the facilities for whole system modelling. A new calibrated tower shadow model was developed at realistic Reynolds No. ranges. A novel means of introducing ADCP flow data directly as inflow parameters was also demonstrated. The system has been validated against a commercial BEMT code and a lifting line theory code. Results compare well to these models. The specific advantages of the system presented in this thesis over existing codes are the ability to model cross flows, the presence of a marine calibrated shadow model and overall flexibility to allow specific generator and yaw control algorithms to be coded.

A method to model the complete system of forces, including inertial loads on the supporting structure as well as the rotor system has been introduced, accelerative loads are included in these calculations. The application of the system to true engineering applications was then demonstrated.

The code developed during this thesis provides a comprehensive modelling system for the design engineer. Specific features enable testing of control systems and design features, allowing preliminary development to be carried out rapidly and without the cost involved in system deployment. The model has already found application in industrial situations for load definition and system modelling with Swanturbines Ltd. where the ability to approximate a true system is of great use.

In Chapter 6, a novel approach to aid concept selection was also presented, this employed yaw performance data produced by the BEMT code and compared the performance of different yawing and blade design concepts at a range of different flow sites. The application of this in a cost benefit analysis of tidal device concepts was suggested.

7.2 Comparison of the developed code to existing models

The code developed during research for this thesis includes some unique features based on novel theory work. The features of two well known blade element modelling codes, GH Bladed [3] and the AeroDyn [4] modelling suite, will now be compared to the capabilities of the present model.

Bladed and AeroDyn both benefit from a significant amount of development and are efficient codes, both are also Germanischer Lloyd certified. AeroDyn is an open source code but it does not have a graphical user interface, it is also developed specifically for wind turbines. Incorporation of supporting structure loading is not accounted for. The inflow is also based on wind and so employing realistic tidal inflows would be difficult. Tower shadow, high induction correction and tip-loss correction are all based on empirical corrections from wind turbine experiments, the applicability of these corrections is therefore dubious in a tidal environment.

A Tidal version of bladed is available, giving options for wave and tide modelling and consideration to the applicability of the corrections employed to the base model. The graphical user interface of Bladed facilitates its use in most cases but does reduce the flexibility of the code to add specific features, making direct collaboration with Garrad Hassan necessary in these circumstances. The modelling of inertial loads on the rotor system itself appears to be absent from the bladed code, this is one area where the code developed in this thesis has an advantage over existing codes. As this theory was proposed by Orme, the only other model to feature this is his model. The structure of Orme's model leads to less flexibility than the code presented in this thesis and the model lacks many of the loss corrections,

shadow modelling, and three-dimensional tracking abilities of the present code. This is to be expected as the research conducted by Orme was used as a base for the present model.

Cross flow is not modelled in the BEMT equation in any other code, again an advantage of the approach presented in this thesis. Also absent from other modelling suites, but available in the presented model, is a tower shadow model developed specifically for tidal turbine systems.

7.3 Recommendations

During the course of research for this thesis, several key areas became apparent as important fields of further research or development of the code that were unfortunately outside of the scope of the project; these are:

- Fluid-Structure Interaction (FSI): The modular, time dependent and three-dimensional features of the model facilitate multi-physics modelling. Loose coupling already exists as the calculated fluid loads are fed into the generator control model and the nacelle yawing model. Further development of this could be to incorporate finite-element modelling of the supporting system and rotor blades. The simplest case of this would be to apply beam theory to the supporting tower and blades in order to calculate deflection in the structure, which would affect the velocity, position and loading of the system. Development of a multi-physics model would enable investigation of flexible blade design, which will become more critical as tidal turbines increase in size.

- Alternative Fluid Model: BEMT is an efficient flow solver and for many circumstances will offer a sufficient degree of accuracy in load prediction. If a more detailed investigation of loadings and effects on the water flow is desired, a more complex flow model will be needed. Implementation of a lifting line or lifting surface theory may be desirable although a prescribed wake (computationally less

demanding) approach will not necessarily offer a great improvement in accuracy for off-design conditions. An un-prescribed or dynamic wake approach would lead to a high computational demand. Alternative prediction techniques could be more rigorously investigated and the most suitable approach could be employed.

- Development of Marine Specific Corrections: BEMT makes several assumptions, one of these is that the rotor blades may be approximated as two-dimensional aerofoils. This implies an infinitely long blade, in reality a radial flow along the blades is encountered which has an effect on stall properties and losses are seen from vortices being shed from the blade root and hub. Within the wind industry, where blade element theory has been used for some time, there are widely accepted corrections for tip and hub losses as well as the turbulent wake state and stall delay (where assumptions in traditional blade element theory become physically invalid). Specific empirical corrections should be validated and developed for tidal stream turbines, this could be achieved using a combination of model testing and CFD simulation. Further validation with real life results as the tidal stream industry grows could lead to a more accurate modelling system.

- Free surface interaction: In chapter 2, research into the effect of a free surface was reviewed in several papers (for example, [1]) it is unclear to what extent the free surface will impact the performance and loading on the system in full-scale operation. Incorporation of this effect will lead to greater accuracy so further research and implementation of this effect is advisable.

- Turbulence: The impact of turbulence on the model was demonstrated to some extent in chapter 6 with ADCP data usage. Available data on marine turbulence of the scale of interest to tidal turbine modelling is not widely available at present but development of

a suitable turbulence model would increase accuracy when dealing with realistic sea conditions.

- Sea-state modelling: Sea state modelling has been discussed in chapters 3 and 6. With the increasing availability of site-specific flow data, ability to define sea state scenarios for potential sites will become more common. Incorporation of a sea-state model will therefore represent a significant development in the precision of the load model and resulting fatigue regime predictions.

- Cavitation: The prediction of cavitation inception was demonstrated in several of the papers reviewed in chapter 2 (Wang *et al.* [2] and Bahaj *et al.* [1]). Incorporation of this research into the developed code or addition of a similar model would provide a useful additional feature to the design engineer.

7.4 Additional publications

During the course of PhD study several conference papers were produced, these were:

- Orme, J., J. Chapman, and I. Masters, "ASPECTS OF THE PERFORMANCE PREDICTION OF TIDAL STREAM TURBINES IN YAWED FLOW" in NAFEMS World Congress 2007. 2007. Vancouver.

- Masters, I., J. Orme, and J. Chapman, "Towards realistic marine flow conditions for tidal stream turbines" in 7th European Wave and Tidal Energy Conference. 2007. Porto, Portugal.

- Masters, I., J. Chapman, and J. Orme, "A Three-Dimensional Tidal Stream Turbine Hydrodynamic Performance Model" in World Renewable Energy congress X. 2008. Glasgow.

- Chapman, J., J. Orme, and I. Masters, "Velocity Mapping Procedures for Tidal Stream Turbines in an Arbitrary Flow Field and the Implications on Performance Due to Non-Uniform Flow" in Fifteenth UK Conference of the Association of Computational Mechanics in Engineering. 2007. Glasgow: Civil-Comp Press.

- Chapman, J., I. Masters, and J. Orme, "Rotor Performance Prediction for Tidal Current Turbines", in A Joint Conference of The Association for Computational Mechanics in Engineering (UK) and The Irish Society for Scientific and Engineering Computation, C.G. Armstrong, Editor. 2006, Queen's University, Belfast: Queen's University, Belfast. p. 103-106.

7.5 References

[1] Bahaj, A., *et al.*, "Power and thrust measurements of marine current turbines under various hydrodynamic flow conditions in a cavitation tunnel and a towing tank." Renewable Energy, 2007. 32: p. 407-426.

[2] Wang, D., M. Atlar, and R. Sampson, "An experimental investigation on cavitation, noise, and slipstream characteristics of ocean stream turbines", Part A: Journal of power and Energy, 2007. 221.

[3] Bossanyi, E.A., GH Tidal Bladed Theory Manual. 2007, Garrad Hassan.

[4] Moriarty, P.J. and A.C. Hansen, AeroDyn Theory Manual. 2005, NREL: Colorado.

Appendix 1: Time Dependent Code Layout

```
Read in blade, lift and drag data and model settings

Pre process all data

for loop over time steps

   Calculate model time from time step length and step number

   if this is the first time loop

      Rotational speed = user defined starting speed

      Rotor azimuth position = user defined azimuth position

   else

      Rotational speed = new rotational speed calculated at end of last
                  time step

      Rotor azimuth position=Previous rotor azimuth
                     - (rotational speed of current time step
                     +rotational speed of last time step)/2
                     *time step length

   end

   if free yawing model is on

      if this is the first time step

         Yaw position = user defined starting yaw position

         Yawing speed = user defined yaw speed

      else
         Yawing speed =updated yawing speed calculated in previous
                  time step

         Yaw position=previous yaw position+
                  ((yaw speed of current time step
                     +yaw speed of previous time step)
                  /2)*time step length;

      end

   end
```

Go to mapping procedure presented in section 3.2 to calculate position of all elements in 3D space

Go to inflow model procedure and update 3D flow grid for current step

Interpolate flow values to element positions for rotor and supporting structure

Resolve flow to local coordinate system

for nb=1:N Loop over blade numbers

Solve BEMT equation for blade elements using the approach in figure 3.5

Store a and b variables in structure

if acceleration modelling is on

Calculate accelerative loads on rotor using Morison's equation (section 3.4)

end of acceleration model if statement

Post process data using a and b to calculate elemental loads using (3.29 and 3.30)

end of blade number loop

if supporting structure modelling is on

Calculate elemental loads on tower, nacelle and nose cone using Morison's equation (section 3.4).

end of supporting structure if statement

Post process data for all elements to obtain out of balance moments, torque and axial thrust.

if free yawing model is on

Sum all yawing torques

Calculate bearing friction (5.4) using loads calculated in post process for all blade elements.

Calculate instantaneous yawing acceleration (5.5)

```
        Use SOR algorithm (5.6) to smooth acceleration

        Calculate new yawing speed using acceleration for present step

        Check if yaw system would stop during current step, set yaw
        acceleration and yaw speed to zero if it does

    end of free yawing model

if rotor has no resistive load

    Generator torque = 0

else if Generator model is on

    Feed rotor torque and other data to bespoke generator model

    Bespoke generator model returns Generator Torque value

else if Simple generator model is on

    Calculate generator torque using (5.7)

    end

elseif Brake model is on & step is before brake cut in

    if Generator model is on

        Feed rotor torque and other data to bespoke generator model

        Bespoke generator model returns Generator Torque value

    elseif Simple generator model is on

        Calculate generator torque using (5.7)

    end

elseif Brake step is on and step is after brake cut in

    Calculate time brake has been applied for

    Braking torque is calculated as a portion of the maximum braking
    Torque (section 5.4)

end  of generator type if statements

if Brake model is not on
```

```
    if rotor is stationary and hydrodynamic torque is less than bearing
      friction

        Rotational acceleration=0

        Rotational speed = 0

    else

        Rotational acceleration= (hydrodynamic torque-friction torque
                                  -generator torque)/Rotational moment
                                  of inertia

    end of rotational acceleration if statement

  Calculate new rotor speed using previous rotational speed and
  rotational acceleration

  end

end of loop over time

  Run error checking and log error warnings

Plot useful data
```